UNIVERSITÀ DEGLI STUDI DI TRIESTE
e
UNIVERSITÀ CA' FOSCARI VENEZIA
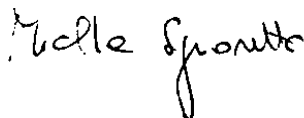
XXXIV CICLO DEL DOTTORATO DI RICERCA IN CHIMICA

Valorization of biomass to chemicals using microporous and mesoporous materials

Settore scientifico-disciplinare: **CHIM/04**

DOTTORANDA
SEYEDEH SOMAYEH TAGHAVI

COORDINATORE
PROF. ALESSIO ENZO

SUPERVISORE DI TESI
PROF. MICHELA SIGNORETTO

CO-SUPERVISORE DI TESI
PROF. MOJGAN ZENDEHDEL

ANNO ACCADEMICO 2020/2021

II

Abstract

The epic challenge of the 21st century is filling the gap between energy, fuels and chemicals supplies and demands with clean, reliable and inexpensive resources. To this end, the main challenge of the thesis is the promotion of sustainable policies that spur economic growth and environmental protection in a global context, particularly in terms of reducing greenhouse-gas emissions that contribute to climate change. Using biomass as a resource can assist at meeting the proposed policies for a safe, green, and sustainable future. Therefore, this thesis took the advantages of different micro-mesoporous heterogenous catalysts for valorization of different biomass-derived model compounds to valuable biochemicals. The first step of research focused on using the carbohydrate fraction of lignocellulosic biomass (glucose and cellulose) and their conversion to levulinic acid over ion-exchanged ZSM-5 zeolite prepared by different techniques and ions, HMS mesoporous silica and their composites as the catalysts. Among all ion-exchanged ZSM-5 catalysts, microwave assisted solid state ion-exchange of ZSM-5 using Cu(II) as the ion could provide balanced and low density of acid site and the highest catalytic performance in glucose conversion to levulinic acid. The tailored morphological, textural features and acid properties of CuZSM-5(60%)@HMS composite improved the formation of the highest yield of levulinic acid from conversion of both glucose and cellulose. In addition, a further transformation of levulinic acid to γ-Valerolactone was studied over bifunctional Ni,Al/activated biochar based catalysts. Aluminium precipitation technique could better improve weak Lewis acid site dispersion and its better activity in dehydration step of the reaction. Among all catalytic supports, activated biochar from tannery shaving waste and from vine wood waste acted as the best ones. The second step of the work focused on essential oil fraction of lignocellulosic biomass (citronellal) and its one-pot transformation to menthol over Ni/H-Beta based catalysts. 15 wt.% Ni on H-Beta-25 displayed the best synergy of the total concentration of acid sites, Lewis to Brønsted acid sites ratio, and metal loading and dispersion giving the best catalytic result. Therefore, the results obtained from catalysts characterisation helped on providing a correlation between the chemical, textural and morphological properties of the catalysts with their different efficiencies in the studied reactions.

Contents

List of abbreviations

AAS	Atomic Absorption Spectroscopy
ACP	Acyclic Products
BET	Brunauer–Emmett–Teller
B.J.H	Barrett-Joyner-Halenda
CAGR	Compound Average Growth Rate
CAL	Citronellal
CB	Liquid phase Carbon Balance
C_B	Brønsted acid sites Concentration
C_L	Lewis acid sites Concentration
CLOL	Citronellol
CP	Cyclic Products
DM	Dimeric ethers
DME	3,7-dimethyloctane
DFP	Defunctionalization Products
DMO	3,7-dimethyloctanol
DR	Dubinin-Radushkevich
DTA	Differential Thermal Analysis
EDS	Energy Dispersive System
EEA	European Environment Agency
FA	Formic acid
FID	Flame Ionization Detector

FTIR	Fourier-Transform Infrared spectroscopy
GC	Gas Chromatography
GC/MS	Gas chromatography/mass spectroscopy
GHG	Greenhouse Gas emission
GVL	γ-Valerolactone
HPLC	High-Performance Liquid Chromatography
ICP-OES	Inductively Couple Plasma–Optical Emission Spectrometry
IIP	($\pm$)-isoisopulegol
IM	($\pm$)-isomenthol
IP	($\pm$)-isopulegol
LA	Levulinic acid
L/B	Lewis to Brønsted acids ratio
ME	Menthol
NH$_3$-TPD	Temperature Programmed Desorption of ammonia
NIIP	($\pm$)-neoisopulegol
MIM	($\pm$)-neoisomenthol
NIP	($\pm$)-neoisopulegol
NEM	($\pm$)-neomenthol
Ps	Pulegols
r	reaction rate
S	Selectivity
SEM	Scanning Electron Microscope
SS	Stereoselectivity

TCD	Thermal Conductivity Detector
TEM	Transmission Electron Microscopies
TEOS	Tetraethyl orthosilicate
TGA	Thermal Gravimetric Analysis
TOF	Turnover frequency
TPD	Temperature Programed Desorption
TPR	Temperature Programed Reduction
TRS	Total Reducing Sugars
X	Conversion
XRD	X-ray Diffraction
Y	Yield
2,6-DMP	2,6-dimethylpyridine
5-HMF	5-hydroxymethyl furfural

Chapter 1. Introduction

The European and global energy and chemical vectors are speedily altering to meet the incremental competition, social challenges, and the growing endeavor for a safe, green, and sustainable future. Although fossil fuels will be charged for at the minimum next three decades, transition to new technologies based on sustainable and renewable energy and chemical resources is viable for the backbone of the future economic cycle. Several factors such as motivations for innovation, socio-environmental value, resource guarantee, and greenhouse gas reduction would regulate the current energy-chemistry nexus changes. Thus, the future scenario of refineries will be established by the ongoing substitution of fossil fuel-derived products with the renewable outcomes [1].

1.1. Climate change mitigation and sustainable future by harnessing the energy, fuels, and chemical resources' transition

In 2017, it was reported that 22% of global GHG emissions was caused by industry [2]. Moreover, the reports by the end of 2010 displayed that the majority of global GHG emission was affected by fossil fuels consumption with an increment of more than 390 ppm concentration, being 39% more than preindustrial levels [3]. Considering that chemical products are omnipresent in this modern world, they come mostly from fossil resources and are the largest and third largest industrial energy user and CO_2 emitter, respectively [4]. In 2022, China has the highest level of CO_2 emissions, producing 11.535 gigatons of CO_2 emissions, followed by the United States with 5.107 gigatons. Italy with 0.33156 gigatons causes 0.87% of world total CO_2 emission (Figure 1.1) [5].

One of the most prominent objectives and key concern of international climate debate has been the management of global warming to not to exceed more than 2 ℃ [3]. Therefore, it is worthwhile to reduce these dangerous emissions and meet the Glasgow COP26 UN conference (November 2021) goal of achieving a net 55% reduction by 2050 compared to levels in 1990 [6]. In fact, every technological development should be in-line with ending destitution and hunger, supplying safe, clean and low-cost energy to everyone, and providing sustainable industrialization and flexible infrastructure with progressive innovation [7].
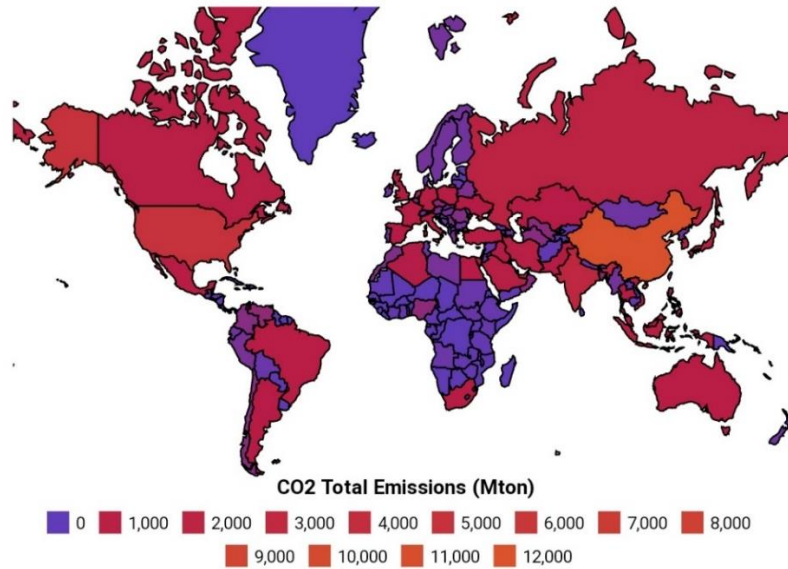
Figure 1.1*. CO2 emission by country in 2022 reported by* [5].

According to the European Environment Agency (EEA) estimation, greenhouse gas (GHG) emissions saw a 31% of drop in 2020 compared to 1990. Indeed, European Member States went beyond their 2020 emission reduction target of 20% (Figure 1.2).
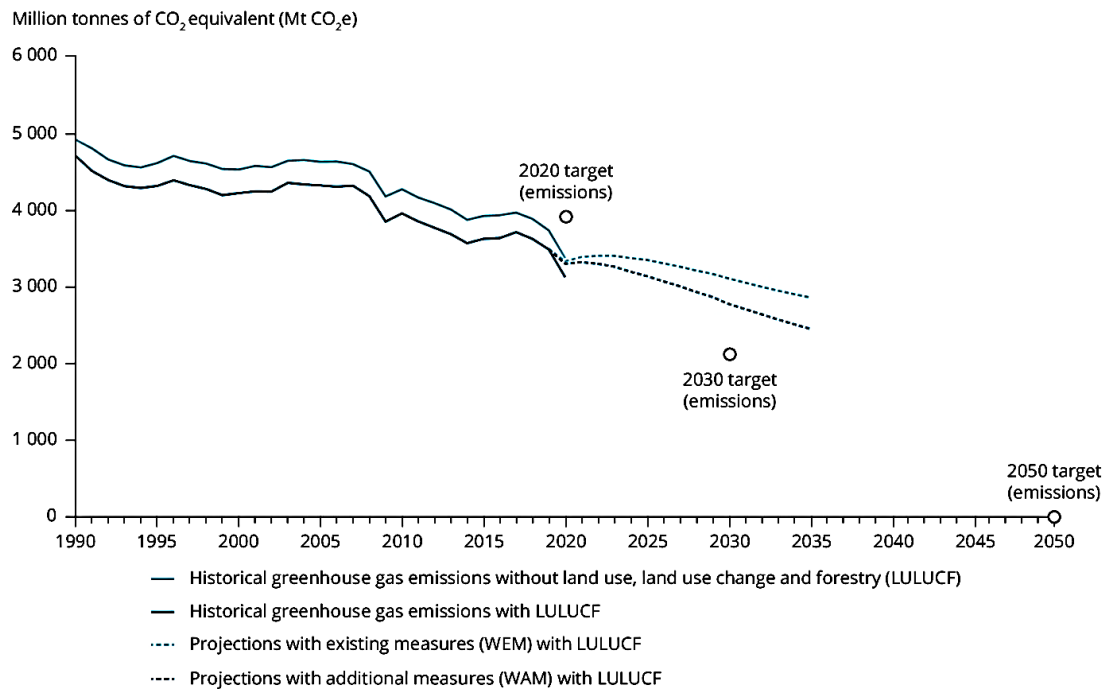
Figure 1.2*. Historical trends and future projections of greenhouse gas emission* [8].

5

To have a continuous emission decline, the European Council approved four significant aims by 2030 including: a) a further decline of 41% GHG emission in Europe; b) achieving to the minimum 27% consumption of renewable energy; c) the increment of energy efficiency up to 27%; and d) reaching to the target of 10% electricity interconnection [9].

In addition, since the world is struggling with the issue of finite fossil resources, the path of renewable resources' utilization is going to be embarking for humanity [10]. Overall, to overcome twin problems of non-renewable resources and climate change, there is a growing desire of rapid and irreversible transition to energy and chemicals production by using effective and sustainable approaches. The advantages of using sustainable technologies are in diminishing secondary waste, being clean and sustainable, and having lower environmental impacts with mitigation of GHG emission [3]. Biomass and biomass waste, solar, geothermal, hydroelectric, and wind are prone and adaptable resources for valuable chemicals, fuels, domestic heating system and electricity generation [10]. Among them, biomass might be a probable raw material for energy and fuel industries and chemical production in several sectors such as polymers, agricultural, pharmaceutical, and plasticizer. In addition, biomass can be a promising substitute for fossil-based raw material due to two important facts: it has a short formation or regrowth time of even a few months, and the CO_2 released from the usage of biomass can be consumed for its production through natural photosynthesis processes [11].

1.2. Biomass as a green and renewable resource

Biomass is any organic substance coming from vegetal and animals' origins, and can be obtained from urban and industrial waste. The plants store the solar energy as chemical bonds through the photosynthesis process. Animals and people get the chemical energy of the plants by consuming them. The organic composition of biomass is affected by its origin and constitutes of 30-60% carbon, 30-40% oxygen, with 5-6% hydrogen, and approximately 1% of nitrogen and sulfur, and chlorines. In addition, inorganic elements, namely ash, are physically bounded to the biomass structure and are mostly extractable by washing process [12].

Compared to fossil-based resources, biomass has been a significant energy, fuels and chemical resource due to much shorter forming duration and reducing greenhouse gas emissions. Indeed, CO_2 emitted from biomass utilization can be consumed through plant growing and hence no net

greenhouse gas influence could exist [13]. Wide variety of products can be obtained from biomass such as gas fuels (H_2 and CH_4), liquid fuels (biodiesel, methanol, ethanol, and vegetable oil), solid fuels (hydrocarbons and biochar), and valuable chemicals from various applications of thermal and electricity energies, vehicle fuels, pharmaceutical, and cosmetic [14]. Importantly, petroleum obtained from fossil resource has a higher H/C and lower O/C mol ratios and, hence, a higher heating value compared to biomass derived feedstocks. Although biomass with high O/C mol ratios needs an upgrading via removal of oxygen in the form of CO, CO_2 and H_2O, this high ratio could be beneficial in the inexpensive extraction of valuable chemicals compared to fossil resources [15,16].

1.3. Biomass generations

Biomass is classified into four generations:

(a) First generation of biomass comes from food crops such as sugar, starchy crops, vegetable oil with vegetal origin, and animal fat with animal origin.

(b) Second generation of biomass is non-edible plants and waste (agricultural, industrial, municipal or domestic) consisting of the waste with vegetal origin such as wood, organic waste, and food crop waste, and with animal origin such as leather tannery waste. Most of vegetal biomasses in this generation are considered as the lignocellulosic biomass.

(c) Third generation comes from marine biomass like algae.

(d) Fourth generation derived from genetically and metabolically modified organisms.

Lignocellulosic biomass is one of the most plentiful and potential biomasses that represents a promising source for biochemical and biofuel production. Lignocellulosic biomass comproses of 40-50 wt.% cellulose, 15-30 wt.% hemicellulose, 16-33 wt.% lignin and 1-10 wt.% extractive materials such as essential oil. The chemical structure of lignocellulosic biomass is displayed in Figure 1.3.
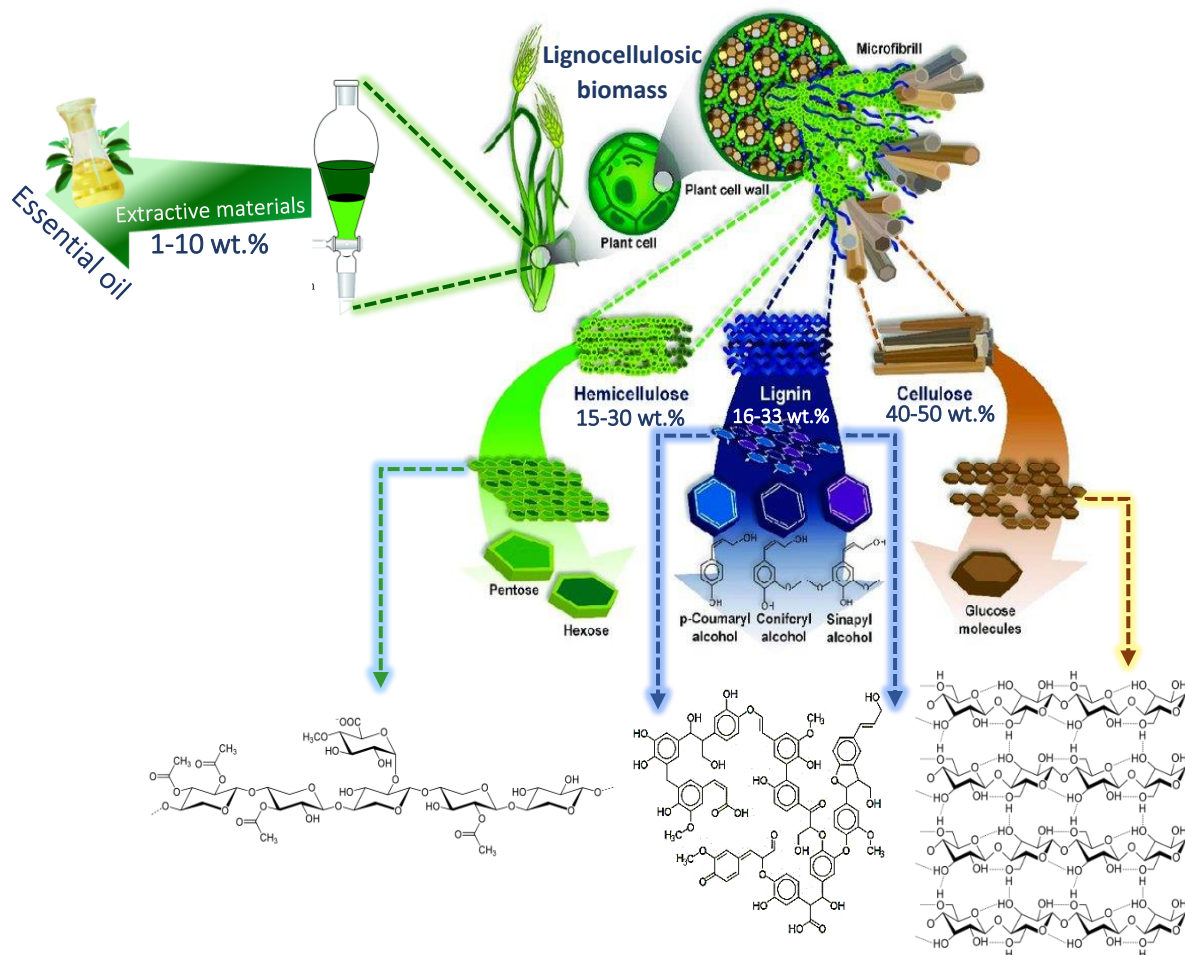
Figure 1.3. *Chemical structure of lignocellulosic biomass* [17].

One-third of lignocellulosic biomass is cellulose, being a potential resource for fuels and chemicals production [18]. Cellulose as a resistant fibrous material comes from cell walls of the plants and is made of linear polymers of glucose monomers connected with β-1,4 glycosidic ester bonds [19–21]. Cellulose with crystal structure is not soluble in water, but it has various hydrogen bonds of both intramolecular and intermolecular nature [22]. It was reported that native cellulose can have an average molecular weight of ca. 100000 g/mol [23,24].

Hemicellulose or polyose is a heteropolysaccharide composed of uronic acid and different mono-sugars such as *D*-glucose, *D*-mannose, *D*-galactose, *L*-arabinose, *D*-xylose, 4-*O*methyl-*D*-glucuronic acid, *D*-galacturonic acid, that are linked with β-1,4 bonds [25]. Hemicellulose has an

amorphous structure that acts as a connective material for cellulose fibers. Moreover, hemicellulose interacts with lignin functional groups and forms hydrogen bond with cellulose [26].

Lignin as a three-dimensional amorphous polymer is classified into three types of softwood, hardwood and herbaceous plant lignin. Softwood lignin is made of coniferyl alcohol and coumaryl alcohol. Hardwood lignin is composed of sinapyl, coniferyl and coumaryl alcohols. Herbaceous plant lignin is formed from *p*-hydroxycinnamic acids and phenylpropane [27].

Wide variety of nonstructural extractive compounds with low molecular weight can be extracted from lignocellulosic biomass using different techniques such as extraction with solvent and steam distillation extraction. The extractive materials could be fats, essential oils, waxes, free fatty acids, tannins, resins, terpenoids, gums, tropolenes, and volatile hydrocarbons. The extractive substances in biomass are responsible for providing biological maintenance [28].

The feedstocks used in this study were mainly originated from second generation biomass of vegetal origin and typically lignocellulosic structure.

1.4. Biomass valorization technologies

Several routes of biomass valorization are schematically presented in Figure 1.4. Hence, the structure of initial biomass feedstock and the technology that is used for its valorization have significant effects on the type and features of final bioproducts. The routes of biomass conversion are:

1) Pretreatment: Biomass' typical lignocellulosic groups have a rigid structure and the poly-sugars in their structure can be hardly hydrolyzed. The cross-linking of lignin with cellulose and hemicellulose importantly can diminish the enzyme or acid interaction with them limiting their hydrolysis to mono-sugars and their further conversion to valuable chemicals and fuels. In addition, sometimes lignocellulosic biomass is interesting due to the presence of a prominent essential oil inside for use in cosmetic and pharmaceutical applications. Thus, several pretreatment techniques were studied to facilitate the extraction of proposed structure in biomass and improve its biodegradability. The four main and common pretreatments are physical, chemical, physicochemical and biological methods (Figure 1.4) [29,30].

2a) Thermochemical conversion: this route is a sort of thermal and chemical processes classified to different methods. In pyrolysis, the decomposition of biomass happens at elevated temperature and inert atmosphere, and three phases of the products including liquid product or bio-oil (gasoline, jet fuel, biodiesel), gas product or biogas (H_2, CH_4, CO, CO_2), and solid product or biochar can be obtained [31]. In gasification, four main steps of oxidation, drying, pyrolysis and reduction are included for production of hydrogen [32]. In the liquefaction process, the decomposition of biomass in liquid phase and inert atmosphere occurs following with the repolymerization of obtained component to large oily components or liquid biofuels [33]. In hydrolysis route, the hydrocarbons of lignocellulosic biomass (cellulose and hemicellulose) go under thermally breakdown and depolymerization process in the presence of acid or enzyme and produce oligosaccharides, mono-sugars, several other intermediate bio-chemicals and biofuels [34]. In the combustion process, biomass is burned in the air and the generated heating energy leads to the production of high-pressure steam from water. Then, the steam is used in turning turbines for electricity generation.

2b) Biochemical conversion: in fermentation, the sugars of biomass transform into ethanol assisted with yeast action. In anaerobic digestion, a mixture of biogas (H_2, CO_2 and CH_4) and ammonia are produced. Although CH_4 is considered as the main product and prominent bioenergy source, this process has not been satisfactory due to economic issues [35]. Besides pyrolysis, gasification, and anaerobic digestion, the photobiological method is another route for hydrogen production.

2c) Chemical conversion: in transesterification, the oil extracted from biomass reacts with alcohol (methanol or ethanol) in the presence of acid or base catalyst and produces biodiesel [36].

Biomass valorization

1) <u>Pretreatment</u>
- Physical
- Chemical
- Physicochemical
- Biological

2a) Thermochemical conversion
- Pyrolysis
- Gasification
- Liquefaction
- **Hydrolysis**
- Combustion

2b) Biochemical conversion
- Fermentation
- Anaerobic digestion
- Photo-biological H_2 Production

2c) Chemical Conversion
- Transesterification
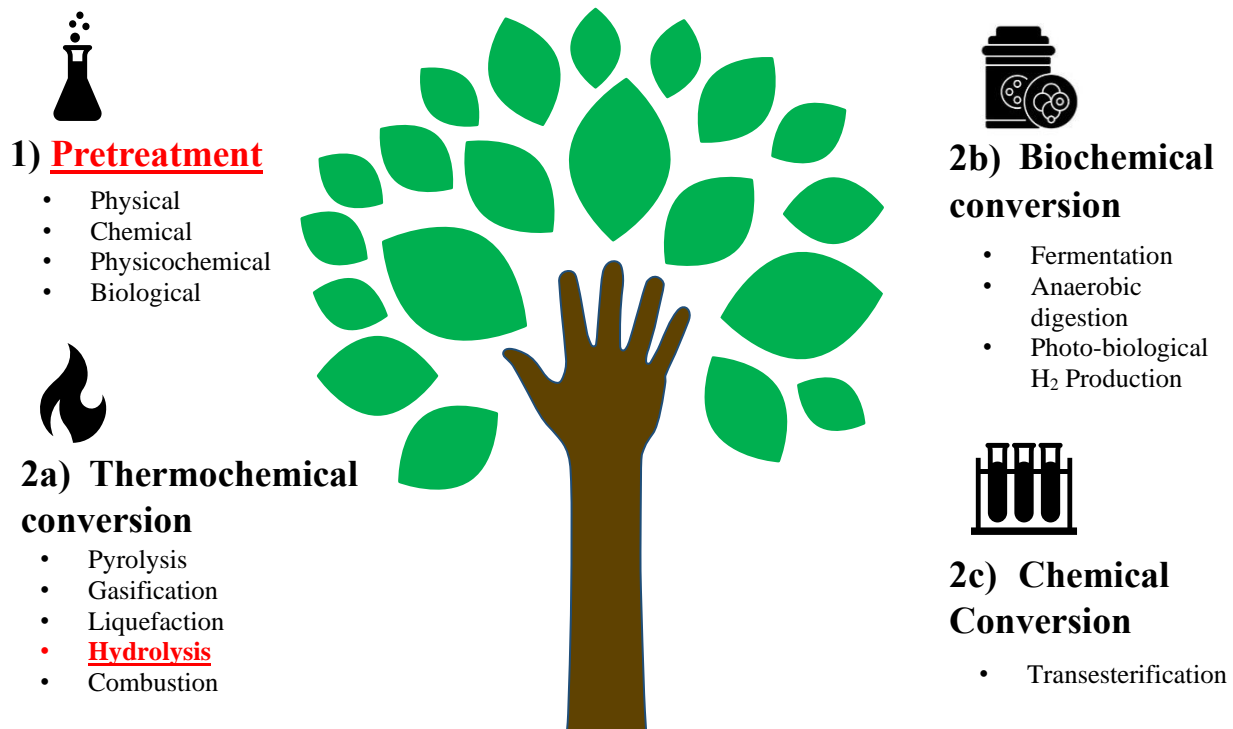
Figure 1.4. Biomass valorization technologies.

In this study, two main routes of lignocellulosic biomass valorization were studied for production of valuable biochemicals and biofuels. In the first section, cellulose as a polymeric carbohydrate in lignocellulosic biomass and its monomer glucose were selected as the target feedstocks and their catalytic valorizations to levulinic acid (LA) and γ-Valerolactone (GVL) were studied. The mentioned feedstocks in this study were used as model compounds. In particular, cellulose derives from pretreatment of lignocellulosic biomass which significantly helps in decreasing the rigid interaction between carbohydrates and lignin in the complex structure of biomass. Hence, the cellulose acid hydrolysis to glucose and other biochemicals would be facilitated. In the second section of the study, citronellal (CAL), a prominent essential oil, was selected as the model feedstock and its catalytic conversion to menthol (ME) was focused. CAL oil can be obtained from hydrogenation of citral, which is an essential oil in the lemongrass (Cymbopogon) lignocellulosic

plant. Citral can be extracted from lemongrass using different treatments such as steam distillation extraction process. The two main routes of the work are schematized in Figure 1.5.
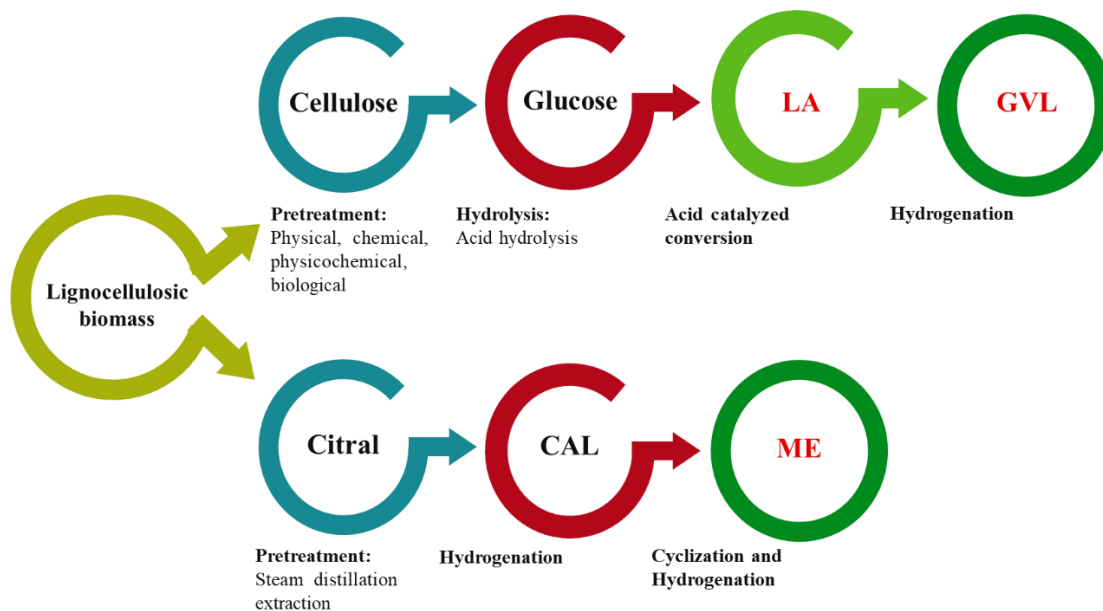
Figure 1.5. Schematic representation of lignocellulosic materials conversion in the present study (note that the starting substrates in this thesis are cellulose, glucose, LA, and CAL)

Therefore, the real aim behind this thesis is the investigation of different low-cost, efficient and sustainable heterogeneous catalysts for valorization of bio-based model components to valuable fuels and chemicals. In the last 50 years, heterogeneous catalysis has been one of the main reasons for petrochemical industry development. Of course, the future biorefinery technologies and renewable-based scenario would desire heterogeneous catalysis as a key factor for the production of biofuels and platform chemicals [37]. Hence, this thesis concepts are divided into two parts schematized in Figure 1.6. The first part is focused on the carbohydrate section of lignocellulosic biomass typically cellulose and glucose and their conversion to LA and GVL. In the second part, the essential oil fraction of lignocellulosic biomass namely CAL and its conversion to ME will be studied.

Lignocellulosic biomass valorization

Lignin

Hemicellulose

Cellulose

Citronellal essential oil

Heterogeneous catalysts

Target product:

Levulinic acid

Target product:

γ-Valerolactone

Target product:

Menthol

❖ **Chapter 2**

Investigation of different ion-exchange techniques for ZSM-5 zeolite as the catalyst of glucose conversion to levulinic acid

Chapter 5 ❖

The effects of acidity and metal loading for H-Beta supported Ni catalysts in transformation of citronellal to menthol

❖ **Chapter 3**

Glucose and cellulose conversions to levulinic acid using the composites of ion-exchanged ZSM-5 and HMS mesoporous silica

❖**Chapter 4**

Conversion of levulinic acid to γ-Valerolactone using bifunctional Ni, Al supported on biochars catalysts

Figure 1.6. *Schematic representation of all the developed topics of the thesis.*

To meet the represented concepts, four chapters will be reported in this thesis (Figure 1.6):

Chapter 2: In this chapter, transformation of glucose to LA was discussed over ion-exchanged ZSM-5 zeolite. For modification of the ZSM-5 based catalysts, different ion-exchanges including aqueous and solid microwave assisted techniques using different ions from fourth period of periodic table were applied and the best catalyst in the aspect of suitable acidic, textural and morphological properties for a better efficiency in the proposed reaction was selected.

Chapter 3: In this chapter, besides glucose, bulky cellulose was applied as the substrate for production of LA. The best ion-exchanged ZSM-5 from chapter 1 was selected as the acid part of the catalyst and to improve the surface area and porosity of the catalyst for increasing the mass transfer of bulky substrate and products, HMS mesoporous silica was used. Different micro mesoporous composites of ion-exchanged ZSM-5 and HMS were formulated and studied for the proposed reaction.

Chapter 4: In this chapter, LA conversion to GVL was investigated over bifunctional Ni, Al-biochar based catalysts. For formulation of catalysts, four different biomasses from vegetal and animal origins were selected, pyrolyzed in an inert atmosphere, and physically activated in the presence of CO_2 agent. The activated biochars were used as the support of catalysts and Al as a Lewis acid site was introduced by wet impregnation and precipitation methods, while Ni as hydrogenation active phase was incorporated to the support by wet impregnation technique. The acidic, textural and morphological properties of the catalysts and their effects on efficiency of proposed reaction was discussed.

Chapter 5: In this chapter, the essential oil fraction of lignocellulosic biomass namely CAL and its conversion to ME over Ni/H-Beta zeolite-based catalysts was studied. The effects of different H-Beta zeolite acidity and different Ni loading on the activity and selectivity of the catalysts in target reaction were investigated.

Lignocellulosic biomass valorization

Lignin

Hemicellulose

Cellulose

Citronellal essential oil

Heterogeneous catalysts

Target product:

Levulinic acid

Target product:

γ-Valerolactone

Target product:

Menthol

❖ **Chapter 2**
Investigation of different ion-exchange techniques for ZSM-5 zeolite as the catalyst of glucose conversion to levulinic acid

Chapter 5 ❖
The effects of acidity and metal loading for H-Beta supported Ni catalysts in transformation of citronellal to menthol

❖ **Chapter 3**
Glucose and cellulose conversions to levulinic acid using the composites of ion-exchanged ZSM-5 and HMS mesoporous silica

❖ **Chapter 4**
Conversion of levulinic acid to γ-Valerolactone using bifunctional Ni, Al supported on biochars catalysts

15

Chapter 2. Investigation of different ion-exchange techniques for ZSM-5 zeolite as the catalyst of glucose conversion to levulinic acid

2.1. Introduction

2.1.1. Levulinic acid production from cellulose and glucose

Levulinic acid (LA) is a C5-alkyl carbon with linear chain that is named as gamma ketovaleric acid or 4-oxopentanoic acid, and 3-acetylpropionic acid. It is a short chain fatty acid with molecular formula $C_5H_8O_3$ [38]. The Biomass Program of the US Department of Energy in 2004 regarded LA as one of the top 12 most promising bio-based platform chemicals [39]. LA can be considered as a potential chemical bridge between biomass and petroleum and an intermediate for production of fuels and fuel additives such as ethyl levulinate, GVL, methyl tetrahydrofuran, and a family of valerate esters [40–46]. Besides renewable biofuels, LA can be transferred to several other chemicals for wide variety applications in industries such as in resins, solvents, chemical intermediates, electronics, polymers, adsorbents, batteries, photography, plasticizers rubber, drug delivery systems, cosmetics, pharmaceutical products, and textiles [47–58].

The market size of LA was around \$27.2 million in 2019, and its annual growth rate (CAGR) has been expected to be 8.8% for the forecast period of 2020–2030. The increase could be due to the growing demand of LA derivatives in the end-use industries, enhancement of bio-based LA production and commercialization. GFBiochemicals Ltd (Italy) acts as the largest LA producer and a key LA market player which is based on biomass conversion [59,60].

Traditionally, LA had been produced from petrochemical conversion of maleic anhydride [54]. In 1840, for the first time LA was synthesized from acid hydrolysis of fructose as a biomass derived feedstock by a Dutch Professor G. J. Mulde and that was the cause of the name, levulinic acid, which came from the former term "levulose" for fructose [61]. However, the commercialization of LA was prolonged to one century after due to the high cost of raw materials and equipment, low yield and difficult recovery [62]. In the 1940s, LA had been commercially produced in the United States by A. E. Staley, Dectur, Illinois. Meanwhile, cellulose as a low-cost material and its derived hexoses were introduced as a potential feedstock for LA production. This could introduce a new

option in the aspect of techno-economic evaluations for applying a suitable source of sugars and overcome the barrier of high-cost raw materials [54,61].

Several renewable starting materials have been introduced for the synthesis of LA including raw biomasses, polysaccharides, monosaccharides, furfural, and 5-hydroxymethyl furfural intermediate (5-HMF). Polysaccharides including starch, cellulose, hemicellulose, and chitin, are the main components of biomass. Their hydrolysis could lead to the formation of monosaccharides, such as glucose and fructose [63]. In cellulose, glucose monomer units are related to β-1,4-glycosidic bonds with large amount of intra and intermolecular hydrogen bonds in the chains. The transformation of cellulose to glucose and other biochemicals through the hydrolysis of its strong bonds is still a challenge for researchers. During hydrolysis of cellulose, the cleavage of β-1,4-glycosidic bonds occur in the presence of a Brønsted acid catalyst [64]. The conversion of glucose to LA passes through several reactions and side reactions. The main and desirable reaction pathway is isomerization of glucose to fructose which requires Lewis acid catalyst followed by dehydration of fructose to 5-hydroxymethylfurfural (5-HMF) and rehydration of 5-HMF to LA and formic acid (FA) using both Lewis and Brønsted acid catalysts (Figure 2.1) [65]. However, in the presence of high Brønsted acid sites, glucose is more prone for direct dehydration to 5-HMF [66] and FA, and fructose is more disposed to degradation into FA and humins [67]. The 5-HMF and consequently LA yields from direct dehydration of glucose are lower due to the glucose's stable pyranoside ring structure and having side reactions [68]. On the contrary, starting from isomerization of glucose to fructose, higher 5-HMF and the LA yields can be produced from fructose [68–72]. In addition, it was reported that the reaction from glucose to LA can also path from furfuryl alcohol intermediate to produce FA and LA in the presence of a high concentration of Brønsted acid catalyst. However, the pathway to 5-HMF intermediate is more favorable than to furfuryl alcohol intermediate in the thermodynamical aspect [73]. Hence, it is also prominent to reveal reaction pathways and limit the formation of byproducts particularly solid humins by optimization of the acidity of the catalyst meaning the density, strength and type of the acid site and reaction conditions. Humins are carbon-based macromolecular substances having furan-rich polymers with various oxygen functional groups. Humins can lead to several problems such as reactor clogging, increase of pressure, decrease of the heat transfer efficiency, deactivation of solid acid catalysts and absorb 5-HMF, LA, carbohydrate, and homogeneous catalyst [65,74].

17
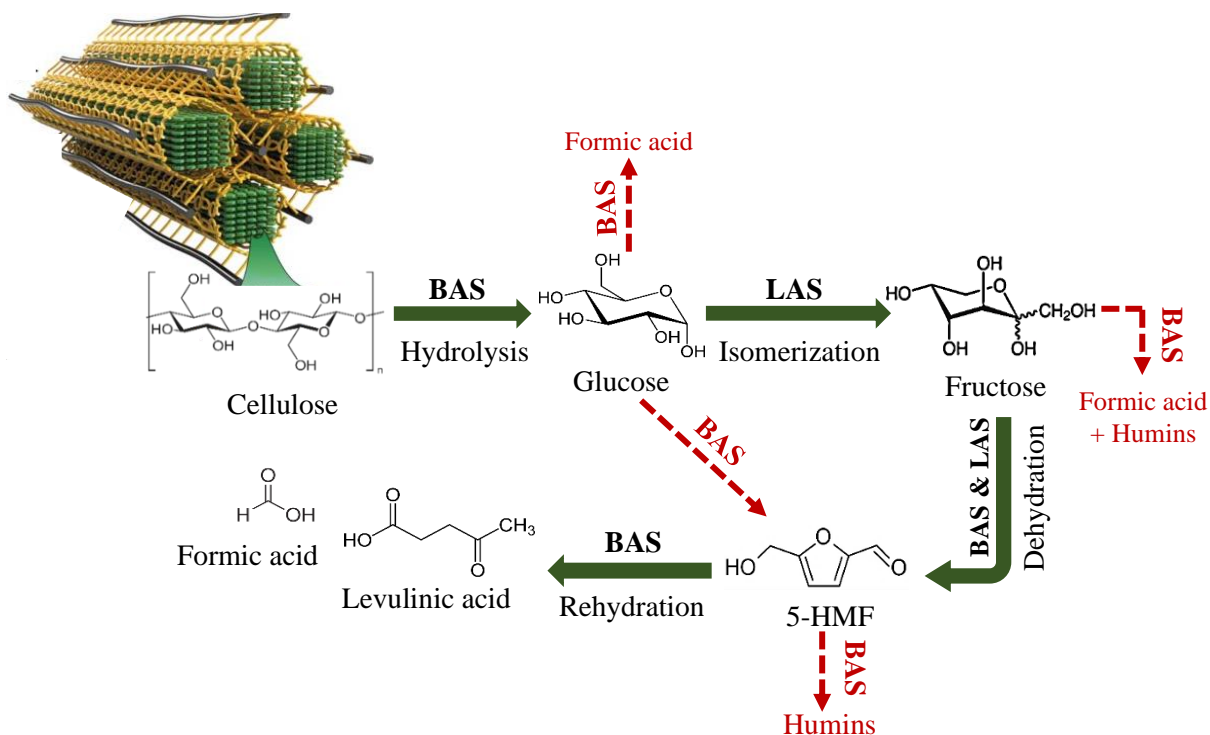
Figure 2.1. Possible reaction pathway from cellulose to levulinic acid. (BAS: Brønsted acid site; LAS: Lewis acid site)

The thermodynamic of the reaction from glucose to LA comprises a very weakly endothermic isomerization of glucose to fructose with enthalpy change of ~ 8.4 kJ/mol, a highly endothermic dehydration of fructose to 5-HMF with enthalpy change up to 92 kJ/mol, and exothermic rehydration of 5-HMF to LA with enthalpy change of minus 133.9 kJ/mol [75].

Therefore, the selection of an appropriate catalyst with a suitable acidic concentration, strength, and balance between the Lewis and Brønsted acid sites is of crucial importance to lead the reaction into desirable pathway and diminish side-reactions. In the next section, a state-of-art about the catalytic systems of the proposed reaction and an introduction about the catalysts used in the present study will be referred.

2.1.2. Catalysts for conversion of glucose to levulinic acid

Traditionally, homogeneous catalysts were extensively applied for conversion of lignocellulosic biomass and also its derived sugars to LA especially in industrial level. Among them, H_2SO_4, HCl, and metal chlorides demonstrated good results [63,76–79]. However, the hard recovery, disposal

matters along with reactor corrosion made heterogeneous catalysts as a sustainable and green option for having an environmentally favorable process. For applying heterogeneous catalysts, several factors must be taken into account such as: (1) development of a hydrothermal hydrolysis using solid catalysts; (2) the stability of catalyst in aqueous and acidic mediums; (3) having high surface area and large pores for the easy access of polymeric substrate to the catalyst active sites; (4) easing the mass transfer between saccharides and catalyst active sites, (5) diminishing solid humins formation; (6) possessing enough concentration and strength of acid sites for hydrolysis of cellulose [64,65,74,80–83].

Different heterogeneous Brønsted and Lewis acid catalysts have been recently reported in the literature for the formation of LA from glucose such as mesoporous silica, zeolites, metal oxide supported metals, and organic polymers [84–87]. Zirconium and aluminum-based catalysts were used for glucose to LA reaction. Zirconium phosphate was more selective to 5-HMF and produced low LA yield (21%) at 160 ℃, and 50 bar initial pressure for 3 h, because of having only Lewis acid site in the catalyst [88]. Al–Zr mixed oxide has indicated a very low LA yield of 6.1% and high yield of lactic acid owing to having both acid and base sites in the catalyst [89]. Literature review displays that zeolite as a cheap, natural, non-toxic, and non-corrosive catalyst with appropriate microporous structure and modifiable Lewis and Brønsted acid sites is suitable for the transformation of glucose to LA [90–92]. Among different zeolites, Y, ZSM-5 and Beta were often applied for related reaction [70,93–95]. For example, Zeng et al. studied the influence of MFI-type ZRP zeolite with different SiO_2/Al_2O_3 ratios for glucose transformation. It was shown that different SiO_2/Al_2O_3 ratios led to the change of zeolite acid sites concentration and strength which had an impact on the yield of LA. The ZRP zeolite with SiO_2/Al_2O_3 ratio of 30 acted as the best catalyst giving 35% of LA yield for 8 h reaction [96]. Garcés and co-workers studied the reaction using pure Beta, Y and ZSM-5 zeolites as heterogeneous catalysts and HCl as a homogeneous catalyst. It was reported that each pure zeolite cannot catalyze LA production and the presence of HCl as a Brønsted acid besides very long reaction time were desired considering that using this acid was far from green chemistry rule [97]. Moreover, a similar work studied ion-exchanged Sn-Beta zeolite as a Lewis acid catalyst for catalyzing the isomerization of glucose to fructose. In this study, the conversion of fructose to LA was catalyzed by Amberlyst-15 catalyst with Brønsted acid site during a long reaction time (12 h) and 52% yield of LA was produced [98]. Zeolite is a microporous and crystalline aluminosilicate material formed by corner-sharing TO_4

(T= Si or Al) tetrahedra, with silicon and aluminum elements connecting by bridging hydroxyl groups. In this thesis, ZSM-5 zeolite was selected as the catalyst for transformation of glucose to LA.

ZSM-5 is a two-dimensional (2D) zeolite with the MFI topology, 10-membered rings, Z-shaped channels (0.51 - 0.55 nm), and straight channels (0.53 - 0.56 nm). Figure 2.2 shows the framework of ZSM-5 zeolite using ordered assembly of smaller unitary units (SBU). In this type of representation, silicon and aluminum tetrahedra are considered. The configuration of six SBU 5–1 tetrahedra (Figure 2.2a) leads to the formation of pentasil-like structural units (Figure 2.2b). Then, a constitution of the chain groups (Figure 2.2c) causes tetrahedrons layers (Figure 2.2d) and makes zeolite porosity. In addition, the configuration of the secondary building units forms the micropores, straight channels with internal sinusoidal channels (Figure 2.2e). The shape (sinusoidal and right) and dimension of the channels are strongly affected by Si/Al ratio [99].
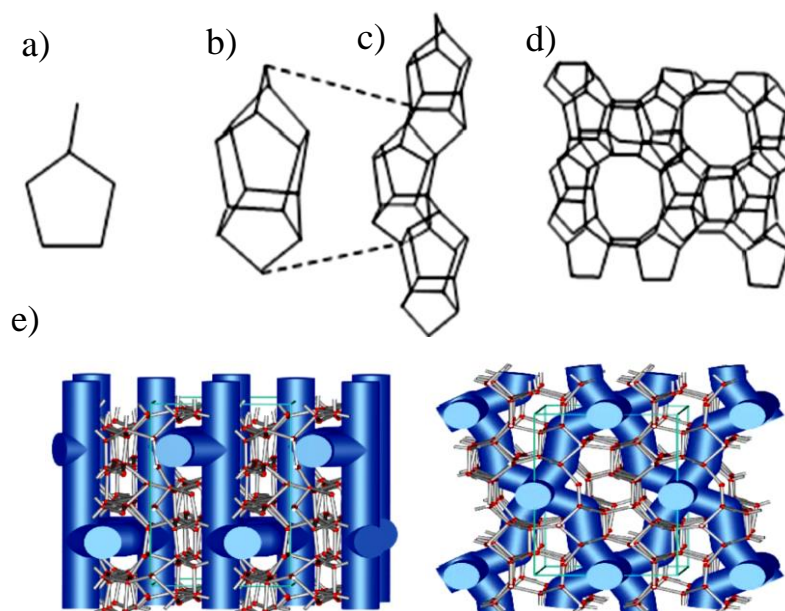
***Figure 2.2**. Elements constituting the structure of a ZSM-5 zeolite. (a) Type 5–1 SBU secondary construction unit. Assembly of secondary building units (b) in pentasil group, (c) in chain, and (d) in layers of tetrahedra. e) The channels of the ZSM-5.* [97]

Zeolite itself has both Lewis and Brønsted acid sites. The Lewis and Brønsted acid sites of zeolite are originated from extra framework Al and hydroxyl groups connecting Si and Al, respectively

which are tunable and can be modified with different ion-exchange techniques. Ion exchange of monovalent cations with polyvalent cations in aqueous medium can make strong Brønsted centers because of hydrolysis phenomena and being fruitful for some organic reactions [100]. Moreover, the number of Lewis acid sites can be (i) increased by enhancing the non-tetrahedrally bonded extra-framework aluminum and (ii) created by incorporation of metals and metals ions into the zeolite structure using solid state ion-exchange technique [101–103]. Solid state ion-exchange can be performed in the solid phase under elevated temperature following traditional methods with electronical furnace or using microwave irradiation [95]. Microwave irradiation assists on the decreases of both temperature and time of metals ions exchange in the zeolite [97,104].

2.1.3. The aim of the chapter

In this chapter, the optimization of different ion-exchanges of ZSM-5 zeolite and the investigation of their performance in glucose to LA conversion were studied. In particular, different ion-exchange methods were applied to modulate ZSM-5 acid sites considering their concentration, strength and type (Lewis and Brønsted) aiming to obtain a green, adjustable, and bifunctional acidic heterogeneous catalyst for the proposed reaction. Therefore, both aqueous and microwave assisted solid ion-exchange methods were applied for ZSM-5 zeolite using NH_4Cl and solid transition metals [Mn(II), Fe(II), Fe(III), Co(II), Ni(II), Cu(II)] chlorides. Morphological and textural features, and acidity of the catalysts were characterized using XRD, SEM, EDX, TG-DTA, N_2-physisorption, NH_3-TPD and FTIR both as such and by adsorbing/desorbing 2,6-dimethylpyridine (2,6-DMP) as probe molecule. Since microwave method mostly improved Lewis acid site of the zeolite, with higher Lewis to Brønsted acids ratio (L/B) and mostly weak and medium acid sites, it could catalyze the proposed reaction through desired pathway and produce a higher yield of LA. Moreover, among different exchanged metal ions, Cu(II) gave a higher performance due to its high charge transfer and introduction of low amount of acid sites to ZSM-5. The results reported in this chapter were published as: "Balanced acidity by microwave assisted ion-exchange of ZSM-5 zeolite as a catalyst for transformation of glucose to levulinic acid", S. Taghavi, E. Ghedini, F. Menegazzo, A. Giordana, G. Cerrato, G. Cruciani, A. Di Michele, M. Zendehdel, M. Signoretto, Biomass Conversion and Biorefinery, (2022) 1-19.

2.2. Experimental

2.2.1. Catalyst preparation

The parent NaZSM-5 zeolite (SiO_2/Al_2O_3 mole ratio = 30; Si/Al=15; Na_2O = 0.01 wt%) was provided from CHINA CATALYST GROUP (Dalian, China). Various ion-exchange approaches were carried out to reach a balanced acid catalyst for transformation of glucose to LA. The ion-exchange treatments are described below:

- *Treatment of NaZSM-5 with NH₄Cl solution:* NaZSM-5 was treated with a 100 ml solution of NH_4Cl (Merk) (1 M) at 90 °C in a flask connected to a reflux condenser stirred for 24 h. The sample was washed with deionized water, dried in the oven at 80 °C for 12 h, and calcined at 550 °C for 6 h. The final catalyst was labelled HZSM5 [105].

- *Aqueous ion-exchange of NaZSM-5 using CuCl₂.2H₂O solution:* 1 g of NaZSM-5 was mixed with 100 ml of $CuCl_2.2H_2O$ (Sigma-Aldrich) (0.1M) solution and then was stirred for 24 h at 25°C. The obtained solid was filtered and washed with deionized water until reaching a colorless filtrate. Finally, the sample was dried in the oven at 80 °C for 12 h. This final sample was labelled CuZSM5-S [106].

- *Microwave assisted solid state Ion-exchange of NaZSM-5:* 1 g of NaZSM-5 zeolite was mechanically mixed and grounded with 1 mmol of each metal salts ($MnCl_2.4H_2O$ (Sigma-Aldrich, ≥99.0 wt%), $FeCl_2$ (Sigma-Aldrich, ≥99.0 wt%), $FeCl_3$ (Sigma-Aldrich), $CoCl_2.6H_2O$ (Sigma-Aldrich, ≥98.0 wt%), $NiCl_2.6H_2O$ (Sigma-Aldrich, ≥99.9 wt%), and $CuCl_2.2H_2O$. Then, a heating procedure was applied for each mixture via microwave oven with 700 W power (about 235°C) for 10 min. The final catalysts were labelled MnZSM5-M, Fe(II)ZSM5-M, Fe(III)ZSM5-M, CoZSM5-M, NiZSM5-M and CuZSM5-M.

2.2.2. Catalytic test

The catalytic test was performed in a batch system made of stainless-steel autoclave (400 mL volume) equipped with mechanical stirrer, an electric heater, and a thermocouple for temperature measurement. The autoclave was charged with 2.7 mmol of glucose, 500 mg of catalyst, 100 mL of deionized water. Then, it was purged ten times with N_2 to remove the air and pressurized with 10 bars of N_2. The temperature was increased, and the reaction time was considered once the temperature reached to desired value. Moreover, the reaction was carried out under stirring rate of

600 rpm. When the test was completed, the autoclave was cooled down to 25 °C and the final mixture was filtered. The filtered sample was analysed by a high-performance liquid chromatography (HPLC) Agilent Technology 1260 Infinity II. An Aminex HPX-87H column was used in HPLC and the analysis was carried out at column temperature of 50 °C, using 5mM H_2SO_4 as the mobile phase with the flow rate of 0.6 mL/min. A UV–vis detector (Λ =195 nm) was used for analytes' identification and quantification. In addition, the effects of reaction temperature, time and glucose amount on the catalytic reaction were studied. The glucose conversion (X), liquid phase carbon balance (CB) and products yields (Y_p) were calculated using the following equations:

$$X\ (\%) = \frac{\Delta n}{n_0} \cdot 100$$

$$Y_p\ (\%) = \frac{n_p}{n_0} \cdot 100$$

$$CB\ (\%) = \frac{\sum(n_p)\cdot(C\ atoms)}{(n_0 \cdot 6)} \cdot 100$$

Where Δn corresponds to the reacted mole of glucose during the reaction. n_0 and n_p represent the mole of glucose at time zero, and the mole of each product and non-reacted glucose in the final liquid phase, respectively. In CB equation, the notation "C atoms" correspond to the number of carbon atoms in each component.

2.3. Results and discussion

2.3.1. Characterizations of the catalysts

N_2 physisorption results of catalysts are shown in Figure 2.3 and Table 2.1. In the isotherms of the samples, the sharp increment at P/P_o<0.1 is assigned to microporous texture. In addition, an isotherm profile of type IV can be observed with the H3 hysteresis loop in the pressure range of 0.5<P/P_o<0.9 that can be ascribed to the capillary condensation of slit-like mesopores attributed to intercrystallite adsorption within aggregates. Particularly, compared to ion-exchanged samples, NaZSM-5 zeolite shows sharper adsorption capacity at low pressure because of the existence of more micropores in the pure zeolite. Hence, the decrease of microporous or external surface area in all exchanged samples confirms the occlusion of open micropores by exchanged metal ions [107]. In different microwave assisted ion-exchanged samples, the sharper alteration in textural properties could be due to the introduction of a higher metal content inside the pores and channels

of ZSM-5 or the segregation of extra-framework aluminum at high temperature. Fe(III)ZSM5-M particularly showed a harsher difference that, besides above reasons, might be related to a larger charge unbalance, induced by introduction of trivalent Fe(III) cation compared to divalent cations and additionally due to amorphous phase formation diminishing the zeolite surface and pores volume [108,109]. Due to this phenomenon, Fe(II)ZSM5-M also exhibits a low surface area compared to others.
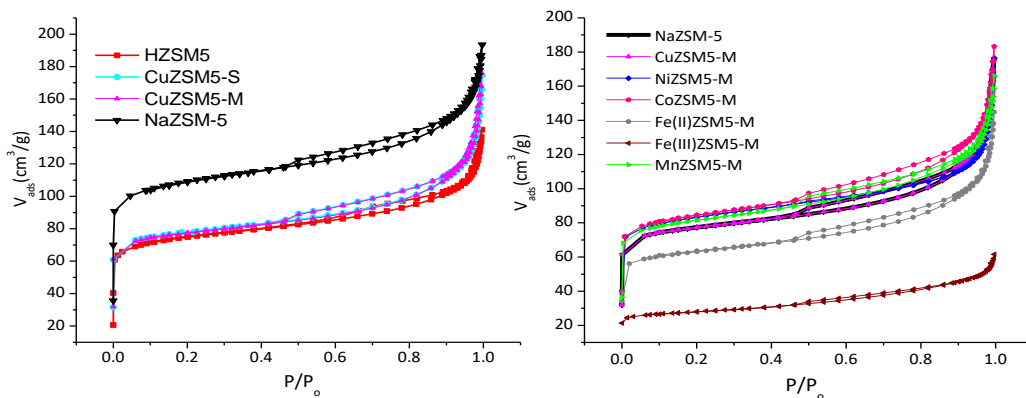
Figure 2.3. *N_2 adsorption-desorption isotherms of NaZSM-5 and ion-exchanged ZSM-5 zeolites.*

Table 2.1. *Metal loading, Textural and structural properties of NaZSM-5 and ion-exchanged ZSM-5 zeolites.*

Sample	Metal loading [a] (wt%)	S_{BET} [b] m²/g	S_{micro} [c] m²/g	V_t [d] cm³/g	V_{micro} cm³/g	Si/Al [e]
NaZSM-5	-	341	253	0.143	0.118	8.3
HZSM5	-	215	170	0.087	0.080	-
CuZSM5-S	0.6	240	184	0.098	0.091	9.5
CuZSM5-M	5.1	235	180	0.095	0.088	9.3
NiZSM5-M	4.8	281	212	0.111	0.089	9.8
CoZSM5-M	5.3	269	201	0.112	0.092	10.1
Fe(II)ZSM5-M	4.1	205	156	0.076	0.069	10.0
Fe(III)ZSM5-M	3.4	91	67	0.036	0.029	10.4
MnZSM5-M	4.5	269	203	0.108	0.090	11.6

a) determined by ICP-OES technique b) Calculated by the BET method, c) Microporous or external surface area calculated by the t-plot method [110], d) Obtained at a relative pressure of 0.99, e) Silicon/aluminium atomic ratio determined by EDS method.

The FTIR results of NaZSM-5 and exchanged samples in Table 2.2 indicate the bands at ~ 450 and 1100 cm^{-1} suggesting the internal vibrations of TO$_4$ (T= Si and Al) tetrahedra in ZSM-5 zeolite, and the bands at 548, 779, and 1228 cm^{-1} describing the external vibration of the bonds between five membered rings tetrahedra typical of MFI topology structure [111,112]. The bands at 1630, 1879 and 1995 cm^{-1} can be ascribed to the silica matrix overtone which did not show a sharp alteration in exchanged samples if compared to NaZSM-5. The band in the wavenumber range of 3000-3750 cm^{-1} is due to stretching vibration of -OH groups.

Table 2.2. The FTIR data for NaZSM-5 and ion-exchanged ZSM-5 zeolites.

Sample	M-O	Int. vibrations (cm^{-1})		Ext. vibrations (cm^{-1})			Overtone bands of silica matrix (cm^{-1})
		T-O bend	T-O (υ_{asym})	T-O (five-rings)	T-O (υ_{sym}) (five-rings)	T-O (υ_{asym}) (five-rings)	
NaZSM-5	-	453	1100	548	799	1228	1626, 1875, 2004
NiZSM5-M	-	451	1088	549	788	1222	1626, 1877, 1993
CoZSM5-M	700	453	1095	548	796	1228	1631, 1883, 2004
Fe(III)ZSM5-M	700	453	1095	551	796	1224	1626, 1875, 1995
Fe(II)ZSM5-M	624	453	1095	548	796	1224	1626, 1867, 2004
MnZSM5-M	688	451	1101	542	792	1222	1635, 1877, 2002
CuZSM5-M	666	457	1103	544	792	1228	1626, 1875, 2004
CuZSM5-S	-	454	1095	547	792	1228	1621, 1879, 1999
HZSM5	-	455	1096	549	801	1222	1635, 1868, 2000

Moreover, the FTIR spectra of pure NaZSM-5 and microwave assisted exchanged samples are shown in Figure 2.4a. Compared to NaZSM-5, the intensity increment of the bands at 1630 cm^{-1} and 3000-3750 cm^{-1} in the exchanged samples might be due to the existence of unreached metal chlorides in the samples. Indeed, all of metal chlorides exhibit the OH stretching and H$_2$O scissors frequencies with the bands at around 3500 cm^{-1} and 1600 cm^{-1}, respectively because they were in the hydrated forms. Furthermore, NiZSM5-M showed broader bands at 3000-3750 cm^{-1} compared to other microwave assisted ion-exchanged samples. This might be due to the different interaction of NiCl$_2$.6H$_2$O with the NaZSM-5 incorporating more hydrated ions and hydroxyl groups into the

zeolite channels and pores. As a matter of fact, all microwave assisted ion exchanged samples, except NiZSM5-M, displayed a weak band in the 600-700 cm^{-1} region (Table 2.2, Figure 2.4b) describing the vibration of new M-O (Cu(II), Mn(II), Fe(II), Fe(III), Co(II)) sites in the ZSM-5 structure [113–118]. Certainly, this can confirm a different interaction in NiZSM5-M sample via microwave assisted ion-exchange procedure.

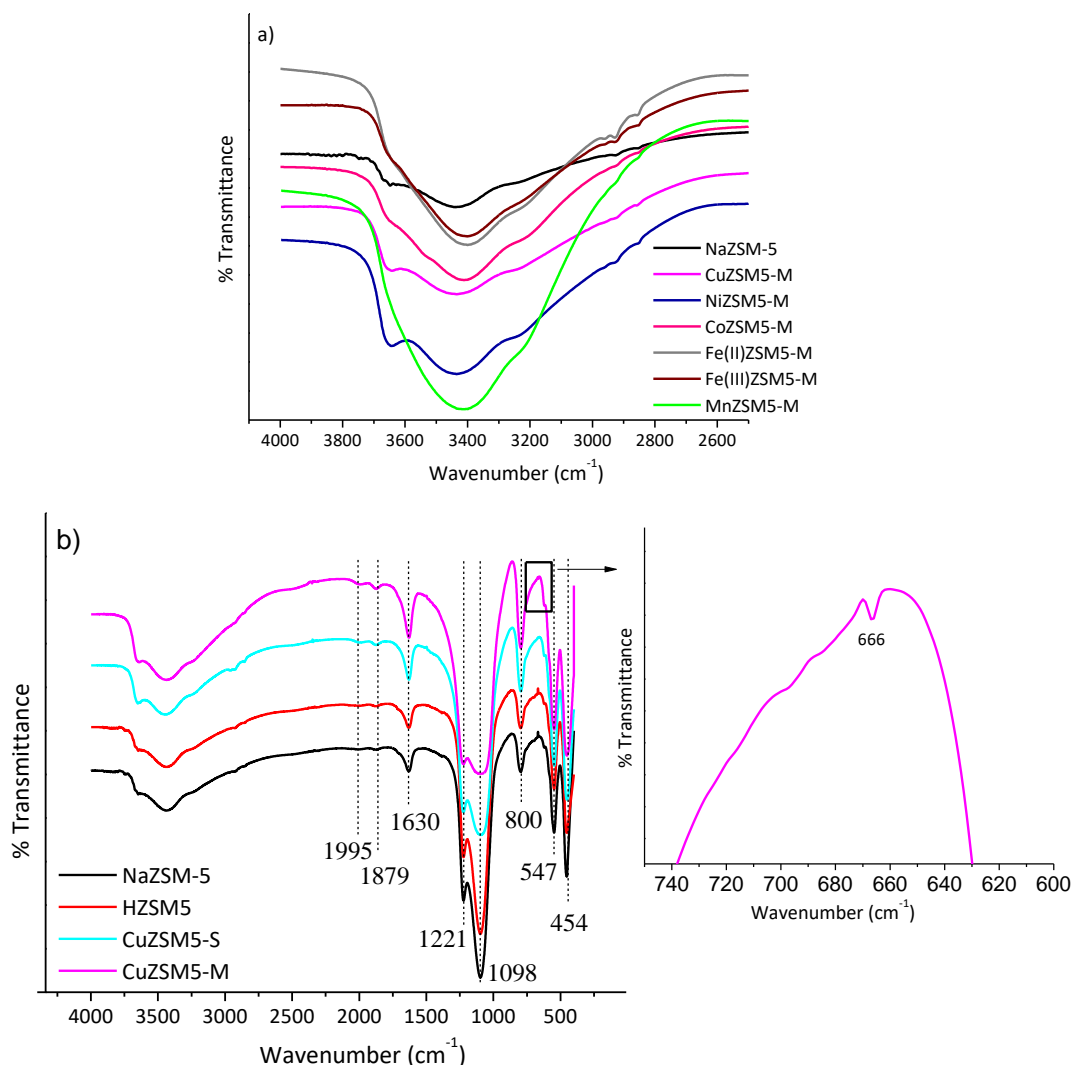*Figure 2.4. FTIR spectra of a) microwave assisted solid state ion-exchanged samples; b) parent and ion-exchanged samples.*

Figure 2.5 exhibits the XRD patterns of NaZSM-5 and ion-exchanged zeolites. The lines at 2θ of 7.90°, 8.82°, 22.96°, 23.82° and 24.32° are ascribed to NaZSM-5 and in agreement with the standard pattern of ZSM-5 MFI structure according to literature [119–121]. Similar XRD patterns

were observed for CuZSM5-S and parent zeolite suggesting that the zeolite maintained its crystallinity fairly well after aqueous ion-exchange procedure. Moreover, no alteration occurred in the crystallinities of CuZSM5-M, Fe(III)ZSM5-M and NiZSM5-M zeolites during microwave assisted solid ion-exchange technique [122,123]. For CuZSM5-M sample, the lines at 2θ of 16.3° and 34° belong to about 13 wt% of the residual $CuCl_2.2H_2O$ crystalline phase as analyzed by Rietveld refinement . For NiZSM5-M, the lines at 2θ of 15.7° and 20.06° ascribed to $NiCl_2$ crystalline phase, and the line at 2θ of 36.9° to $NiCl_2.6H_2O$ [124,125]. In addition, Fe(III)ZSM5-M exhibits the line at around 2θ of 11.9° , assigned to the $FeCl_3$ crystalline phase [126]. Lines related to other phases such as metals outside the zeolite channels or metal oxides were not detected suggesting that their presence, if any, were beyond the detection limit of XRD method [127].
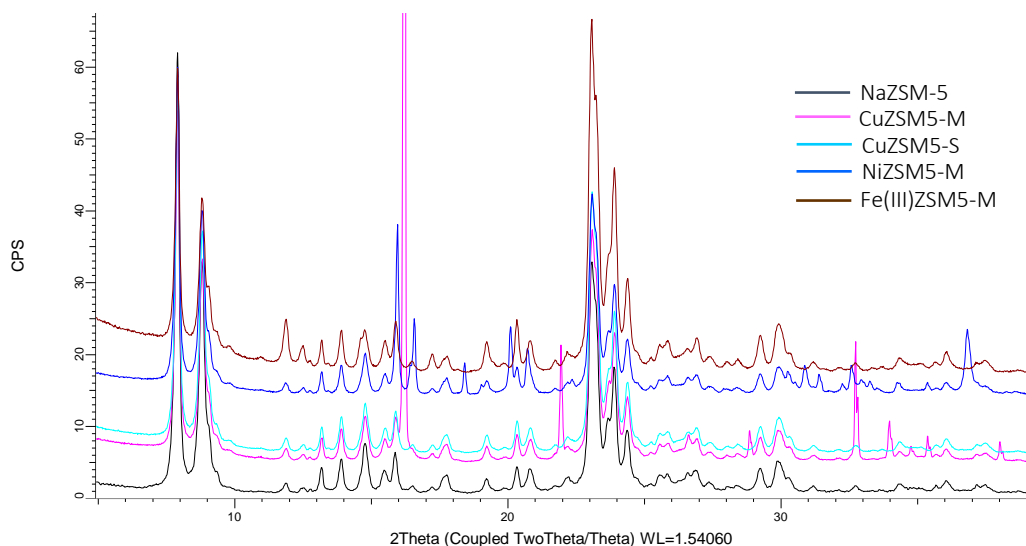
Figure 2.5. XRD patterns of NaZSM-5 and Cu(II)-, Ni(II)-, and Fe(III)-exchanged ZSM-5.

The scanning electron micrographs (SEM) of NaZSM-5 and ion-exchanged ZSM-5 zeolites are shown in Figure 2.6(a-h). NaZSM-5 displays the prismatic crystal shape as the typical morphology of ZSM-5 zeolite [128]. After aqueous ion-exchange, the prismatic morphology of zeolite in CuZSM5-S remained almost unchanged. Moreover, the surface of ZSM-5 crystals became rougher after microwave assisted ion-exchange particularly in the case of $FeCl_2$, $FeCl_3$, and $NiCl_2$. This might be related to the exitance of agglomerated metal chlorides [129–132]. The SEM images at

higher magnifications for ion-exchanged ZSM-5 are shown in the Figure A1 in Appendix. The EDS element distribution maps of introduced metals to NaZSM-5 by microwave method indicate a good dispersion of the Cu(II), Ni(II), Co(II), Mn(II) ions (Figure A2 (a-g)). Although the EDS maps confirmed the ion exchange was successful giving a high dispersion of cations in single atom forms, Fe(II)ZSM5-M and Fe(III)ZSM5-M display iron particles agglomeration on zeolite surface. The SEM-EDS results are consistent with the N_2 physisorption and FTIR behaviors previously discussed.

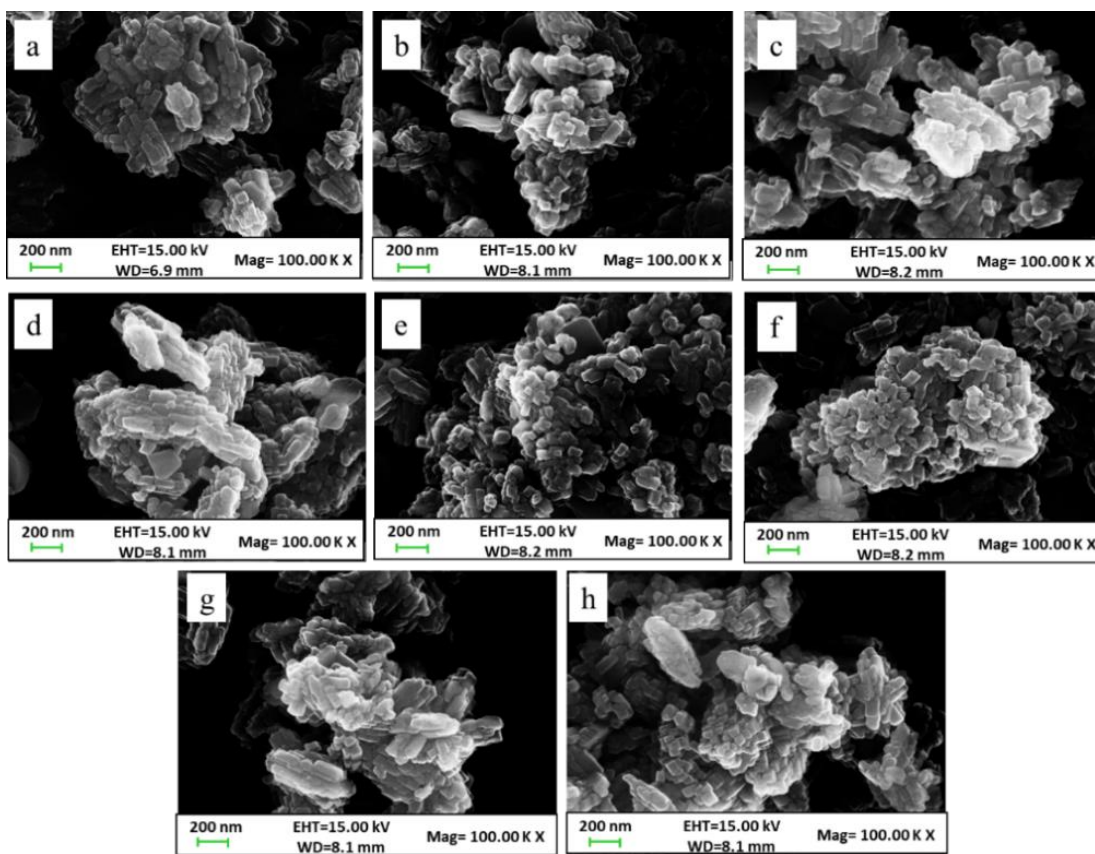*Figure 2.6. SEM images of a) NaZSM-5, b) CuZSM5-S, c) CuZSM5-M, d) NiZSM5-M, e) CoZSM5-M, f) Fe(II)ZSM5-M, g) Fe(III)ZSM5-M, h) MnZSM5-M*

The weight loss of pure and ion-exchanged ZSM-5 was estimated by thermal analysis to study the existence of different forms of metals and their stability in zeolites (Figure 2.7(a,b)).
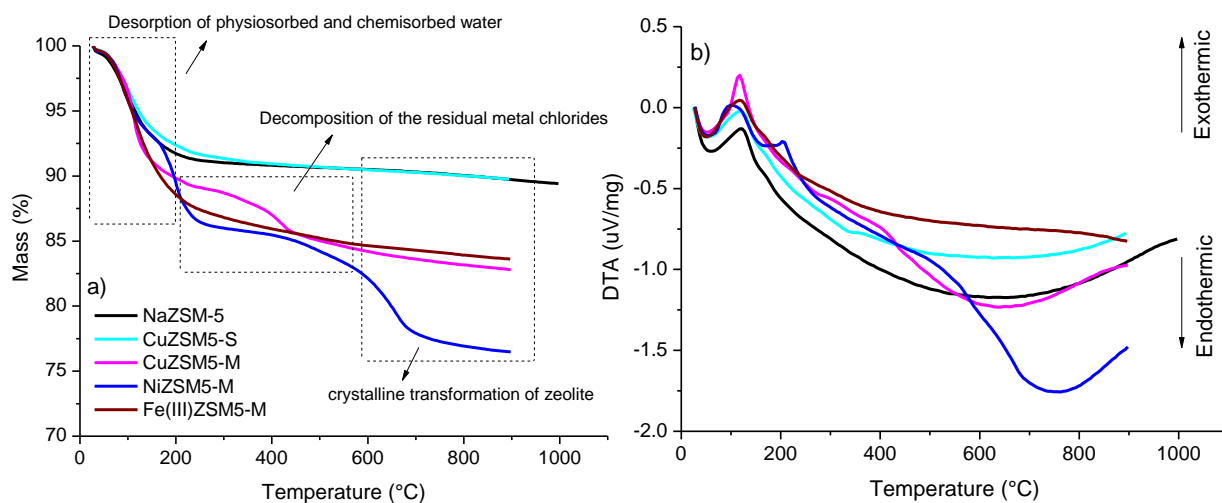
Figure 2.7. *a) TG and b) DTA analyses of NaZSM-5, CuZSM5-S, CuZSM5-M, NiZSM5-M, and Fe(III)ZSM5-M; the weight loss and exchange heat as a function of temperature are reported in the a and b curves, respectively.*

In TGA of all samples, the first step in the temperature range of 25–200 °C is due to desorption of physiosorbed and chemisorbed water molecules with 8.5%,8.2%,10.2%,12.5% and 12.4% weight losses, respectively, being associated to an endothermic DTA peak [133]. Only the CuZSM5-S exhibits a TG curve almost similar to that of the pure NaZSM-5, while in other samples the content of water is increased due to presence of hydrated metal chloride. The microwave assisted ion-exchanged zeolites (CuZSM5-M, NiZSM5-M and Fe(III)ZSM5-M) display higher total weight losses and TG curves with several other weight loss steps. The second step weight loss is likely due to decomposition of the residual metal chlorides in those samples as was detected in the XRD patterns [134]. The third step weight loss at temperature above 600 °C might be due to the crystalline transformation of ZSM-5 [135]. In addition, it can be observed that by incorporating the metal ions under microwave assisted ion-exchange technique, the thermal stability of the samples decreased above 600 °C if compared to the pure NaZSM-5 and CuZSM5-S.

2.3.2. The results of catalytic tests

The catalytic performance of NaZSM-5 and ion-exchanged ZSM-5 was investigated and compared in transformation of glucose to LA at 200 °C for 5 h. The glucose conversion (X), liquid phase carbon balance (CB) and products yields (Y_{LA}, Y_{FA}, Y_{5-HMF}) for catalysts are reported in the Figure

29

2.8. As can be seen, both blank and catalytic systems caused 100% glucose conversion, which could be related to the high reaction temperature. However, for production of LA as the target product, a suitable and optimized acid catalyst was certainly needed. NaZSM-5 zeolite produced 24% LA and CB less than 40%. CuZSM5-M showed a higher yield of LA (37%) and CB (43%) besides a decrease on the FA yield. Compared to CuZSM5-M, the CuZSM5-S and HZSM5 resulted in a lower efficiency. Although according to the reaction stoichiometry, the molar ratio of FA and LA have to be one, a ratio higher than one was obtained for all catalysts. As it was shown in the Figure 2.1, some recent works have investigated that excess FA can be produced from direct degradation of glucose and fructose through a retro-aldol reaction [71,73,136]. Thus, the zeolite can also catalyze the formation of FA from glucose and fructose upon tandem transformation of glucose to LA and FA. On the contrary, it has to be noticed that FA could undergo a thermal degradation to gasses (H_2, CO, CO_2) and water in severe reaction conditions particularly at temperature higher than 180 °C [65,137], and therefore decrease the CB of the reaction. It is prominent to mention that low CB of each catalyst might be due to gas and solid phases by-products production. The gaseous by-products could be produced from degradation of FA as was noticed above, and the solid by-product is mainly humins that can be enhanced because of severe reaction conditions, high acid site concentration and strength, and unbalanced acidity of the catalyst.

In addition, Figure 2.8 shows the results of catalytic tests for microwave assisted ion-exchanged zeolites in which the yield of LA increased with the order of CoZSM5-M < Fe(II)ZSM5-M < MnZSM5-M < NiZSM5-M < Fe(III)ZSM5-M < CuZSM5-M. Catalytic results confirmed that the acid properties of the catalysts (amount, strength, and balance between Lewis and Brønsted acid sites) were the significant factors for following the reaction pathway into desired products. Thus, the relation between acidic features of the catalysts and their efficiencies in the reaction will be deeply discussed in the following section.
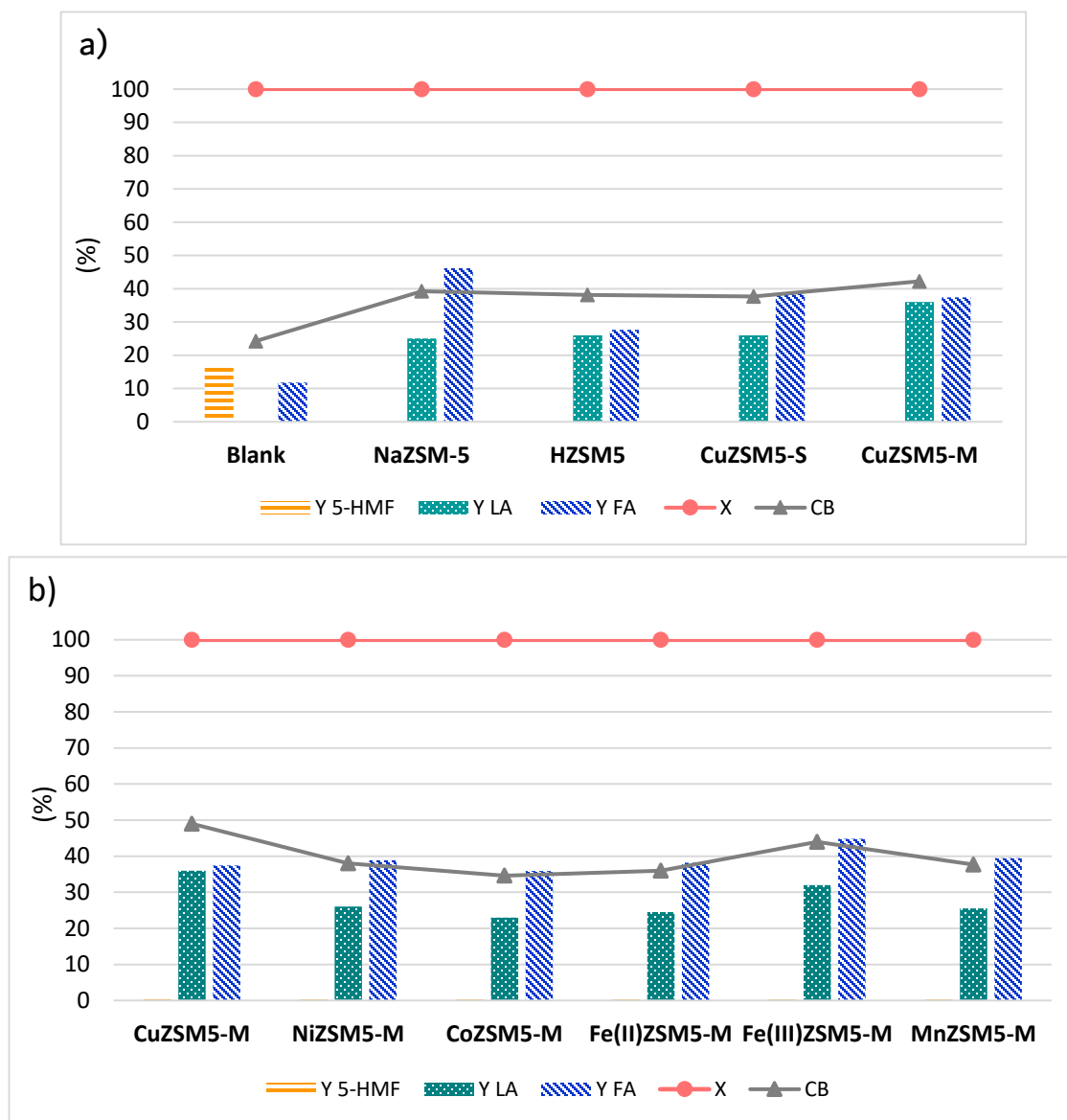
Figure 2.8. *Catalytic performance of NaZSM-5 and ion-exchanged ZSM-5 zeolites.(Reaction conditions: 200 °C, 10 bar of N_2, 5 h, 2.7 mmol glucose, 500 mg catalyst, 100 mL water).*

2.3.3. The effects of catalysts acidity on the glucose conversion to levulinic acid

NH_3-TPD profiles in Figure 2.9 show the amount and strength of acid sites of all samples. There are weak, medium and strong acid sites exhibited by the desorption curves in different temperature ranges from lower to higher acidity strength. NaZSM-5 displays acidic nature similar to those reported in the literature [138,139]. The broad peak in the temperature range of 50-300 °C is due

to the existence of both weak and medium acid sites, whereas the strong acid sites showed the peak in higher temperature of around 300-600 °C [140,141]. As can be seen in Figure 2.9a, by aqueous ion-exchange method, all the three weak, medium and strong acid sites exist in zeolite considering that the intensity of the strong acid site in CuZSM5-S is reduced [141]. These results suggest the presence of various adsorption states of NH_3. NiZSM5-M displayed extremely different behavior during microwave assisted solid state ion-exchange. In particular, it showed all weak, medium and strong acid sites by three separated peaks in the temperature range of 50-200 °C, 200-300°C and 400-600°C, respectively. It can be assumed that Ni by a higher and different interaction with ZSM-5 zeolite could create some new and strong Brønsted acid sites through microwave treatment. This could be due to the creation of hosted Ni^{2+} species with different natures and distributions within NiZSM5-M structure. This result can be confirmed by FTIR in Table 2.2 and Figure 2.4 in which a broader band at wavenumber range of 3000-3750 cm^{-1} and no vibration band for Ni-O were observed. It can be assumed that most of $NiCl_2.6H_2O$ were transferred to the zeolite pores and channel with a hydrated form introducing new Brønsted acid sites and no interaction occurred between Ni(II) and oxygen of ZSM-5 channels wall. Furthermore, when comparing metal cations of fourth period of periodic table, Ni^{2+} as an exchanged metal cation can introduce a strong Lewis acid site [142,143].
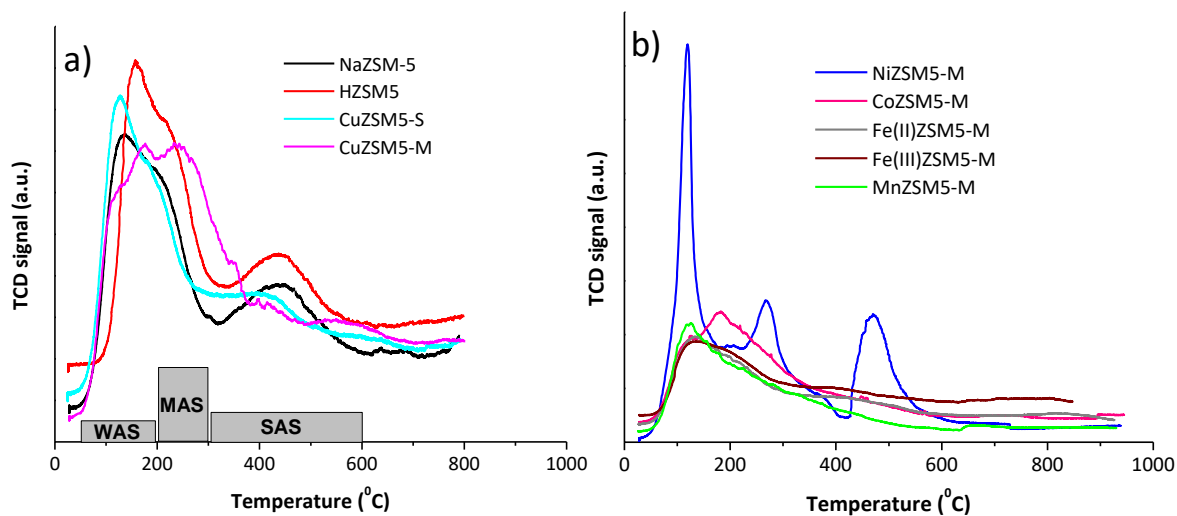
Figure 2.9. NH$_3$-TPD for NaZSM-5 and ion-exchanged ZSM-5 zeolites. (WAS: weak acid site; MAS: medium acid site; SAS: strong acid site)

32

In order to study Lewis and Brønsted acid sites in the zeolites, FTIR adsorption of 2,6-dimethylpyridine (2,6-DMP) was performed and the results are shown in Figure 2.10(a-d) and Table 2.3.
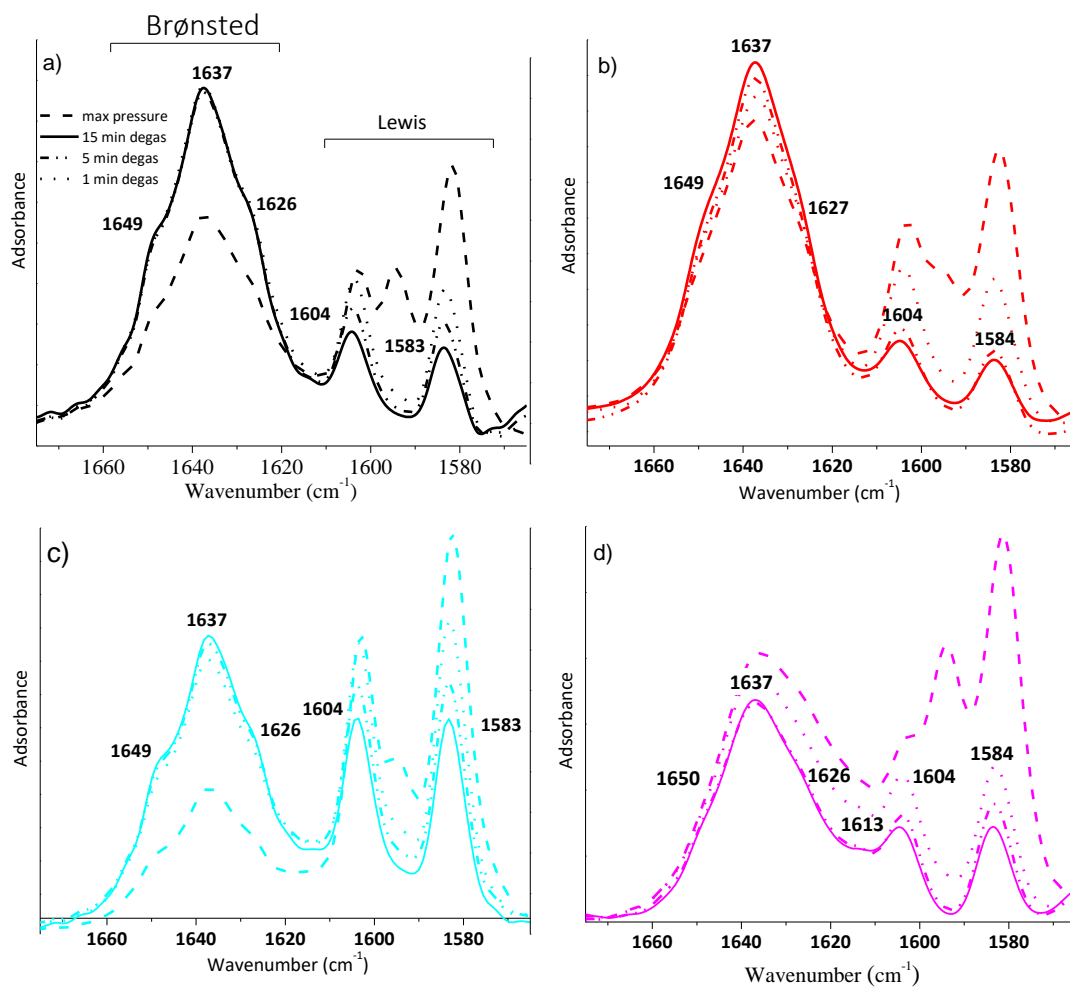
Figure 2.10*. FTIR spectra of 2,6-DMP adsorption/desorption for a) NaZSM-5, b) HZSM5, c) CuZSM5-S, d) CuZSM5-M.*

Table 2.3*. Acid properties of NaZSM-5 and ion-exchanged ZSM-5 zeolite obtained by 2,6-DMP-FTIR.*

Sample	L/B[a]
NaZSM-5	0.62
HZSM5	0.60
CuZSM5-S	1.69
CuZSM5-M	1.98

[a] Ratio between Lewis and Brønsted acid sites calculated on normalized spectra using ε_L=1,1 cm μmol^{-1} and ε_B=3,9 cm μmol^{-1}, as determined by ref [144].

2,6-dimethylpyridine (2,6-DMP) was selected as probe molecule, because it could identify both Brønsted and Lewis acid centers [145]. 2,6-DMP H-bonded and Lewis-bonded onto the surface results in a multiple band in the range of 1580-1620 cm^{-1}, which according to literature can be related to 8a and 8b modes of the adsorbed molecule [145]. The formation of 2,6-dimethylpyridinium ion after adsorption on Brønsted sites causes a multiple band located at higher wavenumbers attributable to 8a and 8b modes of protonated 2,6-DMP (2,6-DMPH$^+$). Particularly, according to the spectrum of NaZSM-5 sample at the maximum pressure of 2,6-DMP (dash line in Figure 2.10a), 8a and 8b modes of physiosorbed and H-bonding 2,6-DMP (1582, 1594 and 1603 cm^{-1}) can be observed. The signals still exist after evacuation at 1604 and 1583 cm^{-1}(solid line) which are assigned to strong Lewis acid. The signals at higher wavenumber are associated to coordinated 2,6-DMP to Brønsted acid sites (1649, 1637 and 1626 cm^{-1}), thus forming 2,6-DMPH$^+$ ions, and their intensity are enhanced after evacuation for 15 minutes (solid line). NaZSM-5 shows a spectrum very similar to the reference system: it is possible to observe 8a and 8b modes of H-bonding 2,6-DMP (at 1582 and 1603 cm^{-1}) and signals attributable to 2,6-DMPH$^+$ species at 1649, 1637 and 1626 cm^{-1}. As it is reported, zeolite itself displays both Brønsted and Lewis acid sites because of hydroxyl groups bridging Si and Al and extra framework Al, respectively [146]. Therefore, both acidities can catalyze the glucose transformation to LA which was observed in the activity result of NaZSM-5 in Figure 2.8. However, as was reported in literature, an optimum density and strength of acid sites, so that a balanced Lewis and Brønsted acid sites, means that an optimum and higher ratio of L/B are desired to achieve a higher yield of target product [127,147]. Thus, different ion-exchange methods were applied to reach an optimum and suitable acid site in zeolite as the catalyst of the proposed reaction.

HZSM5 did not show any sharp change compared to NaZSM-5. CuZSM5-S showed the increment of both Lewis and Brønsted acid sites due to the presence of hydrated Cu cations in the ZSM-5 pores and channels and increase of hydroxyl groups in the channel walls, respectively [148,149]. According to ICP results 0.6% copper was incorporated to the zeolite structure which might lead to the new Lewis acid sites formation. On the contrary, CuZSM5-M showed the main difference by new signal at ≈1615 cm^{-1} which can be associated to 2,6-DMP in Lewis interaction with copper sites. Indeed, ICP showed 5.1% of copper in the CuZSM5-M sample. Therefore, the new Lewis acid site shown in FTIR adsorption of 2,6-DMP could come from creation of Cu-O in the ZSM-5 pores and channels as was shown in FTIR spectra (Table 2.2, Figure 2.4) and Cu crystalline phases

such as the dispersed $CuCl_2$ on the ZSM-5 surface as was shown in the XRD pattern (Figure 2.5). In addition, when comparing NaZSM-5 based samples after desorption for 15 minutes, the signal at 1613 cm^{-1} for CuZSM5-M becomes more evident. It can also be demonstrated that the band of Brønsted sites for sample CuZSM5-M is less structured (in correlation with hydroxyl signals). As already discussed, the type of acidity and L/B ratio play vital role in improvement of the catalyst efficiency. The ratio between Lewis and Brønsted (L/B) acid sites needs the knowledge of molar absorption coefficients (ε) values, specific for each mode and affected by the surface [144,150]. Some researches demonstrated a little variation of ε as a function of solids type and appraised ε values for characteristic of 2,6-DMP adsorbed through H-bounding, protonation and coordination[144]. Using the peak area in normalized spectra, we determined the ratio between the number of Lewis and Brønsted acid sites using 3.9 cm μmol^{-1} and 1.1 cm μmol^{-1} as molar absorption coefficients, respectively, for Brønsted and Lewis related modes. As it can be seen in Table 2.3, CuZSM5-M shows the highest increase of Lewis acidity compared to the NaZSM-5. The L/B ratio increased from 0.62 in NaZSM-5 to 1.98 in CuZSM5-M, whereas the increment of L/B ratio for CuZSM5-S was less than CuZSM5-M due to the enhancement of both Brønsted and Lewis acid sites in this sample. Moreover, L/B ratio of HZSM5 showed a very slight decrease.

Otomo and co-workers [151], reported that the isomerization of glucose to fructose and then the dehydration of fructose to 5-HMS as progressive reactions need an optimized density, strength, and type of acidic active sites acid in the catalyst. Therefore, in this study, by changing the L/B ratio, the efficiency of catalysts in proposed reaction changed. As it is shown in the 2,6-DMP-FTIR results in Figure 2.10 and Table 2.3, CuZSM5-M showed the maximum Lewis acidity and thus the L/B ratio with respect to other ion-exchanged catalysts. Moreover, according to NH_3-TPD result in Figure 2.9, the strong acid site disappeared, and the final catalyst had a moderate acidity. Hence, the Lewis acid sites of CuZSM5-M could faster catalyze the glucose isomerization to fructose. It was reported that strong Lewis acid sites (high L/B ratio) can catalyze the isomerization reaction in a short time by reaching a maximum concentration of fructose [152]. Thereafter, when the density of Brønsted acid site is not sufficient, the dehydration of fructose to 5-HMF can be the rate limiting step and the reverse isomerization of fructose to glucose occurs. Hence, in high L/B ratio, the isomerization reaction can reach to a quasi-equilibrium. Then, enough density of Brønsted acid sites can assist the dehydration of fructose to 5-HMF and the rehydration of 5-HMF to LA and FA considering that a high density could also catalyze the degradation of fructose and

5-HMF to humins [152,153]. Therefore, as it was confirmed in the literature, an optimum and intermediate L/B ratio in catalyst can balance the isomerization and dehydration reactions rates and diminish humins production from fructose and 5-HMF [151]. On the contrary, HZSM5 and CuZSM5-S with lower L/B ratio (Table 2.3), the reaction is more prone to pass through direct dehydration of glucose to 5-HMF and not from isomerization pathway. Indeed, due to the lack of enough Lewis acid site density, achieving to equilibrium in glucose isomerization to fructose is limited. Consequently, the degradation of fructose and specially 5-HMF to humins are faster than 5-HMF conversion to LA and FA because of the presence of strong Brønsted acid sites [152].

As it was discussed in the previous section, the type of metals introduced through microwave technique influenced the efficiency of the catalysts which were enhanced with the order of CoZSM5-M < Fe(II)ZSM5-M < MnZSM5-M < NiZSM5-M < Fe(III)ZSM5-M < CuZSM5-M [154]. It seems the catalytic function of metals in the reaction is associated to their charge density, and acidity (amount, type and strength) that they can introduce to the ZSM-5 zeolite. As it was reported in ref [155], the charge density of the transition metal cations of this study in the high spin state follows the order of $Fe^{3+}>Ni^{2+}>Cu^{2+}>Co^{2+}>Fe^{2+}>Mn^{+2}$. Moreover, according to the intensity of peaks in NH_3-TPD curves (Figure 2.9), the amount of weak and medium acid sites in the ion-exchanged zeolites are decreased with the order of NiZSM5-M>CoZSM5-M>MnZSM5-M>Fe(II)ZSM5-M>CuZSM5-M>Fe(III)ZSM5-M considering that NiZSM5-M also exhibits strong Brønsted acid site. Therefore, among different metals, a cooperation of higher charge density, weak and medium acid strength with lower density might be desirable to reach a better efficiency of catalysts. Thus, CuZSM5-M displayed a higher LA yield at full conversion compared to other ion-exchanged zeolite because of a higher charge density and lower density of acid sites with moderate strength. On the other hand, Fe(III)ZSM5-M with the highest charge density and lowest density of acid sites produced less LA yield compared to CuZSM5-M. This might be due to weak distribution of iron chloride in the ZSM-5 channels and on its surface as was confirmed by FTIR, SEM and TG-DTA results.

2.3.4. The effect of reaction conditions on the catalytic glucose conversion

After selecting CuZSM5-M as the best catalyst, some reactions in different conditions were performed to investigate the effect of glucose amount, reaction time and temperature. Figure 2.11 displays that 2.7 mmol of charged glucose resulted in the best reactivity, and a lower amount of

glucose (1.6 mmol) gave a slightly lower products yields and CB. On the contrary, a higher amount of glucose (3.9 mmol) caused the significant drop of desired products yields and CB. As was suggested in the literature [156–158], a high concentration of glucose can cause side reactions for humins formation, reducing thereby the catalyst stability and the yield of the desired product. It was found that in glucose conversion, the reaction order for humins formation is overall higher than that of LA production and is mostly a second order reaction. In addition, it is generally confirmed that a high concentration of reactant can be resulted in a high yield of humins. By decreasing the reaction time, LA and FA yields decreased. It can be assumed that the time to reach the maximum yield of final product from intermediates has to be further prolonged which was also confirmed with obtaining small amount of 5-HMF and furfural in the products solution [66]. Moreover, decreasing the reaction temperature from 200 °C to 180 °C led to a slight decrease of glucose conversion but no change in products yield happened. Finally, the reaction conditions of 180 °C and 5 h with 2.7 mmol of glucose as substrate was considered for CuZSM5-M catalyst.
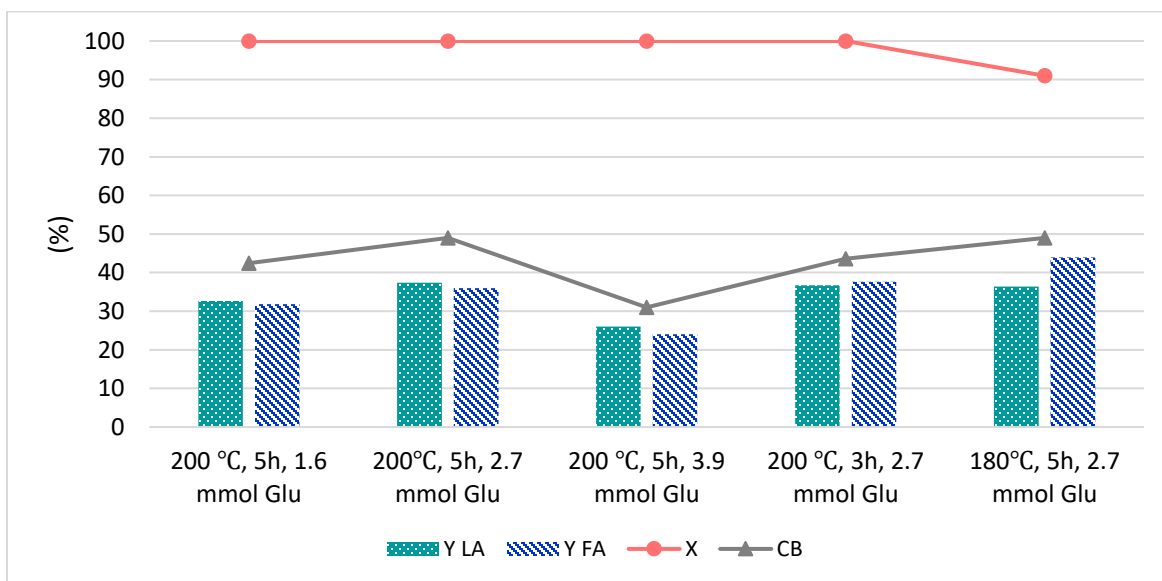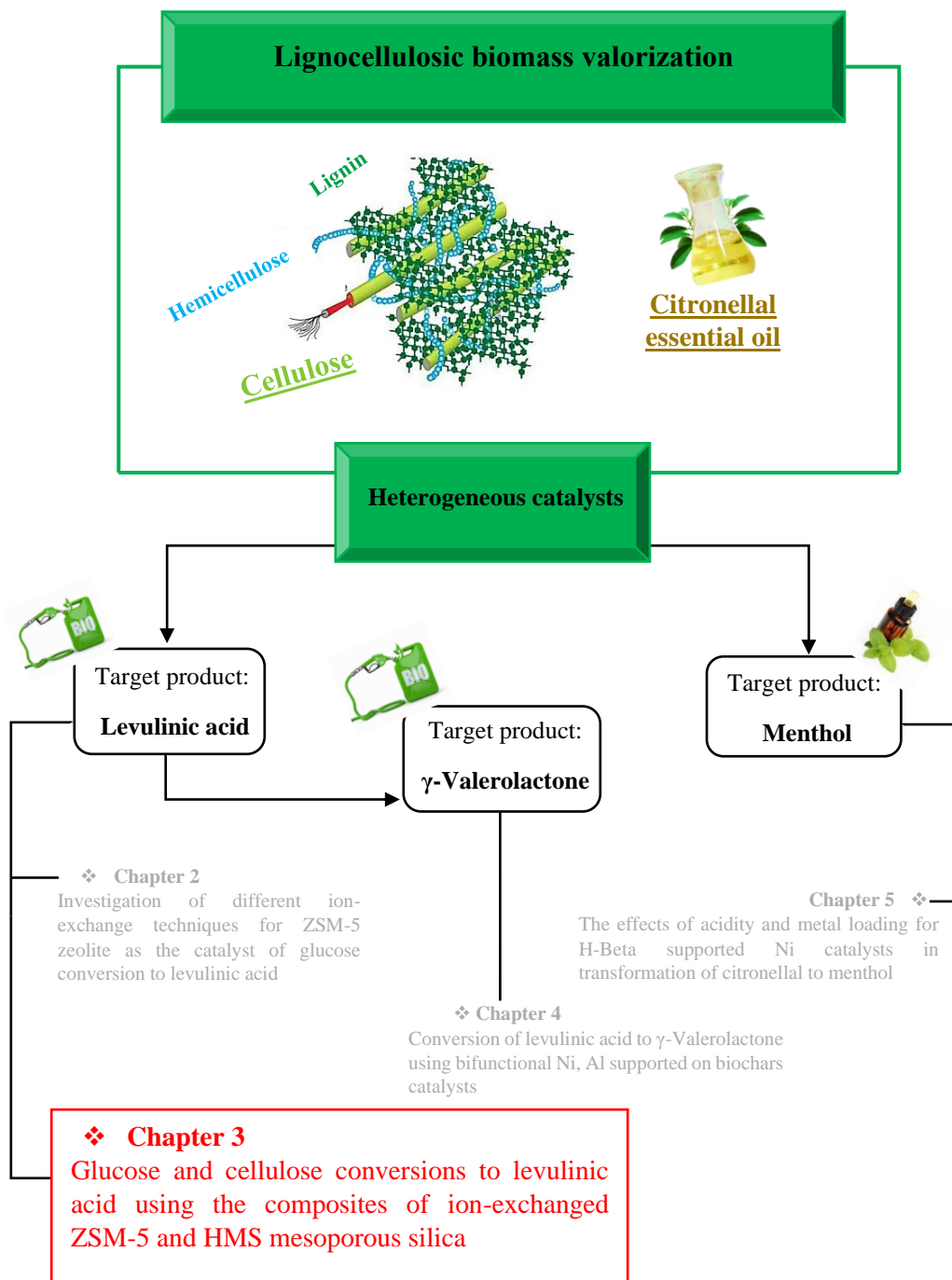

Figure 2.11. *The effect of reaction conditions on the catalytic efficiency of CuZSM5-M in glucose conversion to LA.*

2.4. Conclusion

In this chapter, the modification of ZSM-5-type zeolite was carried out by various ion-exchange methods to obtain bifunctional acid heterogeneous catalysts for glucose transformation to LA. In particular, the aqueous ion-exchange method using NH_4Cl and $CuCl_2$ solutions and the microwave assisted ion-exchange technique using solid salts of transition metals including $MnCl_2$, $FeCl_2$, $FeCl_3$, $CoCl_2$, $NiCl_2$, $CuCl_2$ were applied to obtain a suitable acidity of catalyst with appropriate density and strength of acid sites, and optimum Lewis to Brønsted acid ratio. N_2 physisorption, XRD, SEM results confirmed the preserved textural and morphological properties of all catalysts during ion-exchange procedures. Nevertheless, owing the existence of agglomerated Fe(II) and Fe(III) chlorides, a sharper decrease of surface area and porosity, and a rougher surface morphology were observed for Fe(II)ZSM5-M and Fe(III)ZSM5-M by N_2 physisorption and SEM results, respectively. Aqueous ion-exchange method improved both Brønsted and Lewis acid sites keeping the strong acidity which was not suitable for following the target reaction pathway from glucose isomerization to fructose. On the contrary, all microwave ion-exchanged catalysts showed mainly Lewis acid site improvement except Ni(II) ion having a different interaction with ZSM-5 and formed new Brønsted acid site with different strengths. Hence, microwave ion-exchange technique for most of the ZSM-5 based catalysts increased Lewis to Brønsted acid ratio, and weak and medium acid sites being efficient for target reaction pathway to LA. Among different transition ion-exchanged metals, Cu gave the highest performance having a higher charge transfer, and balanced and low density of acid site in CuZSM5-M. This catalyst exhibited a promising efficiency giving 37% yield of LA from glucose with highest CB (43%) because of less humins by-product production. Therefore, in this chapter, different ion-exchange techniques for ZSM-5 zeolite were optimized allowing to modulate the acidity of ZSM-5 zeolite and make it as an efficient heterogeneous catalyst for glucose transformation to LA. In the next chapter, the best catalyst, meaning CuZSM5-M, will be applied as an acid heterogenous catalyst in the formulation of micro-mesoporous composites for catalytic transformation of bulky sugars (cellulose) to LA.

Lignocellulosic biomass valorization

Lignin

Hemicellulose

Cellulose

Citronellal essential oil

Heterogeneous catalysts

Target product:

Levulinic acid

Target product:

γ-Valerolactone

Target product:

Menthol

❖ **Chapter 2**
Investigation of different ion-exchange techniques for ZSM-5 zeolite as the catalyst of glucose conversion to levulinic acid

Chapter 5 ❖
The effects of acidity and metal loading for H-Beta supported Ni catalysts in transformation of citronellal to menthol

❖ **Chapter 4**
Conversion of levulinic acid to γ-Valerolactone using bifunctional Ni, Al supported on biochars catalysts

❖ **Chapter 3**
Glucose and cellulose conversions to levulinic acid using the composites of ion-exchanged ZSM-5 and HMS mesoporous silica

Chapter 3. Glucose and cellulose conversions to levulinic acid using the composites of ion-exchanged ZSM-5 and HMS mesoporous silica

3.1. Introduction

In this chapter, we are moving to a composite catalytic system made of ion-exchanged ZSM-5 (CuZSM-5) and HMS mesoporous silica materials for glucose and cellulose conversion to LA. A brief introduction about the catalytic system for cellulose conversion is reported below, while an introduction about levulinic acid (LA) production from cellulose and glucose was provided in Chapter 2.

3.1.1. Catalysts for conversion of cellulose to levulinic acid

When using a bulky molecule such as cellulose as the substrate, the porosity of the catalyst is vital to facilitate the mass transfer between bulky substrate and catalyst active sites. Several methods have been applied to add mesoporosity into zeolite texture. For example, hierarchical zeolites were formulated following bottom-up or top-down techniques such as desilication or dealumination approach. However, both of them can cause disorders in the structure of zeolite, strongly changing its acidity, and diminishing its activity and stability in the hydrothermal condition. Thus, the composite of mesoporous materials with zeolite can be applied as the catalyst for reactions possesing bulky molecule [159–162].

Furthermore, side products such as solid humins depositions are serious issues leading to the deactivation of the catalysts. Since humins production is highly related to the reaction conditions and acidic properties of heterogeneous catalysts, it was demonstrated that zeolite with high acid site density, strength and unbalanced Brønsted and Lewis acid ratio is more potential to form humins. In addition, the deactivation of zeolite through blocking active sites and micropores and reducing surface area by humins deposits can be occurred. Mesopores of catalysts can provide a shorter diffusional path length and guarantee the fast exit of bulky molecules, diminishing the humins production inside the catalyst pores and reducing the bulk active sites deactivation [162–165].

Chu *et al*, created hierarchical pores in ZSM-5 zeolite by dealumination and desilication methods using HCl and NaOH solutions, respectively. In addition to hierarchical ZSM-5 modification, the hydrolysis performance of cellulose in aqueous solution was improved by ultrasonic pretreatment and $ZnCl_2$ promoter. Considering the advantages of ultrasonic pretreatment and $ZnCl_2$, both dealuminated and desilicated ZSM-5 zeolites have demonstrated a higher conversion of cellulose and yield of 5-HMF and LA compared to the microporous ZSM-5. This could be related to the presence of mesopores and easier mass transfer properties [166]. Similarly, hierarchical Mn_3O_4/ZSM-5 zeolite could accelerate hydrolysis of cellulose from delignified rice husk biomass into LA with the assistance of phosphoric acid and H_2O_2 used in the reaction solution. This catalytic process gave a 39 (wt%) yield of LA at 130 °C after 5 h [167]. Pham and colleagues [168] used mesoporous silica, SBA-15, as the catalyst to boost the substrate mass transfer, and the catalyst acidity was improved by incorporation of Al via atomic implantation as a post synthesis technique. The final catalyst with optimum Al loading produced 42% yield of 5-HMF from cellulose. In this thesis, the catalyst activity was guaranteed by using Cu(II)-exchanged ZSM-5 zeolite. For facilitation of cellulose penetration as the substrate, a hollow mesoporous silica (HMS) was composed with C(II)-exchanged ZSM-5.

Since 1992, mesoporous silica materials have been widely used in wide variety applications such as catalysis, adsorption, and medication because of their proper textural properties with high surface area and large pore volume [169]. Figure 3.1 represents the formation mechanism of mesoporous silica by sol-gel process. In the synthesis procedure of mesoporous silica, organic structured surfactants act as templates for the creation of final ordered structure in an aqueous solution. Two possible mechanisms were reported to point the role of surfactant including (1) true liquid crystal template mechanism or (2) cooperative self-organization mechanism leading the formation of a lyotropic liquid-crystalline phase. The pH of solution and temperature have significant effects in this step. In the next step, the silica precursor, being often tetraethyl orthosilicate (TEOS), makes a polymerized silica framework around the lyotropic liquid-crystalline phase and forms a supramolecular structure. In fact, in this step, the hydrolysis of inorganic section and its interaction with micelles of surfactant occurs through a cooperative-assembly arrangements and via hydrogen bonding, van der Waals and electrostatic forces. Finally, the template is removed through washing and calcination procedure or solvent extraction [170]. The type of surfactant affects the final type and structure of mesoporous material. For instance,

HMS is usually synthesized from natural and nonionic surfactants from the group of primary alkylamine. Therefore, HMS is mesoporous silica with three-dimensional (3D) and hexagonal channels having a less ordered structure compared to highly oriented mesoporous materials such as SBA-15 and MCM-41. On the other hand, HMS as a hollow mesoporous silica particle displays a more extensively cross-linked frameworks with a large framework wall thickness contributing a higher thermal, mechanical and chemical stability compared to other mesoporous silica materials [169,171,172].
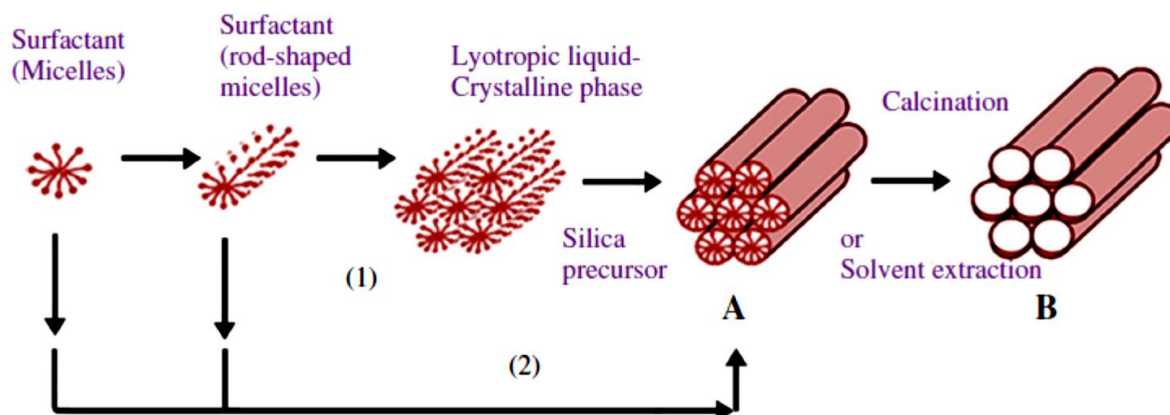

Figure 3.1. *Mechanism of ordered mesoporous material synthesis* [170].

3.1.2. The aim of the chapter

In this chapter, the optimization of zeolite-mesoporous silica-based composites was carried out for glucose and bulky cellulose conversions to LA. The best catalyst of Chapter 2 namely CuZSM5-M zeolite was selected as the acid part of catalysts. In addition, for an easy diffusion of cellulose as the reactant, HMS mesoporous silica material was used. Hence, composites made of different percentages of CuZSM5-M and HMS were formulated for the proposed reactions. Morphological and textural features, and acidity of the catalysts were characterized using XRD, SEM, EDX, TEM, TGA, N_2-physisorption, NH_3-TPD and FTIR both as such and by adsorbing/desorbing pyridine as probe molecule. All catalysts were tested for glucose transformation, and CuZSM5-M and the best composite were selected for cellulose hydrolysis to LA. Overall, the results confirmed that for obtaining a higher efficiency of the catalyst in bulky cellulose hydrolysis to LA, and for reducing

humins by-product production, optimum concentration, strength and Lewis/Brønsted acids ratio of acid sites, and a suitable micro-mesoporous texture and morphology of the catalyst are of crucial importance. Some characterisations of the catalysts such as SEM, TEM, TGA, pyridine-FTIR were performed in Åbo Akademi University of Turku (Finland) under the supervision of Prof. Dmitry Yu. Murzin. The results reported in this chapter are published as: "CuZSM-5@HMS composite as an efficient micro-mesoporous catalyst for conversion of sugars into levulinic acid", S. Taghavi, E. Ghedini, F. Menegazzo, P. Mäki-Arvela, M. Peurla, M. Zendehdel, G. Cruciani, A. Di Michele, D. Yu Murzin, M. Signoretto, Catalysis Today. 390-391 (2022) 146-161.

3.2. Experimental

3.2.1. Catalyst preparation

HMS and composites were synthesized via the sol-gel method following the procedure similar to that reported by Mokaya and Jones [173] and Pinnavaia *et al* [174]. For synthesizing the composite, two solutions were prepared. Solution A: a mixture of 6 mL tetraethyl orthosilicate (TEOS) (Sigma-Aldrich, 98.0 wt%) as the precursor of silica with 9 mL ethanol (VWR Chemicals, 96.0 vol%) were prepared in a beaker with continuous stirring at room temperature for 30 min. Solution B: 1.2 g of dodecylamine (Sigma-Aldrich, 98.0 wt%) as the surfactant, 0.5 mL of the HCl (Merk, ≥37.0 wt%) (1M) solution and 15 mL of deionized water were mixed and stirred at 50 ℃ for 30 min. Solution A was added to solution B followed by 4 h stirring at room temperature. After that, different contents of CuZSM5-M (prepared with the same procedure of Chapter 2) were added to the gel in order to obtain 30, 50, 60 and 70 wt. % of CuZSM5-M in the structure of the composite. Finally, for crystalization, the mixture was continuously stirred for 12 h. A similar procedure was carried out for HMS preparation without adding CuZSM5-M zeolite. The prepared sample was filtered and washed with a solution of distilled water and ethanol and the solid on the filter was dried in the oven at 70 ℃ for 12 h. Then, the sample was calcined at 600 ℃, with temperature increasing rate of 1 ℃/min, in air flow of 30 mL/min for 6 h. The final composites were labeled CuZ(x)@H that x is the percentage of CuZSM5-M and is equal to 30, 50, 60 and 70. wt%.

3.2.2. Catalytic test

The catalytic tests were carried in a stainless-steel autoclave of 400 mL volume equipped with a mechanical mixer for stirring of reaction solution and an electric heater for measuring the temperature. The autoclave was charged with 2.7 mmol glucose or 3 mmol cellulose (cellulose powder, cotton linters, Sigma-Aldrich) as the substrate, 500 mg catalyst, and 100 mL of deionized H_2O as the solvent. Then, the autoclave was pressurized with N_2 (10 bar), and heated to the desired temperature. The time of reaction was started once the temperature achieved to the target value. The reaction was performed for 5 h under the stirring speed of 600 rpm. At the end of the test, the autoclave was cooled down to 25 °C and the final mixture was filtered. The filtered solution was analysed via a high-performance liquid chromatography (HPLC) Agilent Technology 1260 Infinity II. An Aminex HPX-87H column was used in HPLC and the analysis was carried out at column temperature of 50 °C by passing the mobile phase of 5mM H_2SO_4 with the flow rate of 0.6 mL/min. A UV–vis detector (λ =195 nm) was used for analytes' identification and quantification. The glucose conversion (X), liquid phase carbon balance (CB) and products yields (Y_p) were calculated using the following equations:

$$X\ (\%) = \frac{\Delta n}{n_0} \cdot 100$$

$$Y_p\ (\%) = \frac{n_p}{n_0} \cdot 100$$

$$CB\ (\%) = \frac{\Sigma(np) \cdot (C\ atoms)}{(n_0 \cdot C\ atoms\ glucose)} \cdot 100$$

Where Δn corresponds to the reacted mole of substrate during the reaction. n_0 and n_p represent the mole of glucose or cellulose as the substrate at time zero and each product in the final liquid phase, respectively. In CB equation, the notation "C atoms" correspond to the number of carbon atoms in every component. For calculation, we regarded cellulose as a linear polymer of glucose and considered the molecular weight of anhydro glucose ($C_6H_{10}O_5$) unit in cellulose (162 g/mol) according to refs [175–177].

3.3. Results and discussion

3.3.1. Characterizations of the catalysts

N_2-physisorption results of the catalysts are exhibited in Figure 3.2(a,b) and their textural properties are reported in Table 3.1. As can be observed, CuZSM5-M displayed the isotherm profile, combination of type I and IV in IUPAC classification [178]. A H3 type hysteresis loop started from P/P_o= 0.5 demonstrates the capillary condensation of slit-like mesopores which ascribes the intercrystallite adsorption within aggregates. Furthermore, the adsorption isotherm at the pressure range of P/P_o< 0.2 suggests microporous texture of the sample. The pure HMS shows isotherm of type IV attributing to the capillary condensation of N_2 in the bounded mesopores. A monolayer adsorption of N_2 in P/P_o<0.25 demonstrate the existence of micropores in the HMS [179]. An inflection at approximately P/P_o= 0.2-0.4 is related to mesopores filling. The hysteresis loop at P/P_o>0.9 is due to the presence of macropores [180]. It was reported in the literature that the hysteresis loop in P/P_o more than 0.8 can be due to the textural interparticle mesoporosity or microporosity [181,182]. The shape of isotherm and the type of porosity for HMS in this study agree with what reported in the literature [180,183–185]. The isotherms of the composites with lower content of CuZSM5-M are similar to those of the pure HMS. When enhancing the content of CuZSM5-M particularly for CuZ(70%)@H composite, the adsorption volume is decreased being due to the decreased ratio of the mesoporous phase (HMS) versus the non-mesoporous phase (CuZSM5-M).
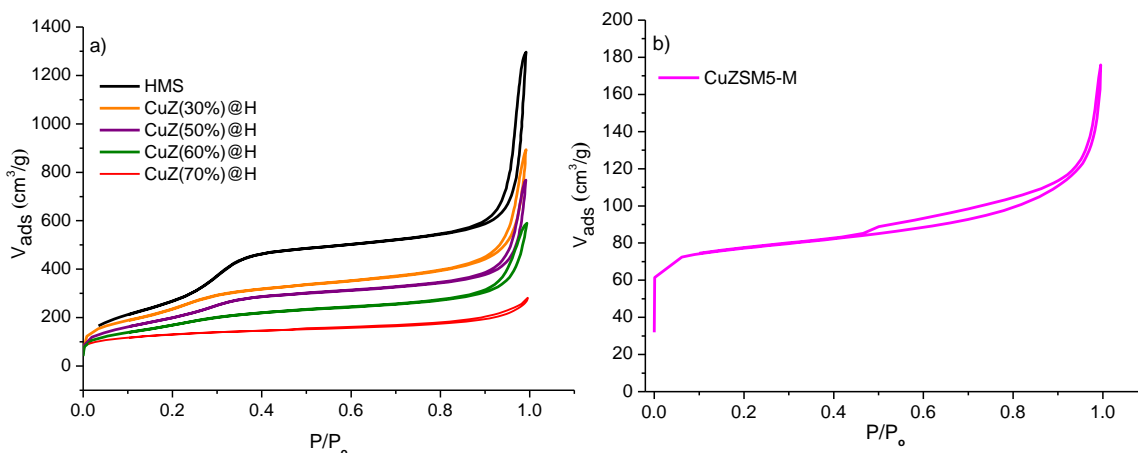

Figure 3.2. *N_2 adsorption-desorption isotherms of a) pure HMS and composites, b) CuZSM5-M.*

In Table 3.1, HMS shows a highly mesoporous texture with very high surface area. However, CuZSM5-M exhibits a high microporous or external but very low mesoporous surface area which is typical properties of zeolites when compared with mesoporous silica materials. By increasing of CuZSM5-M content in the composite, the micropore volume grew and a reduction of the mesopore volume happened because of blending the mesoporous material (HMS) with a non-mesoporous one (CuZSM5-M). Hence, the textural properties of the composites displayed a combined behavior of CuZSM5-M and HMS that was changed according to the percentage of CuZSM5-M in the composites [186].

Table 3.1. *Textural properties of all catalysts*

Sample	S_{BET} [a] m^2/g	S_{micro} [b] m^2/g	S_{meso} m^2/g	V_t [c] cm^3/g	V_{micro} [b] cm^3/g	V_{meso} [d] cm^3/g	Pore diameter [e] (nm)
HMS	992	278	714	0.19	0.020	0.170	2-166
CuZ(30%)@H	885	330	555	0.19	0.022	0.170	2-171
CuZ(50%)@H	732	269	463	0.16	0.026	0.130	2-167
CuZ(60%)@H	610	227	383	0.14	0.028	0.120	2-172
CuZ(70%)@H	444	198	246	0.13	0.062	0.070	2-213
CuZSM5-M	235	180	60	0.09	0.088	0.007	-

a) Calculated by the BET method, b) Microporous or external surface area calculated by the t-plot method [110], c) Obtained at a relative pressure of 0.99, d) Calculated by the BJH method, e) Pore diameter range calculated by BJH method.

Figure 3.3 shows the FTIR spectra of the catalysts. In CuZSM5-M, the bands displayed at 454 and 1098 cm^{-1} ascribes the internal vibration of (Al, Si)O$_4$ tetrahedra, whereas in HMS, they are associated to tetrahedral Si–O bending mode as well as the asymmetric stretching of Si–O–Si [187,188]. All these bands can be observed in the FTIR spectra of the CuZ(x)@H composites. The bands at 547, 800, and 1221 cm^{-1} assigned to the five- and six-membered rings of T–O–T (T = Si or Al) in zeolite being typical of the MFI morphology of ZSM-5. In all samples, the band at 1630 cm^{-1} is related to the OH bending mode of adsorbed water molecules [112,189]. In addition, the

broad bands at wavenumber range of 3000-3750 cm^{-1} are ascribed to the vibration of hydroxyl group in Si-OH-Al groups for ZSM-5, and Si–OH and absorbed water for all samples [190].
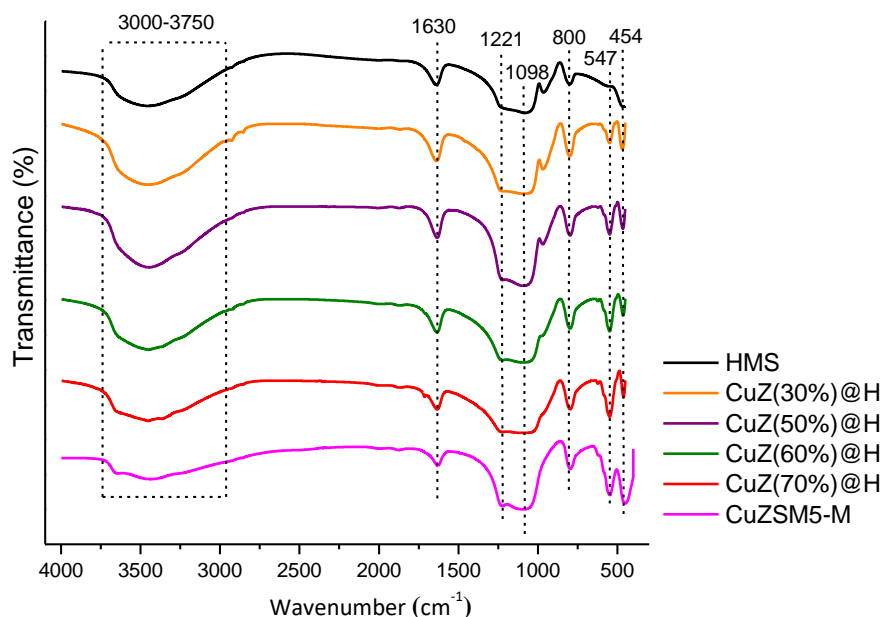

Figure 3.3. FTIR spectra of HMS, CuZSM5-5, and all composites.

The wide angle XRD pattern of CuZSM5-M, low angle XRD pattern of HMS, as well as low and wide angles XRD patters of CuZ(60%)@H composite are shown in Figure 3.4(a,b). In Figure 3.4a, the lines at 2θ=7.90°, 8.82°, 22.96°, 23.82° and 24.32° are associated to the standard pattern of ZSM-5 with MFI topology according to literature [191]. The lines at 2θ=16.3° and 34° are related to the CuCl$_2$.2H$_2$O crystalline phase with 13% content as was measured by Rietveld refinement [192]. In the low angle XRD pattern of the pure HMS in Figure 2b, a single line at 2θ ~2.2° (d=3.9 nm) can be observed, whereas CuZ(60%)@H additionally showed a second line at 2θ ~1.5° (d=5.9 nm). The second peak for CuZ(60%)@H might be due to the entrance of copper to the HMS mesopores through mixing the gel of HMS with CuZSM5-M during composite preparation procedure. Therefore, a partial occlusion of HMS mesopores with Cu atoms/ions (or complexes) occurred. During calcination, the mesopores of HMS that were free from copper, collapsed to d=3.9 nm [35], whereas the occluded ones kept the d=5.9 nm lattice spacing.
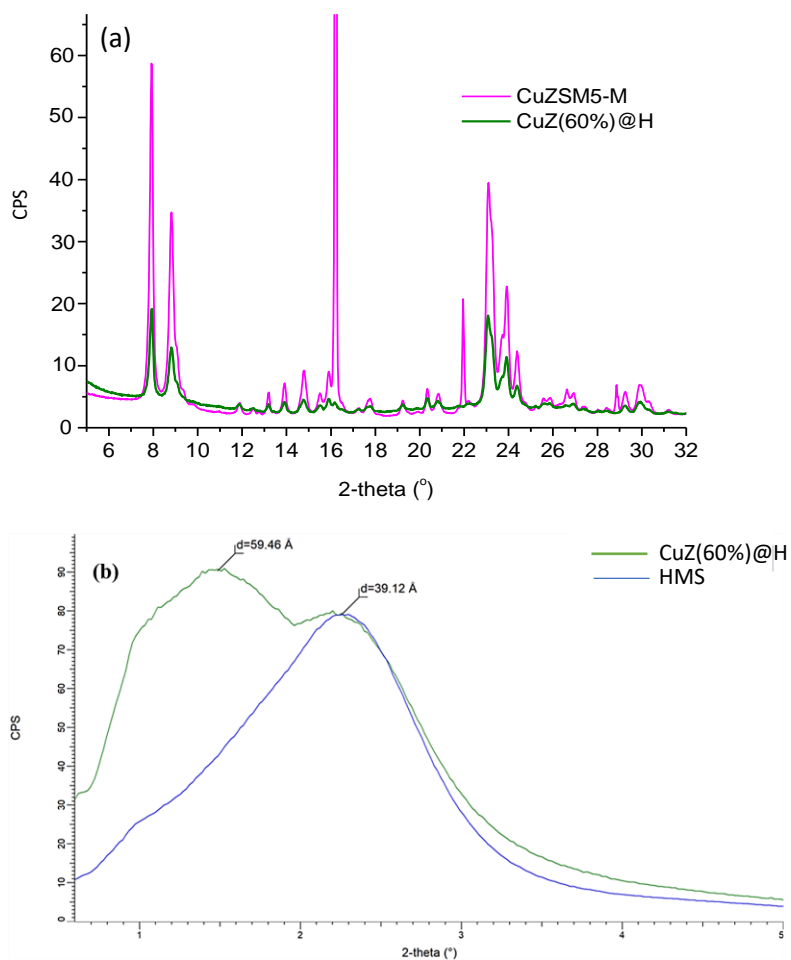
Figure 3.4. *XRD patterns of a) wide-angle 2-theta region CuZ(60%)@H composite compared to the CuZSM5-M and b) low-angle region of the HMS and CuZ(60%)@H composite.*

The wide angle XRD pattern of CuZ(60%)@H composite in Figure 3.4a shows less intense lines or peak broadening of ZSM-5 confirming that the crystallinity of CuZSM-5 was slightly decreased after synthesis of composite. In addition, the line ascribed to $CuCl_2.2H_2O$ crystalline phase can be seen at $2\theta=16.3°$. However, the intensity of line related to $CuCl_2$ is firmly decreased in the composite because of washing of the composite product.

Figure 3.5(a,b) exhibits the SEM images of CuZSM5-M and CuZ(60%)@H catalysts, respectively.
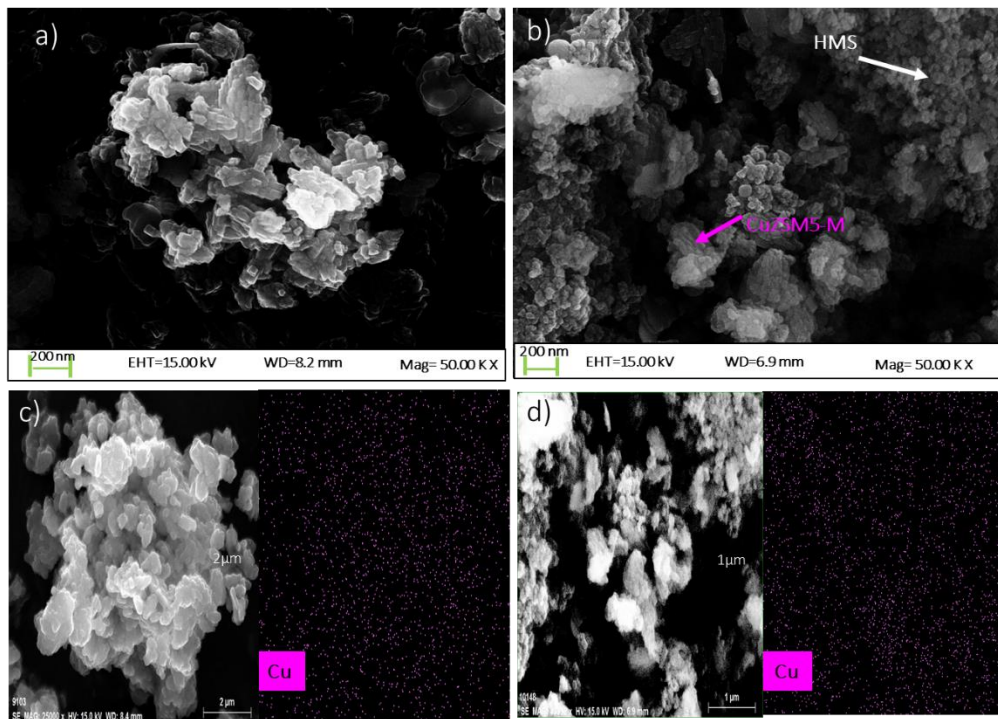
Figure 3.5. SEM images of a) CuZSM5-M, b) CuZ(60%)@H; EDS maps of Cu distribution on c) CuZSM5-M, d) CuZ(60%)@H.

In CuZSM5-M, typical morphology of ZSM-5 meaning prismatic crystal shape can be partially observed which seems to be slightly affected through solid $CuCl_2$ incorporation [193]. In particular, the change of surface morphology for CuZSM5-M is because of microwave ion-exchange procedure which made the prismatic crystallites less regular. In the SEM image of CuZ(60%)@H, both large prismatic CuZSM5-M and small semi spherical HMS can be seen [194,195]. Particularly, in the external part of the composite, HMS phase is mostly visible. Furthermore, distribution maps of the Cu(II) species obtained from X-ray energy dispersive spectroscopy (EDS) for CuZSM5-M and CuZ(60%)@H are displayed in Figure 3.5(c,d), respectively. Both samples show suitable dispersions of Cu(II) ions assisting a higher accessibility and efficiency of incorporated Lewis acid site in the catalytic reaction [196].

The TEM images of CuZ(60%)@H composite are exhibited in Figure 3.6. The well-ordered pore distribution structure of HMS in the composite can be evidently observed in Figure 3.6(a,b) with higher magnification which displays a part parallel to the [001] channels. This observation agrees with XRD results and also with those in the literature [197]. Moreover, highly dispersed Cu(II)

particles located in the channels of ZSM-5 with an average particle size of ca. 4.8 nm can confirm the appropriate distribution and accessibility of the Lewis acid sites.
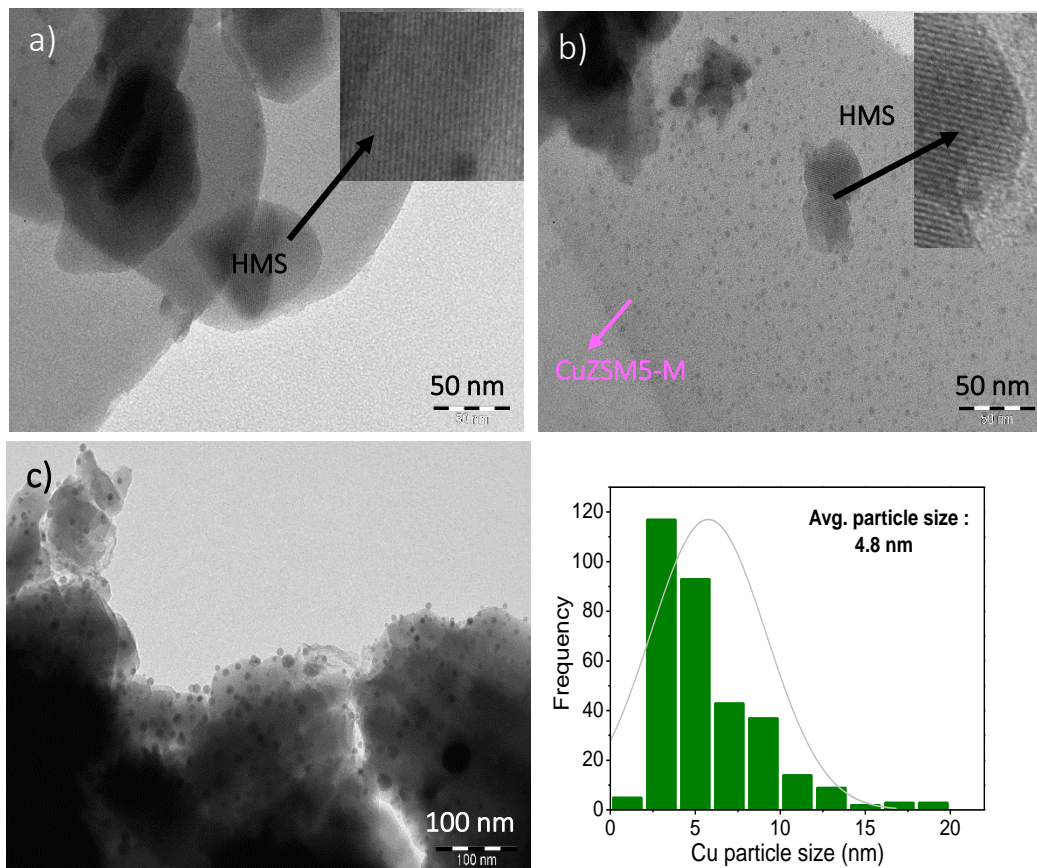

Figure 3.6. TEM images and Cu particle size distribution of CuZ(60%)@H catalyst.

The weight losses of samples were estimated by thermal analyses to study the stability of samples under temperature increase. Figure 3.7(a-c) displays the TGA curves for the CuZSM5-M, HMS and CuZ(60%)@H. For all materials, the weight loss in the first step at the temperature range of 25-200˚C is associated to desorption of physisorbed and chemisorbed H_2O molecules [198]. CuZSM5-M shows the highest weight loss (8.4%) confirming the existence of a higher amount of water in the sample compared to the materials that contain mesoporous silica HMS. The presence of higher amount of water in CuZSM5-M can be due to hydrated $CuCl_2$ coming from microwave ion-exchange procedure. Moreover, the weight loss in the second step is due to the decomposition

of the residual metal chlorides, the removal of hydroxyl groups and decomposition of silanol bridges of the samples in the temperature range of 200-550 ˚C [199,200].
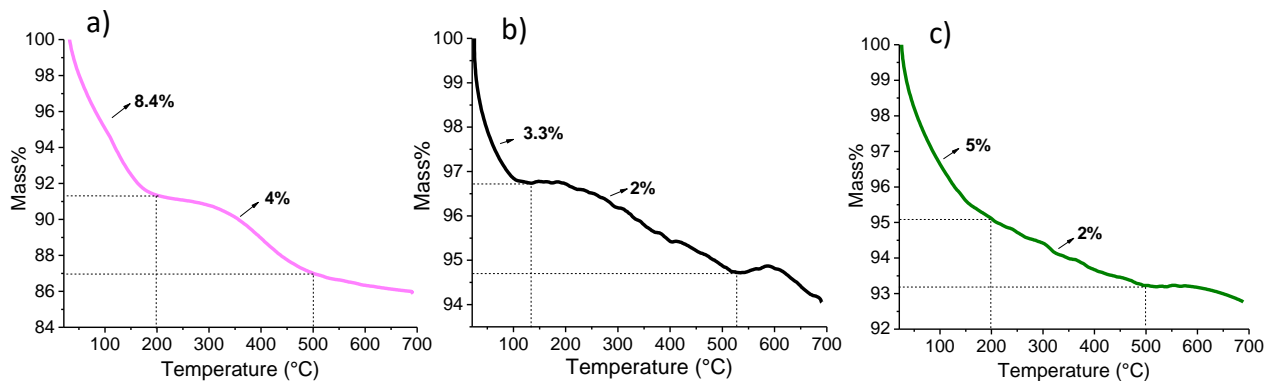

Figure 3.7. *TGA analyses of a) CuZSM5-M, b) HMS and c) CuZ(60%)@H*

3.3.2. Catalytic tests for glucose conversion

The catalytic efficiency of parent HMS, CuZSM5-M and composites were compared in glucose conversion at 200 °C during 5 h. As it is shown in Figure 3.8, all catalysts showed a full glucose conversion due to high reaction temperature. HMS has shown a very low LA yield, while the performance of CuZSM-5 was higher, giving 37% of LA yield. Although the microporous texture of the ZSM-5 can somehow restrict the mass transfer of the involved molecules in the reaction, decreasing the yield of the target product, the use of glucose as a small reactant avoids such strong limitations of mass transfer. Hence, by taking the advantages of the HMS porosity and CuZSM5-M acidity for a suitable ratio in the CuZ(60%)@H composite, a 45% yield of LA, was reached, which was higher than that of CuZSM5-M catalyst.
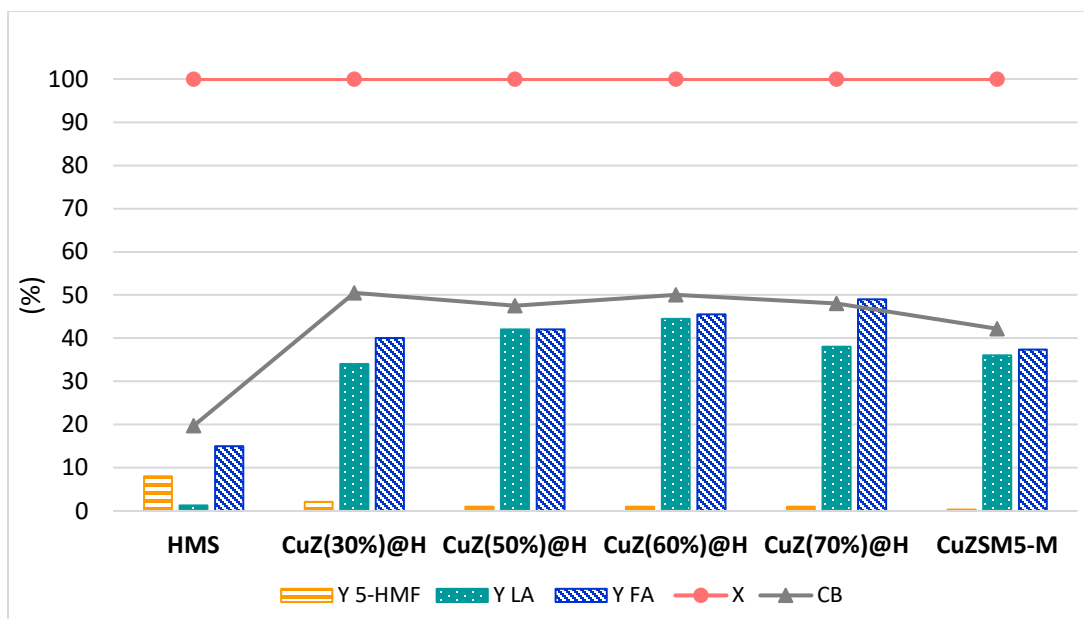
Figure 3.8. *Catalytic performance of all catalysts in glucose conversion.(Reaction conditions: 200 °C, 10 bar of N₂, 5 h, 2.7 mmol glucose, 500 mg catalyst, 100 mL water).*

3.3.3. Catalytic tests for cellulose conversion

The reactivity of CuZSM5-M zeolite and CuZ(60%)@H composite were investigated in cellulose conversion to LA at temperatures of 200 °C, 230 °C and 250 °C. As can be observed in the Figure 3.9, CuZSM5-M displayed a low efficiency toward LA producing 17% LA yield with 20% CB. As discussed about textural properties of CuZSM-5 in Figure 3.2 and Table 3.1, the superior microporosity of the ZSM-5 inhibits the penetration of polymeric cellulose into the pores of catalyst, and limiting its access to the Brønsted acid sites for hydrolysis, hence reducing the mass transfer and yield of LA. In particular, the first reaction step encompassing hydrolysis of cellulose, is most likely catalyzed by the external or superficial acid sites of CuZSM5-M. Thus, the obtained monomer, namely glucose and other intermediates along the reaction pathway could enter the zeolite micropores and reach to acid sites located in the channels and pores.

Moreover, a balance between high acidity of the zeolite, even superficial, for the first step of the reaction, and that located in the zeolite internal channels and pores for the subsequent steps, along with appropriate reaction conditions, was beneficial in obtaining 17% LA yield despite clear steric restrictions. Onda *et al*, studied HZSM-5 and HBeta zeolites for cellulose transformation and

52

achieved glucose yield of 12% at 150 °C and 24 h. In their case, the temperature of reaction was low and the reaction time was long, and low catalytic efficiencies were due to the microporous texture of HZSM-5 and HBeta zeolites which led to mass transfer limitation between bulky cellulose and catalyst acid sites [201]. Zhang *et al*, obtained 37% glucose yield from cellulose over microporous catalyst namely HY zeolite and with the assistance of microwave irradiation at 240 W and [C4mim]Cl solvent after 8 min [202]. However, water is more suggested as a green, environmental friendly, and economic solvent for the process even though heterogeneous catalyst and cellulose are not soluble in water and this could restrict the mass transfer [203]. Hence, high surface area and large pore size of the heterogenous catalyst are vital for cellulose transformation. In some research, hierarchical H-USY and ZSM-5 zeolites with high surface area and meso-microporous structure obtained from desilication and dealumination methods were selected as the catalyst to boost the mass transfer between hemicellulose and cellulose as the substrates and the catalysts. Therefore, hierarchical H-USY was an efficient catalyst for hemicellulose hydrolysis giving 56% yield of total reducing sugars (TRS) when comparing to the parent H-USY with producing 5.8% yield of TRS in the same reaction condition of 140 °C, 7 h [204,205]. However, the applied methods need a very careful control of desilication or dealumination to avoid loss in crystalline structure and alterations in acid properties of zeolite which decrease the activity and stability of the zeolite in the hydrothermal condition.

In this work, the combination of micro mesopores in the CuZ(60%)@H composite (Figure 3.2), assisted efficient mass transfer between bulky cellulose and composite mesopores providing higher accessibility to the acid sites of the catalyst. In addition, the strengths and concentrations of both Lewis and Brønsted acid sites were suitable for cellulose hydrolysis to glucose and its further transformation into LA. Thus, this catalyst was efficient giving 30% yield of LA. When comparing the CuZ(60%)@H activity at different temperatures, it was seen that best results were attained at 230 °C. Cellulose is insoluble in H_2O particularly at low temperature due to the inter- and intra-molecular hydrogen bonding [206]. Although enhancing temperature can improve cellulose hydrolysis, it causes formation of humins as reported by Chen *et al* [207]. A high amount of cellulose was obtained in the microwave assisted hydrolysis of amorphous cellulose of vegetable waste at the temperature higher than 150 °C after 5 min. In addition, Kang *et al*, exhibited that an optimum temperature to reach a maximum yield of LA is needed. Further increase of temperature cannot increase LA yield due to humins and other by-products production [208]. Kang *et al*

suggested that the optimum temperature for hydrolysis of cellulose was 170 ℃ using homogeneous H_2SO_4 catalyst after 2 h reaction. In our work, we found that 200 ℃ was not sufficient to achieve maximum amount of LA. The highest yield of LA was formed in the current case at 230 ℃. By further increasing of the temperature to 250 ℃, we assume that more humins were produced and FA was degraded to gases which was confirmed by giving lower yield of LA and FA, and lower CB, being 22%, 2%, and 28%, respectively.
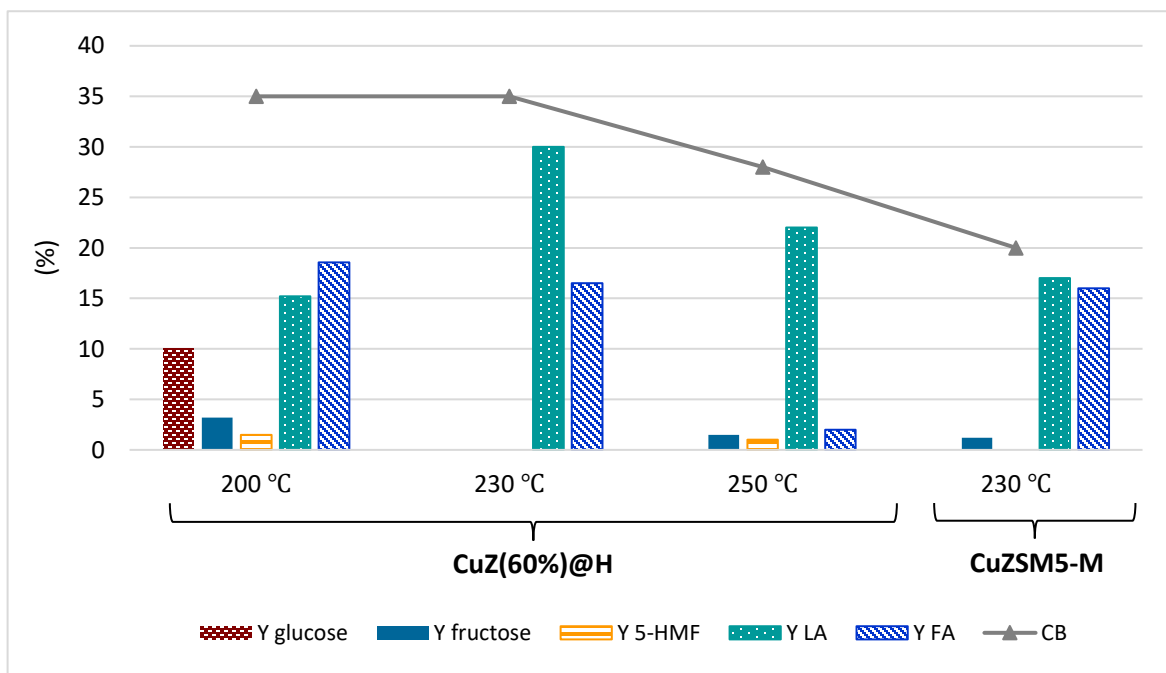
Figure 3.9. *Catalytic performance of CuZ(60%)@H and CuZSM-5 in cellulose conversion. .(Reaction conditions: 10 bar of N_2, 5 h, 3 mmol cellulose, 500 mg catalyst, 100 mL water).*

3.3.4. Acidity of catalysts and its effects on the catalytic performance

Figure 3.10 displays the NH_3-TPD profiles of HMS, CuZSM5-M and of the composites. According to NH_3-TPD profile, three different weak, medium and strong acid sites can be observed at different ranges of temperature. The peak in the range of 50-200 ℃ is associated to the weak acid site of the catalyst. The peaks at ranges of 200-400 ℃ and up to 400 ℃ are related to the moderate and strong acid sites of the catalysts, respectively [209]. Figure 3.10 shows that HMS exhibits a very low density of weak acid site and a high density of weak and medium acid sites is

present in CuZSM5-M [210]. The composites display a balance of the acid sites strength between HMS and CuZSM5-M. CuZ(30%)@H exhibits only weak acid site with the lowest contents of zeolite while by enhancing the amount of CuZSM5-M in the composite the acid sites strength is increased.
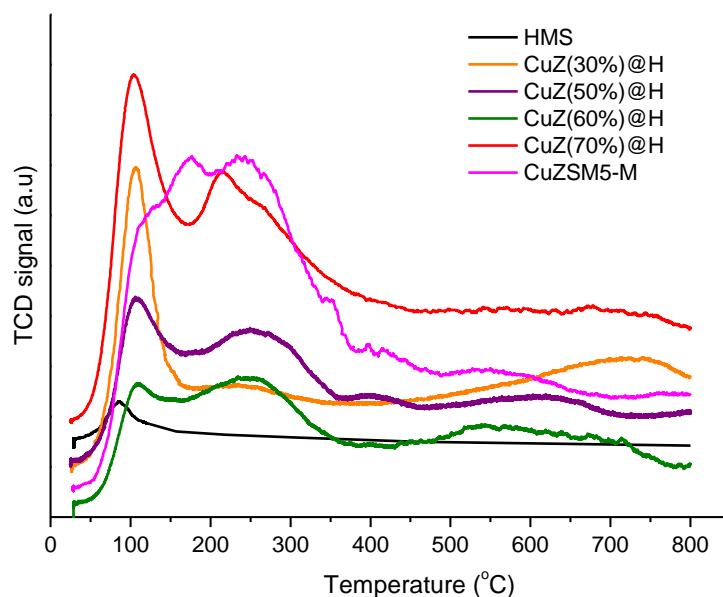

Figure 3.10. *NH₃-TPD profiles of the catalysts.*

The type of acid site in the catalysts was also investigated by FTIR spectroscopy of pyridine adsorption-desorption in the wavenumber range of 1400-1575 cm^{-1}. The concentration of weak, medium and strong Brønsted and Lewis acid sites estimated by desorbing pyridine at different temperatures are reported in Table 3.2. As can be observed, CuZSM5-M shows a high concentration of weak acid site, low concentration of medium without any strong acid site. This was also evident in NH₃-TPD profile. As it can be seen in the results of Table 3.2, the CuZ(30%)@H composite with the lowest content of CuZSM5-M displayed only weak acid sites which was observed also in the NH₃-TPD result. The composites with a higher content of CuZSM5-M showed mostly weak and few medium Brønsted and Lewis acid sites. Moreover, the total acid site concentration rose by increasing the amount of CuZSM5-M in the structure of composites. The result of pyridine-FTIR agree with NH₃-TPD profiles. The Brønsted acid site of

55

the composite comes from protons of the hydroxyl groups bridging framework silicon and aluminum, while the Lewis acid sites are owing to Cu(II) in the pores and channels and coordinated to the oxygen in the framework of zeolite. In addition, it is assumed that some Cu(II) species from residual $CuCl_2$ salts occurring in the CuZSM5-M surface were stabilized in the structure of the composite and other residual $CuCl_2$ salts were removed in the washing step of composite preparation procedure, as observed by the XRD pattern of CuZ(60%)@H reported in Figure 3.4a.

Table 3.2. *Concentration of Brønsted acid sites (C_B) and Lewis acid sites (C_L) in catalysts determined by FTIR with pyridine*

Catalysts	250 °C Weak acid site		350 °C Medium acid site		450 °C Strong acid site	
	C_B (μmol/g)	C_L (μmol/g)	C_B (μmol/g)	C_L (μmol/g)	C_B (μmol/g)	C_L (μmol/g)
CuZ(30%)@H	19	37	-	-	-	-
CuZ(60%)@H	56	103	0.1	0.9	-	-
CuZ(70%)@H	72	105	5.0	4.0	-	-
CuZSM5-M	146	139	14.0	4.0	-	-

As reported in the literature [211], the tandem conversion of glucose starting from isomerization of glucose to fructose followed by fructose dehydration to 5-HMF can be assisted by concentration, strength and type of catalyst's acid sites. The results of catalytic reaction in Figure 3.8 demonstrate a negligible efficiency of HMS into LA owing to lack of the acid sites in the catalyst as was confirmed by NH_3-TPD profile. However, full conversion but low CB for HMS could be due to the formation of insoluble oligomers deposited in the pores of catalyst as was suggested by van der Graaff *et al* [212]. In the literature, various methods were used to boost the acid site of mesoporous silica for glucose transformation. For example, Wang *et al*, improved total concentration of Lewis and Brønsted acids sites of SBA-15 mesoporous silica to 1316 μmol/g via impregnation of different Al/Nb atom ratios and obtained 55% yield of 5-HMF from glucose at 170 °C for 6 h [213]. Importantly, a mild acid site strength and suitable concentrations of Lewis

and Brønsted acid sites are desired to reduce extensive humins formation and boost LA yield as was demonstrated in the literature for the ZSM-5 as a similar catalyst [127, 214]. In our study, CuZSM5-M with weak and medium acid sites and high concentration of Lewis acid site showed an improvement in LA yield and CB compared to non-acidic HMS. As was discussed in the Section 3.3.3, when doing the reaction over composites with higher surface area and larger pore size, the mass transfer of substrate and products was increased. In addition, the acid sites of the catalyst were another prominent factor to improve the efficiency of the catalyst. The acid sites of the composites were tuned by altering the contents of the CuZSM5-M. Among composites, CuZ(30%)@H with low acid site concentration, as was reported in pyridine-FTIR result in Table 3.2, produced low LA yield. By enhancing the content of CuZSM5-M to 60%, and thus raising the acid site concentration, a maximum yield of LA was produced. However, 70% of CuZSM5-M in the composite led to a drop of LA yield because of high acid sites concentration leads to the production of more humins and lower CB.

The relations between the concentration of Brønsted and Lewis acid sites and the LA yield and CB of the catalysts are plotted in Figure 3.11(a,b).
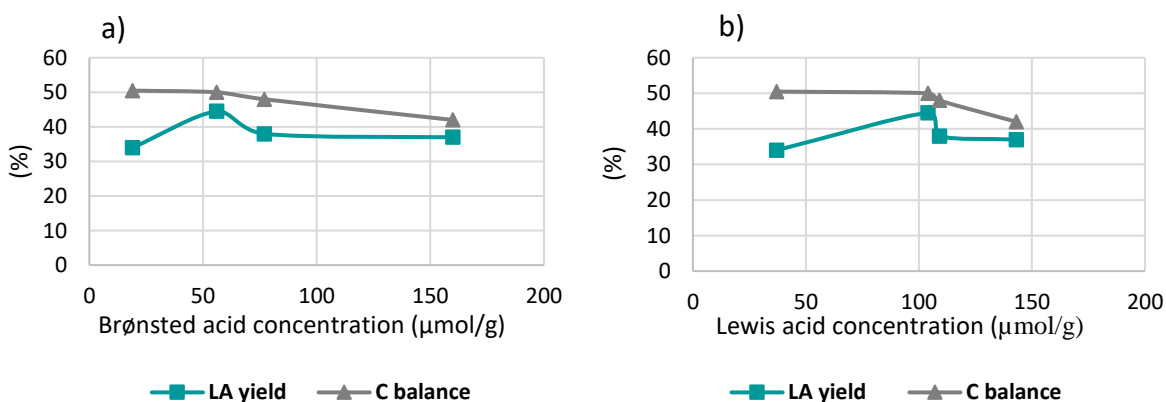
Figure 3.11. The effect of a) Brønsted and b) Lewis acid sites concentrations on the catalytic performance.

As can be observed in Figure 3.11a, by enhancing the concentration of Brønsted acid site from 19 µmol/g to 56 µmol/g, the LA yield increased from 34% to 45% and the CB stayed unchanged. This trend can be due to the importance of possessing sufficient Brønsted acid sites for fructose dehydration to 5-HMF. However, as the reaction is sensitive to the density of Brønsted acid site,

enhancing the concentration of Brønsted acid sites from 56 μmol/g to 160 μmol/g caused the decrease of LA yield and CB from 45% and 50% to 37% and 42%, respectively. Higher concentration of Brønsted acid sites resulted higher humins formation from side reactions and thus lower CB. Furthermore, the relation between Lewis acid site concentration and the LA yield and CB of the catalysts in Figure 3.11b indicates that by increasing of Lewis acid concentration from 37 μmol/g to 104 μmol/g, LA yield increased from 34% to 45% and CB stayed unchanged. As noticed before, an optimum density of Lewis acid site is desired to boost reaction from glucose isomerization pathway for production of higher LA yield. However, further enhancing of Lewis acid site concertation led to lower LA yield and CB at complete conversion that might be due to the simultaneous rise of Brønsted acid site concentration and formation of a higher humins. Thus, for our catalytic system, 56 μmol/g and 104 μmol/g were considered as the optimum Brønsted acid and Lewis acid concentrations containing B/L of 0.53 which resulted the highest yield of LA and CB. However, it is always significant to select a suitable and tunable catalyst and to optimize its textural and morphological features and acid properties as was noticed by Saravanamurugan *et al* [215]. It should be mentioned, however, that a fair comparison with the results obtained in the literature is difficult because of different porosity, surface area, acidity of the catalysts, and mainly by reaction conditions.

3.3.5. The stability of the catalysts

Humins as the by-products of sugars catalytic transformation are sensitive to the catalysts properties. Humins can be formed due to improper reaction conditions and catalyst acidity [216]. In this study, humins formation using both CuZSM5-5 and CuZ(60%)@H catalysts during the transformation of cellulose to LA was studied. As it is shown in Figure 3.12, the color of CuZSM-5 catalyst altered from light green to dark brown upon cellulose transformation, while CuZ(60%)@H exhibited a color change from light gray to dark gray confirming more humin formation on the CuZSM5-M catalyst. It can be assumed that the composite with more meso- and microporous structure and more moderate acidity was efficient and less humins were formed during the reaction.
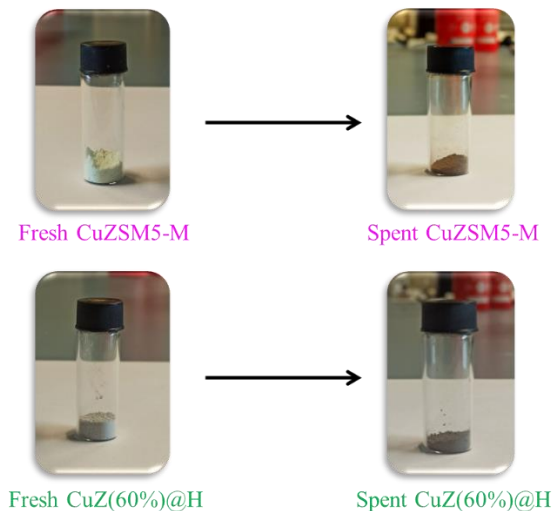
Figure 3.12. *Color change of the CuZSM5-M and CuZ(60%)@H catalysts during cellulose conversion.*

The molecular structure and functionality of humins deposited on the surface of spent catalysts were investigated by FTIR (Figure 3.13). Sumerskii *et al*, found that humins are made of 60% furan rings and 20% ether or acetal aliphatic linkers formed from polycondensation procedure [158]. Lund *and* co-workers reported that humins can be produced from 5-HMF rehydration via aldol condensation [217]. According to FTIR results of spent catalysts, the weak band at around 2922 cm^{-1} is associated to stretching of the aliphatic C–H [218]. Region below 1000 cm^{-1}, named as fingerprint region, the intensity increment of the band at around 800 cm^{-1} in spent catalysts' spectra compared to the fresh ones is related to the C–H out of the plane vibrations of the furan rings [219]. In addition, the small shoulder located at around 1706 cm^{-1} and the broadened band at 1630 cm^{-1} in the spent catalysts might be due to the stretching of C=O and C=C, characteristic of conjugated carbonyl group to an alkene group and also because of the carbonyl group in HMF molecules that was introduced to the structure of humins during reaction [216]. Therefore, the FTIR spectra of both spent catalysts showed the production of humins on the catalysts surface upon the cellulose transformation to LA. However, the weak intensity of bands associated to humins in the spent catalysts confirms that a small amount of humins were formed during the catalytic reaction.
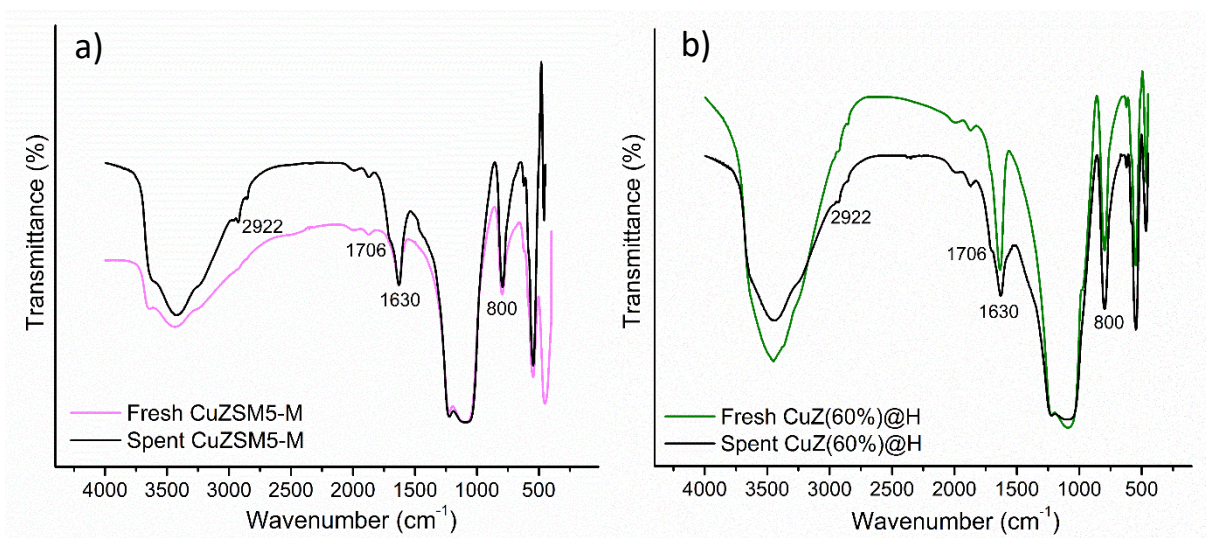
Figure 3.13. FTIR spectra of the fresh and the spent a) CuZSM5-M and b) CuZ(60%)@H catalysts.

Moreover, the morphology of the spent CuZ(60)@H was studied by TEM analysis (Figure 3.14). As can be observed, the high dispersion of copper nanoparticles is maintained after the reaction and a slight increase of particle size from 4.8 nm to 5.5 nm occurred demonstrating that no serious copper nanoparticles agglomeration happened. Particularly, some nanoparticles with the size of 5.5 nm might be associated to the slightly accumulated Cu(II) cations. We assume that small Cu(II) cations might move more freely in the channels of ZSM-5 and be slightly agglomerated in aqueous medium of the reaction [220]. In addition, the decrease of some Cu(II) cations in the channels of ZSM-5 might happened during the reaction and produce copper metallic nanoparticles [221]. We found that the suitable porous texture of the composite assisted the facile initial cellulose depolymerisation on the outer surface of HMS, as well as the mass transfer of intermediates and products in the pores, and formation of higher LA yield. The composite morphology was almost stable upon the reaction which might be due to suitable acidity of the catalyst causing lower humins production. The moderate and balanced acidity of the composite encouraged the desired pathway and lower humins formation as was observed in less color change of the spent composite in the Figure 3.12. Moreover, composite with mesoporous structure could provide a shorter diffusional path length and a fast leaving of bulky compounds diminishing the humins formation inside pores and deactivation of bulk acid sites [163–165,222]. Kang *et al,* reported that because the yield of

60

LA is highly related to the surface area and easy accessibility to the acidic sites of heterogeneous catalysts, it is significant to raise its stability by synthesis of materials with a highly porous structure, high surface area and suitable acidity with high accessibility [165]. Therefore, looking at the color of the spent CuZ(60%)@H and the weak intensity of bands related to humins in the FTIR spectra, it can be affirmed that the composite with high surface area, correct dimension of pores, and suitable acidity formed small amount of humins deposit on the surface. The spent CuZ(60%)@H composite was washed with deionized water and dried in the oven at 90 °C for 12 h and applied for the second run of the reaction. The yield of LA from first to second run decreased from 30% to 22% which could be due to the blockage of some acid sites by humins deposit. Indeed, small amount of humins deposit might be removed from the surface of catalyst by washing with an organic solvent (methanol, ethanol, acetone, methylene chloride) [208,223–225] or calcination procedure.
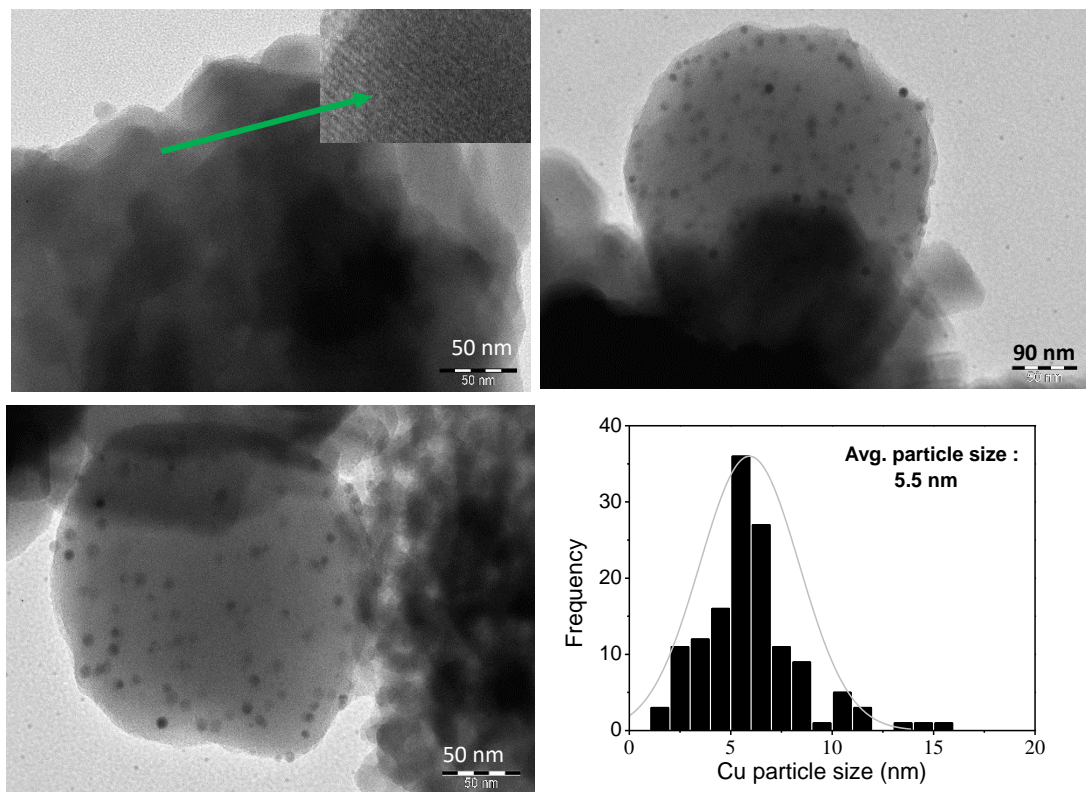

Figure 3.14. TEM images and Cu particle size distribution of spent CuZ(60%)@H catalyst.

61

3.3.6. The proposed mechanism of the reaction over CuZ(60%)@H

A mechanism proposed to explain the reaction route from cellulose into LA over CuZ(60 %)@H catalyst is schematized in Figure 3.15. As it is shown, various steps with several significant intermediates are involved in the cellulose conversion to LA. In the step (I), the hydrolysis or depolymerization of cellulose to glucose could occur over Brønsted acid sites of the catalyst. In particular, electron sharing from the glycosidic oxygen of cellulose with Brønsted acid sites of catalyst by the assistance of water molecule could cause the cleavage of β-1,4-glycosidic bonds to form glucose as was proposed by Lelekakis *et al* [226]. In the step (II-I), the glucose isomerization to fructose could happen catalyzed by Lewis acid site of the composite. The coordination of the electrons from the glucose ring's oxygen with the Lewis acid site of the composite might help on the cleavage of C1-O bond and creating C2-O new bond to form fructose. Moreover, as it can be seen in step (II-II), Brønsted acid site of the catalyst could assist a more facile electron transfer via sharing proton with the hydroxyl group connected to the C2 atom in glucose ring. In the step (III), both Lewis and Brønsted acid sites of the composite might catalyze the fructose dehydration to 5-HMF upon loss of three H_2O molecules. Since 5-HMF is an unstable intermediate in the water, its further rehydration to LA might occur with Brønsted acid site of the catalyst in the Step (IV) of the reaction. During this step, Brønsted acid sites could facilitate the ring opening of 5-HMF being subsequently followed by keto-enol isomerization to produce FA and LA.
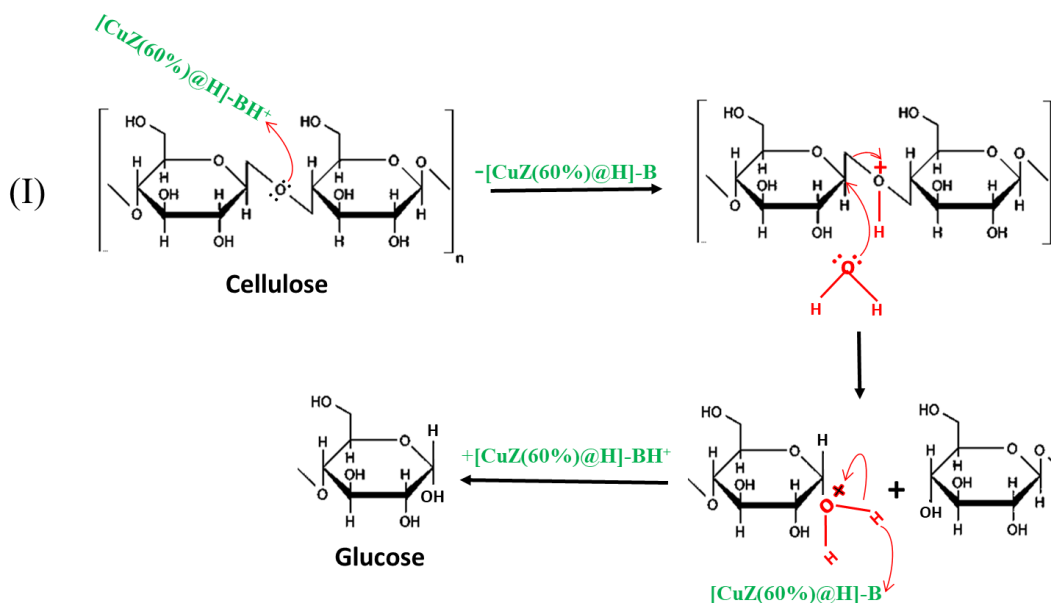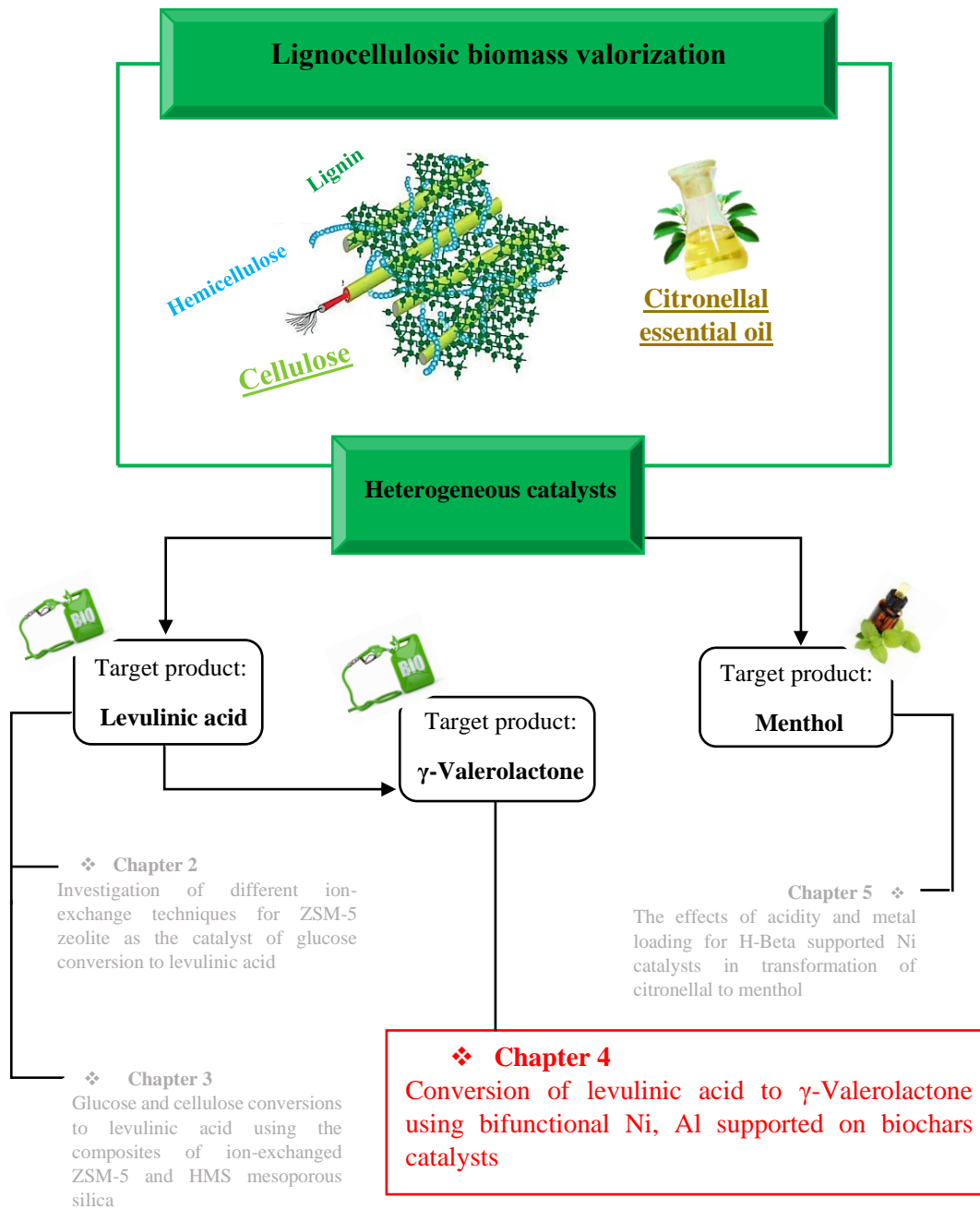
(II-I) Glucose / Fructose

(II-II) Glucose / Fructose

(III) Fructose / 5-HMF

(IV) 5-HMF / 2,5-dioxo-3-hexenal / FA / LA

3.4. Conclusion

In this study, the formulation of heterogeneous catalysts based on Cu(II)-exchanged ZSM-5 zeolite and HMS mesoporous silica was carried out to be applied in catalytic transformation of glucose and cellulose into LA. CuZSM5-M zeolite was selected to have an optimum and tailored concentration, strength and type of acid sites. HMS mesoporous silica was used to obtain a high surface area and suitable porosity needed for the target catalytic reactions. Compared to CuZSM5-M zeolite, HMS exhibited a very high mesoporous surface area (714 m^2/g) and large total pore volume (0.19 cm^3/g) according to the results of N_2 physisorption analysis. CuZ(60%)@H as the best composite synthesized from CuZSM5-M and HMS displayed a high surface area, and large pores being efficient for an easy mass transfer of the sugars particularly polymeric cellulose and also the involved intermediates and products of the reaction. Moreover, TEM images and low-angle XRD profile confirmed the well-ordered pore distribution of HMS in the structure of the composite. CuZ(60%)@H exhibited Brønsted and Lewis acid sites concentrations of 56 μmol/g and 104 μmol/g (B/L= 0.53) being as the optimum acidities for target reaction pathway from sugars to LA and lower amount of solid humins formation. The tailored morphological, textural features and acid properties of CuZ(60%)@H improved the formation of the highest yield of LA (45% and 30%) from conversion of glucose and cellulose, respectively. The best composite displayed a proper stability towards humins by possessing a preserved morphology and Cu(II) dispersion after the reaction. In the next Chapter, we are moving to the valorization of LA to GVL using carbonaceous catalysts (biochar).

Lignocellulosic biomass valorization

Lignin

Hemicellulose

Cellulose

Citronellal essential oil

Heterogeneous catalysts

Target product:

Levulinic acid

Target product:

γ-Valerolactone

Target product:

Menthol

❖ **Chapter 2**
Investigation of different ion-exchange techniques for ZSM-5 zeolite as the catalyst of glucose conversion to levulinic acid

Chapter 5 ❖
The effects of acidity and metal loading for H-Beta supported Ni catalysts in transformation of citronellal to menthol

❖ **Chapter 3**
Glucose and cellulose conversions to levulinic acid using the composites of ion-exchanged ZSM-5 and HMS mesoporous silica

❖ **Chapter 4**
Conversion of levulinic acid to γ-Valerolactone using bifunctional Ni, Al supported on biochars catalysts

Chapter 4. Conversion of levulinic acid to γ-Valerolactone using bifunctional Ni, Al supported on biochars catalysts

4.1. Introduction

4.1.1. γ-Valerolactone production from levulinic acid

γ-Valerolactone (GVL) is a C_5-cyclic ester with the formula $C_5H_8O_2$ and IUPAC name 5-Methyloxolan-2-one. GVL is present in some natural products such as fruits and is used as a food additive and a chemical and sustainable precursor for formation of various products in energy and carbon-based consumers applications. The physical and chemical properties of GVL such as low vapor pressure at high temperature, being non-toxic, and not producing peroxide in the air in a long period of time allow its safe storage and transportation, as well as extensively usage as a green solvent and fuel additive [227]. Another significant property of GVL is its chemical stability, especially in water at maximum 60 ℃ for around one month [228]. GVL can be used as a sustainable substitution of ethanol in the fuel additive application, with a similar mixing ratio of 10 v/v% GVL and 90 v/v% 95-octane gasoline and similar properties. Compared to ethanol, the removal of GVL from water by distillation is easier consuming less energy because it does not produce an azeotrope with water [229]. Another advantage of GVL as a fuel additive respect to the traditional fuels is the reduction of CO, hydrocarbons and smoke emission as the environmental poisoning gases. Moreover, GVL has a quite similar energy combustion with ethanol (29.7 MJ/kg) and keeps more than 97% of energy content of glucose as the initial substrate. Therefore, the utilization of a low-cost feedstock can help on providing GVL with a reasonable price of around 2-3 USD/gallon [230]. Although direct application of GVL as the transportation fuel could simplify its global monitoring and regulation, its higher solubility in water, lower cetane number and energy density compared to fossil fuels make some limitation of the direct disposal. In addition, GVL can be used as a precursor of several other chemicals such as aromas, valeric acid, butene isomers, 1,4-pentanediol, adipic acid (precursor for nylon), methyltetrahydrofuran, and 4-hydroxypentane alkylamides [228]. Kunshan Qiandeng, Inoue Perfumery MFG, and Soda Aromatic are some examples of active participants in the production of GVL. It is expected that

GVL would keep a growing compound annual growth rate (CAGR) in the market by 2025 and reach USD million [230]

GVL can be produced from several substrates such as cellulosic carbohydrates, furfural, furfuryl alcohol, LA, and alkyl levulinates [231]. One of the most common and key routes for GVL production is hydrogenation of LA passing from two possible reaction pathways (Figure 4.1): (1) LA ketonic group hydrogenation to a very active intermediate 4-hydroxypentanoic acid and its simultaneous dehydration passing from an intramolecular esterification and cyclisation giving GVL (Figure 4.1, pathway I), and (2) LA dehydration and cyclisation to intermediates α-angelica lactone or β-angelica lactone and their hydrogenation resulting GVL (Figure 4.1, pathway II).
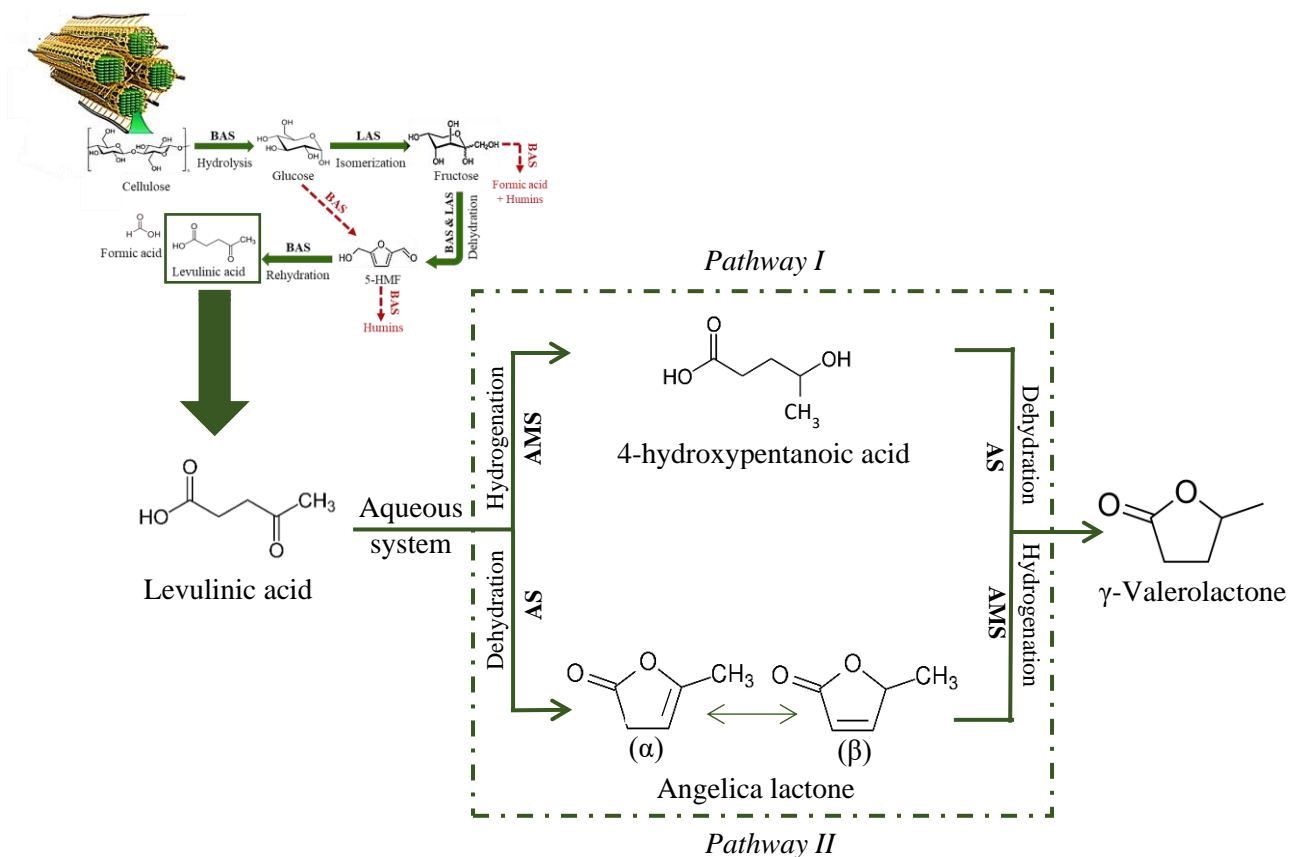

Figure 4.1. *Possible reaction pathways from levulinic acid to γ-Valerolactone (AMS: active metal site; AS: acid site)*

Overall, each hydrogenation step is catalyzed with active metal catalyst, and each dehydration step undergoes over acid active catalyst or acidic condition of the reaction. One of the possible

byproducts of the reaction could be pentanoic acid from subsequent dehydration and hydrogenation of 4-hydroxypentanoic acid in the presence of Brønsted acid sites. Moreover, coke formation is another possible side reaction coming from condensation of LA and especially angelica lactones under severe acidic condition [232].

GVL can be synthesized exothermically from hydrogenation of LA in both gas and aqueous phases with enthalpy changes of 47.73 kJ/mol and 74.5 kJ/mol, respectively [233]. As was mentioned, the catalyst of the reaction must have bifunctional properties of active metal site and acid site for catalyzing hydrogenation and dehydration steps, respectively. In the next section, a state-of-art about the catalytic systems of the target reaction and an introduction about the catalysts used in the present study will be referred.

4.1.2. Catalysts for hydrogenation of levulinic acid to γ-Valerolactone

Researchers have studied catalytic transformation of LA to GVL over a wide variety of catalysts causing different pathways of the reaction and GVL yields. In some studies, formic acid was used as the homogeneous acidic material to catalyze the dehydration step of the reaction. However, besides all drawbacks of a homogeneous acid catalyst, it also needs harsh reaction conditions and another active metal catalyst for hydrogenation step. These make a potential trend towards bifunctional heterogeneous catalytic system to meet a more sustainable and environmental-friendly system [234,235]. Overall, the catalytic activity depends on the combined effects of hydrogenation active metal phase and acid sites. Often, the acidic properties of the catalysts come from the acidic nature of the selected support. Among heterogeneous catalysts, noble and non-noble metals supported materials have been widely used in the literature. In particular, noble metals such as Ru, Pt, Pd, and Ir have been extensively applied as the catalyst's hydrogenation active phase and among them carbon supported Ru materials took the greater part [228,232]. Although noble metals are highly active phases for the proposed reaction, non-noble metals such as Ni, Cu, Fe, Mg and Al are better options due to a higher availability and economic sustainability [235–237]. Ni has been widely used in several studies for the proposed reaction because of its high activity and selectivity to GVL. For example, N-doped multichambered mesoporous carbon microspheres supported Ni catalysts displayed almost full LA conversion and GVL selectivity [238]. In another study, Ni/NiO catalyst with a partial reduced NiO to Ni exhibited a better performance that metallic Ni and NiO giving a full LA conversion to GVL at 120 °C, 20 bar H_2

for 24 h. The formation of Ni/NiO heterojunctions was the main reason of the catalyst' higher efficiency [239]. Hengst and co-workers investigated the effect of different techniques including wet impregnation, flam spray pyrolysis, precipitation with NaOH, and precipitation with urea for the preparation of Ni/Al_2O_3 catalysts. Among them, wet impregnation led to a more suitable Ni particle size (6 nm) and dispersion and a higher catalytic efficiency giving LA conversion of 90% and GVL selectivity of 75% in the aqueous medium at 200 °C, 50 bar H_2, for 5 h [240]. In this study, Ni was selected as a cheap, non-noble and sustainable hydrogenation active phase and was introduced in the catalytic support by wet impregnation method.

In addition, the catalytic supports have had a vital influence on the catalytic activities mostly possessing the acid sites for dehydration step, and catalysts stabilities affecting from coke formation, metal leaching and sintering [241–245]. From the literature, oxide type supports such as ZrO_2, TiO_2, Al_2O_3, SiO_2, MgO, and ZnO, mesoporous silica-based materials such as MCM-41 and SBA-15, microporous zeolites, clays, and carbon-based materials were reported for the target reaction [228,232].

For instance, Ni/Al_2O_3 was investigated as the catalyst of the reaction, and by taking the advantages of Ni as a hydrogenation active phase and alumina acidic properties, 91% yield of GVL in full LA conversion was obtained at harsh reaction conditions of 250 °C, 65 bar H_2 for 2 h [237]. In another study reported by Fu *et al*, $Ni/\gamma-Al_2O_3$ gave 93% yield of GVL at 200 °C, 30 bar H_2 for 3 h [246]. As examples of carbon supported Ru catalysts, Cao *et al*, studied Ru/C and Ru/ZrO@C in both aqueous and acidic mediums and more than 70% LA conversion and GVL yield were obtained at 140 °C and 10 bar H_2 for 2h [247]. In addition, commercial activated carbon was used as the Ni catalyst support in which 99% GVL selectivity in 80% LA conversion was achieved using non-green dioxane as the solvent of reaction at 200 °C and 30 bar H_2, for 4 h [238]. In this study, we aimed to use a sustainable and active catalyst with reduced environmental impact and economic concerns for the proposed reaction. Hence, natural carbon-based materials (biochars) as the solid byproducts of different biomasses pyrolysis were selected as the supports of the catalysts.

Biochar is a composition of carbon, hydrogen, nitrogen, oxygen, sulfur and ash with different proportions. The amounts of each element and ash in biochar are influenced by the origin of initial biomass, the pyrolysis conditions, and each pre- and post-treatment procedure [248]. Through the pyrolysis processes, biomass aliphatic carbon chains are converted to biochar aromatic carbon.

The lower H/C ratio suggests a higher degree of aromatization in biochar structure, while a higher O/C and N/C ratios propose a higher doped and superficial polar functional group which improve the hydrophilicity of biochar [249,250].

In particular, biochar is concidered as a non-graphitic/non-graphitizable carbon. As it is shown in Figure 4.2a, non-graphitic/non-graphitizable carbon materials possess various groups of localized parallel carbon sheets that are hardly cross linked together [251]. Most of the biochars are non-ordered structure with very low surface area and weak porosity limiting their utilization in catalytic application. Several modification procedures such as selection of a proper biomass, controlling the pyrolysis conditions, heteroatom doping, surface functionalization, activation, and composing with other materials have been applied to improve the biochar specific properties [252]. Several techniques have been investigated for biochar activation to develop its localized order and hierarchical porous structure. Examples are given by physical activation (with CO_2, steam, O_3), chemical activation (with KOH, NaOH, NH_3, K_2CO_3, $ZnCl_2$, HCl and H_2SO_4), and activation by hard template approaches such as mesoporous silica [253]. It should be noted that during activation process, the ordered structure of biochar can be improved, but not to an absolutely ordered structure like graphitic carbons. Typically, the crystalline disorder of biochar materials before activation is called turbostratic wherein the successive layer planes are set up roughly parallel and equidistant with a random rotation respect to each other (Figure 4.2b). However, we cannot call them a graphitic structure because they do not have a crystallographic order and the spaces between successive layer planes are larger than graphite [254,255]. Through the activation process and by increasing the activation temperature, a localized crystallization occurs by: -breaking the cross links, providing free carbon sheets and their compression by surrounding cross-linked structures for creating a higher ordered structure; - the removal of more heteroatoms from carbon sheets, creation of carbon radicals, linking the provided carbon radicals to form larger carbon sheets [251,256].
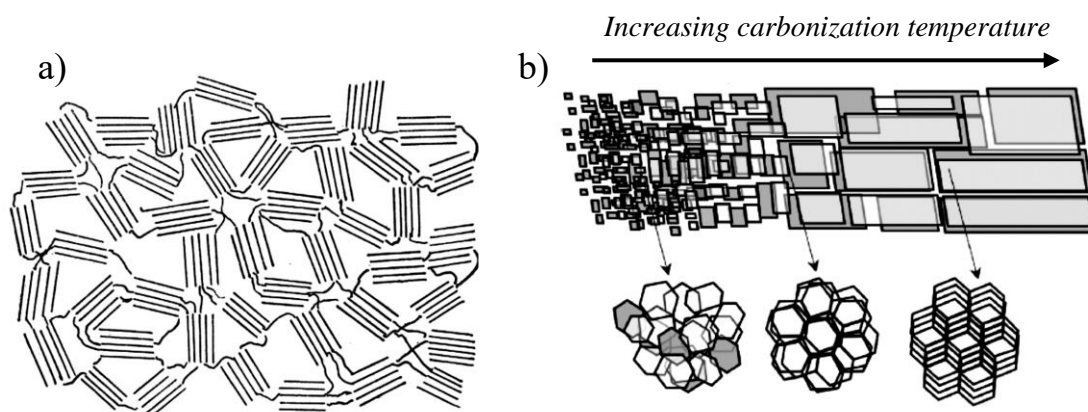
Figure 4.2. *a) Postulated structures of non-graphitizable carbon* [138], *b) The effect of carbonisation temperature on biochar structure development, transferring from turbostratic arrangement (left) to semi graphitic arrangement (right)* [145].

Besides the localized crystallization meaning the ordering process of internal region, the activation procedure leads to an augmented porosity and surface area in biochar structure. In this thesis, physical activation method using CO_2 agent, as an eco-friendly and efficient approach, was applied for improving biochar porosity. In particular, the spaces between the crumpled carbon sheets in biochar compose its porosity. Through physical activation, the oxidation of carbon atoms in the biochar network occurs by CO_2 or steam agent. Hence, the oxygen atoms of activation agents are bonded with biochar carbon atoms resulting in release of CO molecules from the network and generating porosity (Figure 4.3). This process is endothermic and normally happens at the temperatures above 700 °C [62,257]. In this study, four different biomasses were selected for preparation of biochar-based supports: a) Vine wood: a vegetal and agricultural or food waste from second generation biomass, typically lignocellulosic, made of cellulose, hemicellulose, and lignin; b) Barley waste: a vegetal and agricultural or food waste from second generation biomass, typically lignocellulosic, made of cellulose, lignin and arabinoxylans and rich in protein, lipid, fiber, and vitamins; c) Leather tannery waste: an industrial waste and from animal derived raw material, classified as the second generation biomass, rich in collagen, and proteins, and d) *Sargassum* brown macroalgae of Venice lagoon: from third generation biomass, rich in protein, lipid, and carbohydrate. The aim is to investigate the possible utilization and influence of biochars from

71

different origins and generations of biomass as the supports for bifunctional Ni, Al-based catalysts in LA hydrogenation to GVL.
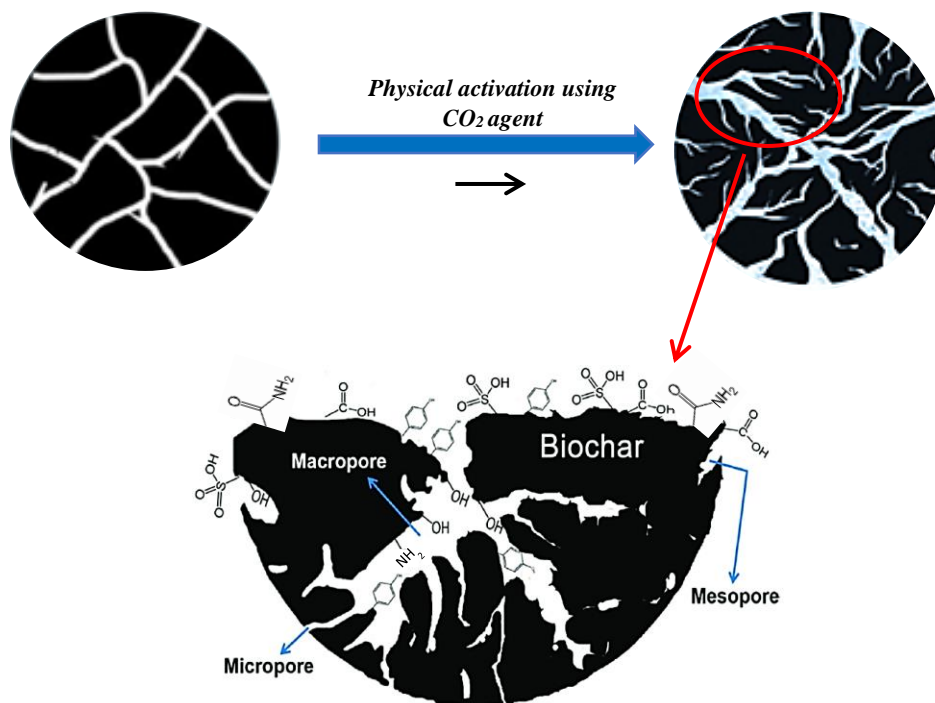

Figure 4.3. Improvement of biochar porosity through physical activation process and biochar surface functionality.

Besides the crucial importance of active metal phase in LA hydrogenation, the acidic feature of the catalyst plays a prominent role in accelerating 4-hydroxypentanoic acid intermediate formation or angelica lactone transformation to GVL [241]. A combination of both Lewis and Brønsted acid sites is desired to guarantee and improve the overall performance of the catalyst. Lewis acid site exhibited a higher efficiency on boosting GVL selectivity than Brønsted acid site. However, besides Lewis acid site, a proper concentration of Brønsted acid sites can accelerate the lactonization process and facilitate the GVL production. For instance, the catalysts with only Lewis acid property such as Al_2O_3, ZrO_2 and SnO_2 could produce less than 10% GVL yields, while the catalyst with both Lewis and Brønsted acid sites such as SnO_2/SBA-15 could significantly improve the GVL yield over 80% with the same reaction conditions [258]. It is significant to note that an excessive Brønsted acid sites concentrations can cause the decrease of GVL selectivity by its

further ring opening and over-conversion to by-products [259–261]. For example, ZrAl-Beta-25 catalyst with a lower Lewis/Brønsted ratio (0.85) produced 71% yield of GVL, while Zr-Beta-100 with a higher Lewis/Brønsted ratio (8.4) gave a higher GVL yield of 96% [262]. In addition, high acid concentration of the catalyst can lead to a rapid deactivation of the catalyst through coke deposition. In the most reported studies, the catalyst acidity has been derived from the catalytic support such as ZrO_2, Al_2O_3, and zeolite [228,232]. Carbon based materials are extensively applied as efficient catalytic supports for several biorefinery catalytic systems due to their typical properties such as high surface area, excellent electronic conductivity and high resistance in acidic condition [263,264]. In literature, carbon-based catalysts have also been used for LA conversion to GVL in which the Brønsted acid site was provided by the acid functionalization of carbon with different reagents such as phosphoric acid and sulfuric acid, and the Lewis acid site was supplied by different coordination of active metal/metal oxide phases [265,266]. Moreover, in one study, the sulfuric acid functionality poisoned Ru metallic site on the ordered mesoporous carbon and diminished the catalytic activity [267]. In another study, the presence of the carboxyl and hydroxyl functional groups in carbon-based bifunctional catalyst (functionalized carbon supported Ni/NiO) could efficiently improve the catalytic performance for LA conversion to GVL in supercritical CO_2-ionic liquid systems [268]. In this study, since biochars as the catalytic supports are provided from pyrolysis of biomasses, they naturally possess the Brønsted acid functionalities affected from the origin of the initial biomasses. This aspect can be considered as a vital inspiration in formulation of a novel and green catalytic system for the proposed bio-based reaction. Moreover, Al-containing structures as the Lewis acid site of the catalyst is introduced to the biochar supports by two different impregnation and precipitation techniques.

4.1.3. The aim of the chapter

In this chapter, the catalytic hydrogenation of LA to GVL was studied. Development of a cheap and sustainable heterogeneous catalyst was the main aim of this chapter. Therefore, activated carbons derived from biomasses (activated biochars) were selected as novel supports for related reaction. In particular, activated biochars were obtained from pyrolysis and CO_2-physical activation of four different biomasses including **t**annery shaving waste (T), vine **w**ood waste (W), **b**arley waste (B) and *Sargassum*, brown macro**a**lgae of Venice lagoon (A). Al-containing species as the Lewis acid site for dehydration step was incorporated to the supports using two different

methods of wet impregnation and precipitation. Ni as a hydrogenation active phase was introduced in the supports via wet impregnation technique. Biochar-based supports and catalysts were characterized by AAS, elemental analysis, FTIR, N_2 physisorption, XRD, SEM, EDS, TEM, TPD, NH_3-TPD and TPR techniques. The catalysts were tested for LA hydrogenation to GVL in a batch system. The results showed that activated biochar supported only Ni was not active in the proposed reaction due to the lack of Lewis acid site for dehydration step. Precipitated Al-containing species on the biochar-based supports demonstrated a higher performance in the reaction compared to impregnated one because of a better Al species dispersion and its different interaction with support and Ni species affected by synthetic approach. Among different supports, the activated biochars obtained from T and W acted as the best ones. A higher catalytic efficiency was strongly influenced by the chemical, textural and morphological properties of activated biochars obtained from different biomasses with different natures.

4.2. Experimental

4.2.1. Catalyst preparation

- *Preparation of biochar-based supports*

Four different biomasses were selected for preparation of biochar-based supports:

1) Tannery shaving waste (T) that was obtained from PASUBIO S.p.A. tannery (Arzignano, Italy), provided by GOAST technology, Green Organic Agents for Sustainable Tanneries (LIFE project)
2) Vine wood waste (W) that was supplied from Conegliano, Italy.
3) Barley waste (B) that was provided from Padova, Italy.
4) *Sargassum*, brown macro**a**lgae (A) that was collected from Venice lagoon.

To obtain biochar, the pyrolysis of biomass was performed in a laboratory-scale prototype plant (Carbolite custom model EVT 12/450B) (Figure 4.4) consists of a vertical oven with a fixed bed tubular quartz reactor. The upper exit of the reactor was connected to the quenching system through a heated outlet pipe (ca. 200 °C) which itself was connected to a water-cooled condenser (20 °C) and a series of glass condensers (0 °C) in an ice bath for collection of liquid fraction or bio-oil. Moreover, the gas fraction was connected to the exit of final glass condenser which was possible

to analyze by GC via GC-TCD injector with an automatic sampling valve. The temperatures of both oven and reactor were adjusted by an electrical heating system comprising N-type thermocouple and PID (Proportional, Integral, Derivative) temperature controller. The flows of gases were controlled by Brooks mass flow controllers.
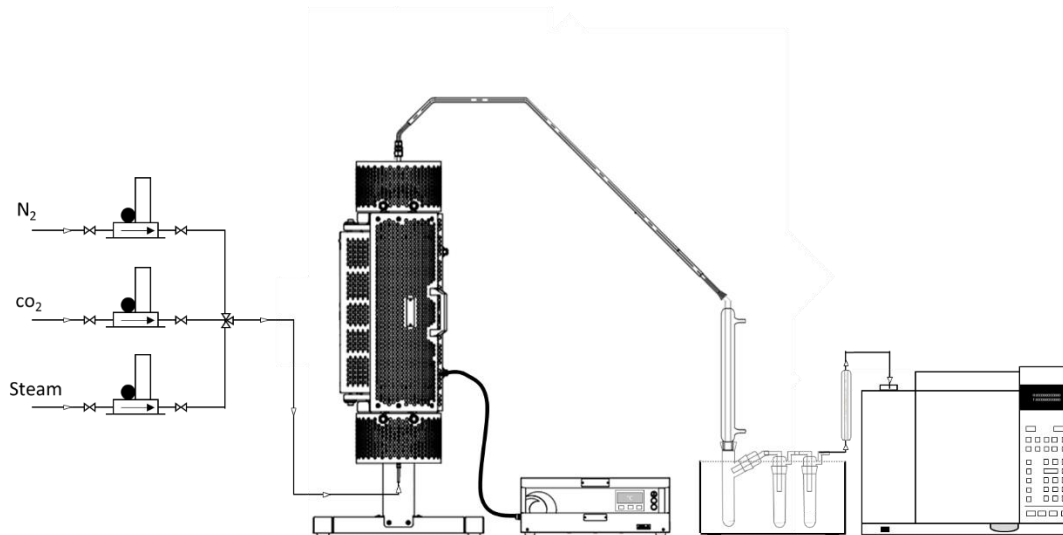

Figure 4.4. The scheme of laboratory-scale pyrolysis setup

Before pyrolysis, T biomass was dried in the air for 48 h, and A was washed with tap water and distilled water, dried in the air for 48 h and further dried in the oven at 110 °C for 2 h. Whereas, W and B were directly used in pyrolysis process without any typical pretreatment.

In a pyrolysis run, first, around 40 g of proposed biomass (size < 0.250 mm) was charged into the reactor and was pyrolyzed at 600 °C, with a heating rate of 5 °C/min, and a residence time of 30 min under N_2 flow of 100 mL/min. The biochars obtained from pyrolysis step were labeled as B_T, B_W, B_B, and B_A for T, W, B, and A biomasses, respectively. After 30 mins of pyrolysis procedure, the temperature was immediately increased to 700 °C with a heating rate of 20 °C/min under N_2 flow of 100 mL/min. Then, the gas was switched to CO_2 as the activation agent with the flow of 100 mL/min and the physical activation was carried out for 4 h. To remove the inorganic residues (ashes), activated biochar was mixed with HCl (Merk, ≥37.0 wt%) (1 M) solution and was sonicated for 1 h. Then, the activated biochar was filtered and washed with deionized water until achieving a neutral pH. The sample was dried in the oven at 110 °C for 12 h. All materials were grinded and sieved to particle size <180 μm in diameter. The final obtained supports were labelled

75

A_T, A_W, A_B, and A_A, respectively. The list and labels of prepared supports are provided in Table 4.1.

Table 4.1. The list and labels of prepared supports.

Biomass	Biochar	Activated biochar
Tannery shaving waste **(T)**	B_T	A_T
Vine **W**ood waste **(W)**	B_W	A_W
Barley waste **(B)**	B_B	A_B
Sargassum brown macro**A**lgae **(A)**	B_A	A_A

- *Incorporation of Al as the Lewis acid site*

Al was introduced to the biochar-based supports using two methods including wet impregnation and precipitation.

1) *Incorporation of Al via wet impregnation method*: First a solution of $Al(NO_3)_3 \bullet 9H_2O$ (Sigma-Aldrich, ≥ 98.0 wt%) in 5 mL deionized water with proper concentration was prepared in order to have a final Al loading of 10 wt.%. Second, the desired amount of A_T activated biochar was added to the solution aimed to have a final catalyst weight of 1.5 g. Then, the mixture was stirred with the rate of 500 rpm, at 25 °C for 1 h. Finally, the solution was evaporated in the oven at 90 °C for 12 h. The final sample of this step was labeled Ali/A_T.

2) *Incorporation of Al via precipitation method*: In this method, first, two solutions were prepared: (A) a 50 mL solution of $Al(NO_3)_3 \bullet 9H_2O$ with proper concentration to have a final Al loading of 10 wt.%, (B) a solution of NaOH (3 M) (Sigma-Aldrich, ≥ 98.0 wt%) as the precipitation agent. Then, the solution A and B were added dropwise to a 100 mL mixture of biochar-based support (A_T, A_W, A_B, A_A) in deionized water using a peristaltic pump. Therefore, $Al(OH)_3$ was precipitated on the support keeping the pH of solution in the range of 7-8 and according to the following formula:

$$Al(NO_3)_3 + 3\ NaOH \longrightarrow Al(OH)_3 + 3\ NaNO_3$$
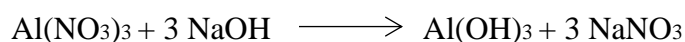
Then, the mixture was filtered, washed with distilled water until reaching the neutral pH. Finally, the sample was dried in the oven at 90 °C for 12 h. The final samples of this step were labeled Alp/A_T, Alp/A_W, Alp/A_B, Alp/A_A.

- *Introduction of Active Ni phase by wet impregnation method*

For impregnation of Ni, a solution of $Ni(NO_3)_2.6H_2O$ (Merck, 99.999%) in 5 mL deionized water with proper concentration was prepared in order to have a final Ni loading of 10 wt.%. Then, the Al incorporated-activated biochar was added to the solution and the mixture was stirred at 25 °C for 1 h. The solution was evaporated in the oven at 90 °C for 12 h. In addition, a catalyst of A_T supported Ni was prepared following the same approach.

- *Calcination and reduction of the catalysts*

All prepared catalysts were calcined in N_2 with flow rate of 50 mL/min, at 550 °C, with a heating rate of 5 °C/min, and a residence time of 4 h. During the calcination, the decomposition of impregnated $Al(NO_3)_3•9H_2O$ and precipitated $Al(OH)_3$ to Al_2O_3 happened [269,270]. Moreover, impregnated $Ni(NO_3)_2.6H_2O$ could be decomposed following the order of Ni_2O_3, Ni_3O_4, NiO [271]. After calcination step, the catalysts were reduced in the presence of pure H_2 with flow rate of 50 mL/min, at 400 °C, with a heating rate of 10 °C/min, for 3 h. The list of prepared catalysts is provided in Table 4.2.

Table 4.2. The list of prepared catalysts.

catalyst	Support	Impregnated Al (wt.%)	Precipitated Al (wt.%)	Impregnated Ni (wt.%)
Ni/A_T	A_T	-	-	10
NiAli/A_T	A_T	10	-	10
NiAlp/A_T	A_T	-	10	10
NiAlp/A_W	A_W	-	10	10
NiAlp/A_B	A_B	-	10	10
NiAlp/A_A	A_A	-	10	10

4.2.2. Catalytic test

For investigation of the catalytic reactivity of different prepared catalyst, all samples were tested in a batch system namely a stainless-steel autoclave of 400 mL volume. A mechanical stirrer was used and the temperature was adjusted using an electric heater with thermocouple. The autoclave was charged with 0.17 M of levulinic acid solution in 50 mL deionized water, and 400 mg catalyst to have a LA/Ni molar ratio of 12.5 : 1 The autoclave was purged ten times with N_2 to remove the air and then was pressurized with 35 bar of H_2. The temperature was increased and the reaction time was considered once the temperature reached to desired value. When the reaction was ended, the autoclave was cooled down to 25 °C and the final mixture was filtered. In addition, the reaction conditions were optimized in the presence of the best catalyst by changing temperature, H_2 pressure, time, and LA/catalyst mass ratio.

For analysis of the products, the filtered solution of each reaction was injected to a high-performance liquid chromatography (HPLC) Agilent Technology 1260 Infinity II. An Aminex HPX-87H column was used in HPLC and the analysis was carried out at column temperature of 57 °C by passing the mobile phase of 5mM H_2SO_4 with the flow rate of 0.6 mL/min. A UV–vis detector (Λ =195 nm) was used for analytes' identification and quantification. The LA conversion (X), GVL yield (Y_{GVL}), and turnover frequency (TOF) were calculated using the following equations:

$$X\ (\%) = \frac{\Delta n}{n_0} \cdot 100$$

$$Y_{GVL}\ (\%) = \frac{n_{GVL}}{n_0} \cdot 100$$

$$TOF = \frac{\Delta n}{\Delta t . n_{Ni}}\ s^{-1}$$

Where Δn corresponds to the reacted mole of LA during the reaction. n_0 and n_{GVL} represent the mole of LA at time zero and GVL in the final liquid phase, respectively. Δt corresponds to the time of the reaction and n_{Ni} is the actual mole of Ni in the catalyst measured by AAS analysis.

4.3. Results and discussion

4.3.1. Characterization of biochar-based supports

The CHNS elemental analyses of biomasses, biochars, and activated biochars are reported in Table 4.3. As can be seen, the pyrolysis and activation processes led to an increase of carbon contents and a decrease of H/C ratio in all materials which can be related to the carbonization and aromatization phenomena [272]. Exceptionally, the activation of B_B to A_B showed an opposite trend which could suggest that the activation of this biochar was not completely performed in the proposed conditions.

Table 4.3. *CHNS elemental analysis of biomasses, biochars, and activated biochars. (The amount of elements is reported in mass percentage).*

Sample	C [%]	H [%]	N [%]	S [%]	O [%]	Ash [%]	H/C	O/C
T	44.6	6.3	11.5	2.5	-	-	0.141	-
B_T	73.6	2.7	12.4	0.7	6.1	4.5	0.036	0.082
A_T	76.6	1.1	9.4	0.6	9.8	2.5	0.014	0.128
W	46.6	6.0	0.5	0.2	-	-	0.128	-
B_W	81.3	1.5	1.1	0.2	8.8	7.1	0.018	0.108
A_W	82.1	0.9	1.3	0.2	13.4	2.1	0.011	0.163
B	49.2	6.7	2.8	0.3	-	-	0.136	-
B_B	72.8	1.3	5.2	0.2	13.4	7.1	0.017	0.184
A_B	67.0	1.5	4.0	0.2	11.6	15.7	0.022	0.170
A	37.1	5.3	4.8	1.3	-	-	0.142	-
B_A	43.4	1.2	3.6	2.0	-	-	0.027	-
A_A	67.1	1.2	6.8	2.8	7.9	14.2	0.017	0.117

When comparing different activated biochars, A_W and A_T showed the highest carbon contents being 82.1% and 76.7%, respectively, demonstrating more aromatic, carbonaceous, and stable structures for catalytic application. Indeed, the heteroatoms distributions of different biochars were affected by the nature of initial biomass. The decrease of hydrogen percentage during pyrolysis and activation is owing to the cracking and cleavage of weak bonds in the biomass and biochar carbonaceous skeletons [273]. In addition, nitrogen and oxygen contents showed different trends through pyrolysis and activation of different biomasses. As was reported, although the

79

carbonization process leads to the cleavage and removal of heteroatoms, this phenomenon is also highly influenced by the strength of C–N and C–O bonds in the biomass and biochar structures [274]. Among different activated biochars, A_T, A_A, and A_B showed the considerable nitrogen contents of 9.4%, 6.8% and 4.0%, respectively, coming from protein fraction of T, A, and B biomasses. A_W and A_B showed higher oxygen contents and O/C ratios compared to A_T and A_A. A higher oxygen content of activated biochars might be derived from carbohydrate and especially lignin fractions of lignocellulosic biomasses. The presences of oxygen and nitrogen heteroatoms could suggest more O,N-doped and functional groups in the activated biochar-based supports, being crucial for a better anchorage of active metal phases in heterogeneous catalysis application [275]. On the other hand, A_A showed a high content of sulfur (2.8%) compared to others coming from lipid fraction of algae which might be a serious issue in catalysis since sulfur can poison the noble and non-noble active metals of the catalysts [276–278]. The higher ash portions of A_B and A_A can be due to the presence of some elements such as Si (Figure A3) which could not be removed by acid washing approach [279].

Figure 4.5(a,b) displays the nitrogen adsorption-desorption isotherms of biochars and activated biochars, respectively, and the textural values are reported in Table 4.4.
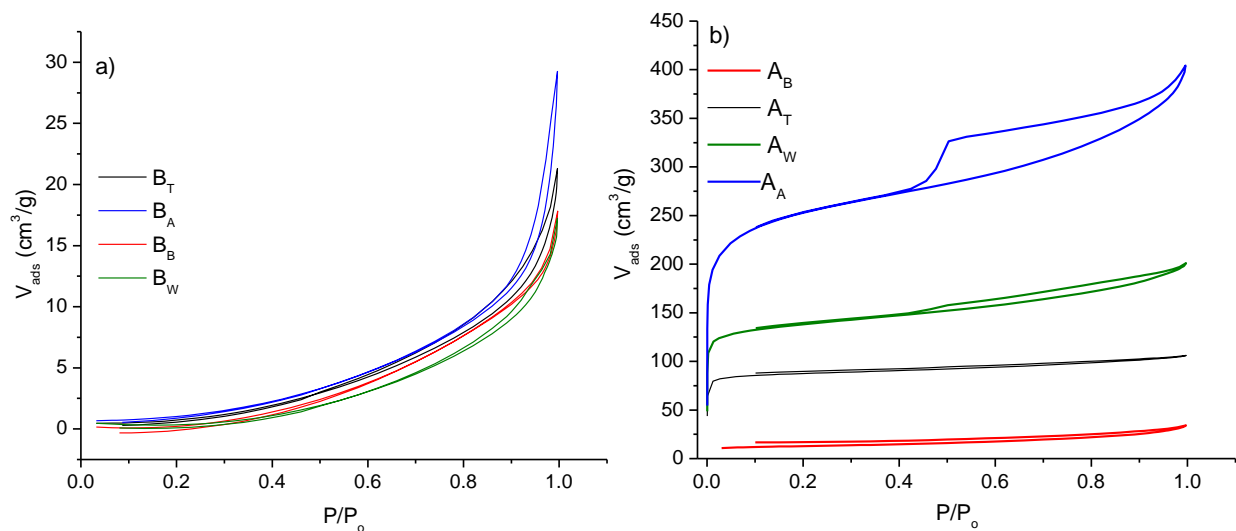

Figure 4.5. N$_2$ adsorption-desorption isotherms of a) biochars and b) activated biochars.

Table 4.4. *Textural properties of activated biochars obtained from N_2 physisorption.*

Sample	$S_{Langmuir}$[a] (m^2g^{-1})	S_{micro}[b] (m^2g^{-1})	V_{tot}[c] (cm^3g^{-1})	V_{micro}[d] (cm^3g^{-1})
A_T	412	356	0.16	0.10
A_W	690	571	0.29	0.14
A_B	79	-	0.04	-
A_A	1305	905	0.56	0.17

a) Calculated by Langmuir method, b) Microporous or external surface area calculated by t-plot method, c) Total pore volume calculated according to the adsorbed amount of N_2 and P/P_o values near 0.98, d) Micropore volume calculated by t-plot method.

All biochars show an isotherm type III which ascribes non-porous material according to IUPAC classification (Figure 4.5a). Moreover, non-porous textures of biochars were confirmed by their very low surface areas and porosities. A low surface area was obtained for the biochar obtained from pyrolysis of the residual soapberry pericarp at 600 °C [280], While the biochar from pyrolysis of hazelnut shells at 600 °C showed a higher BET surface area of 81 m^2g^{-1} [281]. This can confirm that the nature of the initial biomass has a vital role in the texture of the obtained biochar. Moreover, the low surface area and low porosity of a support could be the issues in catalytic application especially for dispersion of active sites and efficient mass transfers of reactants and products. Hence, an activation step was applied to improve the porosity and surface area of the biochar-based supports. Four different biochars showed different textural behaviors through physical activation procedure being affected from the natures of initial biomasses. In particular, A_A and A_W indicate a combination of type I and type IV isotherms suggesting their hierarchical micro-mesoporous textures (Figure 4.5b). The H4 hysteresis loop in the range of $0.4<P/P_o<0.99$ demonstrate narrow slit-shaped pores of the samples. Moreover, the isotherm of A_T shows a microporous texture with a very narrow hysteresis loop and hence the presence of some mesopores in this sample. However, the porous texture of A_B did not significantly change by activation procedure. In particular, A_B shows the a wide hysteresis loop in the isotherm which can be assigned to the presence of large and elongated pores in the sample. When comparing the textural properties of activated biochars in Table 4.4, the surface area and porosity of samples follow the order of $A_A>A_W>A_T>A_B$. Is seems that the biochar from B needed harsher activation conditions for the

improvement of textural properties. Overall, higher surface area and porosity of activated biochars suggest their potential and efficiency to be used as support in heterogenous catalysis.

The functional groups of activated biochars were qualified by FTIR technique. The FTIR spectra of all activated biochars in Figure 4.6 show a band at approximately 3400 cm^{-1} demonstrating the vibrations of O–H functional groups [282]. The higher intensities of these bands for A_T and A_B are related to the vibration of N-containing functional groups namely –NH_2 from amines and amides groups originated from the protein fraction of the initial biomasses. The intense band at around 1600 cm^{-1} is ascribed to the stretching vibration of aromatic C=C and C=O stretching of conjugated quinones and ketones [283,284].
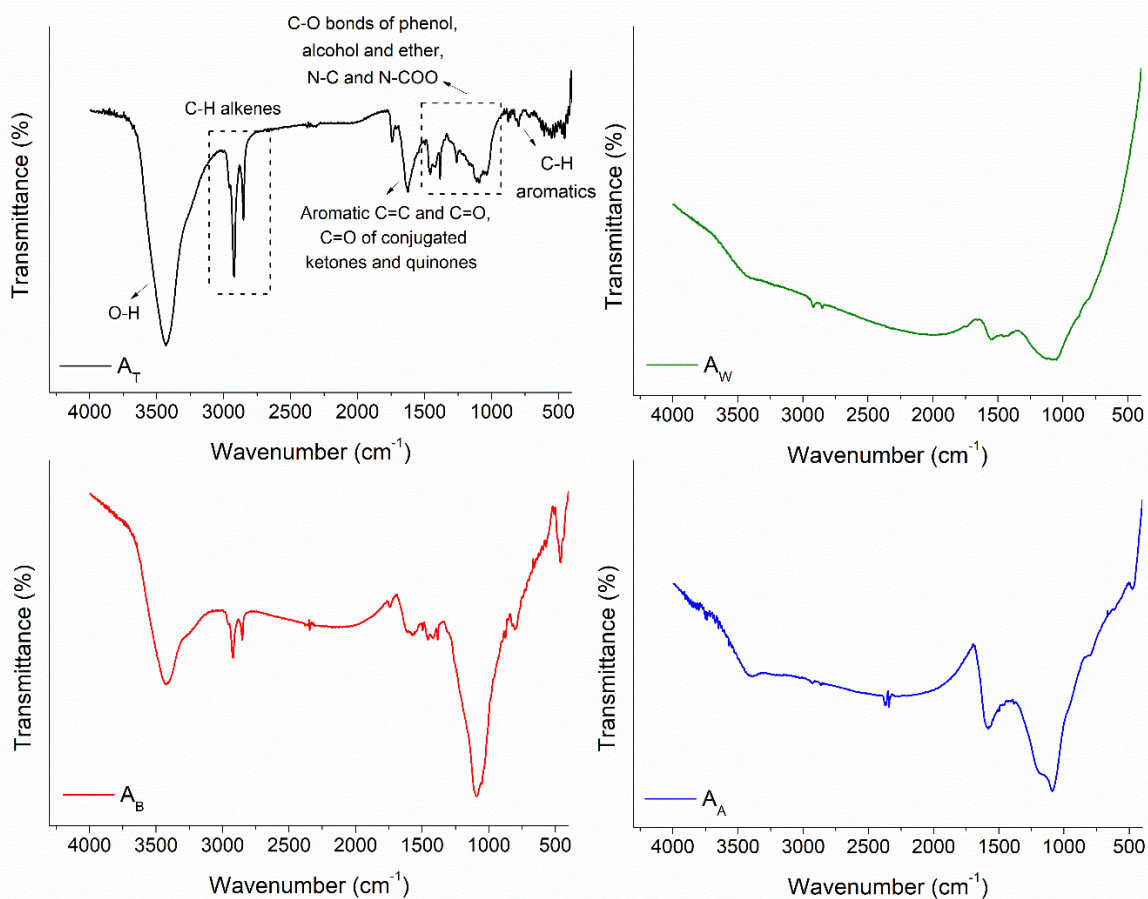
Figure 4.6. *FTIR spectra of activated biochars.*

82

In addition, a series of overlapped bands are observed in the wavenumber range of 1400-900 cm^{-1} which can be related to the N,O-doped heteroatoms and functional groups in the skeleton and surface of activated biochars such as C–O bonds in alcohol, phenol, bridging ether between aromatic rings, and also N–C and N-COO groups [257]. Furthermore, all activated biochars exhibit the C–H of alkenes at 2850 and 2920 cm^{-1}, and aromatic C–H out of plane vibrations at 800 cm^{-1} [285]. Overall, different activated biochars displayed different FTIR spectra and hence different functionalities which were confirmed by the presence of heteroatoms with different contents in CHNS elemental analysis (Table 4.3). These variances were obviously due to different natures of initial biomasses.

To further evaluate the surface oxigenate functionalities of activated biochars, Temperature-programmed Desorption (TPD) analyses were performed and the profiles are shown in Figure 4.7.
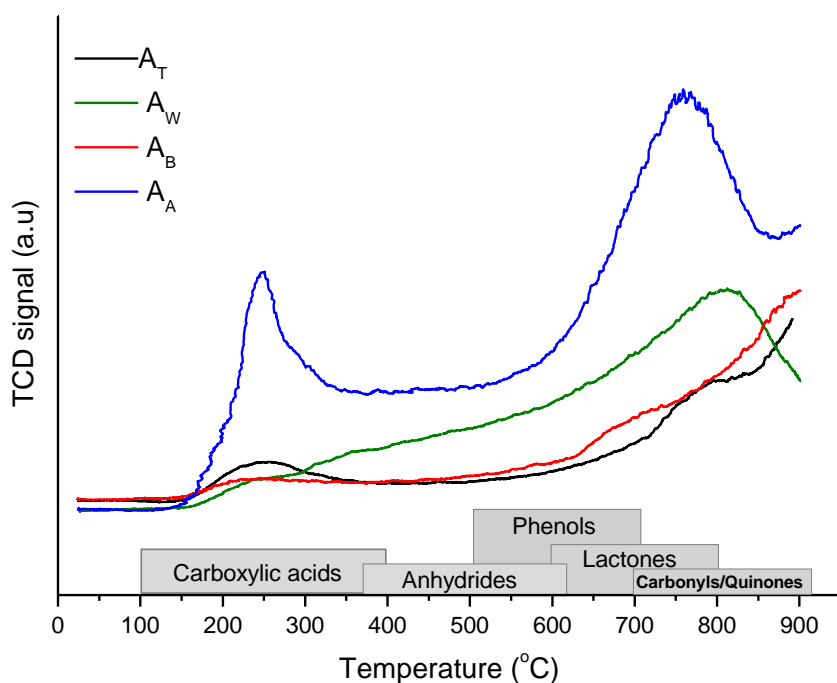

Figure 4.7. TPD profiles of activated biochars

In TPD profile, the peak of decomposed CO_2 can be seen at the temperature ranges of 100-400 °C which ascribes the carboxylates functional groups [286]. Moreover, the peaks of decomposed CO from anhydrides and phenols functionalities can be observed at around 600 °C and from carbonyls

of ketones and quinones at near 900 °C [287,288]. When comparing different activated biochars, A_A shows a high number of carboxylates functional groups and A_T shows a lower content, whereas A_W and A_B did not show any carboxylates. All activated biochars demonstrate the presence of anhydrides and phenols functional groups considering the highest intensity for A_A followed by A_W. Moreover, ketones and quinones are present on the surface of all samples with different intensities. The results of TPD agree with those of FTIR analyses (Figure 4.6).

4.3.2. Characterization of the catalysts

The AAS results in Table 4.5 show that around 7-8% Ni was actually loaded on the supports. The few differences of the actual Ni loading in different catalysts might be related to the textural, morphological properties, and chemical functionality of biochar-based supports which led to a different anchorage and stability of Ni active phase on the support.

The nitrogen adsorption-desorption isotherms are displayed in Figure 4.8(a-d).
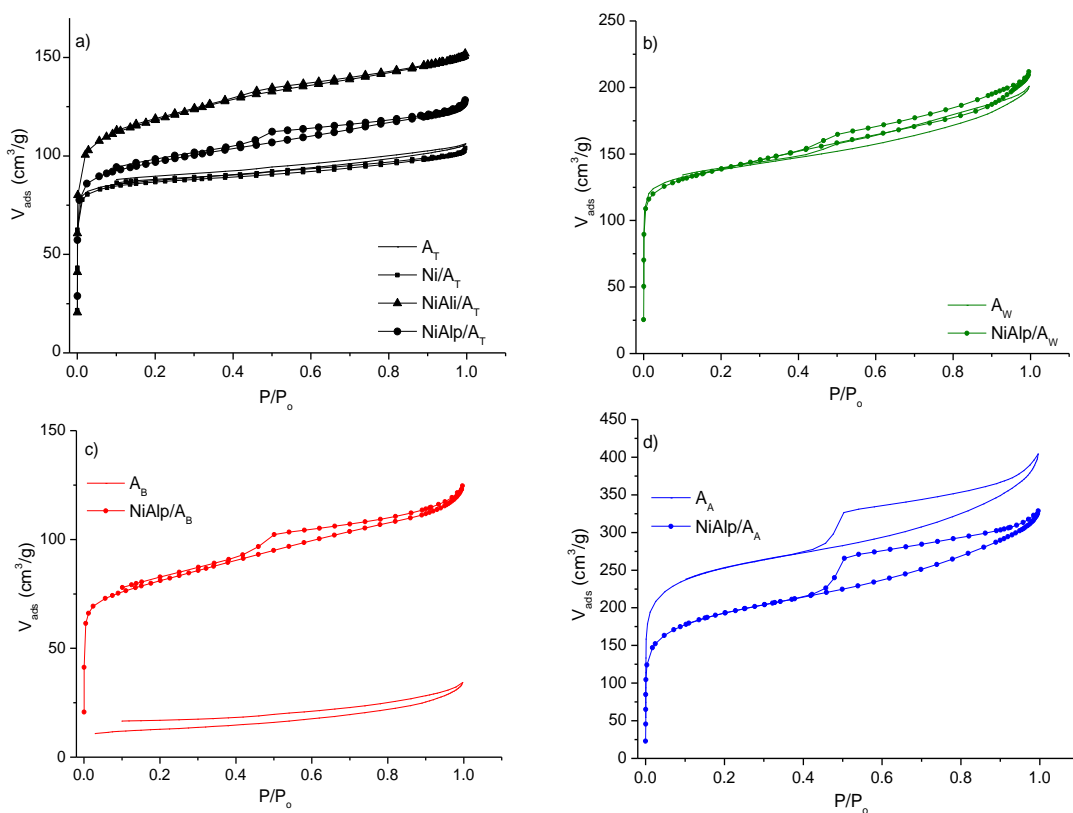

Figure 4.8. *N₂ adsorption-desorption isotherms of the studied catalysts supported on a)A_T, b) A_W, c) A_B, and d) A_A.*

It can be demonstrated that after introduction of the active sites, the form of isotherms of A_W, and A_A activated biochars remained unchanged, while for A_T sample, a partial change in the form of hysteresis loop was observed in some cases after incorporation of Al and Ni especially for NiAlp/A_T catalyst. A stronger change was observed for A_B support after introduction of Al and Ni. NiAlp/A_B showed a combination of isotherm type I and IV with H4 hysteresis loop in the range of $0.40<P/P_o<0.99$ demonstrating the presence of micro and mesopores with narrow slit-shaped in this sample.

The surface areas and pore volumes of the catalysts saw alterations compared to the supports (Table 4.5). Particularly, impregnation of only Ni on A_T led to the surface area and pore volume diminutions. In addition, by introduction of both Al and Ni to A_T, A_W and A_B, the surface area and pore volume increased considering the noticeable increment in the case of NiAlp/A_B. On the contrary, the introduction of Al and Ni on A_A resulted in opposite trend. Overall, we assume that these phenomena could be due to several reasons: a) the introductions of both active sites on the supports could cause a partial blockage of primary micro-mesopores [289], and a decrease of surface are which happened for NiAlp/A_A, b) Alumina itself, if any, has surface area and porosity and its dispersion on the supports could improve secondary superficial areas [290], c) the Ni and Al incorporation procedures could lead to some interactions between these active phases with the nitrogen and oxygen doped and functional groups of activated biochars, and inorganic compounds such as silicate particles within the biochars (Figure A3) [291,292]. According to elemental analysis result of Table 4.3, A_W and A_B samples showed the highest O/C ratio, and A_B and A_T exhibited high mass percentage of N element, which suggest the high N,O-doped and functionality in these samples. The interactions between introduced active phases and doped and functionalized groups of supports could help on a further activation of samples through the catalyst calcination procedure, d) Several studies mentioned the effect of NaOH in removal of silicate based ashes and biochar surface area improvement [293,294]. Since NaOH was used as the precipitation agent in this study and the presence of Si was observed in the EDS analyses of A_T and A_B (Figure A3) of the catalysts, we assume that NaOH interacted with some of silicate-based ash in activated biochars according the formula of $2NaOH(s) + SiO_2(s) \rightarrow Na_2SiO_3(s) + H_2O$ and Na_2SiO_3 was easily removed in the water-washing step of the catalysts. Moreover, in A_T and A_B, the amount of ash is high (~15%) which could well-explain the increase of surface area and porosity after metal

introduction in these samples. Therefore, partial Si-leaching of activated biochars during Al precipitation procedure could also improve their surface areas and porosities [293,294].

Table 4.5. *Ni loading (determined by AAS) and textural properties (obtained from N_2 physisorption) for studied supports and catalysts.*

Sample	Ni loading (wt. %)	$S_{Langmui}$ [a] (m^2g^{-1})	S_{micro} [b] (m^2g^{-1})	V_{tot} [c] (cm^3g^{-1})	V_{micro} [d] (cm^3g^{-1})	Ni crystal size [e] (nm)
A_T	-	412	356	0.16	0.10	-
Ni/A_T	7.5	402	335	0.15	0.09	30
NiAli/A_T	7.9	529	244	0.22	0.10	15
NiAlp/A_T	7.3	487	401	0.18	0.10	18
A_W	-	690	571	0.29	0.14	-
NiAlp/A_W	8.0	726	580	0.30	0.13	-
A_B	-	79	-	0.04	-	-
NiAlp/A_B	8.8	445	353	0.17	0.07	-
A_A	-	1305	905	0.56	0.17	-
NiAlp/A_A	7.3	1049	719	0.47	0.11	-

a) calculated by Langmuir method, b) calculated by t-plot method, c) total pore volume calculated according to the adsorbed amount of N_2 and P/P$_o$ values near 0.98, d) micropore volume calculated by t-plot method, e) calculated by Rietveld method.

The XRD patterns of Ni/A_T, NiAli/A_T, and NiAlp/A_T are shown in Figure 4.9. For all samples, the two broad peaks at the 2θ of ~25° and ~44° can be associated to the (002) and the (100) reflection planes of the carbonaceous material with respect to hexagonal graphite 2H model. The (002) and the (100) peaks could be corresponded to the assembling of aromatic ring layers and aromatic molecules extension in every plane of the layer, respectively [257,295]. In the case of NiAli/A_T, two sharp peaks at $2\theta=21°$ and 27° are ascribed to crystalline silica contaminations (see Figure A3a) which were not completely removed in the acid washing step of A_T sample.

For all samples, the lines of Ni^0 can be observed at 2θ of 44.4°, 51.8°, and 76.4° [296]. It should be noticed that the peak at 2θ of ~44° overlapped with the line of Ni^0 crystal which made the (100) reflection planes less visible. In addition, the crystal size of Ni^0 estimated by Rietveld method (Table 4.5) were 30 nm, 15 nm, and 18 nm for Ni/A_T, NiAli/A_T, and NiAlp/A_T catalysts,

respectively. The presence of three broad and weak peaks at 2θ about 38°, 49° and 65° in the NiAli/A_T, and NiAlp/A_T samples are the effect of Al addition. These diffraction peaks are related to AlOOH phase with (031), (200) and (151) planes. These broad and weak peaks might be attributed to the highly dispersed AlOOH on the biochar and the small size of AlOOH crystal [297]. The fit was achieved by changing the space group of graphite form P 63/mmc to P6/mmm. Moreover, another study suggested that the line at 65° is ascribed to both crystalline AlOOH and amorphous Al_2O_3 [298]. Indeed, it can be predicted that the size and dispersion of Al-containing structures could have a significant influence on the acid properties of the catalyst and hence its performance in the target reaction. In addition, the activity and selectivity of the catalyst in the reaction can be affected from Ni^0 crystallite size. The result for Ni/A_T, NiAli/A_T, and NiAlp/A_T confirm that the presence of Al-containing species and their incorporation method affected the Ni^0 crystal size and distribution on the support.
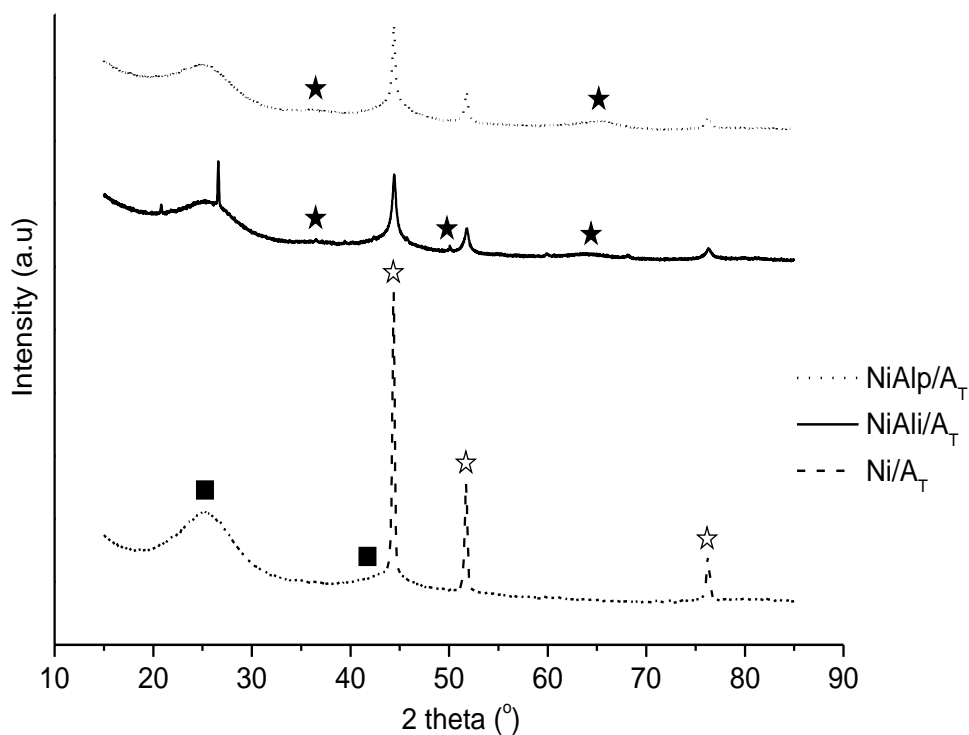

Figure 4.9. *XRD patterns of Ni/A_T, NiAli/A_T, and NiAlp/A_T. (■ A_T, ☆ Ni^0, ★ AlOOH)*

The SEM images of NiAli/A_T, NiAlp/A_T, NiAlp/A_W, and NiAlp/A_B are exhibited in Figure 4.10(a-d), respectively, to study the surface morphologies of the catalysts.
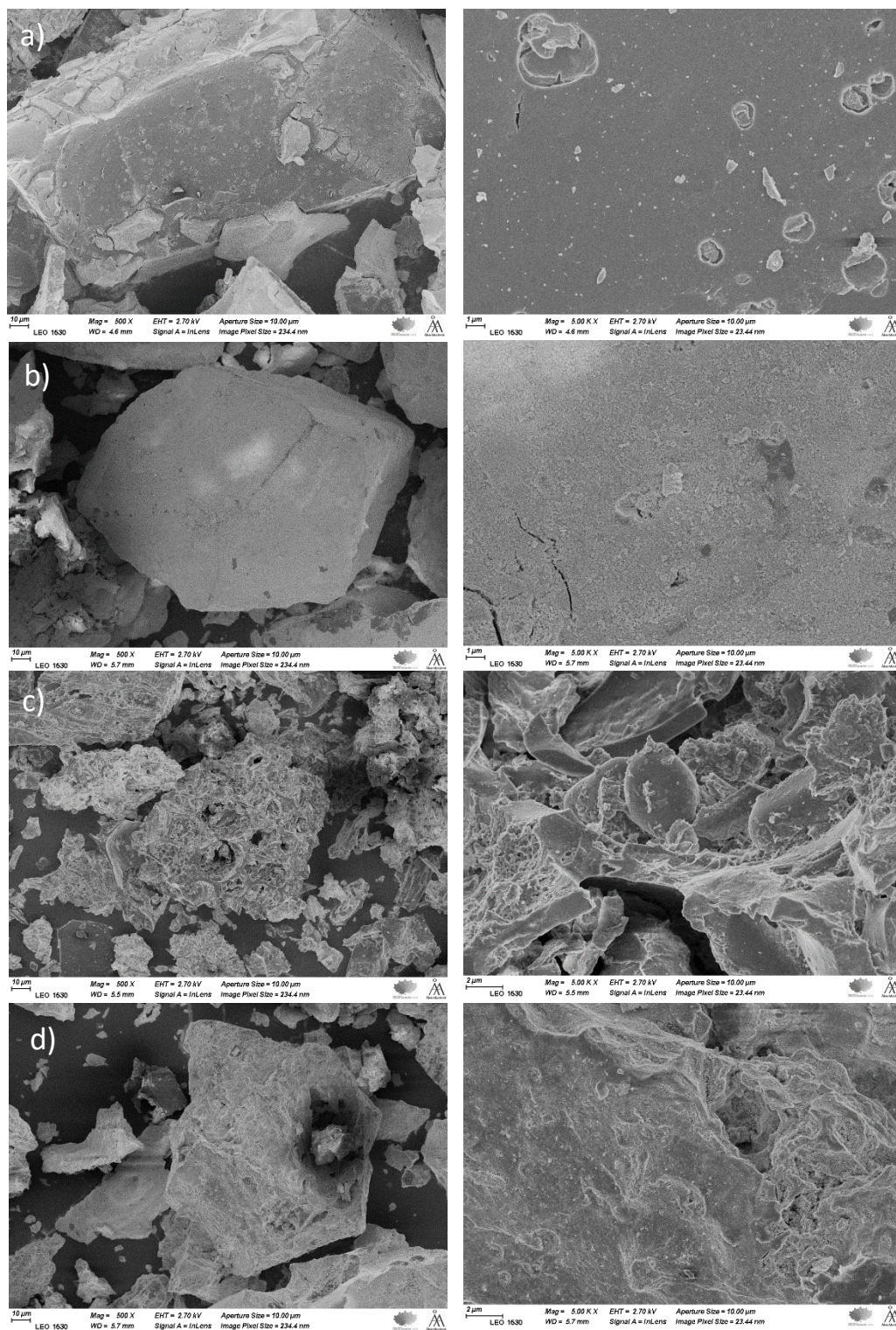
Figure 4.10. The SEM images of a) NiAli/A_T, b)NiAlp/A_T, c) NiAlp/A_W, and d) NiAlp/A_B catalysts, with 500X and 5.00 K X magnifications, respectively for each sample.

The surface morphologies of the catalysts that derived from different biochar-based supports are various. $NiAli/A_T$ and $NiAlp/A_T$ show more flat surfaces with some superficial porosities in macro sizes. We assume that most of the superficial pores in A_T-based catalysts are in micro and meso sizes as it was demonstrated from N_2 physisorption results in Table 4.5. However, the micro and mesopores are not visible with the magnification of SEM images. On the contrary, $NiAlp/A_W$ and $NiAlp/A_B$ have rougher morphologies with irregular surfaces. From the SEM images of $NiAlp/A_W$ (Figure 4.10c), the original wood structure is partially visible containing various types of visible porosities such as holes, pits, cavities resulted from activation procedure which can be confirmed by N_2 adsorption desorption isotherm of the sample in Figure 4.8b. Moreover, the surface morphology of $NiAlp/A_W$ was similar with those of [299,300]. $NiAlp/A_B$ possesses a rigid, uneven surface with few holes, and meso and macropores (Figure 4.10d). Indeed, the isotherm of A_B in Figure 4.5b confirmed the presence of large and elongated pores in this sample. Moreover, the dispersion of active phases on the supports can be observed from the elemental maps of the catalysts in Figure A4.

TEM images of $NiAlp/A_W$ and $NiAlp/A_B$ in Figure 4.11 confirms that the dispersion of active sites in catalysts was affected from the surface area and porosity of the supports.
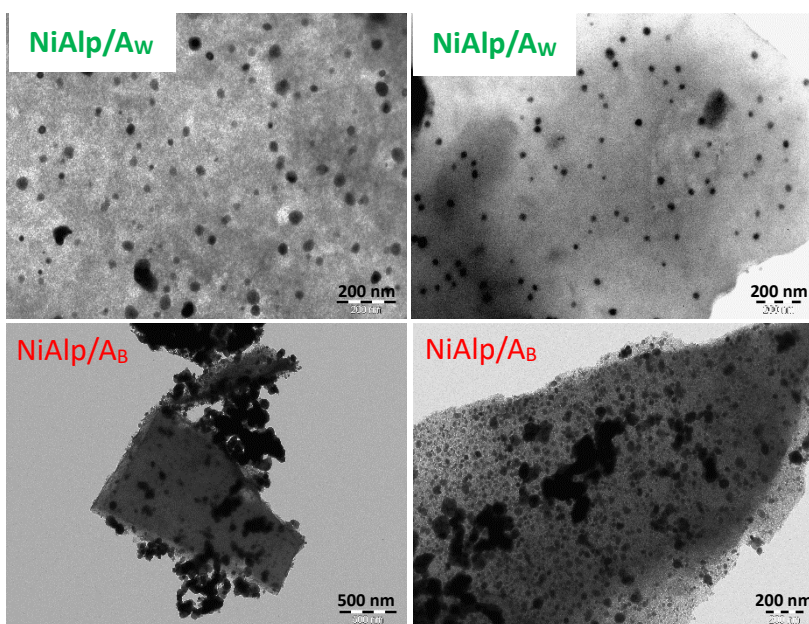

Figure 4.11. *TEM images of NiAlp/Aw and NiAlp/AB catalysts.*

89

In NiAlp/A$_W$, a higher surface area and porous texture of A$_W$ resulted in a highly dispersed active sites, while the active sites in NiAlp/A$_B$ catalyst underwent sintering and agglomeration due to low surface area and little porosity of A$_B$. Indeed, a smaller size and a higher dispersion of active sites are significant to have a high active surface area and hence a high catalytic activity.

The reducibility of the catalysts was studied by TPR analyses and the profiles are displayed in Figure 4.12. Generally, all catalysts exhibit two main reduction peaks, below 450 °C, which were varied with the extent of interaction between NiO and activated biochar supports with different nature and properties, and the catalysts preparation method. In particular, the reduction peak below 300 °C for NiAlp/A$_W$ could be due to the reduction of bulk NiO portions having very weak interaction with support.
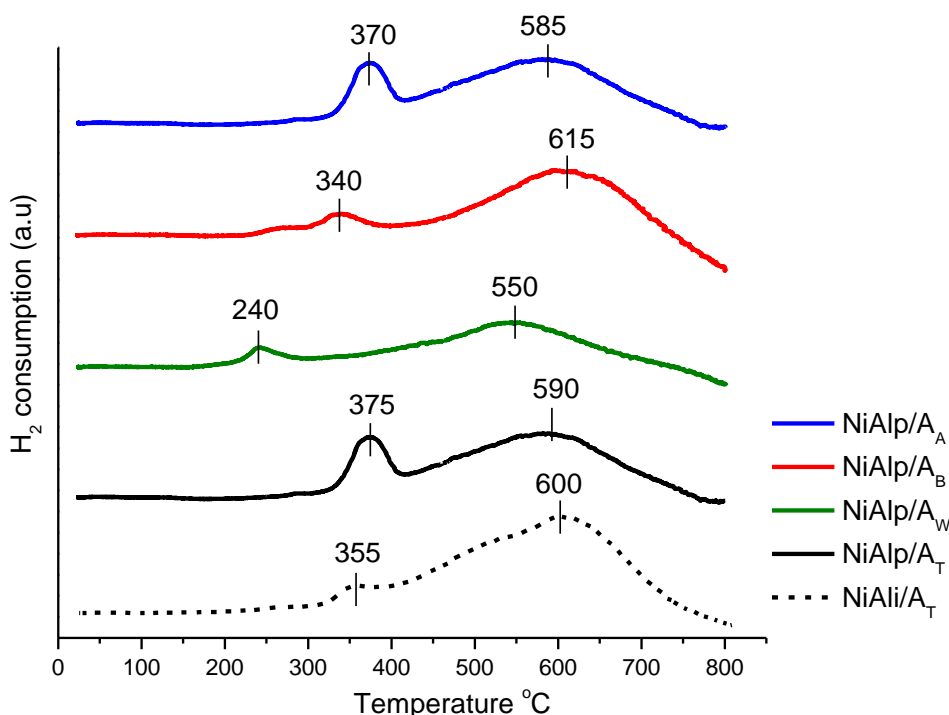

Figure 4.12. H$_2$-TPR profiles of the catalysts.

For all catalysts except NiAlp/A$_W$, the reduction peak between the temperature of 300 °C and 450 °C can be ascribed to the medium interactions of the Ni species with supports. The peaks at the

temperature higher than 450 °C suggest the reduction of NiO with strong Ni-support interaction [301–303]. Moreover, the peaks at the temperature higher than 500 °C might be due to methanation of activated biochars by hydrogen spillover, and the interaction of their surface functional groups with H_2 [295]. Comparing different catalysts, NiAlp/A_W showed the lowest reduction temperatures and hence the weakest Ni-support interaction. This means that NiO was less stabilized on the A_W support which had the lowest N+O elements mass percentage according to elemental analysis (Table 4.3) and hence the lowest superficial functional groups according to FTIR results (Figure 4.6). The reduction temperatures of the others followed the order of NiAlp/A_A>NiAlp/A_T>NiAlp/A_B. Therefore, the presence of more O, N, S-containing functional groups on the activated biochars from different natures (Figure 4.6 and Figure 4.7) led to a higher interaction of Ni species with support, their higher stabilization and more difficult reduction. When comparing NiAlp/A_T with NiAli/A_T, the two reduction peaks of NiAlp/A_T were appeared at slightly higher temperatures because their different preparation procedures affected on a different interaction of NiO with support. It seems that the surface features of the catalyst obtained by precipitation favour a strong interaction of NiO with the support.

The presence of acid sites on the surface of supports and catalysts were studied by NH_3-TPD analysis and the profiles of NiAli/A_T, NiAlpA_T, A_W, and NiAlp/A_W are presented in Figure 4.13(a,b), respectively.
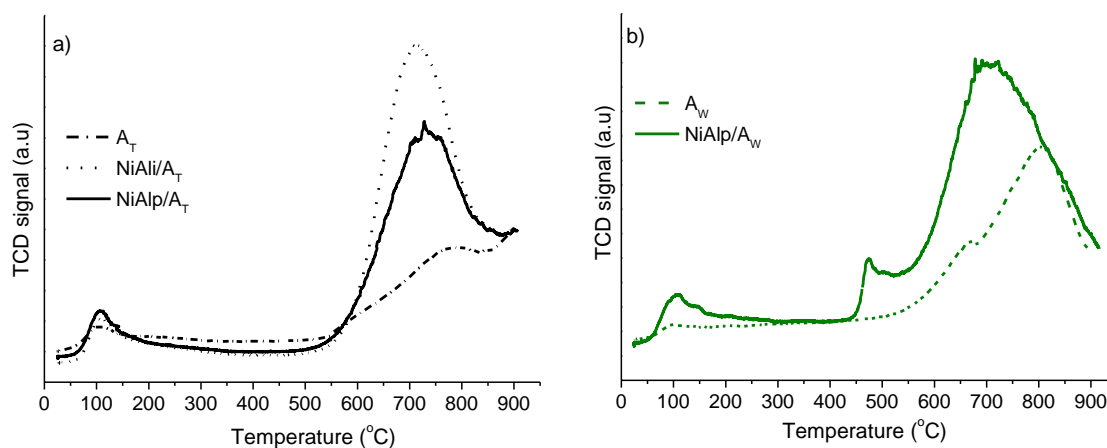

Figure 4.13. NH$_3$-TPD profiles of a) A$_T$, NiAli/A$_T$, NiAlp/A$_T$, and b) A$_W$, NiAlp/A$_W$ samples.

91

In NH$_3$-TPD profiles, three desorption zones at various temperatures display the strength of acid sites in the samples. The desorption peaks at the temperature ranges of 50-300 ℃, 300-600 ℃, and more than 600 ℃ show the weak, moderate and strong Brønsted/Lewis acid sites, respectively [304]. Both A$_T$ and A$_W$ supports exhibited weak, moderate and strong acid sites due to the presence of –COOH and –OH groups which were also observed in FTIR and TPD results in Figure 4.6 and Figure 4.7, respectively. In all samples, Al introduction contributed to the new acid sites formation on the supports probably coming from Al-containing species as was shown in XRD results (Figure 4.9). In the case of A$_T$ sample, Al-containing structures improved weak and strong acid sites of the support considering the higher increments of these types of acid sites in NiAlpA$_T$ and NiAli/A$_T$, respectively. It can be confirmed that all introduced Al-containing species to the A$_T$ support could provide Lewis acidity in final catalysts which might have different distributions due to different Al incorporation techniques (Figure 4.9). On the other hand, precipitated Al on A$_W$ led to the enhancement of weak and strong acid sites and creation of new moderate acid site. The depth characterization carried out has confirmed that the biochars features play a crucial role in directing the final properties of the catalysts.

4.3.3. The effect of Al introduction on the catalytic performance

The performances of synthesized Ni/A$_T$, NiAli/A$_T$, and NiAlp/A$_T$ in the transformation of LA to GVL were investigated in a batch system and aqueous medium (Figure 4.14). Over Ni/A$_T$, LA was slightly converted (11%) and no GVL was produced, whereas bifunctional catalysts were active in the proposed reaction. This can suggest that Ni only was not able to catalyze LA hydrogenation from pathway I (Figure 4.1). Therefore, the catalyst of this study was active in the pathway II where Al-containing species as Lewis acid sites were needed to first dehydrate LA to angelica lactone followed by a hydrogenation step to GVL over active Ni site. Indeed, NH$_3$-TPD profiles showed the acid sites improvement of the A$_T$ based catalysts by introduction of Al (Figure 4.13).
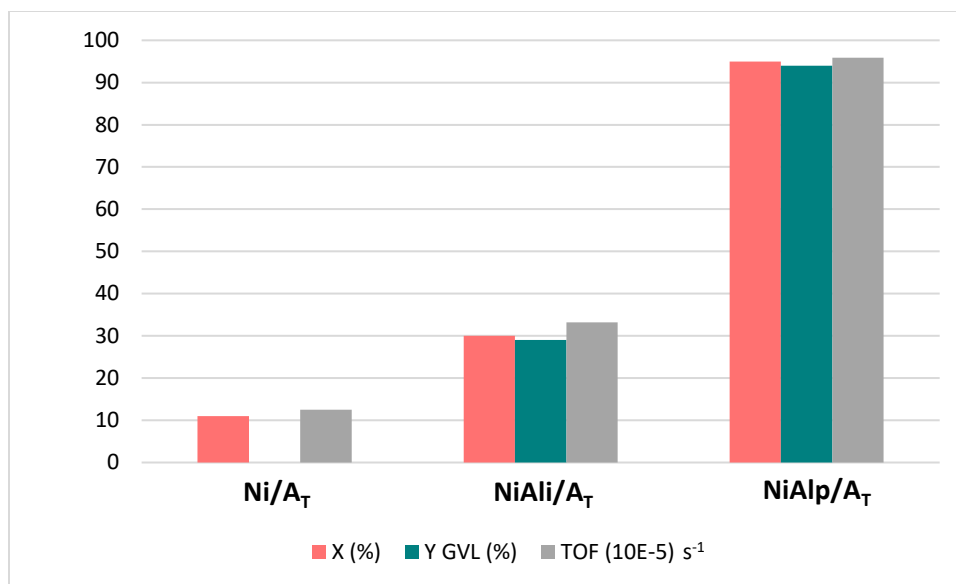
Figure 4.14. Transformation of LA to GVL over Ni/A_T, NiAli/A_T, and NiAlp/A_T catalysts. Reaction conditions: 200 °C, 35 bar H_2, 4 h, 0.17 M LA, 400 mg catalyst, 50 ml H_2O.

A mechanism is proposed for LA to GVL reaction over activated biochar supported Al and Ni in aqueous medium (Figure 4.15). First, the keto form of LA underwent a keto-enol tautomerization at reaction temperature and produced enol form. Then, the coordination of the electron from carboxylic acid oxygen with Al-containing species as the Lewis acid site led to an endothermic dehydration and produced α-/β-angelica lactones. Finally, Ni metal was activated by spillover of hydrogen from H_2 gas and catalyzed the hydrogenation of C=C double bond in angelica lactone to produce GVL. A quite similar mechanism was proposed in some studies of the literature where the bimodal effects of Lewis acid and metal sites were focused and discussed [305–307]
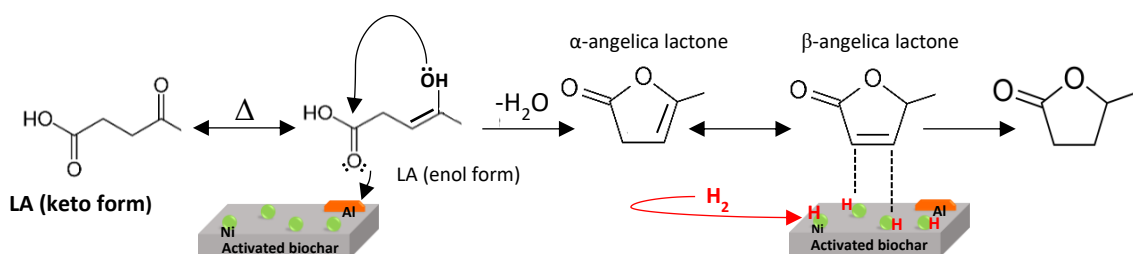

Figure 4.15. Proposed mechanism for hydrogenation of LA to GVL over activated biochar supported Al and Ni catalysts in aqueous medium.

93

When comparing two catalysts with two Al introduction approaches namely NiAli/A_T and NiAlp/A_T, higher activity was achieved from the catalyst with precipitated Al giving 95% LA conversion, 94% GVL yield and TOF of 96.10^{-5} s^{-1}. Although NiAli/A_T showed a higher density of strong acid sites compared to NiAlp/A_T (Figure 4.13), we assume that weak acid sites were more active in catalyzing dehydration step which was more in the case of NiAlp/A_T (Figure 4.13). Indeed, these differences in acidic properties of the catalysts were because of different synthesis approaches for Al incorporation on the catalysts. It can be confirmed that precipitation technique caused a better distribution of Al-containing particles on the supports, their different interaction with A_T, higher weak acid sites dispersion, and hence a higher active phase surface for dehydration step of the reaction. Kumar *et al.*, observed that Lewis acid site is responsible for dehydration of LA to angelica lactones and Brønsted acid site is prone to ring opening of GVL and production of valeric acid and hydrocarbons [308]. In addition, López and co-workers reported that strong acid sites can catalyze the formation of organic carbonaceous deposits such as humins and a fast deactivation of the catalyst [309]. In addition, the Ni^0 crystal size of NiAlp/A_T catalyst (18 nm) was slightly larger that of NiAli/A_T (15 nm) (Table 4.5), but it seems that the activity of the catalyst in this case was more affected from incorporated acid properties.

Hence, Al precipitation as a better method was applied for other activated biochars support and the effect of type of supports on the catalytic activities will be discussed in the next section.

4.3.4. The effect of activated biochar supports on the catalytic performance

The performances of different activated biochars as the supports in the catalytic transformation of LA to GVL were studied (Figure 4.16). A negligible activity was observed over NiAlp/A_A which might be related to the high amount of sulfur in A_A support reported in elemental analysis results (Table 4.3). Several studies demonstrated that sulfur could have poisoning effect, block Ni active site in the catalyst, and hinder its activity [310–312]. Moreover, the activity of NiAlp/A_B was not so high giving 27% GVL yield and TOF of 96.10^{-5} S^{-1} in 42% LA conversion. The medium activity of this catalyst was due to low surface area and porosity of A_B support (Figure 4.5 and Table 4.4). This led to a low dispersion of Al-containing particles and Ni active sites, their sintering and agglomeration (Figure 4.11), and hence low active phases surface.
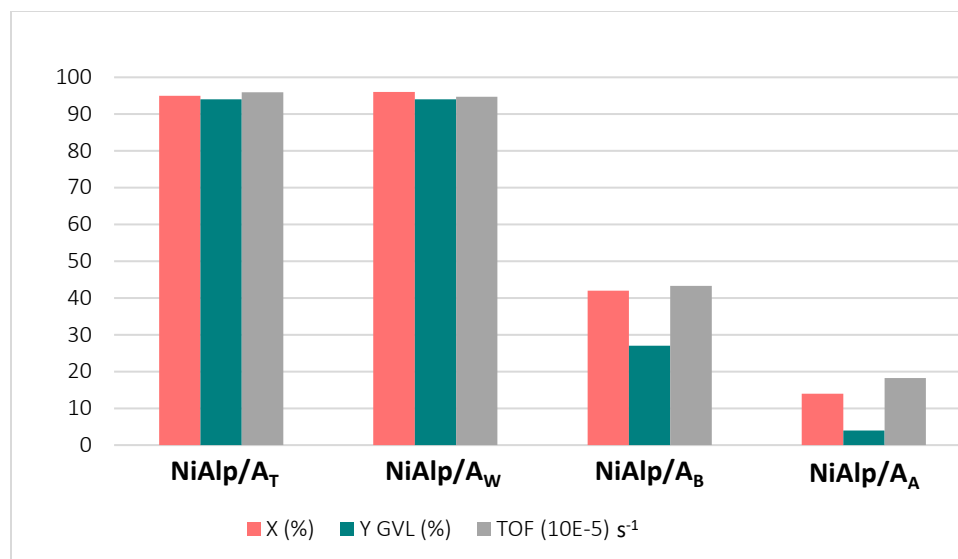
Figure 4.16*. Transformation of LA to GVL over NiAlp/A_T, NiAlp/A_W, NiAlp/A_B, and NiAlp/A_A catalysts. Reaction conditions: 200 °C, 35 bar H$_2$, 4 h, 0.17 M LA, 400 mg catalyst, 50 ml H$_2$O.*

NiAlp/A_T and NiAlp/A_W showed almost the same and the highest activity giving around 95% LA conversion and GVL yield and TOF of ca. 95.10^{-5} S^{-1}. Looking to the chemical aspect, the highest carbon contents of A_T and A_W supports (Table 4.3) compared to others could assist a more aromatic, carbonaceous, and stable structure of the catalysts. In addition, the high oxygen and nitrogen contents in A_T (Table 4.3) could show the presences of more O,N-doped and functionalized groups (Figure 4.6) and a better anchorage and stability of active sites on the support. In textural aspect, both NiAlp/A_T and NiAlp/A_W showed high surface areas and adequate porosities (Figure 4.8 and Table 4.5) compared to NiAlp/A_B being appropriate for a better dispersion of active phases on the support and for an easier mass transfer of reactants and products. Moreover, the porous surface of NiAlp/A_W in SEM image (Figure 4.10), the high dispersion of active phase in NiAlp/A_W according to the TEM image (Figure 4.11), the reasonable Ni^0 particle size in NiAlp/A_T according to the XRD result (Figure 4.9 and Table 4.5) could be the vital morphological reasons for higher activity of the catalysts. Hence, several chemical, textural, and morphological factors guaranteed the high activities of NiAlp/A_T and NiAlp/A_W catalysts. In the literature, carbonaceous materials were often used as the support of Ru based catalyst for the proposed reaction. For instance, Ru supported on synthesized N-doped carbon nanoflakes was used as the catalyst for LA to GVL conversion in the presence of formic acid as the hydrogen

donor and water as the solvent. It was demonstrated that the high Ru nanoparticles dispersion on N-doped carbon guaranteed a high activity of the catalyst giving 99.8 % LA conversion and 100 % selectivity of GVL at 140 °C for 20 h [313]. Carbon supported Ni was also used as the catalyst in some studies. A recent study reported melamine as an N-doped carbonaceous support and introduced Al and Ni via coprecipitation method. They suggested that N-doped carbon assisted the creation of NiNx species and hence a high activity of the catalyst. A similar result was obtained (LA conversion of 96% and GVL yield of 94%) at 130 °C, 10 bar H_2 and 3 h reaction time [314]. Indeed, in our study, the A_T activated biochar in NiAlp/A_T, as one of the best catalysts, naturally had a high amount of nitrogen heteroatom in the structure which could be both doped and functionalized groups as was analyzed by XPS method in one of our recent publication for a different application [257].

In the next section, the optimization of the reaction conditions over NiAlp/A_W as one of the best catalyst will be discussed.

4.3.5. Optimization of the reaction conditions over NiAlp/A_W catalyst

A series of catalytic runs were carried out to study the effect of reaction conditions such as temperature, H_2 pressure, time, and LA/catalyst mass ratio on the catalysts reactivity and finally to select the optimum condition for GVL production. NiAlp/A_W was selected for the optimization step since it was one of the most active catalysts in the screening step. The increase of the reaction temperature from 150 °C to 180 °C increased the LA conversion from 69% to 92%, and GVL yield from 62% to 88%, respectively (Figure 4.17). However, further increment of the temperature to 200 °C did not show a sharp difference in LA conversion and GVL yield. We selected 180 °C as the optimum temperature and we assumed that further increase of the temperature to higher than 200 °C might lead to the formation of degradation compounds such as humins.
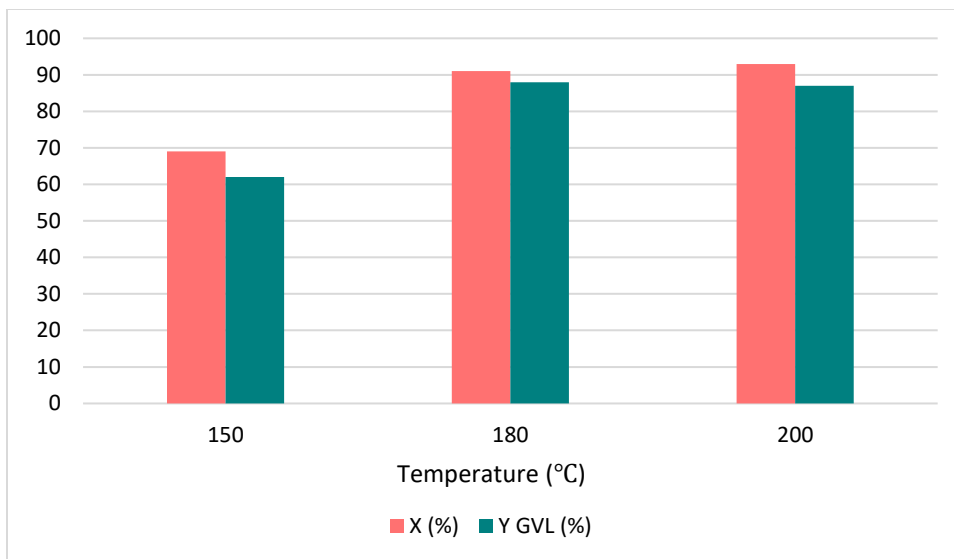
Figure 4.17. *Hydrogenation of LA over NiAlp/A$_W$ catalyst at different temperatures. Reaction conditions: 35 bar H$_2$, 4 h, 0.17 M LA, 400 mg catalyst, 50 ml H$_2$O.*

By enhancing the H$_2$ pressure from 15 bar to 25 bar, the LA conversion and GVL were remarkably raised, and from 25 bar to 35 bar, the LA conversion stayed almost similar but GVL yield slightly increased (Figure 4.18). Therefore, 35 bar of H$_2$ was selected as the optimal value.
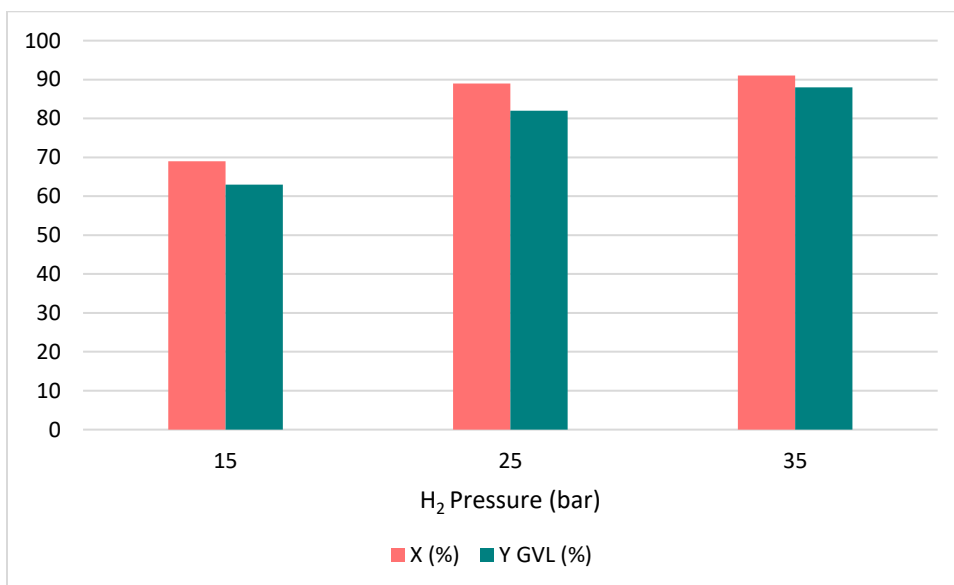

Figure 4.18. *Hydrogenation of LA over NiAlp/Aw catalyst at different H$_2$ pressures. Reaction conditions: 180 ℃, 4 h, 0.17 M LA, 400 mg catalyst, 50 ml H$_2$O.*

Increasing the reaction time from 1h to 3 h resulted in a significant increase of LA conversion and GVL yield (Figure 4.19). Finally, it reached up to the maximum GVL yield after 4 h. However, further prolonging of reaction time did not significantly affect the LA conversion but decreased GVL yield which might be due to the occurrence of side reactions and production of solid residues such as coke and humins.
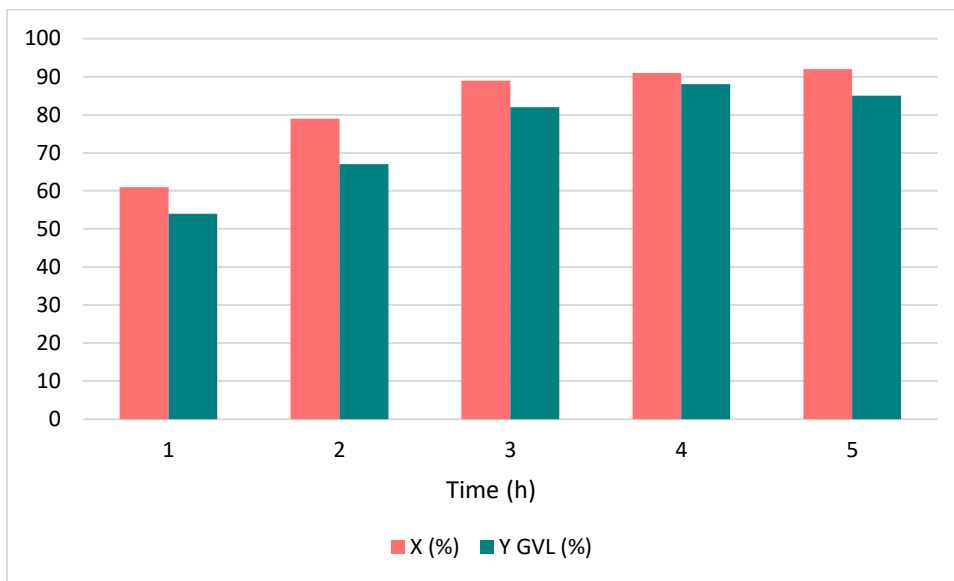

Figure 4.19. Hydrogenation of LA over NiAlp/Aw catalyst at different reaction times. Reaction conditions: 180 °C, 35 bar H_2, 0.17 M LA, 400 mg catalyst, 50 ml H_2O.

Finally, the increase of LA/catalyst mass ratio resulted in a decrease of catalytic activity (Figure 4.20). It is shown that the LA/catalyst mass ratio of 2.5 was the optimum value for the proposed catalytic reaction.
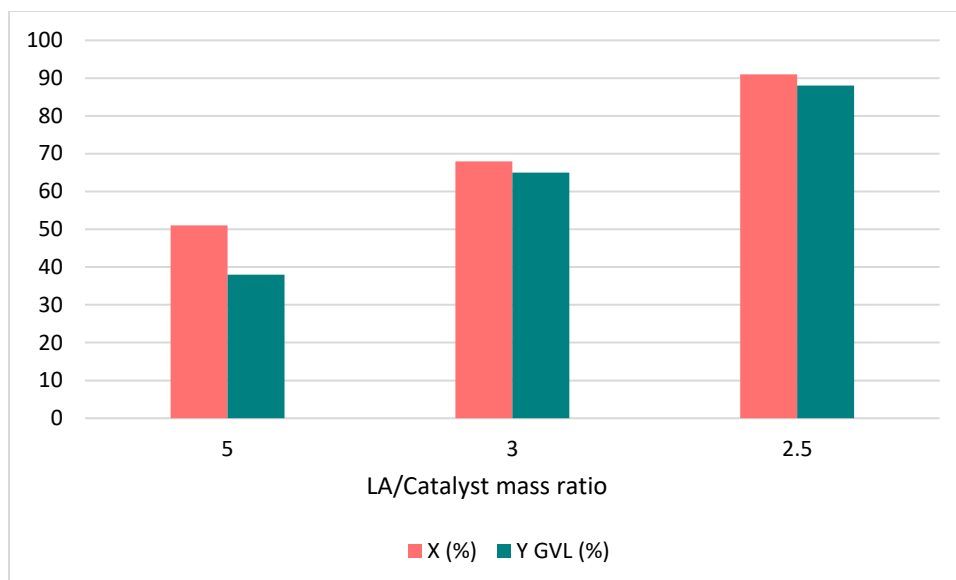
Figure 4.20. *Hydrogenation of LA over NiAlp/Aw catalyst at different LA/catalyst mass ratios. Reaction conditions: 180 °C, 35 bar H₂, 4 h, 50 ml H₂O.*

Overall, when optimizing the reaction conditions, no byproduct was detected in the liquid phase by HPLC and GC/MS analyses. Hence, we assumed that the byproduct might be in solid phase depositing on the catalysts surface. Interestingly, even at softest reaction conditions of this study, the catalyst showed a reasonable productivity being a promising factor in catalytic application.

4.3.6. Catalyst stability and recycling test

The stability and recyclability of NiAlp/A_T as one the best catalyst was studied. First, N_2 physisorption analysis was carried out to investigate any possible texture and surface area alterations of the catalyst after the reaction. As it can be seen in the isotherms of fresh and spent catalysts in Figure 4.21, the form of isotherm did not change during the reaction meaning the texture of the catalyst was stable. Moreover, the surface area and pore volume were slightly decreased which might be due to the coverage of the catalyst surface or partial blockage of the pores by different reaction organic species (Table 4.6).
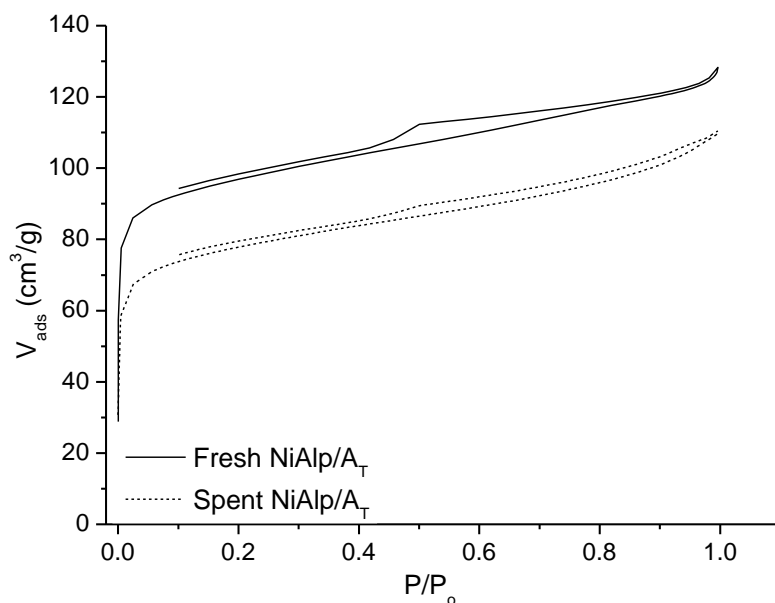
Figure 4.21. *N2 adsorption-desorption isotherms of the fresh and spent NiAlp/AT catalysts.*

Table 4.6. *Textural properties (obtained from N2 physisorption) for fresh and spent NiAlp/AT catalysts.*

Sample	$S_{Langmui}$ [a] (m^2g^{-1})	S_{micro} [b] (m^2g^{-1})	V_{tot} [c] (cm^3g^{-1})	V_{micro} [d] (cm^3g^{-1})
Fresh NiAlp/A_T	487	401	0.18	0.10
Spent NiAlp/A_T	401	316	0.16	0.07

a) Calculated by Langmuir method, b) Microporous or external surface area calculated by t-plot method, c) Total pore volume calculated according to the adsorbed amount of N_2 and P/P_o values near 0.98, d) Micropore volume calculated by t-plot method.
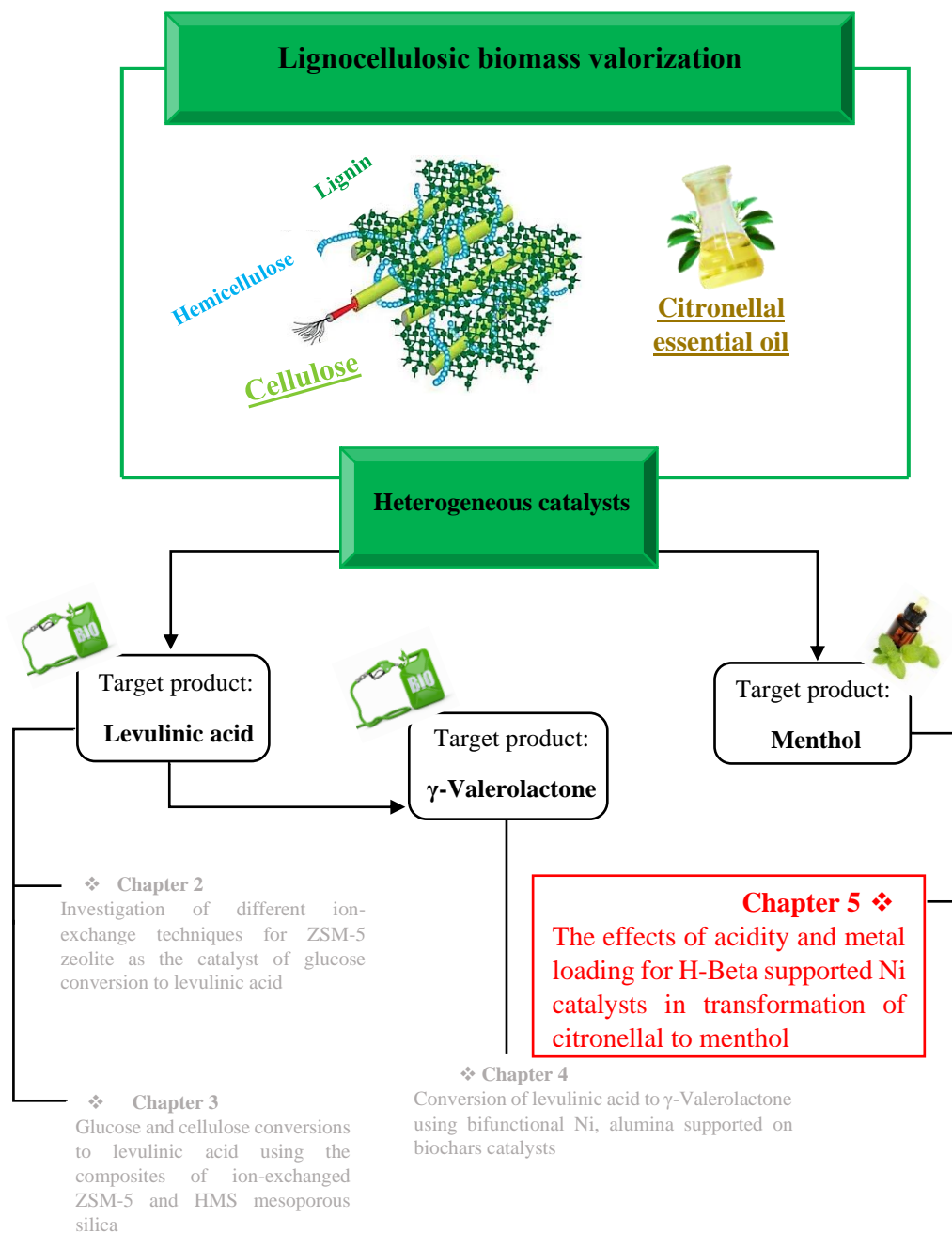
To investigate the recyclability of the catalyst, the spent NiAlp/A_T catalyst was filtered from the solution of first reaction run (Figure 4.16), washed with deionized water several times and dried in the oven at 90 °C for 12 h. Then, the catalyst was tested for the second run keeping the similar reaction conditions of 200 °C, 35 bar H_2, 4 h, 50 ml H_2O. In the second run, LA conversion declined from 95% to 52% and GVL yield dropped from 94% to 45%, respectively. First, we assumed that the reoxidation of the active Ni phase during the reaction might be the reason of this decrement. Therefore, we regenerated the catalyst by reduction at the similar conditions of at 400 °C in

H$_2$ flow for 3 h. When trying the regenerated catalyst in the third run of the reaction, the similar result with the second run was obtained. As a final consideration, the reaction solution after the first run was analyzed by AAS, no leaching was observed in the case of Al but Ni leaching was observed. This might be related to hydrophobic feature of carbonaceous materials and light weight of Ni as a non-noble metal compared to a heavy noble one. This hypothesis requires a further study on the improvement of activated biochar surface functionality using a post functionalization or a chemical activation approach for a better anchorage of light non-noble metals on the carbonaceous support. Moreover, investigation of other Ni introduction methods such as precipitation is needed for prospective study.

4.4. Conclusions

In this chapter, LA was transformed to GVL over bifunctional Ni, Al-catalysts supported on activated biochar as a sustainable and efficient support. First, a comparative investigation among different activated biochars obtained from pyrolysis and CO$_2$-based activation of leather tannery waste, vine wood waste, barley waste, and Venice lagoon brown algae suggested that the chemical, textural and morphological properties of activated biochars are highly affected by the origin of initial biomasses. CHNS elemental analysis showed a higher amount of carbon portion for A$_T$ and A$_W$ confirming their higher aromaticity and stability as catalyst supports. In addition, the highest nitrogen amount for A$_T$ and A$_B$, and oxygen amount for A$_W$ confirmed higher amounts of N,O-doped and functional groups of the supports, as it was also observed in FTIR and TPD results, being suitable for introduction and anchorage of active metal sites. According to N$_2$ physisorption analysis, the porous textures and high surface areas of all supports were successfully achieved through activation procedure except A$_B$ due to a different origin of initial B biomass which required harsher activation conditions. The weak porosity and low surface area of A$_B$ and the existence of poisoning sulfur in A$_A$ were the main reasons for the low activity of their related catalysts. Hence, A$_T$ and A$_W$ acted as the best supports of the catalyst in which all their suitable chemical, textural and morphological properties led to a higher dispersion of active phases (XRD and TEM results) resulting the highest activity and producibility in the proposed reaction. Moreover, Al-containing species as the Lewis acid site was introduced to supports via impregnation and precipitation methods. Precipitation technique could better improve weak Lewis acid site dispersion and its better activity in dehydration step of the reaction. Among all catalysts,

NiAlp/A$_T$ and NiAlp/A$_W$ acted as the best ones producing around 95% LA conversion and GVL yield and TOF of ca. 95.10-5 S^{-1} at 200 °C, 35 bar H$_2$, 4 h in an aqueous medium. The promising results of this chapter introduce sustainable and cheap catalysts for biomass derived chemicals valorizations and also propose some suggestions for an improvement of the catalyst stability for future studies.

Lignocellulosic biomass valorization

Lignin

Hemicellulose

Cellulose

Citronellal essential oil

Heterogeneous catalysts

Target product:

Levulinic acid

Target product:

γ-Valerolactone

Target product:

Menthol

❖ **Chapter 2**
Investigation of different ion-exchange techniques for ZSM-5 zeolite as the catalyst of glucose conversion to levulinic acid

❖ **Chapter 3**
Glucose and cellulose conversions to levulinic acid using the composites of ion-exchanged ZSM-5 and HMS mesoporous silica

❖ **Chapter 5** ❖
The effects of acidity and metal loading for H-Beta supported Ni catalysts in transformation of citronellal to menthol

❖ **Chapter 4**
Conversion of levulinic acid to γ-Valerolactone using bifunctional Ni, alumina supported on biochars catalysts

Chapter 5. The effects of acidity and metal loading for H-Beta supported Ni catalysts in transformation of citronellal to menthol

5.1. Introduction

5.1.1. Menthol synthesis from citronellal

Menthol (ME) as an organic chiral compound with chemical formula $C_{10}H_{20}O$ and IUPAC name 5-Methyl-2-(propan-2-yl)cyclohexan-1-ol exists in eight possible stereoisomers of ($\pm$)-menthol, ($\pm$)-isomenthol, ($\pm$)-neomenthol, and ($\pm$)-neoisomenthol. Among them, ($-$)-menthol has the most functional fresh and cooling sensation [315]. The fresh and cooling sensation and the local anesthetic and counterirritant properties of ME cause its extensive utilization in cosmetic, pharmaceutical, and flavoring applications such as in toothpaste, perfume, mouthwash, ointments, cough drops, chewing gum, and candy [316]. Traditionally, ME crystals were naturally separated from peppermint essential oil, but because of its incremental demand, synthetic ME was introduced by two companies, Takasago International Corp and Haarmann & Reimer. The process of Takasago was based on myrcene conversion to ($-$)-menthol over Rh- BINAP catalyst [316,317]. In Haarmann & Reimer process, m-cresol was used as the substrate and transferred to thymol by propylation followed by hydrogenation to racemic ($\pm$)-menthols over Ru/Al_2O_3 catalyst. Thereafter, a crystallization method was used to separate ($-$)-menthol from racemic ($\pm$)-menthols [2]. At the moment, BASF, Aecher-Daniels-Midland company, Symrise, Takasago International Corporation, and Nectar Lifesciences Ltd are the leaders or major players in the ME market [318].

Recently, CAL as one of the most common Citral derivatives has attracted wide attention for the synthesis of ME [316]. Citral is an essential oil which can be extracted from lemongrass oil (ca. 70–80% citral) via a distillation process [319]. In 2004, BASF company set up a new continuous system for production of citral with annual capacity of 40,000 metric tons in Ludwigshafen, Germany [316]. CAL can be produced from selective hydrogenation of Citral using metal-supported catalysts. In addition, BASF has also established another technology for formation of (+)-(R)-citronellal from different reactants such as neral and geranial by a direct catalytic hydrogenation [320]. In this thesis, CAL was selected as a model reactant, and its catalytic conversions to ME in a batch system were investigated.

ME can be synthesized from CAL via a two steps reaction: first, the cyclisation of CAL to pulegols occurs over an acid catalyst; second, the hydrogenation of pulegols to MEs happens catalyzing by an active metal phase (Figure 5.1). Through this reaction pathway, four different enantiomeric pairs of isopulegol and ME can be synthesized. Moreover, the process can undergo some side reactions such as CAL hydrogenation, CAL and isopulegol defunctionalization, dimerization, and polymerization [320]. Therefore, selection of a suitable catalyst to control the reaction pathways toward the target product and diminish the byproducts formation are vital. In the next section, a state-of-art about the catalytic systems of the target reaction and an introduction about the catalysts used in the present study will be referred.
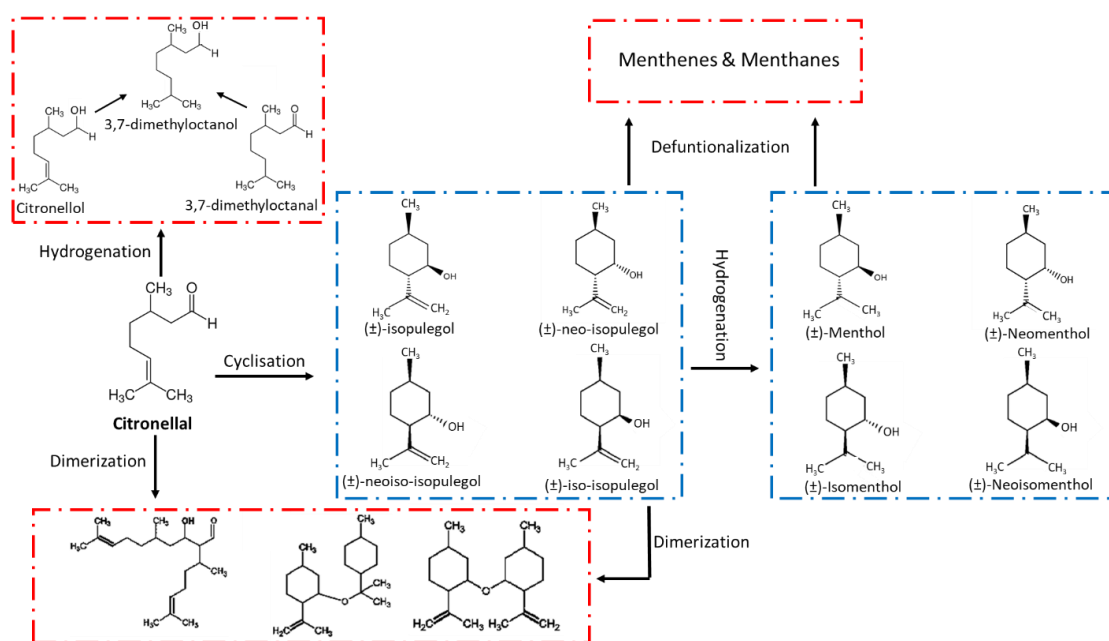
Figure 5.1. *Possible reaction pathways for one-pot synthesis of menthol from citronellal.*

5.1.2. Catalysts for conversion of citronellal to menthol

Different classes of bifunctional catalysts have been used for transformation of CAL to ME in the literature. Heterogeneous catalysts have the priority because of the evident drawbacks of homogeneous catalysts such as economic and environmental issues along with recovering and separation process [321]. Several heterogeneous acidic catalysts such as SiO_2, MCM-41, γ-Al_2O_3, ZrO_2, and zeolite were investigated for efficient CAL cyclisation [322–326]. It must be mentioned that most of studied acidic catalysts were active and produced a high yield of isopulegols.

However, obtaining a high selectivity of (-)-isopulegol was significant, which depended on the textural and acidic properties of the catalysts. Furthermore, for the second step of the reaction, several supported noble and non-noble metal catalysts such as Pt, Pd, Ir, Ru, Ni, Co, and Cu as a hydrogenation active phase have been used. For example, Plößer and co-workers investigated bifunctional metal-acid heterogeneous catalysts, typically H-Beta zeolite supported Pd, Pt and Ru for conversion of CAL to ME. 1 wt.% Ru/H-Beta-25 gave the highest selectivity to ME exceeding 93% [327]. In another study, Pt- and Ru- supported on H-Beta-25 catalysts could catalyze the reaction by ca. 70% stereoselectivity towards (±)-menthol both in batch and trickle bed reactors [328]. Various other studies reported the high activity and selectivity of noble metals as the active phases of the catalysts for hydrogenation step [329–331]. In addition, low-cost non-noble metals, particularly Ni, were studied to convert CAL to a high selectivity of ME. For example, either a dual catalytic system of Zr-Beta and Ni/MCM-41 or a bifunctional Ni/Zr-Beta exhibited 86-97% yield of ME and 90-94% diastereoselectivity to (±)-menthol from CAL. The reaction was performed in two steps including the cyclisation of CAL to give a maximum yield of isopulegols under He atmosphere and isopulegols hydrogenation to ME under hydrogen atmosphere (20 bar) at 80 °C. The first step was catalyzed by the modified Lewis acidity of Zr-Beta catalyst, and the second step underwent by the assistance of Ni active phase of the catalyst [332,333]. A similar strategy was followed in [180] using Ni/γ-Al$_2$O$_3$ as the catalyst in which the hydrogenation step was performed under very mild reaction conditions of 90 °C and 1 bar H$_2$ producing 86% yield of MEs [326]. Moreover, one-pot transformation of CAL to ME was carried out over sulfated zirconia supported Ni under 14 bar of H$_2$ and at 100 °C, and (−)-menthol was synthesized with enantioselectivity of 88% analyzed with an α-DEX Supelco chiral column [334]. However, sulfated zirconia pillared montmorillonite supported Ni, Ni/ZSM-5 and Ni/natural zeolite displayed very low yield of ME [335,336]. In this thesis, Ni/H-Beta based catalysts were used to provide an in-depth study on the synergetic effect of Ni active phase and H-Beta acid sites nature, strength, and concentration on the target reaction.

Beta zeolite (BEA topology) is formed by corner-sharing TO$_4$ (T = Si or Al) tetrahedra and is a three-dimensional (3D) crystalline material with three sets of vertical channels and 12-membered ring porous structure. It is classified as a large-pore microporous material and have two kinds of openings including 5.5 Å × 5.5 Å and 6.4Å × 7.6 Å [337,338]. Beta zeolite is in the group of materials with chiral structure being firstly determined by Newsam *et al* and Higgins *et al*.

independently [339–341]. Chirality is a crucial feature of the nature, but rare in zeolite as an inorganic porous material. Indeed, among 245 types of known zeolite frameworks, only eight types (BEA, GOO, CZP, JRY, -ITV, OSO, LTJ, and STW) displayed chiral structures [342]. The chirality of zeolite could be a significant property in asymmetric catalysis particularly in both shape selectivity and enantioselectivity [343,344]. As a matter of fact, in this study, Beta zeolite was applied for the asymmetric cyclisation of CAL to (±)-isopulegol as an intermediate of (±)-menthol [345]. From the structural aspect, zeolite Beta is made of stacking-fault intergrowth units with various distinct and closely related polymorphs [346]. Polymorphs are groups of stacking sequences in an identical centrosymmetric layer made of secondary building unit enlargement with T-atoms being connected into two directions (Figure 5.2a) [342]. 12-membered ring structure with centrosymmetric 2-dimensional (2D) building layer in top and side views is indicated in Figure 5.2 b and c, respectively, and the overall porous structure of Beta zeolite is shown in Figure 5.2d.
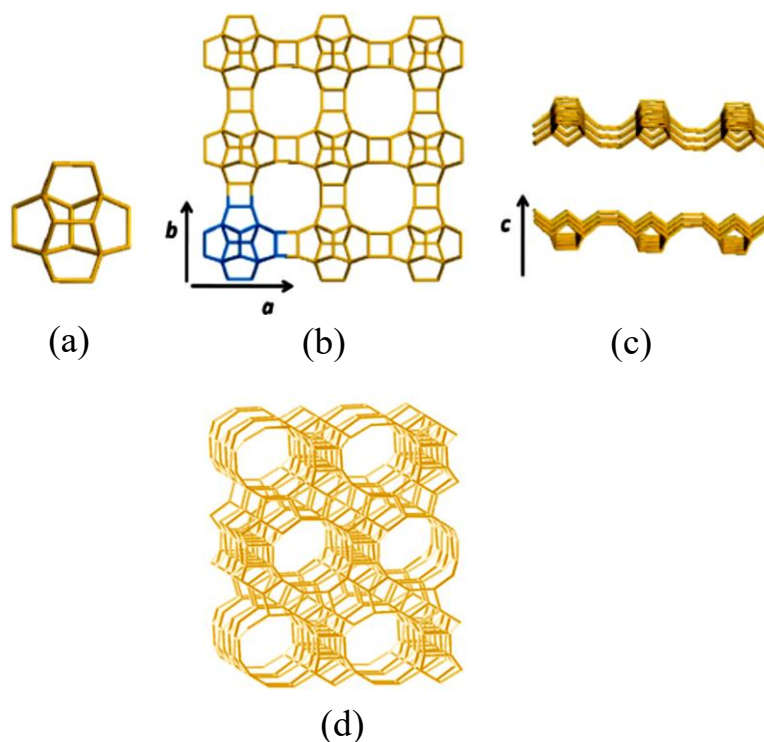

(a)   (b)   (c)

(d)

Figure 5.2. a) Secondary building unit, b) top view and c) side view of centrosymmetric layer [189], d) the pore structure of Beta zeolite.

Normally, the crystallisation of Beta zeolite occurs in framework Si/Al ratio range of 10-30. Interestingly, the acid sites concentration, and the hydrophilic/hydrophobic features of zeolite can

be controlled by SiO_2/Al_2O_3 ratio. Several studies have been reported regarding the expansion of the ratios. A decrease of Si/Al ratio in Beta zeolite can give a high consentration of acid site with a different shape-selective and catalytic properties considering that a Si/Al ratio lower than 8 might disturb the crystalline structure of the zeolite. On the other hand, Beta zeolite with high Si/Al ratios can provide a lower acid site consentration with higher hydrophobic properties. These aspects can be strongly effective on the catalytic behaviour of zeolite in acid site depended on reaction mechanisms and the reaction with polar/non-polar reactants and products [347].

5.1.3. The aim of the chapter

The work reported in this chapter was performed at Åbo Akademi University of Turku (Finland) under the supervision of Prof. Dmitry Yu. Murzin. Typically, the transformation of Citronellal essential oil to menthol was studied. The real aim was to investigate a sustainable, low cost and bifunctional metal/acid catalyst (Ni/H-Beta) and provide a comprehensive study on the synergetic effect of Ni active phase and H-Beta acid sites nature, strength and concentration in the activity and selectivity of target reaction. Therefore, H-Beta zeolite with two different SiO_2/Al_2O_3 molar ratios, 25 and 300, and Ni loading of 5, 10 and 15 wt% were applied for the proposed process. All catalysts were prepared by wet impregnation method and characterized by ICP, N_2 physisorption, XRD, SEM, EDS, TEM, TPR, and FTIR by adsorbing/desorbing Pyridine as probe molecule. The catalysts were tested for citronellal conversion to menthol using a batch system. The result showed that 15 wt.% Ni on H-Beta-25 displayed the best result giving the highest menthols yield of 36% (77% stereoselectivity to ($\pm$)-menthol isomer) at 93% citronellal conversion. The highest catalytic efficiency was due to a suitable synergy and catalyst acidity in the aspect of concentration, strength, and Lewis to Brønsted acid sites ratio, and the metal loading and dispersion. The results reported in this chapter are accepted for publication as: "One-pot transformation of citronellal to menthol over H-Beta zeolite supported Ni catalyst: Effect of catalyst support acidity and Ni loading", S. Taghavi, P. Mäki-Arvela, Z. Vajglová, M. Peurla, I. Angervo, K. Eränen, E. Ghedini, F. Menegazzo, M. Zendehdel, M. Signoretto, D. Yu. Murzin, Catalysis Letters, accepted.

5.2. Experimental

5.2.1. Catalyst preparation

Two different commercial zeolites, namely NH_4-Beta-25 (theoretical SiO_2/Al_2O_3= 25 molar ratio) (CP814E) and H-Beta-300 (theoretical SiO_2/Al_2O_3= 300 molar ratio) (CP811C), were supplied from Zeolyst International. The transformation of ammonium form NH_4-Beta-25 to H-beta-25 was performed by a calcination procedure at the final temperature of 400 °C for 4 h. Ni supported on H-Beta zeolite were synthesized by the evaporation impregnation technique using nickel (II) nitrate hexahydrate ($Ni(NO_3)_2.6H_2O$, Merck, 99.999%) as the precursor of Ni. Thereafter, several catalysts with nominal Ni-metal loadings of 5, 10 and 15 wt.% on H-Beta-25 and H-Beta-300 were prepared. First, $Ni(NO_3)_2.6H_2O$ was dissolved in distilled water (250 mL) inside a flask and the target amount of H-Beta support was added to the solution. It is noticed that all supports were sieved to the fraction below 63 µm to decrease the limitation of internal mass transfer. The impregnation procedure was performed in a rotary evaporator with a rotational speed of 10 rpm at room temperature for 24 h. Thereafter, the aqueous solution evaporation was performed in the rotavapor by a water jet vacuum pump at temperature of 50 °C. The resulted catalyst powder was dried in the oven at 100 °C for 12 h and calcined in static air at 400 °C for 3 h. The final catalysts were once again sieved to the fraction below 63 µm. The catalysts were labeled 5Ni/H-Beta-25 (5 wt.% Ni/H-Beta-25), 10Ni/H-Beta-25 (10 wt.% Ni/H-Beta-25), 15Ni/H-Beta-25 (15 wt.% Ni/H-Beta-25), 15Ni/H-Beta-300 (15 wt.% Ni/H-Beta-300).

5.2.2. Catalytic test

First, the desired weight of catalyst was decreased in an ex-situ glass tube under H_2 flow of 50 mL/min at 400 °C for 3 h. After reduction, the catalyst was cooled down to the room temperature. To avoid the reoxidation of reduced catalyst, 10 mL of cyclohexane as the reaction solvent was added to the reduction tube and the catalyst was sealed.

Citronellal conversions to menthols were carried out by charging 2.6 mmol of citronellal, 300 mg of the pre-reduced catalyst, and 90 mL of cyclohexane (Alfa Aesar, ≥99.9 wt%) solvent into an autoclave. Before starting the reaction, the reactor was flushed with a mixture of N_2 ($\cong$95%) and O_2 ($\cong$5% Ar) for 10 min. Then, the temperature was increased to the desired level under H_2 with the pressure of 20 bar. The 3 h of the reaction time was considered after achieving the target

temperature by starting to stir with the rate of 900 rpm. The small particle size of the catalyst and high speed of stirring were helping on the suppression of external and internal mass transfer limitations. The liquid samples from reaction mixture were taken at definite intervals and analyzed by a GC. An Agilent GC 6890N with an FID detector at 340 °C and DB-1 column (length 30 m, internal diameter 250 μm and film thickness 0.5 μm) was used for the analyses following the temperature program of: 110 °C – 0.4 °C/min – 130 °C – 13 °C/min – 200 °C (held 5 min). In addition, an Agilent GC/MS 6890N/5973N with a DB-1 column (length 30 m, internal diameter 250 μm and film thickness 0.5 μm) was used to confirm the type of products. For regeneration of the catalyst, the final reaction solution was filtered and the solid sample on the filter was collected and washed with cyclohexane. After that, the spent catalyst was dried in the oven at 100 °C for 12 h and reduced following the same procedure as for the fresh one aiming to reduce oxidized Ni formed during the recovery procedure of catalyst, and eventually used in the second run of the reaction.

The citronellal conversion (X), the yield (Y) and selectivity (S) of products, the reaction rate (r) and turnover frequency (TOF) were calculated according to the following equations:

$$X\ (\%) = \frac{C_0 - C_i}{C_0} \times 100$$

where X is the citronellal conversion at time t, C_0 and C_i are the molar concentration (mol L^{-1}) of citronellal at time zero and t, respectively,

$$Y_p\ (\%) = \frac{C_p}{C_0} \times 100$$

$$S_p\ (\%) = \frac{C_p}{\Sigma(C_a + C_b + C_c + \cdots + C_z)} \times 100$$

Where Y_p and S_p correspond to the yield and selectivity of the product p at a certain conversion, respectively, C_p and $(C_a + C_b + C_c + \cdots + C_z)$ are the molar concentrations (mol L^{-1}) of the product p and all products at the same conversion, respectively,

$$r_0 = \frac{\Delta n}{\Delta t . m_{cat}}\ \text{mol s}^{-1}\ \text{g}^{-1}$$

$$\text{Initial TOF} = \frac{\Delta n}{\Delta t.n_{Ni}} \text{ s}^{-1}$$

where r_0 is the initial rate of the reaction and initial TOF is the initial turnover frequency, $\Delta n/\Delta t$ are the number of reacted moles per time interval between 1-15 min, m_{cat} corresponds to the mass of catalyst, n_{metals} corresponds to the moles of exposed Ni active metal ((moles of Ni in the catalyst) $\times$ (dispersion/100)).

5.3. Results and discussion

5.3.1. Catalyst characterization

The ICP results indicate that all catalysts had the Ni loading very close to the nominal value (Table 5.1). The N_2 adsorption–desorption isotherms of the H-Beta-25 and H-Beta-300 zeolites and the catalysts after loading of Ni are exhibited in Figure 5.3. A combination of I and IV type isotherms can be observed for all materials confirming the presence of both micropores and mesopores in all samples similar to what was reported in the literature [348]. Particularly, a sharp increase of adsorption curve at a low P/P_o pressure is related to the existence of micropores in materials, while the hysteresis loops at range of $0.60<P/P_o<0.99$ and $0.50<P/P_o<0.99$ are associated to the inter-crystalline mesopores of H-Beta-25 and H-Beta-300, respectively [349]. After Ni impregnation on both zeolites, the catalysts showed the similar shape of isotherms with those of the supports demonstrating that the texture and crystalline structure of the zeolites were preserved.
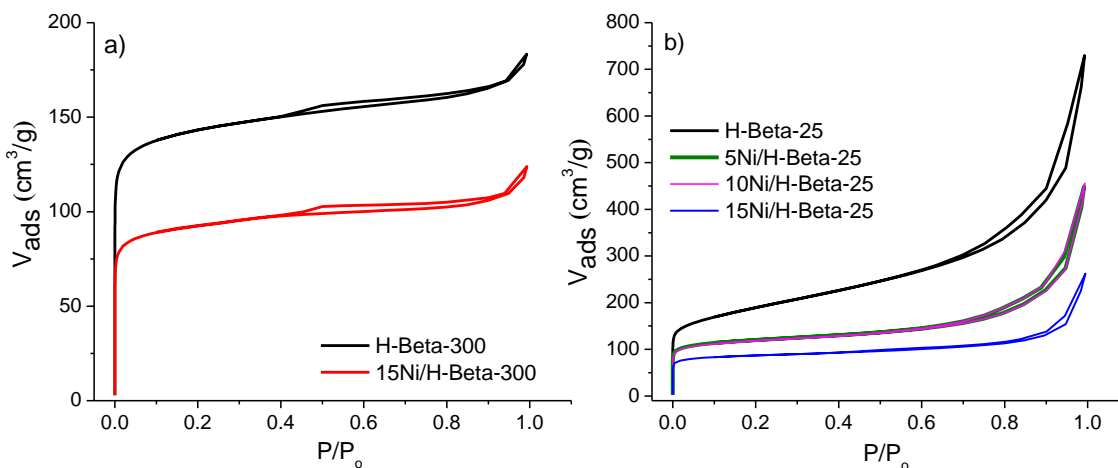

Figure 5.3. *N_2 adsorption-desorption isotherms of a) H-Beta-300 and 15Ni/H-Beta-300; and b) H-Beta-25, 5Ni/H-Beta-25, 10Ni/H-Beta-25, 15Ni/H-Beta-25.*

According to the data in Table 5.1, by Ni impregnation on both H-Beta-300 and H-Beta-25 zeolites, a reduction of surface area and pore volume happened due to Ni introduction into zeolites structure [350]. The difference of surface area for the samples with 5 and 10 wt.% Ni loading on H-Beta-25 is negligible, whereas when the amount of Ni loading increased to 15 wt%, the surface area decreased significantly which might be due to a partial blockage of primary micro-mesopores [351].

Table 5.1. *Ni loading (determined by ICP-OES), textural properties (obtained from N_2 physisorption)and SiO_2/Al_2O_3 ratios (obtained from EDS analysis) for studied supports and catalysts.*

Catalysts	Ni loading (wt%)	S_{DR} [a] (m^2/g)	V_{micro} (cm^3/g)	V_{meso} (cm^3/g)	SiO_2/Al_2O_3 (mol/mol)[b]
H-Beta-300	-	634	0.25	0.05	102
15Ni/H-Beta-300	14.3	406	0.17	0.03	-
H-Beta-25	-	750	0.26	0.70	25
5Ni/H-Beta-25	4.6	524	0.20	0.38	-
10Ni/H-Beta-25	9.9	516	0.20	0.38	-
15Ni/H-Beta-25	13.8	383	0.15	0.18	-

a) Microporous or external surface area calculated by Dubinin-Radushkevich method (DR), b) calculated by EDS technique [352]

TPR profiles display that NiO was completely reduced in all catalysts at the temperature below 650 °C (Figure 5.4). The temperature, shape, and area of the peaks in TPR profiles of different catalysts were differently affected by Ni loading, particles size, dispersion and the interaction between metal and H-Beta support. In all catalysts, the first peak at the temperature lower than 400 °C is associated to the reduction of NiO particles to Ni^0 that are mostly settled on the H-Beta support surface and have weaker interactions [353].
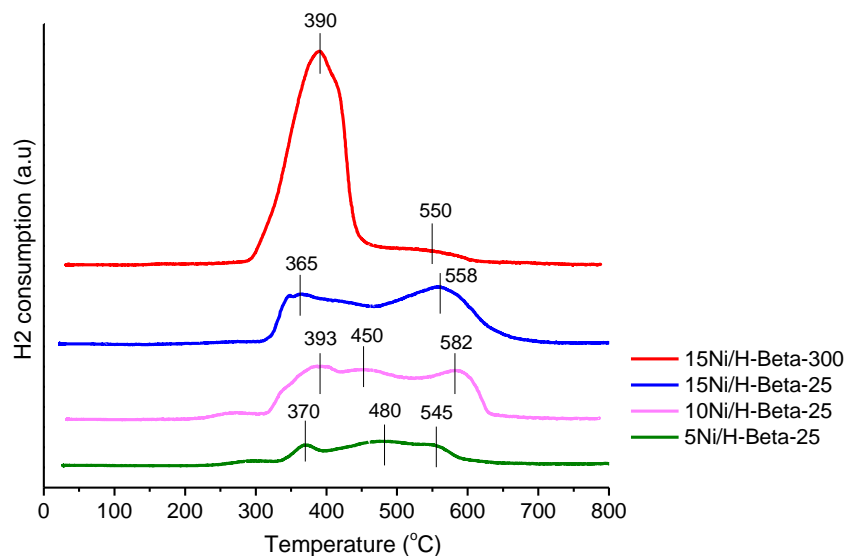
Figure 5.4. *Hydrogen TPR profiles of the catalysts.*

5Ni/H-Beta-25 and 10Ni/H-Beta-25 showed a second peak at 480 °C and 450 °C, respectively, whereas all catalysts exhibited the reduction peak at the temperature higher than 500 °C with different intensities. These peaks might be due to the reduction of NiO located in the inner mesopores or isolated Ni^{2+} inside the pores and channels of the H-Beta support [351,354]. The location of metal species inside the pores of zeolite can be strongly owing to their loading, size, and dispersion. It was reported that during impregnation procedure of the catalyst with a low loading of Ni, the ion-exchange of some Ni^{2+} with the bridging protons (Si-OH-Al) in channels wall of H-Beta zeolite and thus Ni can be stabilized close to the zeolite sites. Moreover, some of the intracrystalline NiO might react with protons of hydroxyl groups in H-Beta during calcination could and form $Ni(OH)^+$ species [355,356]. As the isolated Ni^{2+} ions, NiO and $Ni(OH)^+$ all located in the zeolite channels and pores displayed strong interactions with the structure of H-Beta zeolite, they were hardly reduced at a higher temperature [357]. For this reasons, 5Ni/H-Beta-25 and 10Ni/H-Beta-25 catalysts with lower loadings of Ni, smaller Ni particle sizes and higher dispersions showed two reduction peaks occurring at the higher temperatures. Moreover, a lower loading of Ni loading in 5Ni/H-Beta-25 catalyst caused the smallest peaks H_2-TPR.

Moreover, 15Ni/H-Beta-25 might possess more superficial and intracrystalline NiO particles because only one reduction peak was detected in H_2-TPR profile at a higher temperature (558 °C). It was suggested that a higher Ni loading can result in a continuous segregation of NiO from the

surface of zeolite to the bulk [354]. On the contrary, 15Ni/H-Beta-300 with the highest loading of Ni showed a different TPR profile with the largest H_2-TPR peak area. The first reduction peak at 390 °C had a very high intensity and the second reduction peak at 550 °C exhibited a very low intensity. It can confirm a very different amount of exchange sites in this catalyst. Indeed, low Al content and hydrophobic nature of H-Beta-300 with a very high SiO_2/Al_2O_3 molar ratio of 102 diminished NiO interactions with the support [358].

The XRD patterns of 5Ni/H-Beta-25 and 15Ni/H-Beta-25 catalysts are shown in Figure 5.5.
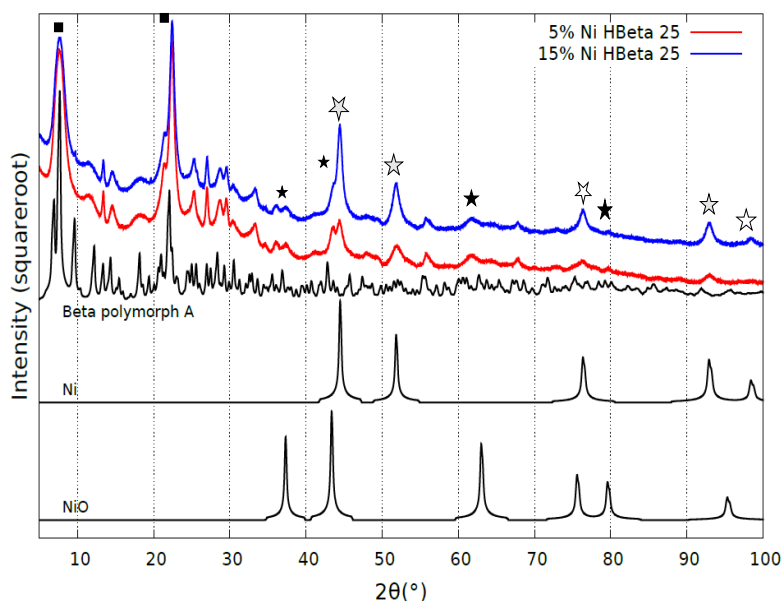
Figure 5.5. High-angle XRD patterns of the reduced 5Ni/H-Beta-25 and 15Ni/H-Beta-25 catalysts; (■ H-Beta-25, ✫ Ni^0, ★ NiO)

As it can be seen, both catalysts display two main lines at 2Θ of 7.8 º and 22.3 º which are typical for Beta zeolites with a high crystallinity agreeing with the literature [359]. The lines at 2Θ of 44.4 º, 51.8 º, 76.4 º and 93 º are related to metallic Ni^0. By increasing of the nickel loading, the intensities of the metallic Ni^0 lines increased. Furthermore, one of the double-line in XRD pattern of 5Ni/H-Beta-25 and a small shoulder in the XRD pattern of 15Ni/H-Beta-25 both located at 2Θ of 43.4 º are ascribed to intracrystalline NiO. This can suggest that the reduction at 400 °C might not entirely convert Ni^{2+} to metallic Ni^0 or reoxidation of Ni^0 in the air may occur before XRD measurement causing the existence of a small content of NiO particles in the catalysts [360–362]. This result is in line with TPR results (Figure 5.4). Therefore, it seems that both Ni^0 and NiO particles (Ni@NiO) existed in the final catalysts which was effective in the catalytic reaction.

Moreover, when comparing the XRD profiles of the catalysts with those of supports, it seems that some amorphization happened in H-Beta-25 upon the catalyst preparation procedure. It is assumed that partial amorphization could occur either at the aqueous solution evaporation under vacuum at 50 °C or most likely at the calcination procedure. Furthermore, TPR profiles of the catalysts confirmed strong interactions of some Ni^{2+} ions and NiO with the structure of zeolite which could cause partial amorphization of the H-Beta-25 structure at the calcination temperature.

The SEM images of H-Beta-25, 5Ni/H-Beta-25 and 15Ni/H-Beta-25 samples are shown in Figure 5.6.

Figure 5.6. SEM images of H-Beta-25, 5Ni/H-Beta-25, and 15Ni/H-Beta-25. (The magnification of all images is 25.00 K X).

H-Beta-25 exhibits a semi-spherical particle typical for crystalline morphology of Beta-zeolite [363]. However, by introduction of Ni, particularly in 15Ni/H-Beta-25 catalyst with a higher loading of Ni, the grain surface of H-Beta zeolite became rough because of the amorphization, as was confirmed by XRD result. The SiO_2/Al_2O_3 (mol/mol) ratios of H-Beta-25 and H-Beta-300 were estimated by EDS analysis (Table 5.1). As can be seen, the theoretical SiO_2/Al_2O_3 ratio for H-Beta-25 was almost like the measured value (SiO_2/Al_2O_3= 25), whereas H-Beta-300 with the nominal SiO_2/Al_2O_3 ratio of 300 showed the measured value close to 100.

A comparison among the TEM images of the four reduced catalysts with different loadings of Ni and supports (Figure 5.7) clearly indicates that the catalyst with lower metal loading has a narrower particle size distribution owing to the presence of smaller Ni@NiO particles, that are less agglomerated.
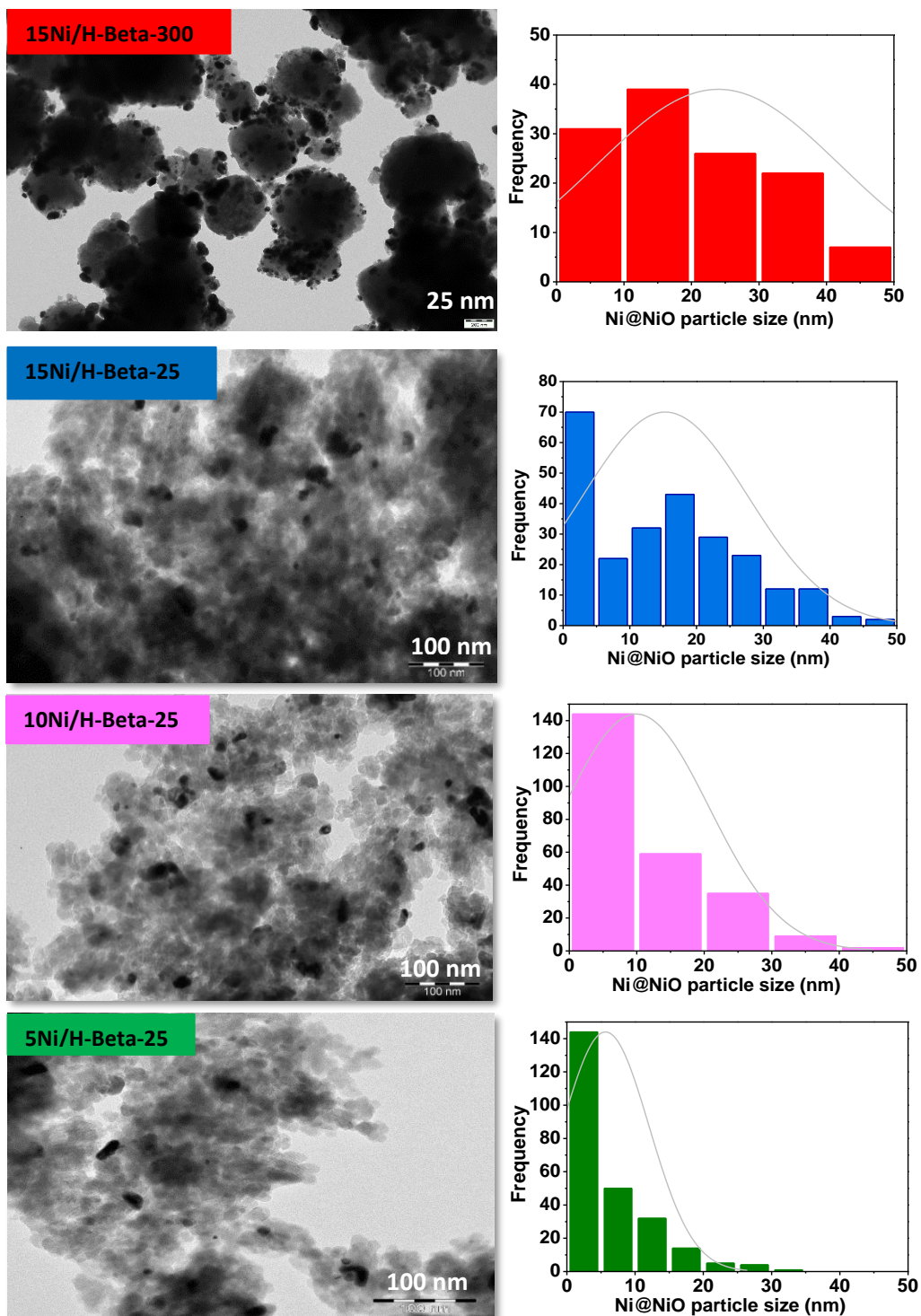
Figure 5.7. TEM images and Ni@NiO particle size distribution histograms of reduced 15Ni/H-Beta-300, 15Ni/H-Beta-25, 10Ni/H-Beta-25, and 5Ni/H-Beta-25.

Additionally, an increasing of the Ni loading caused the increase of the average particle size and hence lower dispersion (Table 5.2). As was demonstrated by TPR and XRD results (Figure 5.4, Figure 5.5), some intercrystallite $Ni(OH)^+$ and NiO, and non-reduced exchanged Ni^{2+} might exist besides metallic Ni^0 in the final catalyst. It is assumed that larger particles size in the TEM images of each catalyst might derived from the intercrystallite NiO as was suggested by Wang *et al,* [354]. This trend was also reported in various studies of the literature [364–366].

Table 5.2. *Average Ni@NiO particle size and dispersion determined from TEM images.*

Catalyst	Avg. particle size (nm)	~Dispersion (%) [a]
15Ni/H-Beta-300	19.4	5
15Ni/H-Beta-25	15	7
10Ni/H-Beta-25	7.5	13
5Ni/H-Beta-25	2	50

A) Dispersion (%) = 101/Avg. particle size determined by TEM (nm) [367]

The concentration of weak, medium and strong Brønsted and Lewis acid sites of the supports and catalysts was investigated via FTIR spectroscopy in the spectrum range of 1400-1575 cm^{-1} using pyridine as the probe molecule. Particularly, the weak, medium, and strong acid sites were determined from desorption of pyridine during 60 min at each 250 °C, 350 °C and 450 °C, respectively. The Brønsted and Lewis acid sites were quantified at each temperature according to the intensity of IR signals at 1545 cm^{-1} and 1455 cm^{-1}, respectively (Figure A5). As can be observed in pyridine-FTIR results of Table 5.3, the concentration of Brønsted acid site decreased and the concentration of Lewis acid site increased after loading of Ni on zeolite. The reduction of Brønsted acid site concentration might be related to the exchange of protons of the hydroxyl groups in the channels wall of H-Beta zeolite with Ni cations. In addition, the increase of Lewis acid site concentration could be due to introduction of non-reduced exchanged Ni^{2+} and NiO and forming new three-coordinated Al in the structure of zeolite upon the catalyst preparation procedure causing an enhancement of zeolite amorphous phase as was exhibited in XRD results (Figure 5.5) and SEM images (Figure 5.6) of the catalysts. H-Beta-300 with SiO_2/Al_2O_3= 102 and 15Ni/H-Beta-300 catalyst showed lower Lewis and Brønsted acid sites concentration compared to H-Beta-25 support with SiO_2/Al_2O_3= 25 and the 15Ni/H-Beta-25 catalyst, respectively. Brønsted acid site comes from proton of hydroxyl groups bridging silicon and aluminum in the channel walls, while

Lewis acid site of the zeolite originates from framework Al located on the edges and extra-framework Al [368]. Hence, by enhancement of the SiO_2/Al_2O_3 ratio and thus reducing both framework and extra-framework Al, both Brønsted and Lewis acid sites decrease as was reported several times [369,370]. Moreover, by decreasing the loading of Ni from 15% to 10% and further to 5% in H-Beta-25 catalysts, a small rise of Brønsted acid site concentrations and significant increase of Lewis acid site concentrations happened. This might be due to higher accessibility of zeolite Brønsted and Lewis acid sites when less Ni particles are present to block the pores and hinder such access. Since the acidity of catalyst is prominent for citronellal cyclization to pulegols [316,371], it was expected different acidities in different catalysts would exhibit different efficiencies.

Table 5.3. *Concentration of Brønsted acid sites (C_B) and Lewis acid sites (C_L) determined by FTIR with pyridine.*

Catalysts	250 ℃ Weak acidity		350 ℃ Medium acidity		450 ℃ Strong acidity		Total acid sites (μmol g⁻¹)	B/L
	C_B (μmol g⁻¹)	C_L (μmol g⁻¹)	C_B (μmol g⁻¹)	C_L (μmol g⁻¹)	C_B (μmol g⁻¹)	C_L (μmol g⁻¹)		
H-Beta-300	66	11	50	5	23	3	158	7.3
15Ni/H-Beta-300	12	27	9	8	-	-	56	0.60
H-Beta-25 [372]	53	35	42	17	191	10	349	4.6
15Ni/H-Beta-25	10	59	74	55	5	31	234	0.61
10Ni/H-Beta-25	6	76	91	92	14	35	313	0.55
5Ni/H-Beta-25	8	84	81	98	5	49	325	0.41

5.3.2. The results of catalytic tests

The results for one-pot conversion of citronellal over 15Ni/H-Beta-300, 15Ni/H-Beta-25, 10Ni/H-Beta-25 and 5Ni/H-Beta-25 catalysts are displayed in Table 5.4 and Figures 5.8-5.13. The relative error of GC analysis was generally less than ±5%.

Table 5.4. Catalytic test results of one-pot conversion of citronellal to menthol. (Conditions: 80 °C, 20 bar H_2, solvent: cyclohexane, amount of catalyst: 300 mg, the initial citronellal concentration: 0.029 M. Conversion of citronellal (X) is given at 3 h of reaction time. Yields (Y) of different products, stereoselectivity (SS), are given at 85% conversion out of brackets and after 3 h of the reaction between brackets.

Catalyst	r_0 (mol/s.g_{cat})	Initial TOF (s^{-1})	X (%)	Y_{Ps} (%)	Y_{MEs} (%)	Y_{ACP} (%)	Y_{CP}/ Y_{ACP}	Y_{DM} (%)	SS_{ME} (%)
15Ni/H-Beta-300	$2.4.10^{-7}$	0.058	88	9.1	30	7	6.6	31.8	79
				(7)	(32)	(8)	(5.9)	(33)	(80)
15Ni/H-Beta-25	$6.6.10^{-7}$	0.023	93	19.8	31.2	2.6	21	28	74
				(11)	(36)	(4)	(13.2)	(35)	(77)
10Ni/H-Beta-25	$6.7.10^{-7}$	0.024	96	33.2	21.7	2.3	24.7	25	78
				(13)	(36)	(2)	(27)	(39)	(77)
5Ni/H-Beta-25	$1.6.10^{-6}$	0.035	98	51.1	3.6	1.5	36.8	28	83
				(21)	(26)	(1)	(49)	(48)	(79)

X: conversion; Y: yield; r_0: initial reaction rate; Ps: pulegols = (±)-isopulegol (IP) + (±)-neoisopulegol (NIP) + (±)-isoisopulegol (IIP) + (±)-neoisopulegol (NIIP); MEs: menthols: (±)-menthol (ME) + (±)-neomenthol (NME)+ (±)-isomenthol (IM) + (±)-neoisomenthol (NIM); CP: cyclic products: pulegols + menthols+ defunctionalization products (DFP); ACP: acyclic monomeric products: citronellol (CLOL) + 3,7-dimethyloctanol (DMO)+ 3,7-dimethyloctane (DME); DM: dimeric ethers; SS_{ME}: stereoselectivity of menthol = ME/ΣMEs.

When comparing the initial TOFs and initial reaction rates of the catalysts with H-Beta-25 support, it can be observed the reaction over 5Ni/H-Beta-25 was the most rapid with the highest TOF giving a rate of $1.6.10^{-6}$ mol s^{-1} g_{cat}^{-1} and TOF of 0.035 s^{-1}. Therefore, the highest activity of this catalyst among H-Beta-25 supported materials might be due to the smallest Ni@NiO particle size and highest concentration of acid sites (Tables 5.2 and 5.3). On the other hand, 15Ni/H-Beta-300 also showed a high initial TOF, though it displayed the lowest acid site concentration, large Ni@NiO particles size, low exposed Ni metal (mole) with a higher Ni loading. Indeed, 15Ni/H-Beta-300 exhibited the largest peak in H_2-TPR (Figure 5.4), but the lowest initial rate. Thus, it can be stated that the initial rate for transformation of citronellal is not only affected by the particle size of Ni@NiO, but also from acidic feature. Typically, cyclisation of citronellal as well as side reactions, such as etherification, occur over acid catalyst [365]. Hence, it can be confirmed that the catalytic behavior of 15Ni/H-Beta-300 was influenced from both metal particles size and mild acidity. Both the initial TOF and initial reaction rate decreased by enhancing the Ni loading and increasing Ni@NiO particle size (Table 5.4, Figure 5.8a).
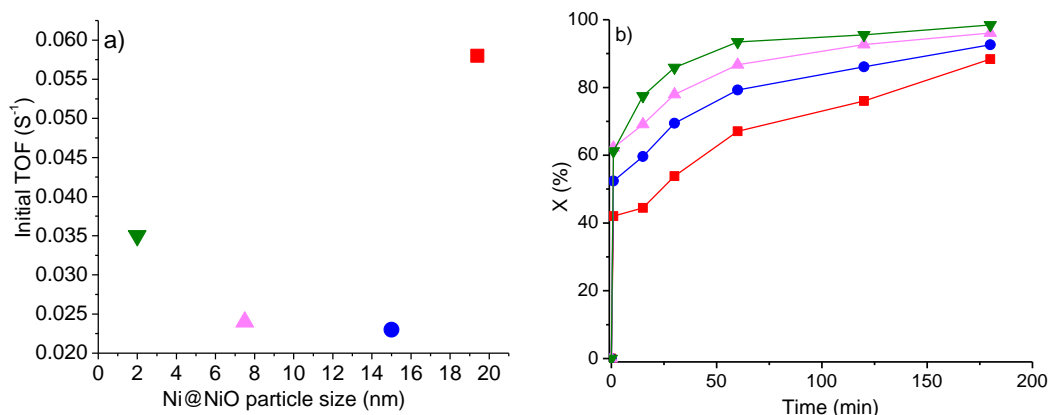
Figure 5.8. One pot transformation of citronellal to menthol: a) The initial TOF as a function of Ni@NiO average particle size and b) conversion vs time for 15Ni/H-Beta-300 (■), 15Ni/H-Beta-25 (●), 10Ni/H-Beta-25 (▲), 5Ni/H-Beta-25 (▼). (Reaction conditions: 80 °C, 20 bar H₂, solvent: cyclohexane, amount of catalyst: 300 mg, the initial citronellal concentration: 0.029 M)

5Ni/H-Beta-25 showed the fastest citronellal transformation in which almost 80% of conversion was reached after 15 min of the reaction. In addition, this catalyst achieved to the highest final conversion after 3 h being 98%, caused by the existence of small Ni@NiO particles and high acid sites concentration. The conversion increased by decreasing Ni loading (Table 5.4) and increasing Lewis acid site concentration (Figure 5.9a). The same trend was reported by Vajglova and co-worker by enhancement of total acid site concentration [373]. Moreover, all catalysts gave complete mass balance closure of the liquid phase.
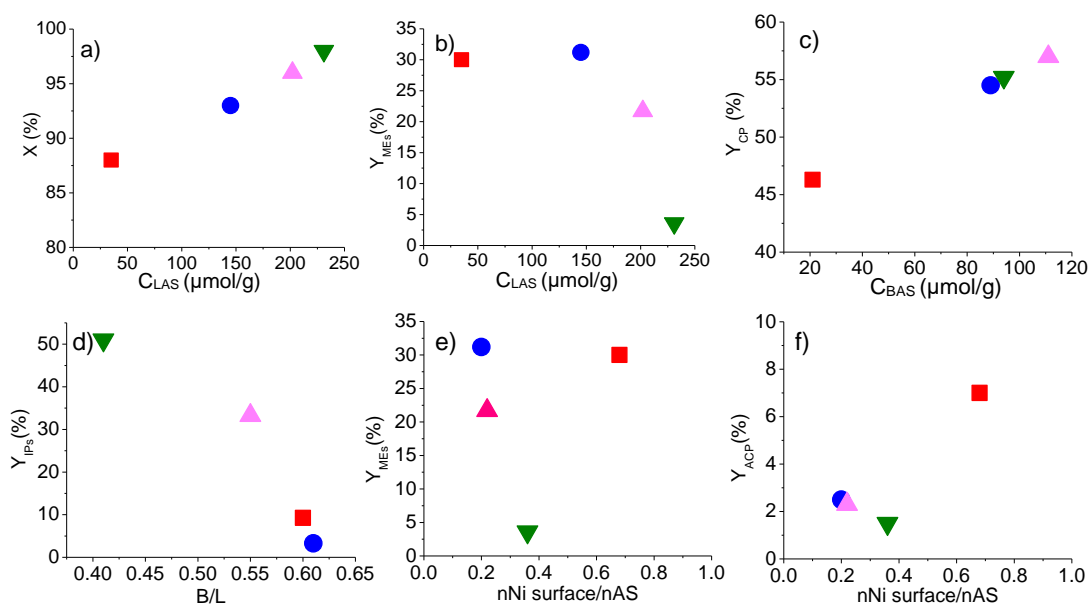
Figure 5.9*. Menthol synthesis from citronellal a) citronellal conversion as a function of Lewis acid sites concentration (C_{LAS}); at 85% conversion, b) yields of menthols (Y_{MEs}) as a function of Lewis acid sites concentration (C_{LAS}); c) cyclization products yield (Y_{CP}) as a function Brønsted acid sites concentration (C_{BAS}); d) yield of isopulegols (Y_{IPs}) as a function of Brønsted to Lewis acid sites ratio (B/L) e) yield of menthols and f) acyclic products yield as a function of mole of surface metal-to-mole of acid sites ratio. Legend: 15Ni/H-Beta-300 (■), 15Ni-H-Beta-25 (●), 10Ni/H-Beta-25 (▲), 5Ni/H-Beta-25 (▼)*

The products formations in the presence of different catalysts is exhibited in Table 5.4 and Figure 5.10(a,c,e,g). The highest (±)-isopulegol concentration was already obtained after 1 min of reaction, because it was even produced during heating processes without any stirring. Then, pulegols were converting further to menthols and menthanes (Figure 5.10(b, d, f, h)). The concentration of (±)-isopulegol after 1 min followed the order of 5Ni/H-Beta-25>10Ni/H-Beta-25>15Ni/H-Beta-25>15Ni/H-Beta-300 which is related to the order of decreasing of total acid site concentration and enhancing of B/L ratio of H-Beta support (Figure 5.9d) and increasing loading of Ni. This was expected, because citronellal cyclisation is catalyzed by acid site of the catalyst [374]. Indeed, Y_{IPs} rose with enhancing strong Brønsted acid sites concentration in other works of literature[373,375].
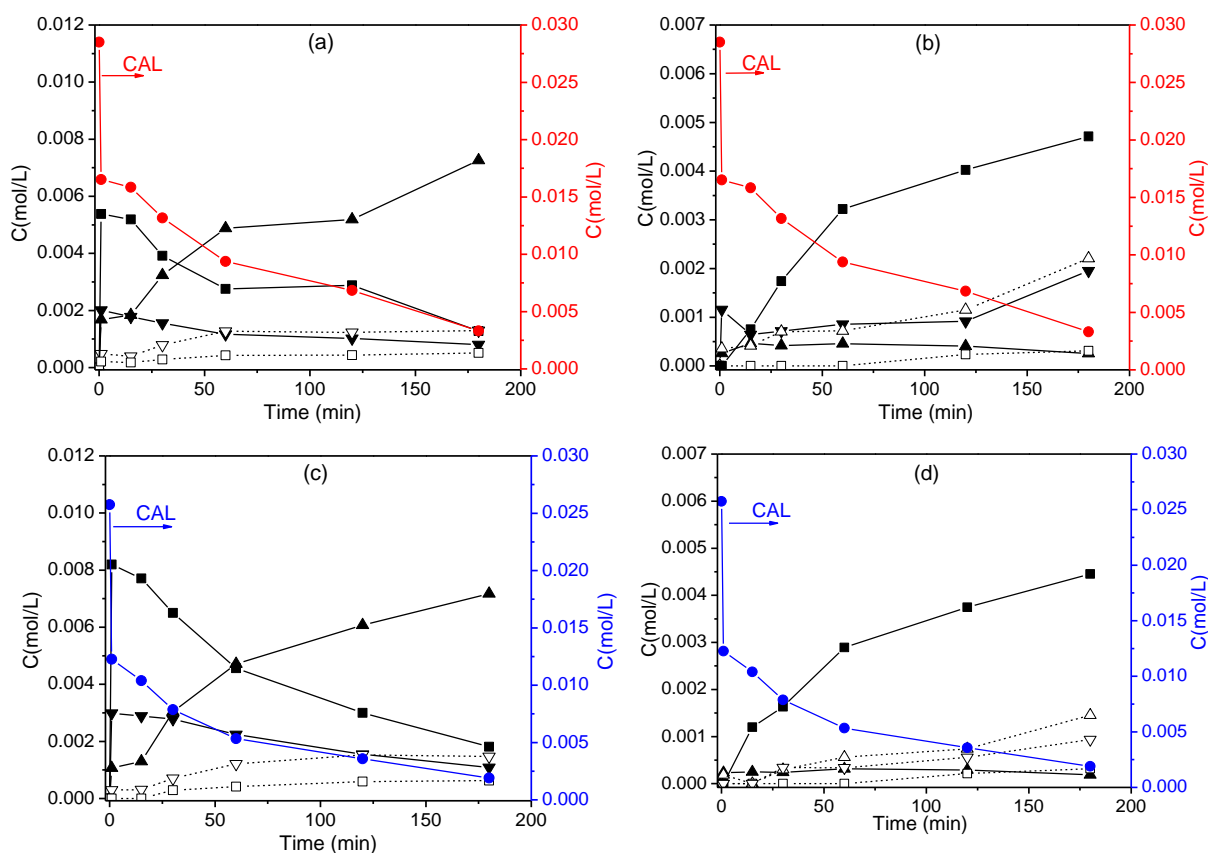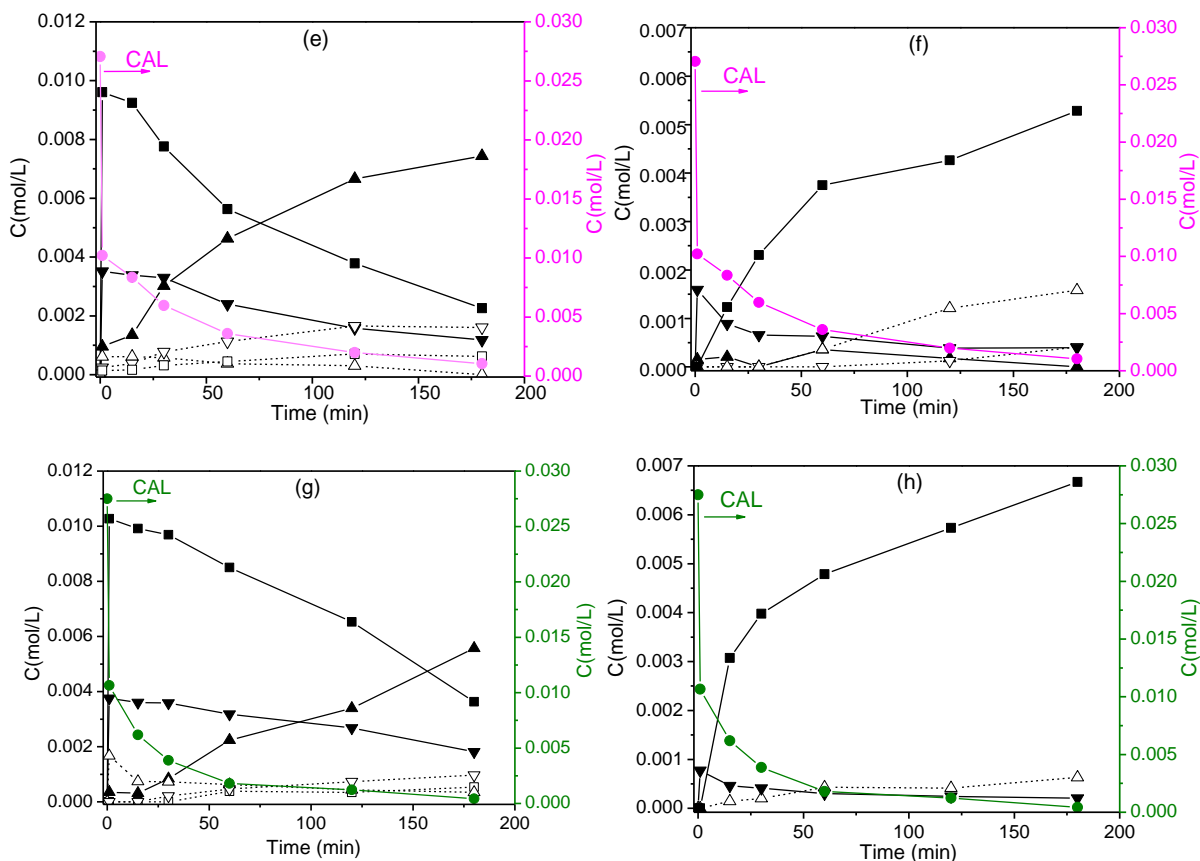
Figure 5.10. *Menthol synthesis from citronellal for (a) 15Ni/H-Beta-300, (c) 15Ni/H-Beta-25, (e) 10Ni/H-Beta-25 and (g) 5Ni/H-Beta-25: Concentration of citronellal (●), (±)-isopulegol (■), (±)-neo-isopulegol (▼), (±)-iso-isopulegol (Δ), (±)-menthol (▲), (±)-neomenthol (▽), (±)-neoisomenthol (□). For (b) 15Ni/H-Beta-300, (d) 15Ni/H-Beta-25, (f) 10Ni/H-Beta-25 and (h) 5Ni/H-Beta-25: Concentration of citronellal (●), citronellol (▼), menthanes (Δ), menthenes (▲), 3,7- dimethyloctanol (□), 3,7-dimethyloctane (▽), dimeric ethers (■).(Reaction conditions: 80 °C, 20 bar H₂, solvent: cyclohexane, amount of catalyst: 300 mg, the initial citronellal concentration: 0.029 M)*

In the second step, (±)-isopulegol hydrogenation to (±)-menthol went on at a rather low rate in the presence of the most acidic catalyst meaning 5Ni/H-Beta-25 (Figure 5.11) despite of its small Ni@NiO particles size. Menthols yield at 85% conversion of citronellal decreased with decreasing Ni@NiO particle size and enhancing especially Lewis acid site concentration.
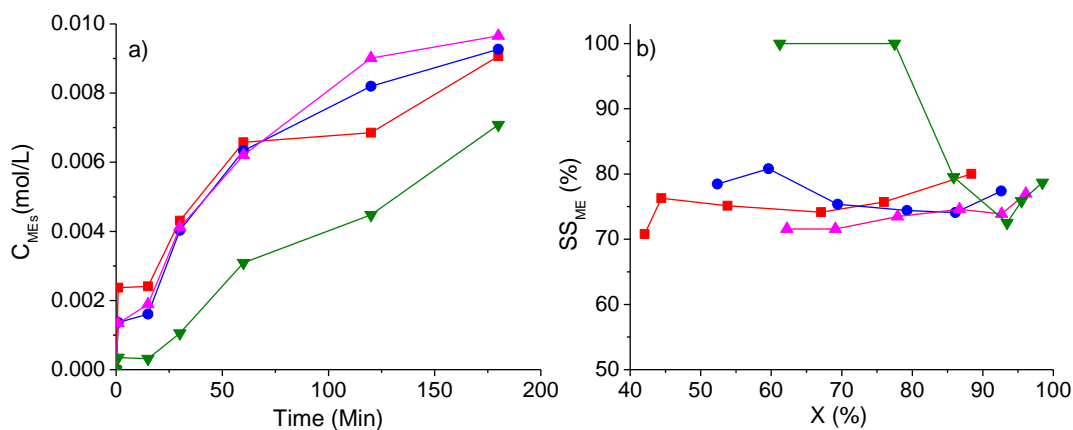
Figure 5.11. Menthol synthesis from citronellal: a) Concentration of menthols as a function of time, b) stereoselectivity of menthol as a function of conversion. Legend: 15Ni/H-Beta-300 (■), 15Ni-H-Beta-25 (●), 10Ni/H-Beta-25 (▲), 5Ni/H-Beta-25 (▼)

This result indicates that even larger Ni@NiO particles of ca. 15 nm facilitated effective pulegols hydrogenation to menthols (Figure 5.10). In addition, the yield of menthol at 85% conversion even increased with rising Ni@NiO particle size (Figure 5.12a).
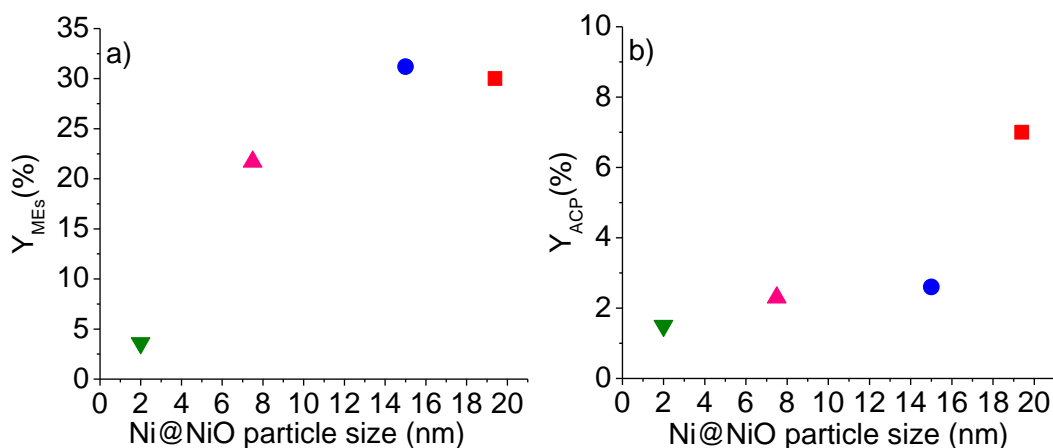

Figure 5.12. Menthol synthesis from citronellal, yields of a) menthols (Y_{MEs}) and b) ACP (Y_{ACP}) at 85% conversion as a function of Ni@NiO particle size. 15Ni-H-Beta-300 (■), 15Ni-H-Beta-25 (●), 10Ni/H-Beta-25 (▲), 5Ni/H-Beta-25 (▼)

The maximum menthols yield, 36% was achieved for 15Ni/H-Beta-25 and 10Ni/H-Beta-25 after 3 h of reaction (Table 5.4). However, the concentrations of neomenthol and neoisomenthol increased in the first hour of the reaction and attained almost a plateau for the reactions over all

123

catalysts (Figure 5.10). From Figure 5.10, it can be clearly observed that already after 15 min, the menthol production rate rose. Among H-Beta-25 supported catalysts, 15Ni/H-Beta-25 displayed the lowest concentration of Brønsted acid sites (Table 5.3) being superior for production of menthol when comparing to two other catalysts. In the work reported by Azkaar et al, Y_{MEs} decreased with enhancing Brønsted acid sites concentration [328]. The Brønsted-to-Lewis acid sites ratio (B/L) of 15Ni/H-Beta-25 catalyst in this study was 0.6 (Table 5.3) which was in line with the results for Ni/ZrS (nickel sulfated zirconia) catalyst showing the same B/L ratio but a higher acid sites concentration of 95 µm/g [334]. That catalyst showed a higher activity in citronellal conversion to menthols compared to nickel on sulfated zirconia with higher B/L ratio of 0.9 and the lower acid sites concentration of 30 µm/g. The highest yield of menthol in [376] was reported 98% at complete citronellal conversion in the presence of 8 wt% Ni-montmorillonite-heteropolyacid catalyst at 80 °C, 50 bar H_2 and after a longer reaction time of 12 h. This catalyst displayed the B/L= 0.3, however, the Ni particle size was not reported. It was reported in [377] that the catalyst with medium Brønsted acid site and strong Lewis acid site is appropriate for the reaction which was also resulted in the current study.

The highest stereoselectivity to (±)-menthol was at first for 5Ni/H-Beta-25, decreasing, however, with increasing conversion to the same level, ca. 78%, as resulted for other catalysts (Figure 5.11b). A comparison of the stereoselectivity to (±)-menthol for nickel-based catalysts reported in the literature [334] shows that sulfated zirconia supported nickel reached to 70% of stereoselectivity to (±)-menthol at a complete citronellal conversion, at 100 °C, 14 bar H_2 pressure for 30 min with the citronellal to catalyst mass ratio of 0.6. It should be noticed that different reaction conditions from [334] were applied in the current study, namely 80 °C, 20 bar total pressure, 3 h reaction time and the citronellal to catalyst mass ratio of 1.3.

Production of the undesired acyclic hydrogenation products (ACP), mostly citronellol, enhanced by increasing the loading of Ni and its particle size (Figure 5.9, Table 5.2). Besides citronellol, small amounts of 3,7-dimethyloctanol were produced. In particular, by enhancing the molar ratio of the exposed metal to total acid sites, the ACP yield decreased over Ni/H-Beta-25 catalysts (Figure 5.9f) similar with what was reported in ref [322], whereas 15Ni/H-Beta-300 catalyst with a mild acidic feature (Table 5.3) formed large concentrations of both citronellol and 3,7-dimethyloctanol, and no 3,7-dimethyloctanol was produced in the presence of 5Ni/H-Beta-25.

The formation of dimer was significant over all studied catalysts (Table 5.4, Figures 5.10). 5Ni/H-Beta-25 as the most acidic catalyst produced the highest number of dimeric products (Figure 5.10h). As was expected, dimer production was not affected from the Ni@NiO average particle size. As a comparison, less than 10% menthol yield and high yield of byproducts being more than 40% were obtained at 24-100% citronellal conversion using Ni/ZSM-5 and natural zeolite supported Ni catalysts [378], even though the reaction conditions were very different from the current study being performed at 70 °C, 20 bar of H_2, for 7 h, and with the citronellal to catalyst mass ratio of 7 [378]. On the contrary, when the reaction was performed at a higher temperature of 200 °C and 20 of bar H_2 pressure, 50% menthol yield, 10% isopulegol yield, and 35% byproducts yield were achieved using Ni/NZB (acidified natural zeolite) catalyst [379].

From reaction mechanism point of view, it was significant to relate production of acyclic hydrogenation products vs cyclic products. For that aim, the sum of acyclic hydrogenation products (ACP) versus the sum of the desired cyclisation products (CP=IPs+MEs) was plotted in Figure 5.13.
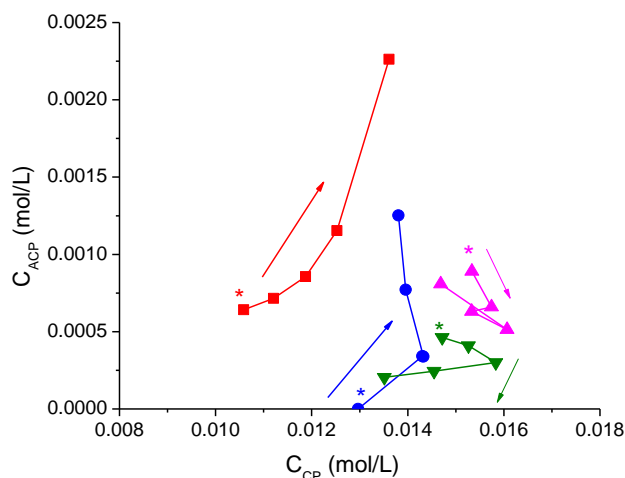
Figure 5.13. Sum of hydrogenation acyclic products concentrations (ACP) vs the sum of desired cyclization products concentrations (CP=IPs+MEs) at 80 °C, 20 bar total pressure in the presence of hydrogen for 15Ni/H-Beta-300 (■), 15Ni-H-Beta-25 (●), 10Ni/H-Beta-25 (▲), 5Ni/H-Beta-25 (▼), first point (, denoted reaction time 15 min).*

15Ni/H-Beta-300 with the highest loading of Ni loading and the mild acidity showed the increment of the concentration of both cyclic and acyclic products after 15 min of the reaction time and with enhancing the reaction time, more acyclic hydrogenation products were produced. Because of a mild acidity, cyclisation was not as significant as with the other catalysts. On the contrary, for

15Ni/H-Beta-25 catalyst, only cyclic products were formed in the first 15 min of the reaction, then acyclic hydrogenation products formation was started owing to cyclisation suppression. 10Ni/H-Beta-25 and 5Ni/H-Beta-25 formed the maximum cyclic products concentrations after 120 min and 60 min of the reaction, respectively. The highest concentrations of acyclic hydrogenation products were produced in the presence of 15Ni/H-Beta-300, which displayed the largest peak in H_2-TPR (Figure 5.4) and mild acidity (Table 5.3). Instead, the second highest ACP concentration was obtained over the catalyst with 15 nm Ni@NiO particles (Table 5.2) and medium acidity, whereas the smallest Ni@NiO particles, 2 nm, present in 5Ni/H-Beta-25 with the highest acidity among the studied Ni/H-Beta catalysts (Table 5.3) improved production of cyclisation products. These results slightly contradict the ones reported by Azkaar *et al*. [328], who suggested that highly acidic Ru catalyst increased ACP production.

5.3.3. Stability, regeneration and reuse of catalysts

Textural properties of the 15Ni/H-Beta-25 catalyst after the first and second catalytic run (Figure 5.14, Table 5.5), 5Ni/H-Beta-25, 10Ni/H-Beta-25 and 15Ni/H-Beta-300 after first run of the reaction (Figure A6, Table 5.5) confirm that fresh and spent catalysts displayed similar isotherms, and subsequently the texture of the catalysts was maintained upon the reaction.
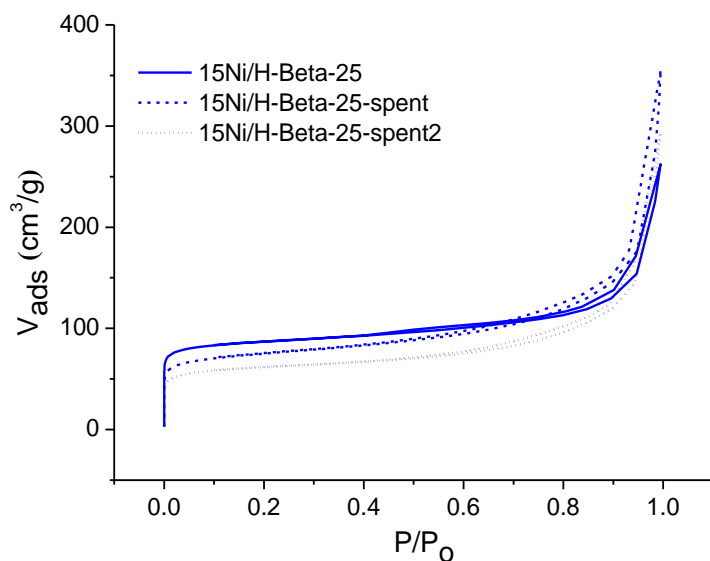
Figure 5.14. N_2 adsorption-desorption isotherms of fresh and spent 15Ni/H-Beta-25 after first and second run of the reaction.

Nevertheless, for all catalysts, a decrease of surface areas and the micropores volume was observed, whereas mesopores volume enhanced compared to the fresh ones (Table 5.1, Table 5.5). This might be due to the blockage of some catalytic pores with agglomerated Ni particles, polymeric solid byproducts, and by coke formation [328].

Table 5.5. *Textural properties (obtained from N_2 physisorption) for spent catalysts.*

Catalysts	S_{DR} [a] (m^2/g)	V_{micro} (cm^3/g)	V_{meso} (cm^3/g)
15Ni/H-Beta-300-spent	335	0.14	0.04
15Ni/H-Beta-25-spent	324	0.12	0.28
15Ni/H-Beta-25-spent2	266	0.10	0.25
10Ni/H-Beta-25-spent	422	0.16	0.37
5Ni/H-Beta-25-spent	339	0.13	0.33

a) Microporous or external surface area calculated by Dubinin-Radushkevich method (DR).

A comparison between the SEM image of the 15Ni/H-Beta-25-spent catalyst with that of the fresh one (Figure 5.15a, Figure 5.6) indicates that the Beta-zeolite morphology stayed almost unchanged after the reaction. In addition, TEM image of 15Ni/H-Beta-25-spent in Figure 5.15b displays that a slight agglomeration of Ni@NiO nano particles happened during the reaction enhancing the average Ni@NiO particle size from 15 nm to 18.4 nm and meanwhile particle dispersion decreased from ~7 to ~5.4%. More importantly, it seems that the fraction of Ni@NiO particles of size below 5 nm was very much decreased.
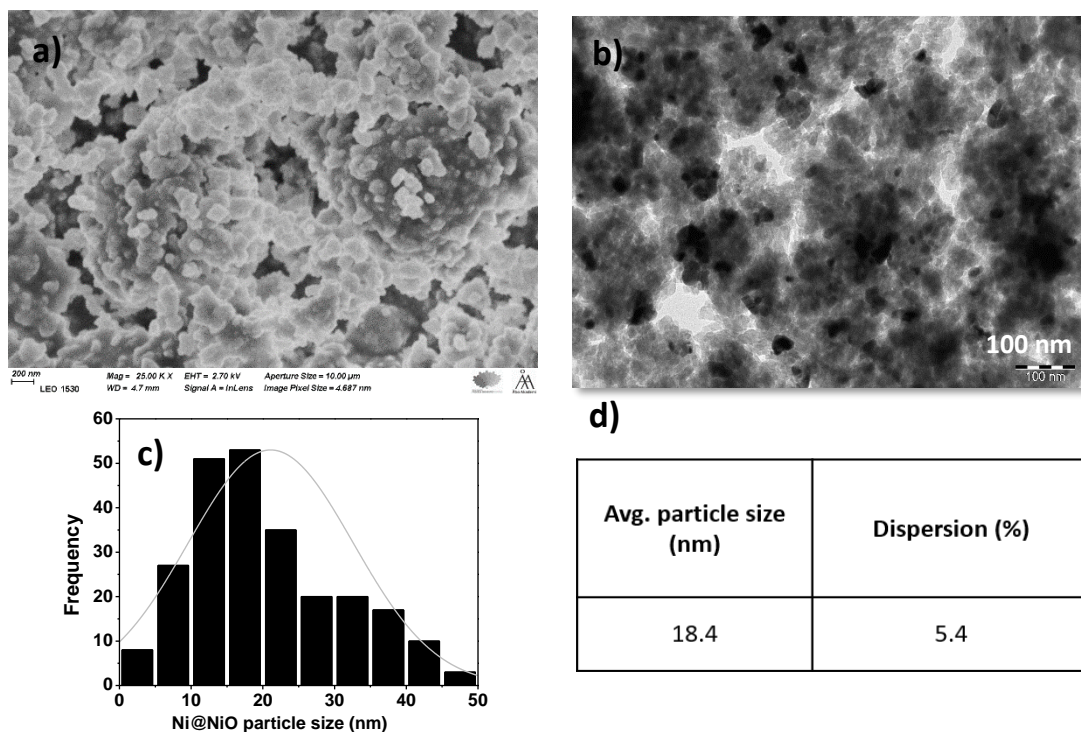
Figure 5.15. *a) SEM image, b) TEM image, c) Ni@NiO particle size distribution histograms, d)* average Ni@NiO particle size and dispersion determined from TEM images *for 15Ni/H-Beta-25-spent catalyst.*

Therefore, the characterization results suggested the textural and morphological features of the catalysts after the reaction were maintained. Thereafter, 15Ni/H-Beta-25 as the best catalyst was selected to study the recyclability of catalytic system. However, since minor leaching of Ni was detected from ICP-OES measurements, the spent 15Ni/H-Beta-25 catalyst was regenerated by a washing step cyclohexane as the reaction solvent followed by drying and reduction steps. Then, the regenerated catalyst was applied for the reactivity test and the results are reported in Figure 5.16. It can be demonstrated that very similar reactivity namely conversion, yields of pulegols and menthols, along with stereoselectivity to (±)-isopulegol and (±)-menthol were achieved in the second run of the reaction, being a promising achievement in the aspect of catalyst recyclability.
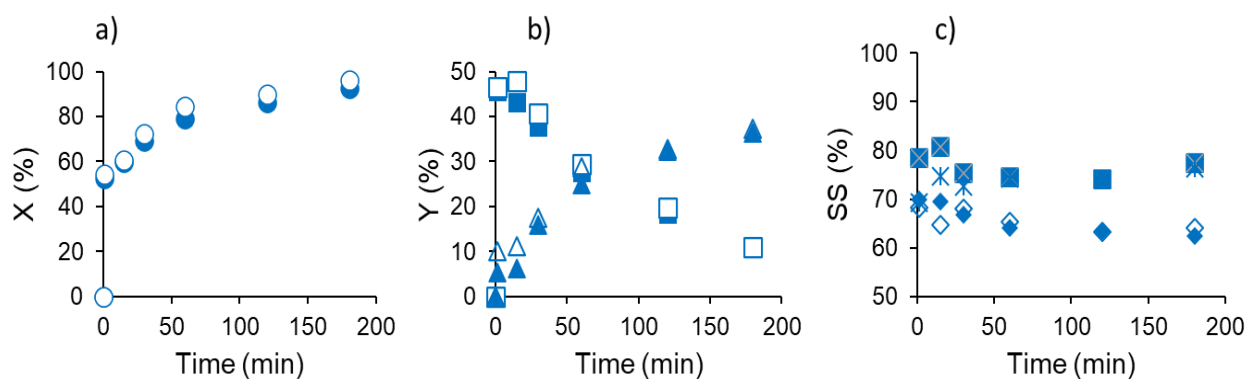
Figure 5.16. a) Conversion of citronellal, X (●, ○), b) yield of pulegols, Y_{Ps} (■, □) and yield of menthols, Y_{MEs} (▲, ∆), c) stereoselectivity to (±)-isopulegol (◆, ◇) and (±)-menthol (★, ✳) as a function of time in one-pot synthesis of menthol from citronellal over 15Ni/H-Beta-25. Symbols: fresh catalyst (filled symbol), regenerated catalyst (open symbol).

5.4. Conclusions

Ni/H-Beta catalysts with two different silica to alumina ratios (SiO_2/Al_2O_3= 25, 102) and thus acidic properties, and different Ni loadings of 5, 10 and 15 wt.% were synthesized and applied in the one-pot conversions of citronellal to menthol in a batch system. Different Ni loadings influenced the Ni@NiO particle size and dispersion and moreover H-Beta-25 acid sites accessibility. An appropriate synergy between Ni loading and dispersion, and H-Beta acidity was needed to handle the cascade reaction to (±)-menthol isomer as the main cyclic product and to limit undesired side reactions, such as dimerization of pulegols and citronellal, and acyclic hydrogenation. Among the tested catalysts, 15 wt.% Ni on H-Beta-25 displayed the best synergy of the total concentration of acid sites, Lewis to Brønsted acid sites ratio, and metal loading and dispersion. The reaction in the presence of 15 wt% Ni/H-Beta-25 caused 93% citronellal conversion with production of the highest yield of menthols being 36% (77% stereoselectivity to (±)-menthol isomer). Regeneration and recyclability of the best catalyst was efficient since the spent catalyst after washing with the cyclohexane and reduction exhibited a similar performance as the fresh one. Thus, the study of this chapter proposed a low-cost and sustainable catalyst with modified acid/metal bifunctionality which was promising and efficient for the one-pot selective transformation of citronellal to menthol.

Chapter 6. Concluding remarks

In this thesis, the formulation and modulation of applicable, sustainable and potentially scalable catalysts were studied for development of biomass valorization processes. In particular, two different fractions of lignocellulosic biomass were applied as the substrates of the model reactions. In first section, the transformation of carbohydrate fraction (glucose, cellulose) was studied to obtain levulinic acid and γ-Valerolactone as the target products. In the second part of the study, one-pot transformation of essential oil fraction (citronellal) of lignocellulosic biomass was investigated to achieve menthol as the target product. Hence, efficient heterogeneous catalysts were optimized for each proposed process.

In Chapter 2, glucose conversion to levulinic acid was studied over ZSM-5 based catalysts. The acid properties of NaZSM-5 zeolite were modulated via aqueous technique using NH_4Cl and $CuCl_2$ solutions and the microwave assisted ion-exchange method using solid salts of transition metals including $MnCl_2$, $FeCl_2$, $FeCl_3$, $CoCl_2$, $NiCl_2$, $CuCl_2$. Microwave was a more efficient ion-exchange method which could increase Lewis to Brønsted acid ratio, and weak and medium acid sites being favorable for the target reaction pathway from glucose to levulinic acid. In addition, Cu(II)-exchanged ZSM-5 gave the best reactivity compared to other transition metals which was affected from a higher charge transfer, and balanced and low density of acid site in this catalyst.

In Chapter 3, glucose and cellulose transformation to levulinic acid was investigated using a composite of CuZSM5-M zeolite and HMS mesoporous silica. The best result in the aspect of activity, selectivity and stability of the catalyst in both proposed reactions was obtained over the composite of 60% CuZSM5-M with HMS. The high performance of this catalyst was due to the combination of optimum and tailored concentration, strength and type of acid sites derived from CuZSM5-M for following the desired reaction pathway, and a high surface area, and large pores size derived from HMS for a facile mass transfer of the substrates, intermediates and products of the reaction.

In Chapter 4, bifunctional Ni,Al catalysts supported on activated biochars derived from four different biomasses (tannery shaving waste, vine wood waste, barley waste, and sargassums macroalgae) were assessed in levulinic acid conversion to γ-Valerolactone. Aluminum deposition

by precipitation method resulted in a different interaction of Al-containing species with support, a higher dispersion and a better improvement of weak and medium Lewis acid sites compared to Al impregnation technique which helped on a higher activity of the catalyst in levulinic acid dehydration step. The highest performances of the catalysts based on activated biochar from tannery shaving waste and vine wood waste were due to the presence of higher O-N-doped and functional groups in these supports, their high surface area and advanced porosity, and high dispersion of active phases. Therefore, it was found that the origin of initial biomass had a strong impact on the chemical, textural and morphological properties of the final support for the target catalytic application.

In Chapter 5, the correlation between the acid properties, metal loading, size and dispersion of Ni/H-Beta based catalysts with their performance in one-pot transformation of citronellal to menthol were investigated. The reaction over 15 wt.% Ni on H-Beta-25 exhibited the highest activity and selectivity to (±)-menthol due to the suitable synergy of the total concentration of acid sites, Lewis to Brønsted acid sites ratio, and Ni metal loading and dispersion.

In conclusion, it can be pointed that some significant criteria must be considered for the selection of a proper catalyst applicable in liquid phases reactions of biomass valorization process. First, a comprehensive knowledge about the mechanism of proposed reaction can give a precise viewpoint about the desired acidic, chemical, textural and morphological properties of the catalysts. Second, the reaction conditions, reaction medium, and hydrophobic/hydrophilic balance of the materials must be strongly considered in the design of an active, selective and stable catalyst. Indeed, it is highly applicable to tailor and modulate the properties of the catalyst by development of fruitful synthesis and post synthesis modification approaches.

Appendix

A1. Supplementary information of Chapter 2

Samples characterization techniques

The metals contents in ion-exchanged ZSM-5 samples were determined by microwave plasma–atomic emission spectrometry (Agilent Technology 4210 MP-AES). About 50 mg of the catalyst was digested with a mixture containing 5 mL of HCl (37%): HNO3(65%)= 3:1 and 5 mL of deionized water.After demineralization, dilutionto 50 mL was done using deionized water.

Fourier transform infrared (FTIR) analysis was performed by Perkin Elmer Spectrum One spectrometer with a wave number range of 400-4000 cm^{-1} and resolution of 4 cm^{-1} at room temperature.

X-ray powder diffraction (XRD) analyses were carried out in the laboratory of Prof. Giuseppe Cruciani at University of Ferrara by a Bruker D8 Advance Da Vinci diffractometer equipped with LynxEye detector and a sealed tube providing Cu Kα radiation at an accelerated voltage of 40 kV and an applied current of 30 mA.

Scanning Electron Microscope (SEM) was performed in the laboratory of Dc. Alessandro Di Michele at the University of Perugia. The images were obtained using a Field Emission Gun Electron Scanning Microscopy LEO 1525, after metallization with chromium. The images were acquired by Inlens detector while elemental composition was determined using Bruker Quantax Energy Dispersive System (EDS).

Thermal analyses (TG-DTA) were performed in the laboratory of Prof. Giuseppe Cruciani at University of Ferrara on a NETZSCH STA 409 PC/PG instrument in air flux (20 mL/min) using a temperature rate set at 5 °C/min in the 25–800 °C temperature range.

Specific surface areas and pore size distributions were evaluated from N_2 adsorption/desorption isotherms at -196 °C using a Tristar II Plus Micromeritics. Specific and micropores surface area were calculated using the BET and t-plot methods, respectively [380]. Micropores volume was calculated by t-plot method. Total pore volume was obtained at relative pressure of 0.99 and mesopores volume was calculated using Barrett-Joyner-Halenda (B.J.H) method.

Temperature-programmed Desorption (NH_3-TPD) analyses were performed via a lab-made equipment to investigate the strength and total acidity of the catalysts. First, 100 mg of the catalyst was charged in a quartz reactor and pretreated in He with a flow rate of 40 mL/min at 500 °C for 90 min. After cooling the system to 25 °C, the adsorption of 5% NH_3/He with a flow rate of 40 mL/min for 30 min was followed. The physisorbed ammonia was desorbed from the catalyst surface by passing He (40 mL/min) at 25°C for 10 min. The desorption profile of NH_3-TPD was recorded using a thermal conductivity detector (Gow-Mac TCD) from 25 to 1000 °C at a heating rate of 10 °C/min under 40 mL/min flow of He.

Brønsted and Lewis acid sites of the samples were analyzed in the laboratory of Prof. Giuseppina Cerrato in the University of Turin. The analyses were carried out by Fourier transform infrared (FTIR) spectra using 2,6-dimethylpyridine (2,6-DMP) as a probe molecule with a Bruker Vector 22 spectrometer equipped with a MCT detector at 2 cm^{-1} resolution and accumulating 128 scans. The solid samples, in form of self-supported pellets (~10 mg cm^{-2}), were inserted in a conventional quartz vacuum cell equipped with KBr windows connected to a glass vacuum line (residual pressure < 10^{-5} Torr) that allows to perform in situ adsorption/desorption runs. Prior to adsorption/desorption experiments of 2,6-dimethylpyridine (2,6-DMP), all samples were activated at 300 °C in an oxidizing atmosphere. 2,6-DMP adsorption/desorption tests were carried out at IR beam temperature (BT). First a relatively large amount of base (~ 4 Torr) was allowed on the samples and left in contact for 2 min in order to reach a complete 2,6-DMP monolayer formation, and then the 2,6-DMP excess was evacuated at BT for increasing times in the 1-15 min range in order to put into evidence only the more strongly held fraction.
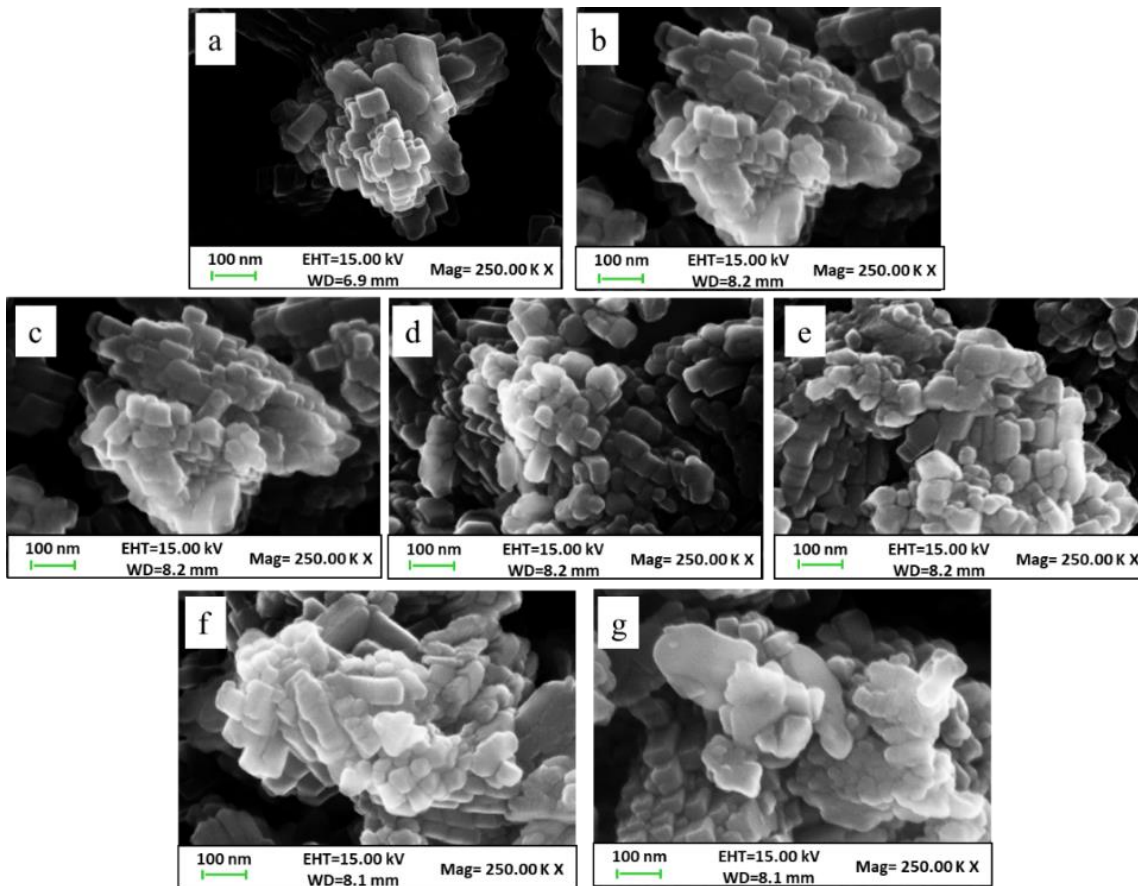
Characterization results

Figure A1. SEM images of a) CuZSM5-S, b) CuZSM5-M, c) NiZSM5-M, d) CoZSM5-M, e) Fe(II)ZSM5-M, f) Fe(III)ZSM5-M, g) MnZSM5-M
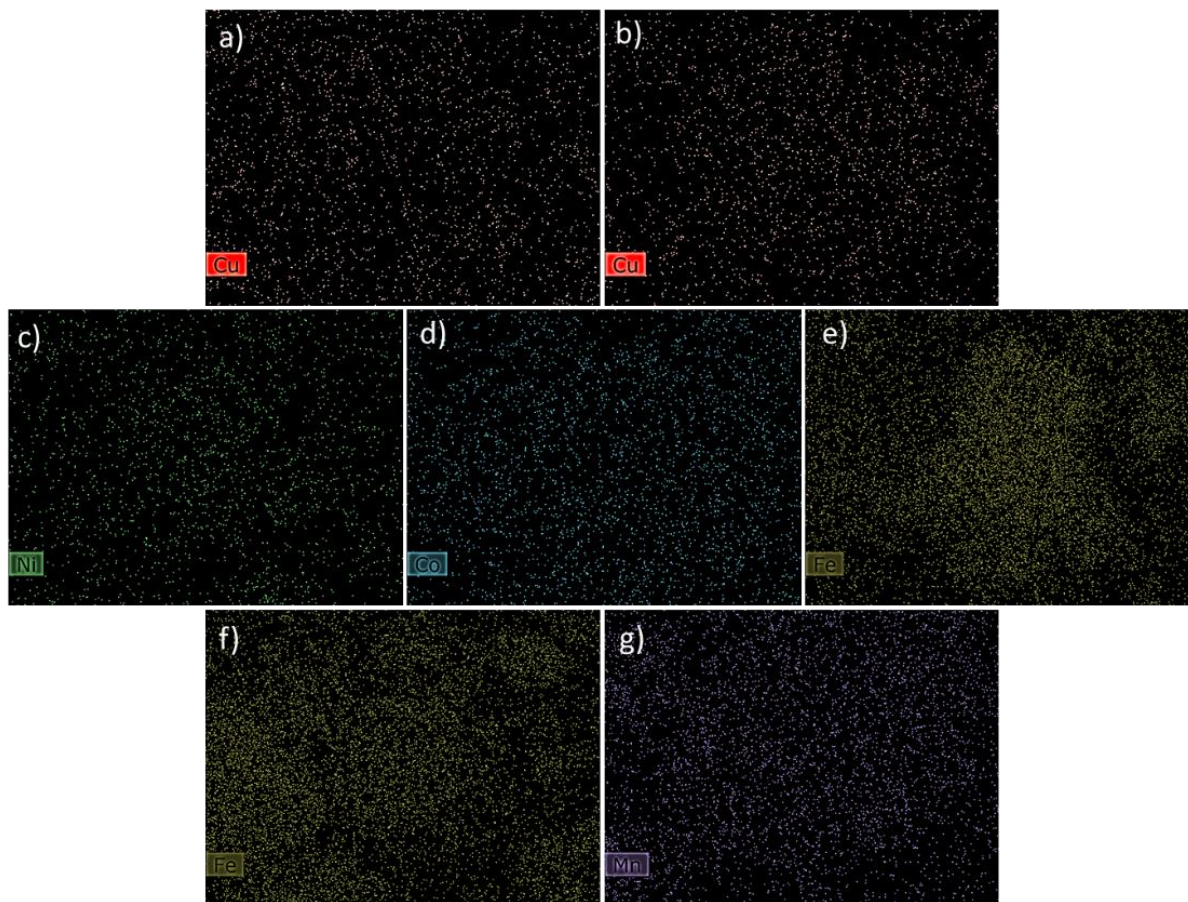
Figure A2. *EDS map of elements distribution for: a) CuZSM5-S, b) CuZSM5-M, c) NiZSM5-M, d) CoZSM5-M, e) Fe(II)ZSM5-M, f) Fe(III)ZSM5-M, g) MnZSM5-M.*

A2. Supplementary information of Chapter 3

Samples characterization techniques

Fourier transform infrared (FTIR) analyses were performed by Perkin Elmer Spectrum One spectrometer with a wave number range of 400-4000 cm^{-1} and resolution of 4 cm^{-1} at room temperature.

X-ray powder diffraction (XRD) analyses were carried out in the laboratory of Prof. Giuseppe Cruciani at University of Ferrara by a Bruker D8 Advance Da Vinci diffractometer equipped with LynxEye detector and a sealed tube providing Cu Kα radiation at an accelerated voltage of 40 kV and an applied current of 30 mA.

Scanning electron microscopies (SEM) were performed in the Åbo Akademi University of Turku (Finland) under the supervision of Prof. Dmitry Yu. Murzin. SEM images were obtained using a Field Emission Gun Electron Scanning Microscopy LEO 1525, after metallization with chromium. The images were acquired by Inlens detector while elemental composition was determined using Bruker Quantax EDS.

Transmission electron microscopies (TEM) were performed in the Åbo Akademi University of Turku (Finland) under the supervision of Prof. Dmitry Yu. Murzin. TEM images were used to determine the morphology of catalysts, periodic porous order of HMS, and the distributions of Cu nanoparticles on the composite. The instrument applied for the measurements was JEM-1400Plus, JEOL Ltd with an acceleration voltage of 120 kV and resolution of 0.98 nm using Quemsa II MPix bottom mounted digital camera. TEM was performed with a suspension of the gold catalyst in ethanol.

Specific surface areas and pore size distributions were evaluated from N_2 adsorption/desorption isotherms at -196 °C using a Tristar II Plus Micromeritics. Specific and micropores surface area were calculated using the BET and t-plot methods, respectively [380]. Micropores volume was calculated by t-plot method. Total pore volume was obtained at relative pressure of 0.99 and mesopores volume was calculated using Barrett-Joyner-Halenda (B.J.H) method.

Thermogravimetric analyses were carried out in the Åbo Akademi University of Turku (Finland) under the supervision of Prof. Dmitry Yu. Murzin. A TA Instruments SDT Q600 analyzer was

used for TGA analyses. The heating rate in the TGA was 10 °C/min from 25 °C to 700 °C under 100 cm^3/min flow of synthetic air. The weight of the sample was measured as a function of temperature.

Temperature-programmed Desorption (NH$_3$-TPD) analyses of samples were carried out using lab-made equipment in order to study the acidity of the catalysts. First, 100 mg of the catalyst was charged in a quartz reactor and degassed in He with a flow rate of 40 mL/min at 500 °C for 90 min. The catalyst was then cooled down to 25 °C prior to adsorption of ammonia. Then, the adsorption of 5% NH$_3$/He with a flow rate of 40 mL/min at 25 °C for 30 min was performed. The physisorbed ammonia was removed from the catalyst surface by passing He (40 mL/min) at 25°C for 10 min. The desorption profile of NH$_3$-TPD was recorded using a thermal conductivity detector (Gow-Mac TCD) from 25 to 1000 °C at a heating rate of 10 °C/min under the flow of He (40 mL/min).

Characterization of the Brønsted and Lewis acid sites, their amount and strength were done using pyridine (Sigma Aldrich, $\geq$ 99.5%) adsorption-desorption. This analysis was carried out in the Åbo Akademi University of Turku under supervision of Prof. Dmitry Yu. Murzin. The measurements were performed with ATI Mattson FTIR using 20 mg of catalyst pellets. The catalyst was activated in the IR cell by heating from room temperature to 200 °C under vacuum (1×10^{-4} Pa). In order to discriminate between weak, medium and strong acid sites, desorption of pyridine was performed at 150 °C, 250 °C and 350 °C, respectively. Pyridine was desorbed for 60 min at each temperature. Quantification of Brønsted and Lewis acid sites was done by considering intensity of IR signals at 1545 cm^{-1} and 1455 cm^{-1}, respectively, using the molar extinction factor given by Emeis [381].

A3. Supplementary information of Chapter 4

Samples characterization techniques

The CHNS elemental analyses of biomasses, biochars, and activated biochars were carried out using UNICUBE organic elemental analyzer (Elementar). Then, the amount of inorganic residues (ashes) was measured via the thermo-gravimetric analysis (TGA 8000 PerkinElmer) following the ASTM-D7582 protocol [382] The percentage of oxygen was calculated according to the equation below:

$$O\ (\%) = 100 - (C\% + H\% + N\% + S\% + ash\%)$$

The Ni content was determined by atomic absorption spectroscopy (AAS) after digestion of the samples (100 mg), using a Perkin-Elmer Analyst (Perkin-Elmer, Waltham, MA, USA) 100 spectrometer.

Fourier transform infrared (FTIR) analyses were performed by Perkin Elmer Spectrum One spectrometer with a wave number range of 400-4000 cm^{-1} and resolution of 4 cm^{-1} at room temperature.

X-ray powder diffraction (XRD) analyses were carried out in the laboratory of Prof. Giuseppe Cruciani at University of Ferrara by a Bruker D8 Advance Da Vinci diffractometer equipped with LynxEye detector and a sealed tube providing Cu Kα radiation at an accelerated voltage of 40 kV and an applied current of 30 mA. The determination of the Ni crystallite size was accomplished using the Rietveld method as implemented in the TOPAS v.5 program (Bruker AXS). The crystallite size was calculated as volume-weighted mean column heights based on integral breadths of peaks according to the Double-Voigt approach.

Scanning electron microscopies (SEM) were performed in the Åbo Akademi University of Turku (Finland) under the supervision of Prof. Dmitry Yu. Murzin. SEM images were obtained using a Field Emission Gun Electron Scanning Microscopy LEO 1525, after metallization with chromium. The images were acquired by Inlens detector while elemental composition was determined using Bruker Quantax EDS.

Transmission electron microscopies (TEM) were performed in the Åbo Akademi University of Turku (Finland) under the supervision of Prof. Dmitry Yu. Murzin. TEM images were used to

determine the morphology of biochar based supports, and the distributions of Ni nanoparticles and Al-containing nanostructures on the support. The instrument applied for the measurements was JEM-1400Plus, JEOL Ltd with an acceleration voltage of 120 kV and resolution of 0.98 nm using Quemsa II MPix bottom mounted digital camera. TEM was performed with a suspension of the gold catalyst in ethanol. ImageJ software was used to determine the particle size of Cu from TEM images.

Specific surface areas and pore size distributions were evaluated from N_2 adsorption/desorption isotherms at -196 °C using a Tristar II Plus Micromeritics. Micropores and total surface area were calculated using the t-plot and Langmuir methods, respectively [380]. Micropores volume was calculated by t-plot method. Total pore volume was obtained according to the adsorbed amount of N_2 and P/P_o values near 0.98.

Temperature-programmed Desorption (TPD) analyses of samples were carried out using a lab-made equipment in order to study the presence of oxygenate functional groups on the surface of carbon-based materials. First, 100 mg of the catalyst was charged in a quartz reactor and was heated up to 900 °C with the heating rate of 10 °C/min, under He with the flow of 40 mL/min. During heating procedure, the decomposition of oxygenated functional groups occurred by releasing CO and CO_2 gases which was recorded using a thermal conductivity detector (Gow-Mac 24-550 TCD instrument CO, Bethlehem, PA, USA).

Temperature-programmed Desorption (NH_3-TPD) analyses of samples were carried out using lab-made equipment in order to study the acidity of the catalysts. First, 100 mg of the catalyst was charged in a quartz reactor and degassed in He with a flow rate of 40 mL/min at 500 °C for 90 min. The catalyst was then cooled down to 25 °C prior to adsorption of ammonia. Then, the adsorption of 5% NH_3/He with a flow rate of 40 mL/min at 25 °C for 30 min was performed. The physisorbed ammonia was removed from the catalyst surface by passing He (40 mL/min) at 25°C for 10 min. The desorption profile of NH_3-TPD was recorded using a thermal conductivity detector (Gow-Mac TCD) from 25 to 1000 °C at a heating rate of 10 °C/min under the flow of He (40 mL/min).

Temperature-Program Reduction (TPR) of catalysts was performed using a lab-made instrument to study the reducibility and metal-support interaction of the catalysts. First, 100 mg of the sample was charged in a quartz reactor and the sample was heated from 25 °C to 800 °C, with a ramp of

10 °C/min, under 5 vol% H_2 in Ar with flow of 40 mL/min. The effluent gases were analyzed by a Micrometrics 2900 analyzer equipped with a TCD detector (Gow-Mac 24-550 TCD instrument CO, Bethlehem, PA, USA).
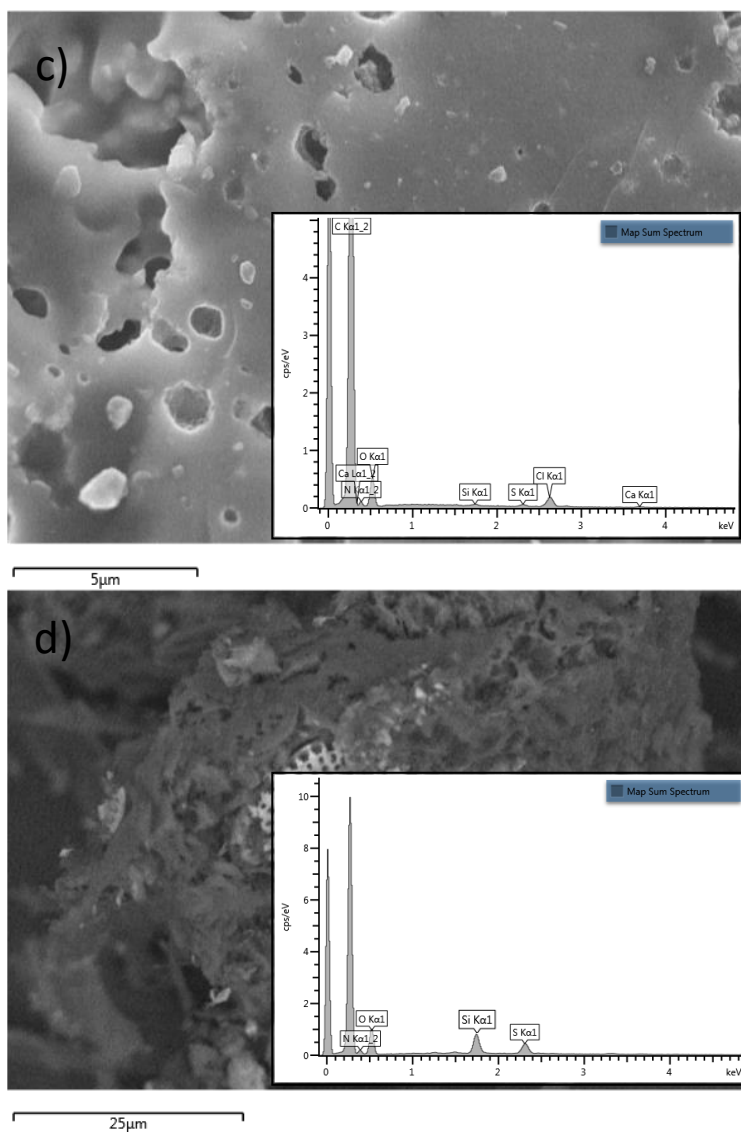
Characterization results
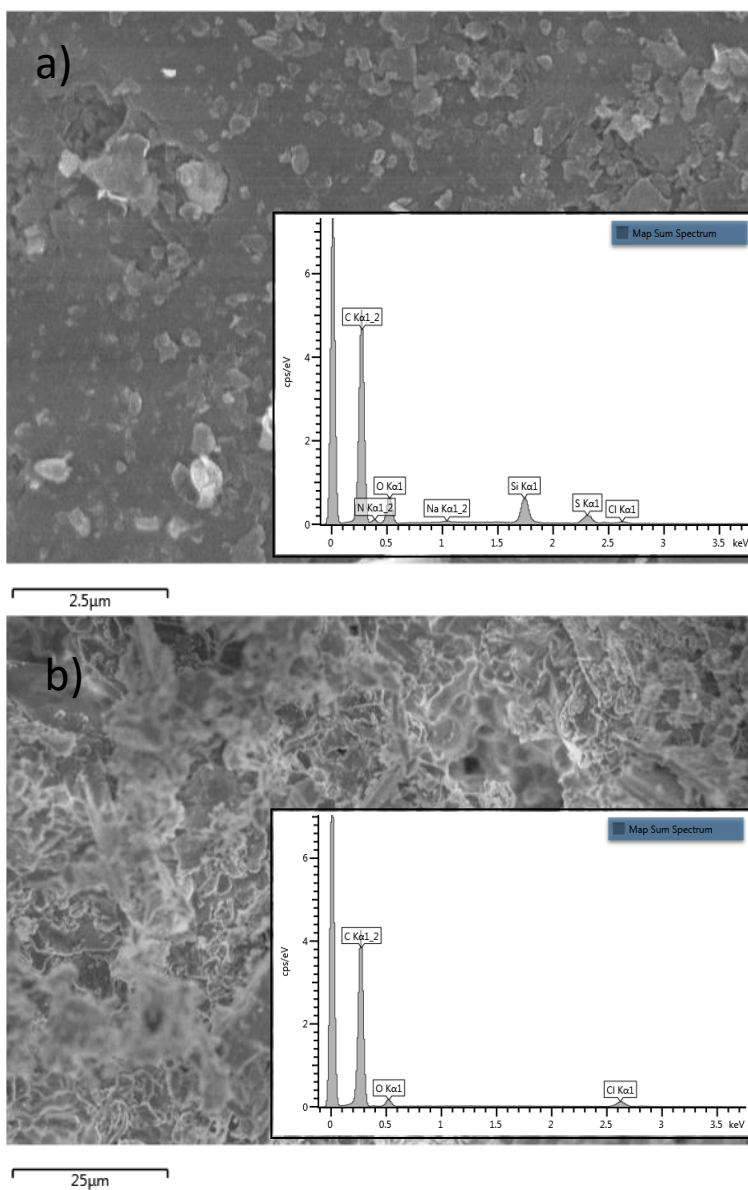
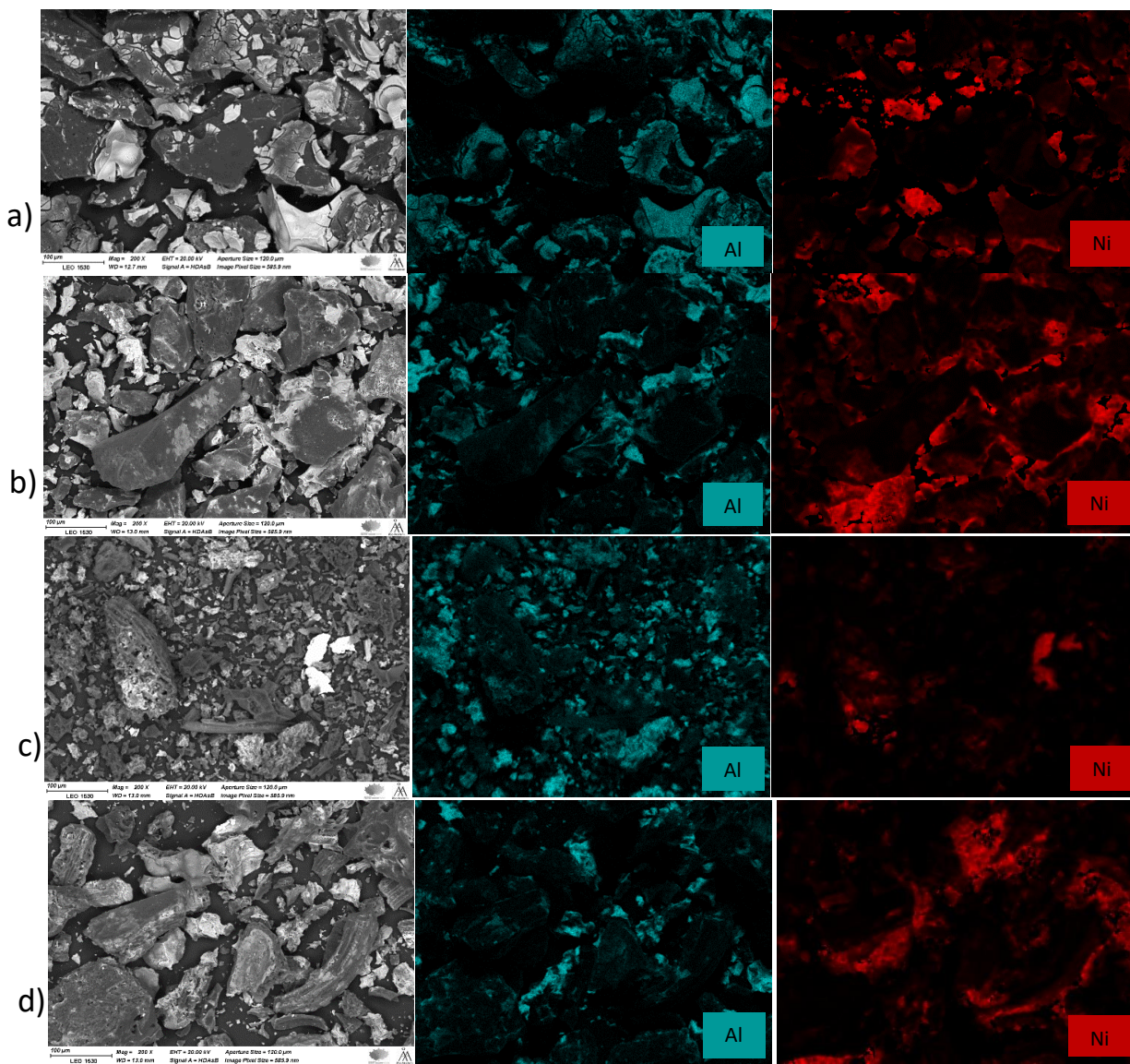*Figure A3*. EDS analysis of a) A_T, b) A_W , c) A_B, and d) A_A samples.

Figure A4. EDS elemental (Al, Ni) maps of a) NiAli/A$_T$, b)NiAlp/A$_T$, c) NiAlp/A$_W$, and d) NiAlp/A$_B$ catalysts,

A4. Supplementary information of Chapter 5

Samples characterization techniques

All characterizations except TPR were performed in the Åbo Akademi University of Turku (Finland) under the supervision of Prof. Dmitry Yu. Murzin.

The effective amount of Ni was analyzed by inductively couple plasma–optical emission spectrometry (ICP-OES, PerkinElmer Optima 5300 DV instrument). About 0.1 g of the catalyst was microwave digested with a mixture containing 9 mL of 37% HCl, 3 mL of 65% HNO_3 and 1 mL of 50% HBF_4. After digestion, dilution to 100 mL was done using distilled water.

The X-ray diffraction (XRD) characterization was performed using PANalytical Empyrean diffractometer with five axis goniometers. The incident beam optics consisted of Bragg-Brentano HD X-ray mirror, fixed ¼° divergence slit, 10 mm mask, 0.04 rad soller slit and 1 ° anti scatter slit. The diffracted beam optics consisted of 7.5 mm divergence slit, 0.04 rad soller slit and PIXcel detector array. The used X-ray tube was Empyrean Cu LFF. The X-ray radiation was filtered to include only Cu Kα1 and Cu Kα2 components. The results were analyzed with MAUD (Material Analysis Using Diffraction) analysis program [383]. Instrumental broadening was evaluated with Si standard sample. The results were obtained with $\theta - 2\theta$ scan range from 5 ° to 120 °.

Scanning Electron Microscopy (Zeiss Leo Gemini 1530) (SEM)was used to investigate the surface morphology and the shape of the fresh and spent catalysts. 10–15 mg of the catalyst was used for analysis on a thin film coated with activated carbon. SEM images were obtained by using an accelerating voltage of 2.7 kV with a working distance of 2–7 mm.

Transmission Electron Microscopy (TEM, Jeol JEM-14000 plus) was carried out to determine the Ni metal particle size distribution. ImageJ software was used to determine the particle size of Ni from TEM images.

Textural properties were studied by nitrogen physisorption (Micrometrics 3Flex-3500) at -196 °C. The specific surface area and porosity (pore volume, pore size distribution) were calculated using the Dubinin-Radushkevich (DR) and the density functional theory methods (DFT), respectively.

Temperature Programed Reduction (TPR) was carried out with a lab-made instrument under 5 vol% H_2 in Ar flow, which was heated from 25 °C to 800 °C with a ramp of 10 °C/min. The

effluent gases were analyzed by a Micrometrics TPDTPR 2900 analyzer equipped with a TCD detector (Gow-Mac 24-550 TCD instrument CO, Bethlehem, PA, USA).

Characterization of the Brønsted and Lewis acid sites, their amount and strength were performed using pyridine (Sigma Aldrich, ≥ 99.5%) adsorption-desorption with FTIR method. The analysis was carried out in the Åbo Akademi University of Turku under supervision of Prof. Dmitry Yu. Murzin. The measurements were performed with ATI Mattson FTIR using ca. 20 mg of the catalyst pellet. The catalyst was pretreated in the IR cell by heating from room temperature to 450 °C under vacuum (1×10^{-4} Pa). In order to discriminate between weak, medium and strong acid sites, desorption of pyridine was performed at 250 °C, 350 °C and 450 °C, respectively. Pyridine was desorbed for 60 min at each temperature and the spectra were taken at 100 °C. Quantification of Brønsted and Lewis acid sites was done by considering intensity of IR signals at 1545 cm^{-1} and 1455 cm^{-1}, respectively, using the molar extinction factor given by [381] .

Characterization results
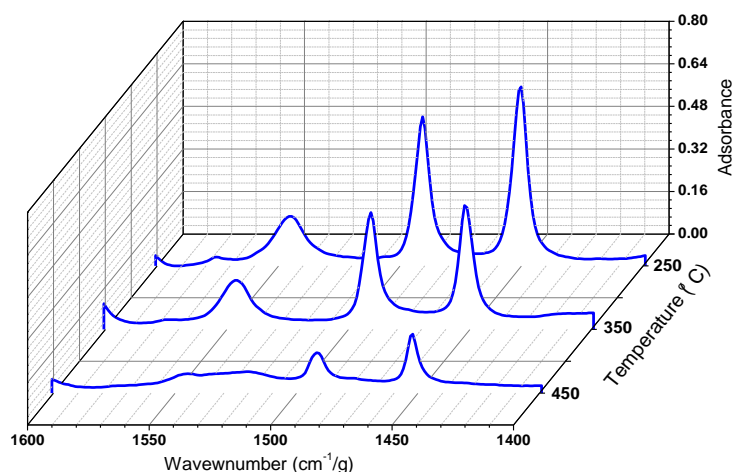
Figure A5. *FT-IR spectra of pyridine adsorption/desorption for 15Ni/H-Beta-25.*
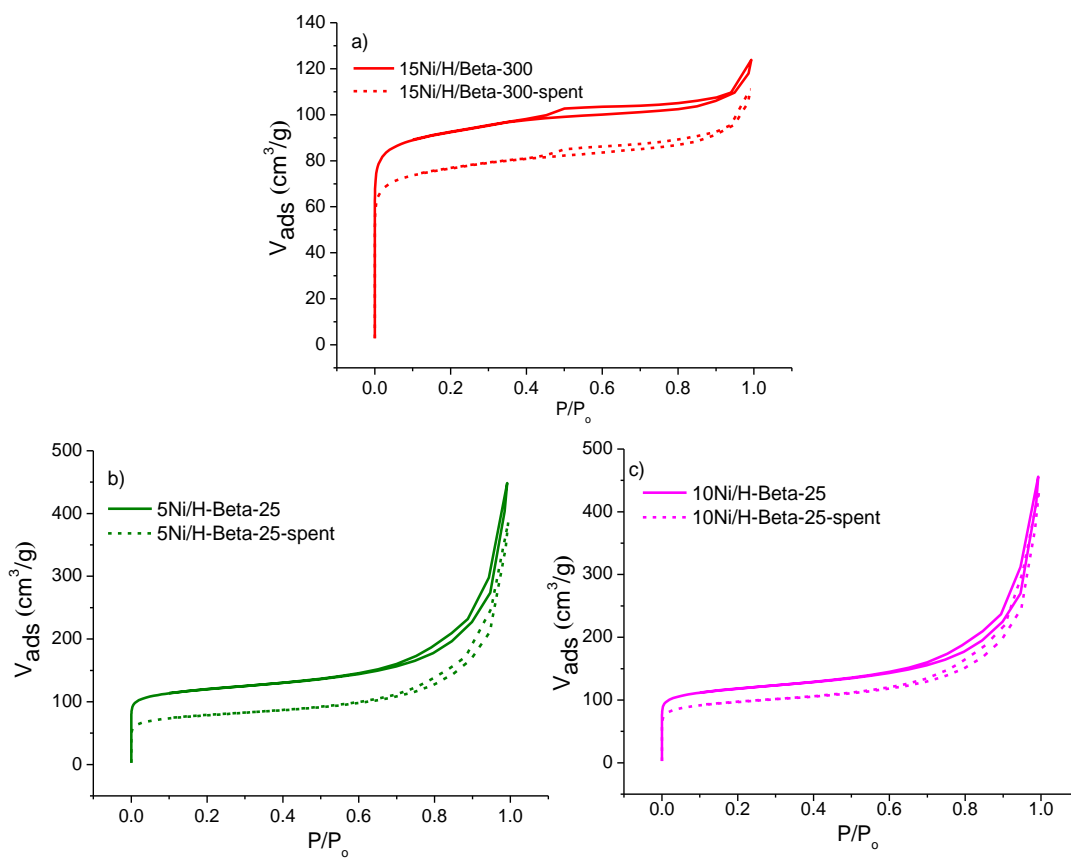
Figure A6. *N₂ adsorption-desorption isotherms of a) 15Ni/H-Beta-300 and 15Ni/H-Beta-300-spent, b) 5Ni/H-Beta-25 and 5Ni/H-Beta-25-spent, and c) 10Ni/H-Beta-25, 10Ni/H-Beta-25-spent.*

References

[1]   S. Abate, P. Lanzafame, S. Perathoner, G. Centi, la chimica e l'industria (2016) 32-36. Pdf available on-line: http://dx.medra.org/10.17374/CI.2016.98.2.32.

[2]   Technology Roadmap - Energy and GHG Reductions in the Chemical Industry via Catalytic Processes, IEA Technology report , June (2013). Report available on-line: https://www.iea.org/reports/technology-roadmap-energy-and-ghg-reductions-in-the-chemical-industry-via-catalytic-processes.

[3]   PA. Owusu, AA Sarkodie, Cogent Engineering 3 (2016) 1167990.

[4]   P.G. Levi, J.M. Cullen, Environmental Science and Technology 52 (2018) 1725–1734.

[5]   CO2 Emissions by Country, Accessed 2 May 2022. Available on-line: https://worldpopulationreview.com/country-rankings/co2-emissions-by-country.

[6]   COP26 summary report, November 2021. Pdf available on-line: https://www.ieta.org/resources/Resources/COP/COP26-Summary-Report.pdf.

[7]   J JK. Nørskov, B. Weckhuysen, G. Centi, I. Chorkendorff, R. Schl¨ogl, G. Marin, Energy-X (2019) 49–57.

[8]   Regulation (EU) 2018/842 of the European Parliamanet and the Council of 30 May 2018. Official Journal of the European Union (2018) 26–42. Available on-line: https://eur-lex.europa.eu/legal-content/EN/ALL/?uri=celex:32018R0842.

[9]   Total greenhouse gas emission trends and projections in Europe. Accessed 2 May 2022. Available on-line: https://www.eea.europa.eu/ims/total-greenhouse-gas-emission-trends.

[10] W. Strielkowski, L. Civín, E. Tarkhanova, M. Tvaronavičienė, Y. Petrenko, Energies 2021, 14 (2021) 8240.

[11] D. Gielen, F. Boshell, D. Saygin, M.D. Bazilian, N. Wagner, R. Gorini, Energy Strategy Reviews 24 (2019) 38–50.

[12] M. Kumar, A. Olajire Oyedun, A. Kumar, Renewable and Sustainable Energy Reviews 81 (2018) 1742–1770.

[13] R.E.H. Sims, A. Hastings, B. Schlamadinger, G. Taylor, P. Smith, Global Change Biology 12 (2006) 2054–2076.

[14] S. Nizamuddin, H.A. Baloch, G.J. Griffin, N.M. Mubarak, A.W. Bhutto, R. Abro, S.A. Mazari, B.S. Ali, Renewable and Sustainable Energy Reviews 73 (2017) 1289–1299.

[15] C. Wang, Z. Du, J. Pan, J. Li, Z. Yang, Journal of Analytical and Applied Pyrolysis 78 (2007) 438–444.

[16] J.J. Bozell, G.R. Petersen, Green Chemistry 12 (2010) 539–554.

[17] J.U. Hernández-Beltrán, I.O. Hernández-De Lira, M.M. Cruz-Santos, A. Saucedo-Luevanos, F. Hernández-Terán, N. Balagurusamy, Applied Sciences 2019, Vol. 9, Page 3721 9 (2019) 3721.

[18] L. Hu, L. Lin, Z. Wu, S. Zhou, S. Liu, Applied Catalysis B: Environmental 174–175 (2015) 225–243.

[19] H.B. Goyal, D. Seal, R.C. Saxena, Renewable and Sustainable Energy Reviews 12 (2008) 504–517.

[20] M. Stöcker, M. Stöcker, Angewandte Chemie International Edition 47 (2008) 9200–9211.

[21] R.J. Moon, A. Martini, J. Nairn, J. Simonsen, J. Youngblood, Chemical Society Reviews 40 (2011) 3941–3994.

[22] P.L. Dhepe, A. Fukuoka, ChemSusChem 1 (2008) 969–975.

[23] P. McKendry, Bioresource Technology 83 (2002) 37–46.

[24] R.C. Saxena, D.K. Adhikari, H.B. Goyal, Renewable and Sustainable Energy Reviews 13 (2009) 167–178.

[25] D. Mohan, C.U. Pittman, P.H. Steele, Energy and Fuels 20 (2006) 848–889.

[26] F. Hu, A. Ragauskas, Bioenergy Research 5 (2012) 1043–1066.

[27] S.K. Maity, Renewable and Sustainable Energy Reviews 43 (2015) 1427–1445.

[28] A. Pattiya, Direct Thermochemical Liquefaction for Energy Applications (2018) 3–28.

[29] P. Ning, G. Yang, L. Hu, J. Sun, L. Shi, Y. Zhou, Z. Wang, J. Yang, Biotechnology for Biofuels 14 (2021) 1–22.

[30] A. Naser, M. Ahsanul, H. Rechana, R.M. Naebe, Cellulose 25 (1965) 5455–5477.

[31] O. Norouzi, S. Taghavi, P. Arku, S. Jafarian, M. Signoretto, A. Dutta, Journal of Analytical and Applied Pyrolysis 158 (2021) 105280.

[32] A. Molino, S. Chianese, D. Musmarra, Journal of Energy Chemistry 25 (2016) 10–25.

[33] A. Demirbaş, Energy Conversion and Management 41 (2000) 633–646.

[34] R. Rinaldi, F. Schüth, ChemSusChem 2 (2009) 1096–1107.

[35] M. Caliceti, E. Argese, A. Sfriso, B. Pavoni, Chemosphere 47 (2002) 443–454.

[36] E. Ghedini, S. Taghavi, F. Menegazzo, M. Signoretto, Sustainability 13 (2021) 10479.

[37] J.C. Serrano-Ruiz, R. Luque, J.H. Clark, The Role of Catalysis for the Sustainable Production of Bio-Fuels and Bio-Chemicals (2013) 557–576.

[38] A. Morone, M. Apte, R.A. Pandey, Renewable and Sustainable Energy Reviews 51 (2015) 548–565.

[39] T. Werpy, G. Petersen, Top Value Added Chemicals from Biomass Volume I—Results of Screening for Potential Candidates from Sugars and Synthesis Gas, US Departent of Energy, (2004) 1-67.

[40] S.G. Wettstein, D. Martin Alonso, E.I. Gürbüz, J.A. Dumesic, Current Opinion in Chemical Engineering 1 (2012) 218–224.

[41] P. Dagaut, C. Togbé, Fuel 89 (2010) 280–286.

[42] J.P. Lange, R. Price, P.M. Ayoub, J. Louis, L. Petrus, L. Clarke, H. Gosselink, Angewandte Chemie International Edition 49 (2010) 4479–4483.

[43] W. Luo, U. Deka, A.M. Beale, E.R.H. van Eck, P.C.A. Bruijnincx, B.M. Weckhuysen, Journal of Catalysis 301 (2013) 175–186.

[44] C.E. Chan-Thaw, M. Marelli, R. Psaro, N. Ravasio, F. Zaccheria, RSC Advances 3 (2013) 1302–1306.

[45] J.J. Bozell, Science 329(5991) (2010) 522-523.

[46] T. Pan, J. Deng, Q. Xu, Y. Xu, Q.X. Guo, Y. Fu, Green Chemistry 15 (2013) 2967–2974.

[47] A.D. Dwivedi, K. Gupta, D. Tyagi, R.K. Rai, S.M. Mobin, S.K. Singh, ChemCatChem 7 (2015) 4050–4058.

[48] Z.P. Yan, L. Lin, S. Liu, Energy and Fuels 23 (2009) 3853–3858.

[49] S. Song, S. Yao, J. Cao, L. Di, G. Wu, N. Guan, L. Li, Applied Catalysis B: Environmental 217 (2017) 115–124.

[50] S. Kang, J. Yu, Industrial and Engineering Chemistry Research 54 (2015) 11552–11559.

[51] B.C. Windom, T.M. Lovestead, M. Mascal, E.B. Nikitin, T.J. Bruno, Energy and Fuels 25 (2011) 1878–1890.

[52] B. Girisuta, Levulinic acid from lignocellulosic biomass, PhD thesis, University of Groningen, (2007).

[53] F.D. Pileidis, M.M. Titirici, ChemSusChem 9 (2016) 562–582.

[54] L. Axelsson, M. Franzén, M. Ostwald, G. Berndes, G. Lakshmi, N.H. Ravindranath, Biofuels, Bioproducts and Biorefining 6 (2012) 246–256.

[55] S. Roy Goswami, M.J. Dumont, V. Raghavan, Starch - Stärke 68 (2016) 274–286.

[56] K. Yan, C. Jarvis, J. Gu, Y. Yan, Renewable and Sustainable Energy Reviews 51 (2015) 986–997.

[57] J.J. Martínez, L. Silva, H.A. Rojas, G.P. Romanelli, L.A. Santos, T.C. Ramalho, M.H. Brijaldo, F.B. Passos, Catalysis Today 296 (2017) 118–126.

[58] D. He, I.T. Horváth, Journal of Organometallic Chemistry 847 (2017) 263–269.

[59] GFBiochemicals. Accessed 2 May 2022. Available on-line: http://www.gfbiochemicals.com/company/.

[60] Levulinic Acid Market Size, Industry Trends, Growth and Forecast to 2020-2030. Accessed 2 May 2022. Available one-line: https://www.psmarketresearch.com/market-analysis/levulinic-acid-market.

[61] B. Kamm, M. Kamm, P.R. Gruber, S. Kromus, Handbook of Waste Management and Co-Product Recovery in Food Processing 2 (2009) 479-514.

[62] R.H. Leonard, Industrial and Engineering Chemistry 48 (1956) 1330–1341.

[63] M. Signoretto, S. Taghavi, E. Ghedini, F. Menegazzo, Molecules 24 (2019) 2760.

[64] A.J. Ragauskas, C.K. Williams, B.H. Davison, G. Britovsek, J. Cairney, C.A. Eckert, W.J. Frederick, J.P. Hallett, D.J. Leak, C.L. Liotta, J.R. Mielenz, R. Murphy, R. Templer, T. Tschaplinski, Science 311 (2006) 484–489.

[65] S. Kang, J. Fu, G. Zhang, Renewable and Sustainable Energy Reviews 94 (2018) 340–362.

[66] T. Dallas Swift, H. Nguyen, A. Anderko, V. Nikolakis, D.G. Vlachos, Green Chemistry 17 (2015) 4725–4735.

[67] T.D. Swift, H. Nguyen, Z. Erdman, J.S. Kruger, V. Nikolakis, D.G. Vlachos, Journal of Catalysis 333 (2016) 149–161.

[68] L. Hu, G. Zhao, W. Hao, X. Tang, Y. Sun, L. Lin, S. Liu, RSC Advances 2 (2012) 11184–11206.

[69] P. Daorattanachai, P. Khemthong, N. Viriya-Empikul, N. Laosiripojana, K. Faungnawakij, Carbohydrate Research 363 (2012) 58–61.

[70] M. Watanabe, Y. Aizawa, T. Iida, R. Nishimura, H. Inomata, Applied Catalysis A: General 295 (2005) 150–156.

[71] X. Qi, M. Watanabe, T.M. Aida, R.L. Smith, Catalysis Communications 9 (2008) 2244–2249.

[72] P.M. Grande, C. Bergs, P. Domíngue De María, ChemSusChem 5 (2012) 1203–1206.

[73] L. Yang, G. Tsilomelekis, S. Caratzoulas, D.G. Vlachos, ChemSusChem 8 (2015) 1334–1341.

[74] S.S. Chen, T. Maneerung, D.C.W. Tsang, Y.S. Ok, C.H. Wang, Chemical Engineering Journal 328 (2017) 246–273.

[75] R.S. Assary, P.C. Redfern, J.R. Hammond, J. Greeley, L.A. Curtiss, Journal of Physical Chemistry B 114 (2010) 9002–9009.

[76] K. Lappalainen, N. Vogeler, J. Kärkkäinen, Y. Dong, M. Niemelä, A. Rusanen, A.L. Ruotsalainen, P. Wäli, A. Markkola, U. Lassi, Biomass Conversion and Biorefinery 8 (2018) 965–970.

[77] A. Mukherjee, M.J. Dumont, V. Raghavan, Biomass and Bioenergy 72 (2015) 143–183.

[78] H. Heeres, R. Handana, D. Chunai, C. Borromeus Rasrendra, B. Girisuta, H. Jan Heeres, Green Chemistry 11 (2009) 1247–1255.

[79] L. Peng, L. Lin, J. Zhang, J. Zhuang, B. Zhang, Y. Gong, Molecules 15 (2010) 5258–5272.

[80] Á. Szabolcs, M. Molnár, G. Dibó, L.T. Mika, Green Chemistry 15 (2013) 439–445.

[81] G.W. Huber, S. Iborra, A. Corma, Chemical Reviews 106 (2006) 4044–4098.

[82] T. Ennaert, J. van Aelst, J. Dijkmans, R. de Clercq, W. Schutyser, M. Dusselier, D. Verboekend, B.F. Sels, Chemical Society Reviews 45 (2016) 584–611.

[83] F. Guo, Z. Fang, C.C. Xu, R.L. Smith, Progress in Energy and Combustion Science 38 (2012) 672–690.

[84] E. Lam, J.H.T. Luong, ACS Catalysis 4 (2014) 3393–3410.

[85] C. Pizzolitto, E. Ghedini, F. Menegazzo, M. Signoretto, A. Giordana, G. Cerrato, G. Cruciani, Catalysis Today 345 (2020) 183–189.

[86] S. Taghavi, E. Ghedini, F. Menegazzo, M. Signoretto, D. Gazzoli, D. Pietrogiacomi, A. Matayeva, A. Fasolini, A. Vaccari, F. Basile, G. Fornasari, Processes 8 (2020) 843.

[87] C. Pizzolitto, E. Ghedini, S. Taghavi, F. Menegazzo, G. Cruciani, M. Peurla, K. Eränen, I. Heinmaa, A. Aho, N. Kumar, D.Y. Murzin, T. Salmi, M. Signoretto, Microporous and Mesoporous Materials 328 (2021) 111459.

[88] R. Weingarten, W.C. Conner, G.W. Huber, Energy & Environmental Science 5 (2012) 7559–7574.

[89] W. Zeng, D.G. Cheng, F. Chen, X. Zhan, Catalysis Letters 133 (2009) 221–226.

[90] M. Zendehdel, A. Mobinikhaledi, A. Asgari, Journal of Inclusion Phenomena and Macrocyclic Chemistry 60 (2008) 353–357.

[91] J. Jae, G.A. Tompsett, A.J. Foster, K.D. Hammond, S.M. Auerbach, R.F. Lobo, G.W. Huber, Journal of Catalysis 279 (2011) 257–268.

[92] W. Zeng, D.G. Cheng, H. Zhang, F. Chen, X. Zhan, Reaction Kinetics, Mechanisms and Catalysis 100 (2010) 377–384.

[93] T.C. Acharjee, Y.Y. Lee, Environmental Progress & Sustainable Energy 37 (2018) 471–480.

[94] D. Garcés, L. Faba, E. Díaz, S. Ordóñez, ChemSusChem 12 (2019) 924–934.

[95] W. Zeng, D.G. Cheng, H. Zhang, F. Chen, X. Zhan, Reaction Kinetics, Mechanisms and Catalysis 100 (2010) 377–384.

[96] H. Zhang, L. Han, A. Duan, C. Xu, Z. Zhao, Y. Wei, G. Jiang, J. Liu, D. Wang, Z. Xia, RSC Advances 7 (2017) 28038–28047.

[97] D. Garcés, L. Faba, E. Díaz, S. Ordóñez, ChemSusChem 12 (2019) 924–934.

[98] T.C. Acharjee, Y.Y. Lee, Environmental Progress & Sustainable Energy 37 (2018) 471–480.

[99] L. Zoubida, B. Hichem, Nanocrystals and Nanostructures, Chapter 3 (2018) 44-56.

[100] M. Zendehdel, N.F. Far, Z. Gaykani, Journal of Inclusion Phenomena 53 (2005) 47–49.

[101] Y. Chu, X. Yi, C. Li, X. Sun, A. Zheng, Chemical Science 9 (2018) 6470–6479.

[102] Z. Wang, L. Wang, Y. Jiang, M. Hunger, J. Huang, ACS Catalysis 4 (2014) 1144–1147.

[103] M. Zendehdel, G. Cruciani, M. Dondi, Journal of Porous Materials 19 (2012) 361–368.

[104] M. Zendehdel, A. Mobinikhaledi, F. Hasanvand Jamshidi, Journal of Inclusion Phenomena and Macrocyclic Chemistry 59 (2007) 41–44.

[105] O. Mazaheri, R.J. Kalbasi, RSC Advances 5 (2015) 34398–34414.

[106] M. Zendehdel, A. Mobinikhaledi, F. Hasanvand Jamshidi, Journal of Inclusion Phenomena and Macrocyclic Chemistry 59 (2007) 41–44.

[107] Z. Wan, W. Wu, W. Chen, H. Yang, D. Zhang, Industrial and Engineering Chemistry Research 53 (2014) 19471–19478.

[108] K.A. Tarach, K. Pyra, K. Góra-Marek, J. Datka, W. Mozgawa, D. Rutkowska-Zbik, Molecules 25 (2020) 2878.

[109] E. Díaz, S. Ordóñez, A. Vega, J. Coca, Applied Catalysis B: Environmental 56 (2005) 313–322.

[110] T. Fu, J. Chang, J. Shao, Z. Li, Journal of Energy Chemistry 26 (2017) 139–146.

[111] H. Zhang, L. Han, A. Duan, C. Xu, Z. Zhao, Y. Wei, G. Jiang, J. Liu, D. Wang, Z. Xia, RSC Advances 7 (2017) 28038–28047.

[112] A. Fahmy, K.S. El-Nasser, I.O. Ali, T.M. Salama, K. Altmann, J. Friedrich, Journal of Adhesion Science and Technology 31 (2017) 2641–2656.

[113] M. Gotić, S. Musić, Journal of Molecular Structure 834–836 (2007) 445–453.

[114] A. Sahai, N. Goswami, S.D. Kaushik, S. Tripathi, Applied Surface Science 390 (2016) 974–983.

[115] D. Manyasree, P. Kiranmayi, V. Kolli, Indo American Journal of Pharmaceutical Research 8 (2019) 1852.

[116] M. Veneranda, J. Aramendia, L. Bellot-Gurlet, P. Colomban, K. Castro, J.M. Madariaga, Corrosion Science 133 (2018) 68–77.

[117] H. Cai, Q. Wei, H. Xiao, H. Liu, J. Wang, Journal of Materials Science: Materials in Electronics 31 (2020) 7606–7615.

[118] C. Stella, N. Soundararajan, K. Ramachandran, Superlattices and Microstructures 71 (2014) 203–210.

[119] Z. Zhu, Z. Liu, S. Liu, H. Niu, Applied Catalysis B: Environmental 30 (2001) 267–276.

[120] M. Hamidzadeh, M. Ghassemzadeh, A. Tarlani, S.S. Far, Oriental Journal of Chemistry 32 (2016) 481–490.

[121] R. Karimi, B. Bayati, N. Charchi Aghdam, M. Ejtemaee, A.A. Babaluo, Powder Technology 229 (2012) 229–236.

[122] Y.M. Zhukov, A.Y. Efimov, M.G. Shelyapina, V. Petranovskii, E. v. Zhizhin, A. Burovikhina, I.A. Zvereva, Microporous and Mesoporous Materials 224 (2016) 415–419.

[123] D. He, H. Zhang, Y. Yan, Royal Society Open Science 5 (2018).

[124] A. V. Vorotyntsev, A.N. Petukhov, I. V. Vorotyntsev, T.S. Sazanova, M.M. Trubyanov, I.Y. Kopersak, E.N. Razov, V.M. Vorotyntsev, Applied Catalysis B: Environmental 198 (2016) 334–346.

[125] J.C. Xing, Y.L. Zhu, Q.J. Jiao, Journal of New Materials for Electrochemical Systems 17 (2014) 209–211.

[126] F.A. Ibrahim, Silicon 10 (2017) 131–136.

[127] M. Moreno-Recio, J. Santamaría-González, P. Maireles-Torres, Chemical Engineering Journal 303 (2016) 22–30.

[128] Y. Chen, S. Cong, Q. Wang, H. Han, J. Lu, Y. Kang, W. Kang, H. Wang, S. Han, H. Song, J. Zhang, Journal of Hazardous Materials 349 (2018) 18–26.

[129] R. Sakai, K. Murakami, Y. Mizutani, Y. Tanaka, S. Hayashi, A. Ishikawa, T. Higo, S. Ogo, H. Tsuneki, H. Nakai, Y. Sekine, ACS Omega 5 (2020) 6846–6851.

[130] E.F. Mohamed, G. Awad, H. Zaitan, C. Andriantsiferana, M.H. Manero, Environmental Technology (2017) 878–886.

[131] S. Kumar, S. Rayalu, N. Russo, G.S. Kanade, H. Kusaba, Y. Teraoka, N. Labhsetwar, Catalysis Letters 132 (2009) 248–252.

[132] L. Giraldo, G. Camargo, J. Tirano, J.C. Moreno-Piraján, E-Journal of Chemistry 7(2010) 1138-1147.

[133] T.R.D. Mendonça, J.R. Santos, L.R.A. Sarmento, D.C.M. Silva, O.M.S. Cysneiros, A.O.S. Silva, Cerâmica 65 (2019) 378–387.

[134] J.K. Geon, S.A. Wha, Applied Catalysis 71 (1991) 55–68.

[135] X.L. Seoane, A. Arcoya, J.A. González, N. Travieso, Journal of Materials Science 26 (1991) 172–176.

[136] T.D. Swift, C. Bagia, V. Choudhary, G. Peklaris, V. Nikolakis, D.G. Vlachos, ACS Catalysis 4 (2014) 259–267.

[137] J. Ahlkvist, J. Wärnå, T. Salmi, J.P. Mikkola, Reaction Kinetics, Mechanisms and Catalysis 119 (2016) 415–427.

[138] H. Jouini, I. Mejri, C. Petitto, J. Martinez-Ortigosa, A. Vidal-Moya, M. Mhamdi, T. Blasco, G. Delahay, Microporous and Mesoporous Materials 260 (2018) 217–226.

[139] N.Y. Topsøe, K. Pedersen, E.G. Derouane, Journal of Catalysis 70 (1981) 41–52.

[140] V.P.S. Caldeira, A.G.D. Santos, S.B.C. Pergher, M.J.F. Costa, A.S. Araujo, Quim. Nova 39 (2016) 292–297.

[141] H. Jouini, I. Mejri, C. Petitto, J. Martinez-Ortigosa, A. Vidal-Moya, M. Mhamdi, T. Blasco, G. Delahay, Microporous and Mesoporous Materials 260 (2018) 217–226.

[142] C. Bernardon, M. ben Osman, G. Laugel, B. Louis, P. Pale, Comptes Rendus Chimie 20 (2017) 20–29.

[143] X. Han, K. Ouyang, C. Xiong, X. Tang, Q. Chen, K. Wang, L.L. Liu, C. te Hung, S. bin Liu, Applied Catalysis A: General 543 (2017) 115–124.

[144] T. Onfroy, G. Clet, M. Houalla, Microporous and Mesoporous Materials 82 (2005) 99–104.

[145] C. Pizzolitto, E. Ghedini, F. Menegazzo, M. Signoretto, A. Giordana, G. Cerrato, G. Cruciani, Catalysis Today 345 (2020) 183–189.

[146] G.L. Woolery, G.H. Kuehl, Zeolites 19 (1997) 288–296.

[147] S. Taghavi, E. Ghedini, F. Menegazzo, A. Giordana, G. Cerrato, G. Cruciani, A. Di Michele, M. Zendehdel, M. Signoretto, Biomass Conversion and Biorefinery (2022) 1-9.

[148] T. Yumura, H. Yamashita, H. Torigoe, H. Kobayashi, Y. Kuroda, Physical Chemistry Chemical Physics 12 (2010) 2392–2400.

[149] L. Martins, R.P.S. Peguin, E.A. Urquieta-González, Química Nova 29 (2006) 223–229.

[150] A.J. McCue, G.A. Mutch, A.I. McNab, S. Campbell, J.A. Anderson, Catalysis Today 259 (2016) 19–26.

[151] R. Otomo, T. Yokoi, J.N. Kondo, T. Tatsumi, Applied Catalysis A: General 470 (2014) 318–326.

[152] T.D. Swift, H. Nguyen, Z. Erdman, J.S. Kruger, V. Nikolakis, D.G. Vlachos, Journal of Catalysis 333 (2016) 149–161.

[153] U. Lohse, R. Bertram, K. Jancke, I. Kurzawski, B. Parlitz, E. Löuffler, E. Schreier, Journal of the Chemical Society, Faraday Transactions 91 (1995) 1163–1172.

[154] M. Salciccioli, M. Stamatakis, S. Caratzoulas, D.G. Vlachos, Chemical Engineering Science 66 (2011) 4319–4355.

[155] Charge Densities of Selected Ions, appendix 2. Pdf available on-line: https://bcs.whfreeman.com/WebPub/Chemistry/raynercanham6e/Appendices/Rayner-Canham%205e%20Appendix%202%20-%20Charge%20Densities%20of%20Selected%20Ions.pdf.

[156] B. Girisuta, L.P.B.M. Janssen, H.J. Heeres, Chemical Engineering Research and Design 84 (2006) 339–349.

[157] B.F.M. Kuster, Carbohydrate Research 54 (1977) 177–183.

[158] I. V. Sumerskii, S.M. Krutov, M.Y. Zarubin, Russian Journal of Applied Chemistry 83 (2010) 320–327.

[159] Y. Wang, D. Cui, Q. Li, Microporous and Mesoporous Materials 142 (2011) 503–510.

[160] H.K. Min, V. Chidambaram, S.B. Hong, Journal of Physical Chemistry C 114 (2010) 1190–1193.

[161] L. Zhang, S. Liu, S. Xie, L. Xu, Microporous and Mesoporous Materials 147 (2012) 117–126.

[162] X. Jia, W. Khan, Z. Wu, J. Choi, A.C.K. Yip, Advanced Powder Technology 30 (2019) 467–484.

[163] W. Khan, X. Jia, Z. Wu, J. Choi, A.C.K. Yip, Catalysts 9 (2019) 127.

[164] Y.B. Huang, T. Yang, Y.T. Lin, Y.Z. Zhu, L.C. Li, H. Pan, Green Chemistry 20 (2018) 1323–1334.

[165] S. Kang, J. Fu, G. Zhang, Renewable and Sustainable Energy Reviews 94 (2018) 340–362.

[166] S. Chu, L. Yang, X. Guo, L. Dong, X. Chen, Y. Li, X. Mu, Molecular Catalysis 445 (2018) 240–247.

[167] A.P. Pratama, D.U.C. Rahayu, Y.K. Krisnandi, Catalysts 10 (2020) 327.

[168] S.T. Pham, M.B. Nguyen, G.H. Le, T.T.T. Pham, T.T.T. Quan, T.D. Nguyen, T. le Son, T.A. Vu, Journal of Chemistry 2019 (2019).

[169] L. Li, N. Tang, Y. Wang, W. Cen, J. Liu, Y. Zhou, Nanoscale Research Letters 10 (2015) 1–7.

[170] L. Hermida, H. Amani, S. Saeidi, A.Z. Abdullah, A.R. Mohamed, Reviews in Chemical Engineering 34 (2018) 239–265.

[171] H.Y. Lin, Y.L. Pan, Y.W. Chen, Journal of Porous Materials 12 (2005) 151–164.

[172] M.A. al Roaya, F. Manteghi, M. Haghverdi, Silicon 11 (2018) 1401–1411.

[173] P.T. Tanev, T.J. Pinnavaia, Science 267 (1995) 865–867.

[174] R. Mokaya, W. Jones, Journal of Catalysis 172 (1997) 211–221.

[175] R. Palkovits, K. Tajvidi, J. Procelewska, R. Rinaldi, A. Ruppert, Green Chemistry 12 (2010) 972–978.

[176] J.J. Wiesfeld, P. Peršolja, F.A. Rollier, A.M. Elemans-Mehring, E.J.M. Hensen, Molecular Catalysis 473 (2019) 110400.

[177] K. Wang, J. Ye, M. Zhou, P. Liu, X. Liang, J. Xu, J. Jiang, Cellulose 24 (2017) 1383–1394.

[178] K.S.W. Sing, Pure and Applied Chemistry 54 (1982) 2201–2218.

[179] E. Binaeian, M. Mottaghizad, A. Hoseinpour Kasgary, S. Babaee Zadvarzi, Solid State Sciences 103 (2020) 106194.

[180] W. Huang, Y. Zhu, J. Tang, X. Yu, X. Wang, D. Li, Y. Zhang, Journal of Materials Chemistry A 2 (2014) 8839–8848.

[181] T.A. Zepeda, A. Infantes-Molina, J.N.D. de Leon, R. Obeso-Estrella, S. Fuentes, G. Alonso-Nuñez, B. Pawelec, Journal of Molecular Catalysis A: Chemical 397 (2015) 26–35.

[182] J. Chen, J. Zhou, R. Wang, J. Zhang, Industrial and Engineering Chemistry Research 48 (2009) 3802–3811.

[183] V. la Parola, M.L. Testa, A.M. Venezia, Applied Catalysis B: Environmental 119–120 (2012) 248–255.

[184] E. Baďurová, K. Raabová, R. Bulánek, Dalton Transactions 43 (2014) 3897–3905.

[185] D.F. Enache, E. Vasile, C.M. Simonescu, D. Culita, E. Vasile, O. Oprea, A.M. Pandele, A. Razvan, F. Dumitru, G. Nechifor, RSC Advances 8 (2017) 176–189.

[186] N. Parsafard, M.H. Peyrovi, M. Rashidzadeh, Microporous and Mesoporous Materials 200 (2014) 190–198.

[187] H. Zhang, L. Han, A. Duan, C. Xu, Z. Zhao, Y. Wei, G. Jiang, J. Liu, D. Wang, Z. Xia, RSC Advances 7 (2017) 28038–28047.

[188] X. Li, B. Li, J. Xu, Q. Wang, X. Pang, X. Gao, Z. Zhou, J. Piao, Applied Clay Science 50 (2010) 81–86.

[189] C. He, P. Li, J. Cheng, H. Wang, J. Li, Q. Li, Z. Hao, Applied Catalysis A: General 382 (2010) 167–175.

[190] M. Zendehdel, G. Cruciani, M. Dondi, Journal of Porous Materials 19 (2012) 361–368.

[191] C. Li, J. Ma, Z. Xiao, S.B. Hector, R. Liu, S. Zuo, X. Xie, A. Zhang, H. Wu, Q. Liu, Fuel 218 (2018) 59–66.

[192] F.S. Xiao, W. Xu, S. Qiu, R. Xu, MRS Online Proceedings Library 344 (2011) 139–144.

[193] C. Janssens, P.J. Grobet, R.A. Schoonheydt, J.C. Jansen, Zeolites 11 (1991) 184–191.

[194] P.Y. Dapsens, C. Mondelli, J. Pérez-Ramírez, Chemical Society Reviews 44 (2015) 7025–7043.

[195] S. Mandal, C. Santra, R. Kumar, M. Pramanik, S. Rahman, A. Bhaumik, S. Maity, D. Sen, B. Chowdhury, RSC Advances 4 (2013) 845–854.

[196] T.R.D. Mendonça, J.R. Santos, L.R.A. Sarmento, D.C.M. Silva, O.M.S. Cysneiros, A.O.S. Silva, Cerâmica 65 (2019) 378–387.

[197] Y. Xia, R. Mokaya, Journal of Materials Chemistry 13 (2003) 3112–3121.

[198] H. Guo, H. Qian, S. Sun, D. Sun, H. Yin, X. Cai, Z. Liu, J. Wu, T. Jiang, X. Liu, Chemistry Central Journal 5 (2011) 1–10.

[199] T. Tamoradi, M. Ghadermazi, A. Ghorbani-Choghamarani, Journal of Saudi Chemical Society 23 (2019) 846–855.

[200] S. Chaowamalee, C. Ngamcharussrivichai, Nanoscale Research Letters 14 (2019) 1–13.

[201] A. Onda, T. Ochi, K. Yanagisawa, Green Chemistry 10 (2008) 1033–1037.

[202] Z. Zhang, Z.K. Zhao, Carbohydrate Research 344 (2009) 2069–2072.

[203] P. Daorattanachai, S. Namuangruk, N. Viriya-empikul, N. Laosiripojana, K. Faungnawakij, Journal of Industrial and Engineering Chemistry 18 (2012) 1893–1901.

[204] L. Zhou, M. Shi, Q. Cai, L. Wu, X. Hu, X. Yang, C. Chen, J. Xu, Microporous and Mesoporous Materials 169 (2013) 54–59.

[205] S.S. Chen, T. Maneerung, D.C.W. Tsang, Y.S. Ok, C.H. Wang, Chemical Engineering Journal 328 (2017) 246–273.

[206] S. Deguchi, K. Tsujii, K. Horikoshi, Chemical Communications (2006) 3293–3295.

[207] S.S. Chen, I.K.M. Yu, D.C.W. Tsang, A.C.K. Yip, E. Khan, L. Wang, Y.S. Ok, C.S. Poon, Chemical Engineering Journal 327 (2017) 328–335.

[208] S. Kang, J. Yu, Industrial and Engineering Chemistry Research 54 (2015) 11552–11559.

[209] V.P.S. Caldeira, A.G.D. Santos, S.B.C. Pergher, M.J.F. Costa, A.S. Araujo, Quim. Nova 39 (2016) 292–297.

[210] H. Jouini, I. Mejri, C. Petitto, J. Martinez-Ortigosa, A. Vidal-Moya, M. Mhamdi, T. Blasco, G. Delahay, Microporous and Mesoporous Materials 260 (2018) 217–226.

[211] R. Otomo, T. Yokoi, J.N. Kondo, T. Tatsumi, Applied Catalysis A: General 470 (2014) 318–326.

[212] W.N.P. van der Graaff, C.H.L. Tempelman, F.C. Hendriks, J. Ruiz-Martinez, S. Bals, B.M. Weckhuysen, E.A. Pidko, E.J.M. Hensen, Applied Catalysis A: General 564 (2018) 113–122.

[213] Y. Wang, L. Zhu, Y. Zhang, H. Cui, W. Yi, F. Song, P. Zhao, X. Sun, Y. Xie, L. Wang, Z. Li, ChemistrySelect 3 (2018) 3555–3560.

[214] M. A. Mellmer, J. M. R. Gallo, D. M. Alonso, J. A. Dumesic, ACA Catalysis 5 (2015) 3354–3359.

[215] S. Saravanamurugan, A. Riisager, US patent US 9,676,697 B2, (2017).

[216] G. Tsilomelekis, M.J. Orella, Z. Lin, Z. Cheng, W. Zheng, V. Nikolakis, D.G. Vlachos, Green Chemistry 18 (2016) 1983–1993.

[217] S.K.R. Patil, C.R.F. Lund, Energy and Fuels 25 (2011) 4745–4755.

[218] I. van Zandvoort, E.R.H. van Eck, P. de Peinder, H.J. Heeres, P.C.A. Bruijnincx, B.M. Weckhuysen, ACS Sustainable Chemistry and Engineering 3 (2015) 533–543.

[219] S. Wang, H. Lin, Y. Zhao, J. Chen, J. Zhou, Journal of Analytical and Applied Pyrolysis 118 (2016) 259–266.

[220] B. Pereda-Ayo, U. de La Torre, M.J. Illán-Gómez, A. Bueno-López, J.R. González-Velasco, Applied Catalysis B: Environmental 147 (2014) 420–428.

[221] M.C. Dalconi, G. Cruciani, A. Alberti, P. Ciambelli, Microporous and Mesoporous Materials 94 (2006) 139–147.

[222] H.G. Karge, Studies in Surface Science and Catalysis 58 (1991) 531–570.

[223] C. Tian, Y. Oyola, K.M. Nelson, S.H. Chai, X. Zhu, J.C. Bauer, C.J. Janke, S. Brown, Y. Guo, S. Dai, RSC Advances 3 (2013) 21242–21246.

[224] V. Heguaburu, J. Franco, L. Reina, C. Tabarez, G. Moyna, P. Moyna, Catalysis Communications 27 (2012) 88–91.

[225] K.B. Sidhpuria, A.L. Daniel-Da-silva, T. Trindade, J.A.P. Coutinho, Green Chemistry 13 (2011) 340–349.

[226] N. Lelekakis, J. Wijaya, D. Martin, D. Susa, IEEE Electrical Insulation Magazine 30 (2014) 19–26.

[227] I.T. Horváth, H. Mehdi, V. Fábos, L. Boda, L.T. Mika, Green Chemistry 10 (2008) 238–24.

[228] S. Dutta, I.K.M. Yu, D.C.W. Tsang, Y.H. Ng, Y.S. Ok, J. Sherwood, J.H. Clark, Chemical Engineering Journal 372 (2019) 992–1006.

[229] I.T. Horváth, Green Chemistry 10 (2008) 1024–1028.

[230] S. Kondawar, C. Rode, Current Opinion in Green and Sustainable Chemistry 35 (2022) 100607.

[231] Z. Zhang, ChemSusChem 9 (2016) 156–171.

[232] Z. Yu, X. Lu, H. Bai, J. Xiong, W. Feng, N. Ji, Chemistry - An Asian Journal 15 (2020) 1182–1201.

[233] M. Jędrzejczyk, E. Soszka, J. Goscianska, M. Kozanecki, J. Grams, A.M. Ruppert, Molecules 25 (2020).

[234] H. Heeres, R. Handana, D. Chunai, C. Borromeus Rasrendra, B. Girisuta, H. Jan Heeres, Green Chemistry 11 (2009) 1247–1255.

[235] M. Chia, J.A. Dumesic, Chemical Communications 47 (2011) 12233–12235.

[236] S.S.R. Gupta, M.L. Kantam, Catalysis Today 309 (2018) 189–194.

[237] I. Obregón, E. Corro, U. Izquierdo, J. Requies, P.L. Arias, Cuihua Xuebao/Chinese Journal of Catalysis 35 (2014) 656–662.

[238] D. Liu, L. Zhang, W. Han, M. Tang, L. Zhou, Y. Zhang, X. Li, Z. Qin, H. Yang, Chemical Engineering Journal 369 (2019) 386–393.

[239] S. Song, S. Yao, J. Cao, L. Di, G. Wu, N. Guan, L. Li, Applied Catalysis B: Environmental 217 (2017) 115–124.

[240] K. Hengst, D.A.J.M. Ligthart, D.E. Doronkin, K.M. Walter, W. Kleist, E.J.M. Hensen, J.D. Grunwaldt, Industrial and Engineering Chemistry Research 56 (2017) 2680–2689.

[241] W. Luo, U. Deka, A.M. Beale, E.R.H. van Eck, P.C.A. Bruijnincx, B.M. Weckhuysen, Journal of Catalysis 301 (2013) 175–186.

[242] C. Moreno-Marrodan, P. Barbaro, Green Chemistry 16 (2014) 3434–3438.

[243] D.M. Alonso, J.M.R. Gallo, M.A. Mellmer, S.G. Wettstein, J.A. Dumesic, Catalysis Science and Technology 3 (2013) 927–931.

[244] A. García, R. Sanchis, P.J. Miguel, A.M. Dejoz, M.P. Pico, M.L. López, I. Álvarez-Serrano, T. García, B. Solsona, RSC Advances 10 (2020) 20395–20404.

[245] L. Zhang, J. Mao, S. Li, J. Yin, X. Sun, X. Guo, C. Song, J. Zhou, Applied Catalysis B: Environmental 232 (2018) 1–10.

[246] J. Fu, D. Sheng, X. Lu, Catalysts 6 (2015).

[247] W. Cao, W. Luo, H. Ge, Y. Su, A. Wang, T. Zhang, Green Chemistry 19 (2017) 2201–2211.

[248] G. Ferraro, G. Pecori, L. Rosi, L. Bettucci, E. Fratini, D. Casini, A.M. Rizzo, D. Chiaramonti, Biomass Conversion and Biorefinery (2021).

[249] Q. Fang, B. Chen, Y. Lin, Y. Guan, Environmental Science and Technology 48 (2014) 279–288.

[250] L. Han, L. Qian, J. Yan, M. Chen, Environmental Science and Pollution Research 24 (2017) 5554–5565.

[251] R.E. Franklin, P.R.S.L. A, Proceedings of the Royal Society of London. Series A. Mathematical and Physical Sciences 209 (1951) 196–218.

[252] F. Cheng, X. Li, Catalysts 8 (2018) 1–35.

[253] J. Xi, H. Li, J. Xi, S. Tan, J. Zheng, Z. Tan, Environmental Science and Pollution Research 27 (2020) 20675–20684.

[254] K. S. Are, Biochar and Soil Physical Health, Chapter 2, (2019) 21-35.

[255] B. Sajjadi, W.Y. Chen, N.O. Egiebor, Reviews in Chemical Engineering 35 (2019) 735–776.

[256] H.O. Pierson, Handbook of Carbon, Graphite, Diamonds and Fullerenes (1993) 226–243.

[257] P. Salimi, S. Tieuli, S. Taghavi, E. Venezia, S. Fugattini, S. Lauciello, M. Prato, S. Marras, T. Li, M. Signoretto, P. Costamagna, R.P. Zaccaria, Green Chemistry 24 (2022) 4119–4129.

[258] S. Xu, D. Yu, T. Ye, P. Tian, RSC Advances 7 (2017) 1026–1031.

[259] V.V. Kumar, G. Naresh, M. Sudhakar, J. Tardio, S.K. Bhargava, A. Venugopal, Applied Catalysis A: General 505 (2015) 217–223.

[260] V. Mohan, C. Raghavendra, C.V. Pramod, B.D. Raju, K.S. Rama Rao, RSC Advances 4 (2014) 9660–9668.

[261] P. Sun, G. Gao, Z. Zhao, C. Xia, F. Li, ACS Catalysis 4 (2014) 4136–4142.

[262] J. Wang, S. Jaenicke, G.K. Chuah, RSC Advances 4 (2014) 13481–13489.

[263] J. Barrio, M. Volokh, M. Shalom, Journal of Materials Chemistry A 8 (2020) 11075–11116.

[264] T. Wang, H. Ma, X. Liu, Y. Luo, S. Zhang, Y. Sun, X. Wang, J. Gao, J. Xu, Chemistry – An Asian Journal 14 (2019) 1515–1522.

[265] Y. Guo, Y. Li, J. Chen, L. Chen, Catalysis Letters 146 (2016) 2041–2052.

[266] S. Cattaneo, M. Stucchi, G.M. Veith, L. Prati, D. Wang, W. Wang, A. Villa, Catalysis Today 357 (2020) 143–151.

[267] Y. Wang, Z. Rong, Y. Wang, T. Wang, Q. Du, Y. Wang, J. Qu, ACS Sustainable Chemistry and Engineering 5 (2017) 1538–1548.

[268] H. Guo, Y. Hiraga, X. Qi, R.L. Smith, Journal of Supercritical Fluids 147 (2019) 263–270.

[269] B. Pacewska, M. Keshr, Thermochimica Acta 385 (2002) 73–80.

[270] B.S. Vasile, G. Dobra, S. Iliev, L. Cotet, I.A. Neacsu, V.A. Surdu, A.I. Nicoara, A. Boiangiu, L. Filipescu, Ceramics 4 (2021) 564–575.

[271] W. Brockner, C. Ehrhardt, M. Gjikaj, Thermochimica Acta 456 (2007) 64–68.

[272] D. Angin, Bioresource Technology 128 (2013) 593–597.

[273] P.S. Thue, D.R. Lima, E.C. Lima, R.A. Teixeira, G.S. dos Reis, S.L.P. Dias, F.M. Machado, Journal of Environmental Chemical Engineering 10 (2022) 107632.

[274] H.S. Jatav, V.D. Rajput, T. Minkina, S.K. Singh, S. Chejara, A. Gorovtsov, A. Barakhov, T. Bauer, S. Sushkova, S. Mandzieva, M. Burachevskaya, V.P. Kalinitchenko, Sustainability 13 (2021) 10362.

[275] H. Shan, X. Li, Y. Cui, D. Xiong, B. Yan, D. Li, A. Lushington, X. Sun, Electrochimica Acta 205 (2016) 188–197.

[276] S. De, J. Zhang, R. Luque, N. Yan, Energy & Environmental Science 9 (2016) 3314–3347.

[277] C.H. Bartholomew, G.D. Weatherbee, G.A. Jarvi, Journal of Catalysis 60 (1979) 257–269.

[278] A. Kolpin, G. Jones, S. Jones, W. Zheng, J. Cookson, A.P.E. York, P.J. Collier, S.C.E. Tsang, ACS Catalysis 7 (2017) 592–605.

[279] L. Liu, Y. Liu, W. Wang, Y. Wang, G. Li, C. Hu, Toxins 13 (2021) 542.

[280] W.T. Tsai, T.J. Jiang, Y.Q. Lin, H.L. Chang, C.H. Tsai, Fermentation 7 (2021) 228.

[281] A. Makalesi, / Research, A.N. Kaya, Z. Yildiz, S. Ceylan, Politeknik Dergisi 21 (2018) 765–776.

[282] J.M. de la Rosa, M. Paneque, A.Z. Miller, H. Knicker, Science of The Total Environment 499 (2014) 175–184.

[283] B. Ma, Y. Huang, Z. Nie, X. Qiu, D. Su, G. Wang, J. Yuan, X. Xie, Z. Wu, RSC Advances 9 (2019) 20424–20431.

[284] Y. Liu, Z. He, M. Uchimiya, Modern Applied Science 9 (2015).

[285] S. Javadian, Z. Parviz, P. Salimi, M. Nasrollahpour, H. Gharibi, H. Kashani, A. Morsali, R.P. Zaccaria, Journal of Alloys and Compounds 898 (2022) 162849.

[286] J.L. Figueiredo, M.F.R. Pereira, M.M.A. Freitas, J.J.M. Órfão, Carbon N Y 37 (1999) 1379–1389.

[287] J.B. Donnet, Carbon N Y 6 (1968) 161–176.

[288] J.L. Figueiredo, M.F.R. Pereira, Catalysis Today 150 (2010) 2–7.

[289] M. González-Castaño, C. Morales, J.C. Navarro de Miguel, J.H. Boelte, O. Klepel, J.I. Flege, H. Arellano-García, Green Energy & Environment (2021).

[290] I.K.M. Yu, X. Xiong, D.C.W. Tsang, L. Wang, A.J. Hunt, H. Song, J. Shang, Y.S. Ok, C.S. Poon, Green Chemistry 21 (2019) 1267–1281.

[291] L. Qian, B. Chen, Journal of Agricultural and Food Chemistry 62 (2014) 373–380.

[292] H.K.D. Nguyen, V. v. Pham, H.T. Do, Catalysis Letters 146 (2016) 2381–2391.

[293] T.H. Liou, S.J. Wu, Journal of Hazardous Materials 171 (2009) 693–703.

[294] M.M. Alam, M.A. Hossain, M.D. Hossain, M.A.H. Johir, J. Hossen, M.S. Rahman, J.L. Zhou, A.T.M.K. Hasan, A.K. Karmakar, M.B. Ahmed, Processes 8 (2020) 203.

[295] L. Longo, S. Taghavi, E. Ghedini, F. Menegazzo, A. di Michele, G. Cruciani, M. Signoretto, ChemSusChem (2022).

[296] X. Liu, Y. Zhang, M.A. Nahil, P.T. Williams, C. Wu, Journal of Analytical and Applied Pyrolysis 125 (2017) 32–39.

[297] Q. Yin, H. Ren, R. Wang, Z. Zhao, Science of The Total Environment 631–632 (2018) 895–903.

[298] I.K.M. Yu, X. Xiong, D.C.W. Tsang, L. Wang, A.J. Hunt, H. Song, J. Shang, Y.S. Ok, C.S. Poon, Green Chemistry 21 (2019) 1267–1281.

[299] J.L. Santos, P. Mäki-Arvela, A. Monzón, D.Y. Murzin, M.Á. Centeno, Applied Catalysis B: Environmental 268 (2020) 118423.

[300] J.M.V. Nabais, C. Laginhas, P.J.M. Carrott, M.M.L.R. Carrott, Journal of Analytical and Applied Pyrolysis 87 (2010) 8–13.

[301] H.K.D. Nguyen, V. v. Pham, H.T. Do, Catalysis Letters 146 (2016) 2381–2391.

[302] Y. Wang, Z. Zhang, S. Zhang, Y. Wang, S. Hu, J. Xiang, X. Hu, Fuel 278 (2020) 118341.

[303] C. Quan, H. Wang, N. Gao, International Journal of Energy Research 44 (2020) 5749–5764.

[304] J.M. Rafi, A. Rajashekar, M. Srinivas, B.V.S.K. Rao, R.B.N. Prasad, N. Lingaiah, RSC Advances 5 (2015) 44550–44556.

[305] R. Gundeboina, S. Gadasandula, V.K. Velisoju, N. Gutta, L.R. Kotha, H.P. Aytam, ChemistrySelect 4 (2019) 202–210.

[306] V.K. Velisoju, G.B. Peddakasu, N. Gutta, V. Boosa, M. Kandula, K.V.R. Chary, V. Akula, Journal of Physical Chemistry C 122 (2018) 19670–19677.

[307] A. Seretis, P. Diamantopoulou, I. Thanou, P. Tzevelekidis, C. Fakas, P. Lilas, G. Papadogianakis, Frontiers in Chemistry 8 (2020) 221.

[308] V.V. Kumar, G. Naresh, M. Sudhakar, J. Tardio, S.K. Bhargava, A. Venugopal, Applied Catalysis A: General 505 (2015) 217–223.

[309] C. López-Aguado, M. Paniagua, J.A. Melero, J. Iglesias, P. Juárez, M.L. Granados, G. Morales, Catalysts 10 (2020) 678.

[310] M. Wolf, C. Schüler, O. Hinrichsen, Journal of CO2 Utilization 32 (2019) 80–91.

[311] C.H. Bartholomew, G.D. Weatherbee, G.A. Jarvi, Journal of Catalysis 60 (1979) 257–269.

[312] S.L. Lakhapatri, M.A. Abraham, Catalysis Science & Technology 3 (2013) 2755–2760.

[313] A. Chauhan, A.K. Kar, R. Srivastava, Applied Catalysis A: General 636 (2022) 118580.

[314] L. Jiang, G. Xu, Y. Fu, Green Chemistry 23 (2021) 7065–7073.

[315] F. Neaţu, S. Coman, V.I. Pârvulescu, G. Poncelet, D. de Vos, P. Jacobs, Topics in Catalysis 52 (2009) 1292–1300.

[316] I. Simakova, P. Mäki-Arvela, M. Martinez-Klimov, J. Muller, Z. Vajglova, M. Peurla, K. Eränen, D.Yu. Murzin, Applied Catalysis A: General 636 (2022) 118586.

[317] M. Emura, H. Matsuda, Chemistry and Biodiversity 11 (2014) 1688–1699.

[318] Menthol Market, Global Industry Report, 2030. Accessed 2 May 2022, available on-line: https://www.transparencymarketresearch.com/menthol-market.html.

[319] A.F. Trasarti, A.J. Marchi, C.R. Apesteguía, Catalysis Communications 32 (2013) 62–66.

[320] C. Vladiskovic, A. Restelli, B. Gabriele Razzetti, United State patent, US 8,314,241 B2 (2009).

[321] M. Vandichel, F. Vermoortele, S. Cottenie, D.E. de Vos, M. Waroquier, V. van Speybroeck, Journal of Catalysis 305 (2013) 118–129.

[322] Z. Vajglová, N. Kumar, M. Peurla, K. Eränen, P. Mäki-Arvela, D.Y. Murzin, Catalysis Science and Technology 10 (2020) 8108–8119.

[323] P. Mäki-Arvela, N. Kumar, V. Nieminen, R. Sjöholm, T. Salmi, D.Y. Murzin, Journal of Catalysis 225 (2004) 155–169.

[324] G.D. Yadav, J.J. Nair, Chemical Communications (1998) 2369–2370.

[325] C. Jimeno, J. Miras, J. Esquena, Catalysis Letters 143 (2013) 616–623.

[326] E.D. Iftitah, M. Muchalal, W. Trisunaryanti, R. Armunanto, R. Psaro, N. Ravasio, F. Santoro, L. Sordelli, Journal of Applied Sciences Research 7 (2011) 680–689.

[327] J. Plößer, M. Lucas, P. Claus, Journal of Catalysis 320 (2014) 189–197.

[328] M. Azkaar, P. Mäki-Arvela, Z. Vajglová, V. Fedorov, N. Kumar, L. Hupa, J. Hemming, M. Peurla, A. Aho, D.Y. Murzin, Reaction Chemistry and Engineering 4 (2019) 2156–2169.

[329] P. Mertens, F. Verpoort, A.N. Parvulescu, D. de Vos, Journal of Catalysis 243 (2006) 7–13.

[330] K.A. da Silva Rocha, P.A. Robles-Dutenhefner, E.M.B. Sousa, E.F. Kozhevnikova, I. v. Kozhevnikov, E. v. Gusevskaya, Applied Catalysis A: General 317 (2007) 171–174.

[331] A.M. Balu, J.M. Campelo, R. Luque, A.A. Romero, Organic and Biomolecular Chemistry 8 (2010) 2845–2849.

[332] Y. Nie, W. Niah, S. Jaenicke, G.K. Chuah, Journal of Catalysis 248 (2007) 1–10.

[333] Y. Nie, G.K. Chuah, S. Jaenicke, Chemical Communications i (2006) 790–792.

[334] C.B. Cortés, V.T. Galván, S.S. Pedro, T.V. García, Catalysis Today 172 (2011) 21–26.

[335] I.B. Adilina, R. Pertiwi, A. Sulaswatty, Biopropal Industri 6 (2015) 1–6.

[336] I. Fatimah, D. Rubiyanto, T. Huda, S. Handayani, O.M. Ilahi, S.P. Yudha, Engineering Journal 19 (2015) 43–53.

[337] S. Mintova, M. Reinelt, J. Senker, T.H. Metzger, T. Bein, Chemical Communications 3 (2003) 326–327.

[338] B. Mihailova, V. Valtchev, S. Mintova, A.C. Faust, N. Petkov, T. Bein, Physical Chemistry Chemical Physics 7 (2005) 2756–2763.

[339] M.M.J. Treacy, J.M. Newsam, Nature 332 (1988) 249–251.

[340] J.A. Lawton, S.L. Lawton, M.E. Leonowicz, M.K. Rubin, Studies in Surface Science and Catalysis 98 (1995) 250–251.

[341] J.M. Newsam, M.M.J. Treacy, W.T. Koetsier, C.B. de Gruyter, Proceedings of The Royal Society of London, Series A: Mathematical and Physical Sciences 420 (1988) 375–405.

[342] T. Lu, W. Yan, R. Xu, Inorganic Chemistry Frontiers 6 (2019) 1938–1951.

[343] M.E. Davis, ACS Catalysis 8 (2018) 10082–10088.

[344] J. Yu, R. Xu, Journal of Materials Chemistry 18 (2008) 4021–4030.

[345] H. Itoh, H. Maeda, S. Yamada, Y. Hori, T. Mino, M. Sakamoto, Organic Chemistry Frontiers 1 (2014) 1107–1115.

[346] M. Tong, D. Zhang, L. Zhu, J. Xu, F. Deng, R. Xu, W. Yan, CrystEngComm 18 (2016) 1782–1789.

[347] S. Mintova, V. Valtchev, T. Onfroy, C. Marichal, H. Knözinger, T. Bein, Microporous and Mesoporous Materials 90 (2006) 237–245.

[348] P. Lanzafame, S. Perathoner, G. Centi, E. Heracleous, E.F. Iliopoulou, K.S. Triantafyllidis, A.A. Lappas, ChemCatChem 9 (2017) 1632–1640.

[349] R. Martínez-Franco, C. Paris, M.E. Martínez-Armero, C. Martínez, M. Moliner, A. Corma, Chemical Science 7 (2016) 102–108.

[350] X. Wei, Y. Li, Z. Hua, L. Chen, J. Shi, ChemCatChem 12 (2020) 6285–6290.

[351] S. Wang, B. He, R. Tian, C. Sun, R. Dai, X. Li, X. Wu, X. An, X. Xie, Molecular Catalysis 453 (2018) 64–73.

[352] Z. Vajglová, N. Kumar, M. Peurla, J. Peltonen, I. Heinmaa, D.Y. Murzin, Catalysis Science & Technology 8 (2018) 6150–6162.

[353] P. Cañizares, A. de Lucas, F. Dorado, A. Durán, I. Asencio, Applied Catalysis A: General 169 (1998) 137–150.

[354] M. Popova, P. Djinović, A. Ristić, H. Lazarova, G. Dražić, A. Pintar, A.M. Balu, N.N. Tušar, Frontiers in Chemistry 6 (2018) 1–12.

[355] D. v. Peron, V.L. Zholobenko, M.R. de la Rocha, M. Oberson de Souza, L.A. Feris, N.R. Marcilio, V. v. Ordomsky, A.Y. Khodakov, Journal of Materials Science 54 (2019) 5399–5411.

[356] D. Karthikeyan, N. Lingappan, B. Sivasankar, Korean Journal of Chemical Engineering 25 (2008) 987–997.

[357] C.M.N. Yoshioka, T. Garetto, D. Cardoso, Catalysis Today 107–108 (2005) 693–698.

[358] P. Losch, W. Huang, O. Vozniuk, E.D. Goodman, W. Schmidt, M. Cargnello, ACS Catalysis 9 (2019) 4742–4753.

[359] J. Li, H. Liu, T. An, Y. Yue, X. Bao, RSC Advances 7 (2017) 33714–33725.

[360] S. Tieuli, P. Mäki-Arvela, M. Peurla, K. Eränen, J. Wärnå, G. Cruciani, F. Menegazzo, D.Y. Murzin, M. Signoretto, Applied Catalysis A: General 580 (2019) 1–10.

[361] M. Niculescu, P. Budrugeac, Revue Roumaine de Chimie 58 (2013) 381–386.

[362] J.T. Richardson, R. Scates, M. v. Twigg, Applied Catalysis A: General 246 (2003) 137–150.

[363] S. Taghavi, C. Pizzolitto, E. Ghedini, F. Menegazzo, G. Cruciani, M. Peurla, K. Eränen, I. Heinmaa, A. Aho, N. Kumar, D.Y. Murzin, T. Salmi, M. Signoretto, Catalysis Letters (2022).

[364] A. Bermejo-López, B. Pereda-Ayo, J.A. González-Marcos, J.R. González-Velasco, Journal of CO2 Utilization 34 (2019) 576–587.

[365] Y. Yang, P. Ghildiyal, M.R. Zachariah, Langmuir 35 (2019) 3413–3420.

[366] A.E. Fetohi, R.S. Amin, R.M.A. Hameed, K.M. El-Khatib, Electrochimica Acta 242 (2017) 187–201.

[367] G. Bergeret, P. Gallezot. Particle Size and Dispersion Measurements. Handbook of Heretogeneous Catalysis, 2, Wiley-VCH (2008) 738-765.

[368] S. Taghavi, E. Ghedini, F. Menegazzo, P. Mäki-Arvela, M. Peurla, M. Zendehdel, G. Cruciani, A. di Michele, D.Y. Murzin, M. Signoretto, Catalysis Today 390–391 (2022) 146–161.

[369] N.J. Venkatesha, Y.S. Bhat, B.S. Jai Prakash, RSC Advances 6 (2016) 18824–18833.

[370] T. Crémoux, I. Batonneau-Gener, A. Moissette, J.L. Paillaud, M. Hureau, E. Ligner, C. Morais, S. Laforge, C. Marichal, H. Nouali, Physical Chemistry Chemical Physics 21 (2019) 14892–14903.

[371] G.K. Chuah, S.H. Liu, S. Jaenicke, L.J. Harrison, Journal of Catalysis 200 (2001) 352–359.

[372] V. V. Zhivonitko, Z. Vajglová, P. Mäki-Arvela, N. Kumar, M. Peurla, D.Y. Murzin, Russian Journal of Physical Chemistry A 95 (2021) 547–557.

[373] Z. Vajglová, N. Kumar, P. Mäki-Arvela, K. Eränen, M. Peurla, L. Hupa, D.Y. Murzin, Organic Process Research and Development 23 (2019) 2456–2463.

[374] Z. Vajglová, I.L. Simakova, K. Eränen, P. Mäki-Arvela, N. Kumar, M. Peurla, S. Tolvanen, A. Efimov, L. Hupa, J. Peltonen, D.Y. Murzin, Applied Catalysis A: General 629 (2022) 1–11.

[375] Z. Vajglová, N. Kumar, P. Mäki-Arvela, K. Eränen, M. Peurla, L. Hupa, M. Nurmi, M. Toivakka, D.Y. Murzin, Industrial and Engineering Chemistry Research 58 (2019) 18084–18096.

[376] G. Bergeret, P. Gallezot, G. Bergeret, P. Gallezot, P. Size, D. Measurements, (2021) 738–765.

[377] A.K. Shah, G. Maitlo, A.A. Shah, I.A. Channa, G.A. Kandhro, H.A. Maitlo, U.H. Bhatti, A. Shah, A.Q. Memon, A.S. Jatoi, Y.H. Park, Reaction Kinetics, Mechanisms and Catalysis 128 (2019) 917–934.

[378] I.B. Adilina, R. Pertiwi, A. Sulaswatty, Biopropal Industri 6 (2015) 1–6.

[379] R. Pertiwi, S. Tursiloadi, I.B. Adilina, K.C. Sembiring, Y. Oaki, Jurnal Kimia Terapan Indonesia 18 (2017) 132–138.

[380] P.H. Emmett, S. Brunauer, J Am Chem Soc 59 (1937) 1553–1564.

[381] C.A. Emeis, Journal of Catalysis 141 (1993) 347–354.

[382] Standard Test Methods for Proximate Analysis of Coal and Coke by Macro Thermogravimetric Analysis, ASTM-D7582 - 2015 EDITION.

[383] L. Lutterotti, Nuclear Instruments and Methods in Physics Research, Section B: Beam Interactions with Materials and Atoms 268 (2010) 334–340.

Curriculum Vitae

I am Seyedeh Somayeh Taghavi, born in 1988, Noor, Iran. I graduated in Applied Chemistry at University of Tehran, Iran in 2010. At the same University, I got my Master Degree in Applied Chemistry with the thesis title of "Synthesis and application of Ru-Co/CNTs nano catalyst for conversion of syngas to mid-distillates" in excellent level. After my master study, I became a postgraduate researcher for four years at the Group of Catalysts and Reaction Engineering, University of Tehran, Iran where I continued my research on catalysis and their applications in gas-phase reactions for production of energy and fuels. During my four-year research period, I obtained a highly competitive international research fellowship as a visiting researcher in Italy (October 2016-April 2017) at CATMAT Laboratory, Ca' Foscari University of Venice where I got new experiences in my field. Since December 2018, I am working as a PhD student joint between University of Trieste and Ca' Foscari University of Venice (CATMAT). My work has been focused on valorization of biomass to chemicals using microporous and mesoporous materials. In particular, I have worked on the formulation and modification of different heterogenous catalysts based on zeolite, mesoporous silica martials, and carbonaceous materials (biochars), their characterizations and applications in several model reactions of biomass valorization topic. To further improve my international experience in my field, I spent three months in Finland (April-July 2021) at laboratory of Industrial Chemistry and Reaction Engineering, Process Chemistry Center, Åbo Akademi University of Turku.

The outcome of my research activities has been disseminated by some publications in peer-reviewed international journals, and national and international congresses.

List of publications and conference presentations based on this thesis

Chapter 1

Publication

- Michela Signoretto, Somayeh Taghavi, Elena Ghedini, Federica Menegazzo "*Catalytic production of levulinic acid (LA) from actual biomass*" Molecules, 24 (2019) 2760.

Chapter 2

Publication

- Somayeh Taghavi, Elena Ghedini, Federica Menegazzo, Alessia Giordana, Giuseppina Cerrato, Giuseppe Cruciani, Alessandro Di Michele, Mojgan Zendehdel, Michela Signoretto "*Balanced Acidity by Microwave Assisted Ion-exchange of ZSM-5 Zeolite as a Catalyst for Transformation of Glucose to Levulinic acid* " Biomass Conversion and Biorefinery, (2022) 1-19.

Chapter 3

Publication

- Somayeh Taghavi, Elena Ghedini, Federica Menegazzo, Päivi Mäki-Arvela, Markus Peurla, Mojgan Zendehdel, Giuseppe Cruciani, Alessandro Di Michele, Dmitry Yu. Murzin, Michela Signoretto "*CuZSM-5@HMS composite as an efficient micro-mesoporous catalyst for conversion of sugars into levulinic acid* " Catalysis Today, 390-391 (2022) 146-161.

Conference presentation

- Somayeh Taghavi, Elena Ghedini, Federica Menegazzo, and Michela Signoretto "*Catalytic transformation of glucose to levulinic acid by using micro meso HZSM5-HMS composites*" Merk Young Chemist Symposium, Rimini, Italy, November 25-27, 2019. (ISBN 978-88-94952-15-5)

- Somayeh Taghavi, Mojgan Zendehdel, Federica Menegazzo, Giuseppe Cruciani, Michela Signoretto "*CU-ZSM5@HMS composite as an efficient catalyst for conversion of mono- and poly-sugars into levulinic acid*" on-line conference on Molecular Sieves and Catalysis (CIS 2021), Spain, September 6-8, 2021. Oral communication, presenting author Somayeh Taghavi.

- Somayeh Taghavi, Mojgan Zendehdel, Michela Signoretto "*Micro-mesoporous CuZSM-5@HMS composite for transformation of biomass derived sugars to levulinic acid* " 7th Zeolite Conference of Iranian Chemical Society, August 30,31, 2022, Chemistry and Chemical Engineering Research Center of Iran. Oral communication, presenting author Somayeh Taghavi.

Chapter 4

Conference presentations

- Somayeh Taghavi, Martina Tretti, Sebastiano Tieuli, Päivi Mäki-Arvela, Markus Peurla, Dmitry Yu. Murzin, Federica Menegazzo, Michela Signoretto "*Biomass-derived levulinic acid hydrogenation to GVL using bifunctional biochar-based catalysts*" XXVII Congresso Nazionale Della Socita Chimica Italiana (SCI 2021), Italy, September 14-23, 2021. Oral communication, presenting author Somayeh Taghavi.

Chapter 5

Publication

- Somayeh Taghavi, Päivi Mäki-Arvela, Zuzana Vajglová, Markus Peurla, Ilari Angervo, Kari Eränen, Elena Ghedini, Federica Menegazzo, Mojgan Zendehdel, Michela Signoretto, Dmitry Yu. Murzin "*One-pot transformation of citronellal to menthol over H-Beta zeolite supported Ni catalyst: Effect of catalyst support acidity and Ni loading*" Catalysis Letters, (2022) accepted.

Conference presentations

- Somayeh Taghavi, Elena Ghedini, Federica Menegazzo, Mojgan Zendehdel, Dmitry Yu. Murzin, Michela Signoretto " *Potential of H-Beta zeolite supported Ni catalyst for One-pot transformation of citronellal to menthol*" GIC-2022 - XXII National Congress on Catalysis Riccione, September 11-14, 2022. Oral communication, presenting author Somayeh Taghavi.

Other publications

- Somayeh Taghavi, Omid Norouzi, Ahmad Tavasoli, Francesco Di Maria, Michela Signoretto, Federica Menegazzo, Alessandro Di Michele "*Catalytic conversion of Venice lagoon brown marine algae for producing hydrogen-rich gas and valuable biochemical using algal biochar and Ni/SBA-15 catalyst*" International Journal of Hydrogen Energy, 43 (2018) 19918-19929.

- Somayeh Taghavi, Elena Ghedini, Federica Menegazzo, Michela Signoretto, Delia Gazzoli, Daniela Pietrogiacomi, Aisha Matayeva, Andrea Fasolini, Angelo Vaccari, Francesco Basile, Giuseppe Fornasari "*MCM-41 Supported Co-Based Bimetallic Catalysts for Aqueous Phase Transformation of Glucose to Biochemicals*" Processes, 8 (2020) 843.

- Cristina Pizzolitto, Elena Ghedini, Somayeh Taghavi, Federica Menegazzo, Giuseppe Cruciani, Markus Peurla, Kari Eränen, Ivo Heinmaa, Atte Aho, Narendra Kumar, Dmitry Yu Murzin, Tapio Salmi, Michela Signoretto "*Acid sites modulation of siliceous-based mesoporous material by post synthesis methods*" Microporous and Mesoporous Materials, 328 (2021) 111459.

- Omid Norouzi, SomayehTaghavi, PreciousArku, Sajedeh Jafarian, Michela Signoretto, Animesh Dutta "*What is the best catalyst for biomass pyrolysis?*" Journal of Analytical and Applied Pyrolysis, 158 (2021) 105280.

- Elena Ghedini, Somayeh Taghavi, Federica Menegazzo, Michela Signoretto "*A Review on the Efficient Catalysts for Algae Transesterification to Biodiesel"* Sustainability, 13 (2021) 10479.

- Somayeh Taghavi, Cristina Pizzolitto, Elena Ghedini, Federica Menegazzo, Giuseppe Cruciani, Markus Peurla, Kari Eränen, Ivo Heinmaa, Atte Aho, Narendra Kumar, Dmitry Yu. Murzin, Tapio Salmi, Michela Signoretto "*Levulinic acid production: comparative assessment of Al-rich ordered mesoporous silica and microporous zeolite*" Catalysis Letters, (2022) DOI:10.1007/s10562-022-03955-y.
- Lilia Longo, Somayeh Taghavi, Elena Ghedini, Federica Menegazzo, Alessandro Di Michele, Giuseppe Cruciani, Michela Signoretto "*Selective hydrogenation of HMF to 1-hydroxy-2,5-hexanedione by biochar supported Ru catalysts*" ChemSusChem, 18 May 2022, 15(13):e202200437.
- Pejman Salimi, Sebastiano Tieuli, Somayeh Taghavi, Eleonora Venezia, Silvio Fugattini, Simone Lauciello, Mirko Prato, Sergio Marras, Tao Li, Michela Signoretto, Paola Costamagna, Remo Proietti Zaccaria "*Sustainable lithium-ion batteries based on metal-free tannery waste biochar*" Green Chemistry, 24 (10) (2022) 4119-4129.

Other conference presentations

- Somayeh Taghavi , Michela Signoretto, Federica Menegazzo "*Catalytic conversion of Venice lagoon brown marine algae for producing hydrogen-rich gas and valuable biochemical using algal biochar and Ni/SBA-15 nanocatalyst*" Iranian Inorganic Chemistry Seminar, Arak University, Arak, Iran, August 28-29,2019. Oral communication, presenting author Somayeh Taghavi.
- Somayeh Taghavi , Michela Signoretto, Federica Menegazzo, Alessandro Di Michele "*Catalytic conversion of Venice lagoon brown marine algae for producing hydrogen-rich gas and valuable biochemical using algal biochar and Ni/SBA-15 catalyst*" Summer school in Making business with green chemistry & sustainable energy, Sarteano, Italy, July 22-27, 2019. Poster communication, presenting author Somayeh Taghavi.
- Gea Bortolomiol, Somayeh Taghavi, Elena Ghedini, Cristina Pizzolitto, Giuseppe Cruciani, Federica Menegazzo, Michela Signoretto "*Development of mesoporous catalysts*

for valuable chemical production from glucose" AIZ-CIS-GIC Jointly Meeting 2019, Amantea, Italy, July 12, 2019. Poster communication, presenting author Somayeh Taghavi.

Teaching and guidance activities

- Thesis Co-Supervision, " Sviluppo di un catalizzatorte eterogeneo per la trasformazione della biomassa lignocellulosica", Filippo Danese, April 2020, Bachelor degree in Sustainable Chemistry and Technologies.

- Thesis Co-Supervision, " Studio del biochar come nuovo supporto catalitico per la sintesi del γ-valerolattone", Martina Tretti, May 2021, Master degree in Sustainable Chemistry and Technologies.

- Thesis Co-Supervision, "Da scarto a risorsa: nuovi catalizzatori per le reazioni di idrogenazione", Margherita Riello, July 2022, Master degree in Sustainable Chemistry and Technologies.

- Giving a lecture, for the course of "Sustainable processes and Catalysis" provided by Prof. Michela Signoretto, for master students. A.Y. 2020/2021.

- Tutoring activity, Laboratory of Industrial Chemistry II, given by Pro. Michela Signoretto, for master students. A.Y. 2018/2019.

- Tutoring activity, Laboratory of Chemistry and Industrial Technologies, given by Pro. Michela Signoretto, for master students. A.Y. 2020/2021.

- Tutoring activity, at " Benedetti Tommaseo Liceo Scientifico" with the title of "Chemistry in the Kitchen", March 2019.

- Tutoring activity, the event of "Kids University at Ca' Foscari", May 2019.

- Tutoring activity, the event of "Venetonight", September 2019.

- Tutoring activity, at "Istituto Comprensivo Marta Minerbi, Mogliano Veneto, Scuola Primaria Giuseppe Verdi", January 2020.

Acknowledgement